THE TRANSVERSE AND LONGITUDINAL RESPONSE FUNCTIONS IN ^{4}He(e,e') FOR THE RANGE 0.55 GeV/$c \leq |\vec{q}| \leq$ 1.0 GeV/c

Kai Jin

Nanjing, Jiangsu, China

B.S., University of Science and Technology of China (2012)

A Dissertation Presented to the Graduate Faculty

of the University of Virginia in Candidacy for the Degree of

Doctor of Philosophy

Department of Physics

University of Virginia

August, 2020

Abstract

In electron scattering off a nuclear target, the Coulomb sum is defined as the integration of the longitudinal response function R_L over the energy loss of the incident electron in the quasi-elastic nucleon knock-out process. The Coulomb Sum Rule states that at sufficient high three-momentum-transfer $|\vec{q}|$, the Coulomb sum should equal to the total number of protons in the nucleus: $S_L \to 1$. Previously, precision data existed only up to $|\vec{q}| = 600$ MeV/c due to the limited beam energy used, and one data point existed for $|\vec{q}| = 1.14$ GeV/c but with limited precision. During Jefferson Lab experiment E05-110, electron scattering cross sections were measured in the quasi-elastic region on ^{4}He, ^{12}C, ^{56}Fe and ^{208}Pb targets at four scattering angles $(15°, 60°, 90°, 120°)$. The longitudinal and transverse response functions R_L and R_T were extracted in the momentum transfer range 0.55 GeV/$c \leq |\vec{q}| \leq$ 1.0 GeV/c using the Rosenbluth separation method. The Coulomb sum was formed in the same $|\vec{q}|$ range. The focus of this thesis is the extraction of $R_{L,T}$ from the ^{4}He target data. Preliminary results on $R_{L,T}$ and the Coulomb sum S_L for ^{4}He will be presented. The Coulomb sum for ^{4}He is found to be in good agreement with previous data, and still indicate quenching ($S_L < 1$) for the $|\vec{q}|$ region measured by this experiment.

Acknowledgments

First I would like to thank my advisor, Xiaochao Zheng for giving me the opportunity to work in her research group. She has constantly supported and encouraged me during my Ph.D. study. I benefited so much from her knowledge of physics and guidance in academic research. I sincerely appreciate her help in correcting many versions of this thesis and preparation for defense so patiently.

I would like to give special thanks to Jian-Ping Chen as my supervisor at JLab. He supervised me patiently in my research on E05-110 experiment data analysis and the polarized ^{3}He target upgrade. He would ask me all kinds of questions I might never think about myself, and always encourage me to develop my critical thinking and problem solving abilities. His great experiment and knowledge helped me to get a clear picture in both physics and research.

I would like to thank the E05-110 co-spokespersons, Seonho Choi, Jian-Ping Chen Alexandre Camsonne and Zein-Eddine Meziani for their guidance and advice during the CSR weekly meetings. I learned so much from the discussions during these meetings.

I would like to thank Michael Paolone who helped me with the analysis and gave me many suggestions. I want to thank the other students, Hamza Atac and Yan Huang who were working on this experiment with me. I also want to thank to all people who contributed to the E05-110 experiment.

I would like to thank Phil Arras, Stefan Baessler, Jian-Ping Chen, Kent Paschke and Xiaochao Zheng for being my thesis committee members.

I would like to thank Peng Peng, Jie Liu, Nguyen Ton, Longwu Ou, Dien Nguyen, Yang Wang, Xinzhan Bai, Haoyu Chen, Danning Di, and other friends at University of Virginia and JLab for the joyful time we shared.

I would like to thank my parents for their unconditional love and support for all decisions I made.

Contents

List of Figures

List of Tables

Chapter 1

Introduction

1.1 Electron Scattering

The building blocks of all visible matter are the nucleons. The properties of free nucleons have been studied extensively. On the other hand, nucleons in nuclei are in bound states and their properties are affected by the nuclear medium. Understanding medium modification of the nucleon structure inside the nucleus is an essential topic in nuclear physics.

To investigate the properties of nucleons in the nuclear medium, the electron is often used as a probe because of several advantages over hadron probes: First, the electromagnetic interaction between the electron and nuclei is much weaker than the strong interaction, and the physics of the nucleus is easier to extract compare with the more complicated hadron-probe system. In addition, the electromagnetic interaction is very well understood through Quantum Electrodynamics (QED). Therefore, the electron probe can provide the cleanest information about the nucleon and the nuclear structure.

In electron scattering process off a nuclear target, as shown in Fig. 1-1, an electron with initial energy E and momentum $\vec{k}$ scatters off a nucleus of mass M_A at rest. The scattered electron is then measured by a detector package at angle θ with scattered energy E' and momentum $\vec{k'}$. In the Born approximation, the process happens with

the exchange of a virtual photon γ with energy $\omega = E - E'$ and $\vec{q} = \vec{k} - \vec{k'}$. And

$$Q^2 = |\vec{q}|^2 - \omega^2 \tag{1.1}$$

gives the negative four momentum squared of the exchanged virtual photon.

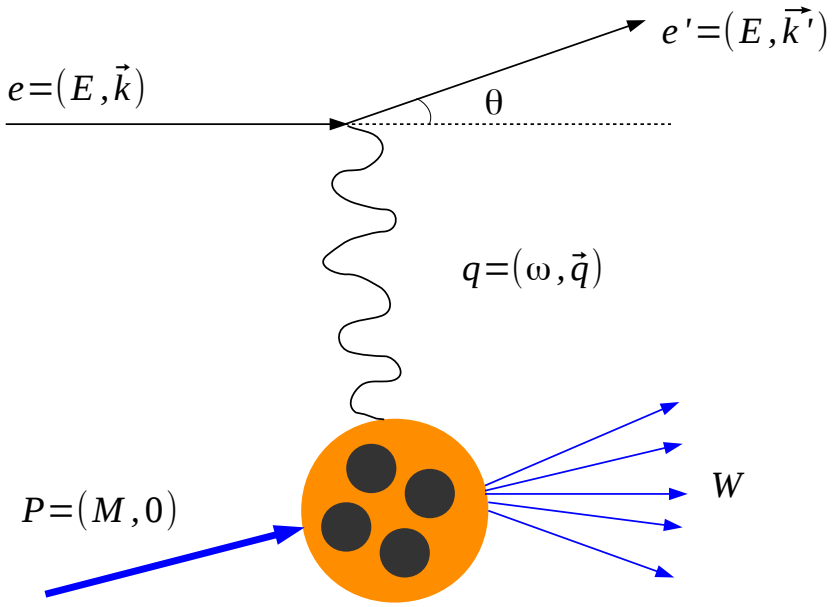

Figure 1-1: Inclusive electron scattering in the Born Approximation.

1.2 Inclusive Electron Scattering Spectrum

Figure 1-2 shows the spectrum of scattering cross section for typical electron inclusive scattering off a nuclear target. In inclusive scattering, only the scattered electrons are measured by detectors.

As shown in Fig. 1-2, different nuclear response structures can be observed as the energy loss of the electron ω varies. The nuclear response structures can be classified from low to high ω as: elastic peak, nuclear excitation peaks, giant resonances, quasi-elastic peak, contribution from meson exchange currents (MEC), Δ resonance peak, higher resonances, and deep inelastic scattering (DIS).

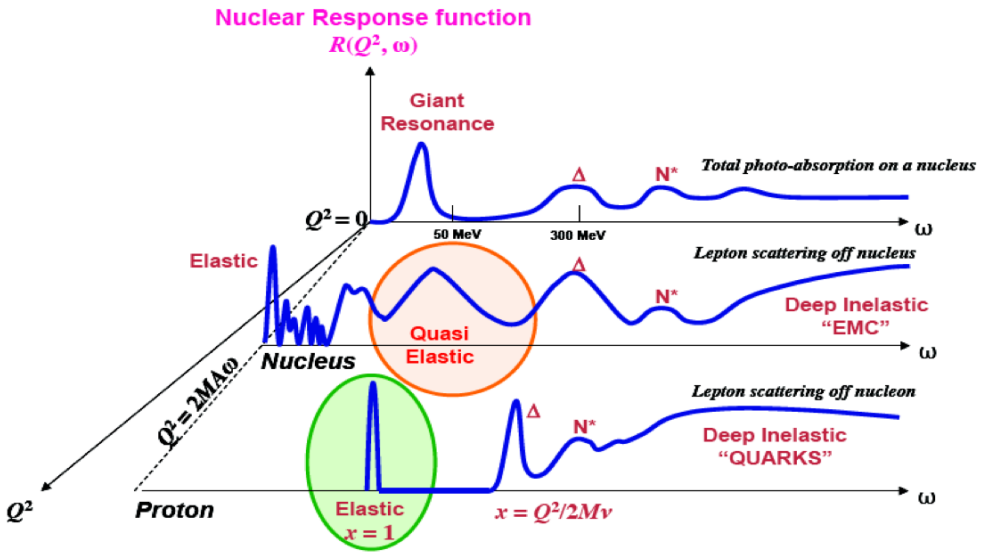

Figure 1-2: Nuclear responses to electron scattering. Figure reproduced from Ref. [1].

At small values of ω, the first structure seen is the elastic peak at $\omega = Q^2/2M_A$ where M_A is the nuclear mass, i.e, the electron's energy loss equals to the recoil energy of the nucleus. When the electron's energy loss is larger than the recoil energy, the nucleus enters excitation states, shown as the excitation peaks in the spectrum.

When ω is large enough the electron can knock out a single nucleon from the nucleus. This corresponds to the quasi-elastic peak in the spectrum. The quasi-elastic peak is a broad peak located slightly above $\omega = Q^2/2M_N$, where M_N is the mass of the nucleon and N can be either the proton or the neutron. The shift of the center of the quasi-elastic peak from $Q^2/2M_N$ is due to nucleon separation energy. The width of the quasi-elastic peak is due to the motion of nucleon in the nucleus, which is characterized by the Fermi momentum k_F and magnitude of the three-momentum-transfer $|\vec{q}|$.

If the energy loss continues to increase, the knocked out nucleon is excited into the Δ resonance state. Above the Δ resonance, there are higher resonances and then the deep inelastic scattering region.

1.3 Elastic Electron Scattering off the Nucleon

The differential cross section of electrons elastic scattering off a nucleon target can be expressed as:

$$\frac{d\sigma^2}{d\Omega} = \frac{\alpha^2}{4E^2 \sin^4(\theta/2)} \frac{E'}{E} \left(\frac{G_E^2 + \tau G_M^2}{1+\tau} \cos^2 \frac{\theta}{2} + 2\tau G_M^2 \sin^2 \frac{\theta}{2} \right), \tag{1.2}$$

where θ is the electron scattering angle, α is the fine-structure constant, τ is given by

$$\tau = \frac{Q^2}{4M_N}, \tag{1.3}$$

and $G_E(Q^2)$ and $G_M(Q^2)$ are the nucleon electric and magnetic form factors, respectively. In the absence of relativistic effects, $G_E(Q^2)$ and $G_M(Q^2)$ can be interpreted as Fourier transforms of the internal charge and magnetic moment distributions of the nucleon $\rho(\boldsymbol{r})$ and $\mu(\boldsymbol{r})$, respectively:

$$G_E(Q^2) \approx \int e^{i\boldsymbol{q}\cdot\boldsymbol{r}} \rho(\boldsymbol{r}) d^3\boldsymbol{r}, \tag{1.4}$$

$$G_M(Q^2) \approx \int e^{i\boldsymbol{q}\cdot\boldsymbol{r}} \mu(\boldsymbol{r}) d^3\boldsymbol{r}, \tag{1.5}$$

where $Q^2 = \boldsymbol{q}^2 - \omega^2$.

The form factors $G_E(Q^2)$ and $G_M(Q^2)$ are connected to the Dirac and Pauli form factors $F_1(Q^2)$ and $F_2(Q^2)$:

$$G_E(Q^2) = F_1(Q^2) + \frac{Q^2}{4M_N^2} \kappa_N F_2(Q^2), \tag{1.6}$$

$$G_M(Q^2) = F_1(Q^2) + \kappa_N F_2(Q^2), \tag{1.7}$$

where κ_N is the anomalous magnetic moment: $\kappa_p = \mu_p - 1 = 1.793$ and $\kappa_n = \mu_n - 0 = -1.913$ with μ the magnetic moment of the proton or the neutron.

1.4 Quasi-Elastic Electron Scattering

In the Born approximation, the differential cross section of unpolarized electrons scattering can be written as:

$$\frac{d^2\sigma}{d\Omega d\omega} = \sigma_M \left[W_2(Q^2,\omega) + 2W_1(Q^2,\omega)\tan^2\left(\frac{\theta}{2}\right)\right], \tag{1.8}$$

where

$$\sigma_M = \frac{4\alpha^2\cos^2(\theta/2)}{4E^2\sin^4(\theta/2)} \tag{1.9}$$

is the Mott cross-section for electron scattering off a point-like and infinitely heavy target. W_1 and W_2 are structure functions of the target. One can also separate contributions from longitudinal and transverse polarized virtual photons:

$$\frac{d^2\sigma}{d\Omega d\omega} = \sigma_M \left[\frac{Q^4}{\vec{q}^4} R_L(Q^2,\omega) + \frac{Q^2}{2\vec{q}^2\varepsilon} R_T(Q^2,\omega)\right] \tag{1.10}$$

where

$$\varepsilon(Q^2,\omega,\theta) = \left[1 + \frac{2\vec{q}^2}{Q^2}\tan^2\frac{\theta}{2}\right]^{-1} \tag{1.11}$$

is the virtual photon polarization, R_L is the longitudinal response function, and R_T is the transverse response function of the nucleus. Eqs. 1.10 is called Rosenbluth formula.

The functions R_L and R_T are related to W_1 and W_2 as:

$$R_T(Q^2,\omega) = 2W_1(Q^2,\omega), \tag{1.12}$$

and

$$\frac{Q^2}{|\vec{q}|^2} R_L(Q^2,\omega) = W_2(Q^2,\omega) - \frac{Q^2}{|\vec{q}|^2} W_1(Q^2,\omega), \tag{1.13}$$

One can interpret R_L as a measure of the charge component and R_T the magnetic component of the electromagnetic current of the nucleus. For quasi-elastic scattering

and in a non-relativistic frame, R_L can be expressed in the form:

$$R_L(Q^2,\omega) = \sum_f^{\infty} |\langle f|\hat{\rho}|i\rangle|^2 \delta(\omega - E_f + E_i), \tag{1.14}$$

where $|i\rangle$ and $|f\rangle$ are the initial and final states of the nucleus and $\hat{\rho}$ is the nuclear charge operator:

$$\hat{\rho} = \sum_{k=1}^{Z} F_1^p(q^2) e^{i\vec{q}\cdot\vec{r'}_k} + \sum_{k=1}^{N} F_1^n(q^2) e^{i\vec{q}\cdot\vec{r'}_k} \ , \tag{1.15}$$

where Z and N are the atomic and the neutron numbers of the nucleus, respectively. In Eq. 1.15, $\vec{r'}_k$ is the intrinsic coordinate operator for the individual nucleons:

$$\vec{r'}_k = \vec{r}_k - \frac{1}{A}\sum_{i=1}^{A} \vec{r}_i, \tag{1.16}$$

with $A = Z + N$ the nuclear mass number. Because the charge effects of neutrons are small and are usually neglected, we can write $\hat{\rho}$ as:

$$\hat{\rho} = \sum_{k=1}^{Z} F_1^p(q^2) e^{i\vec{q}\cdot\vec{r'}_k}. \tag{1.17}$$

Experimentally, R_L and R_T can be extracted by measuring cross sections at a given (Q^2,ω) at two or more angles as follows: If one plots $\varepsilon\frac{d\sigma^2}{d\Omega d\omega}/\sigma_M$ versus ε, the data measured at different angles should fall on a straight line. The slope of this line is $(Q^4/\vec{q}^4)R_L$, and the intercept is $(Q^2/2\vec{q}^2)R_T$. This technique is called Rosenbluth separation.

1.5 Coulomb Sum Rule

The Coulomb sum rule can be used to compare experimental results with theoretical predictions at high enough momentum transfer. The non-relativistic Coulomb sum [2] is defined as the integration of the ratio of the longitudinal response function $R_L(|\vec{q}|,\omega)$ to the nucleon charge form factor over the full range of energy loss ω and

at a constant three-momentum-transfer magnitude $q \equiv |\vec{q}|$:

$$\begin{aligned} C_{NR}(q) &= \int_{\omega_{el}}^{q} \frac{R_L(|\vec{q}|,\omega)}{F_1^2(Q^2)} d\omega + \Delta C \\ &= \sum_f |\langle f|\rho|i\rangle|^2, \end{aligned} \tag{1.18}$$

where $F_1^2(Q^2)$ is the nucleon charge form factor and $\omega_{el} = Q^2/2M$ corresponds to the elastic peak. The q in the integral upper limit is constrained by the virtuality of the exchanged photon: $\omega \leq |\vec{q}|$. ΔC is the contribution from outside the physically accessible region ($\omega > q$), which is small except at small q.

Using Eqs. 1.14-1.15 and the closure relation

$$\sum_f |f\rangle\langle f| = 1, \tag{1.19}$$

and neglecting ΔC and elastic peak contribution, one can write:

$$C_{NR}(q) = \int_{\omega_{el}^+}^{q} \frac{R_L(|q|,\omega)}{F_1^2(Q^2)} d\omega = Z + C_2, \tag{1.20}$$

where Z is the charge number of the target nucleus and C_2 is the two-nucleon correlation function. More detailed derivation can be found in Ref. [3].

At high momentum transfer, the relativistic effects and neutron contributions can be taken into account by using:

$$\tilde{G}_E^2 = |\tilde{G}_E^p(Q^2)|^2 + (N/Z)|\tilde{G}_E^n(Q^2)|^2, \tag{1.21}$$

where

$$\tilde{G}_E^{p(n)}(Q^2) = G_E^{p(n)}(Q^2)\sqrt{\frac{1+Q^2/4M_N^2}{1+Q^2/2M_N^2}}, \tag{1.22}$$

Using these new functions, another form of the Coulomb sum is defined:

$$C_L(Q^2) = \int_{\omega_{el}^+}^{\omega_{max}} \frac{R_L(Q^2,\omega)}{|\tilde{G}_E(Q^2)|^2} d\omega, \tag{1.23}$$

where $\omega_{max} = |\vec{q}|$ as before. Here we define C_L as a function of Q^2 instead of $|\vec{q}|$, because Q^2 is a Lorentz invariant.

The Coulomb sum normalized by the charge number of the nucleus Z, S_L, can be written as:

$$S_L(Q^2) = \frac{1}{Z}\int_{\omega_{el}^+}^{\omega_{max}} \frac{R_L(Q^2,\omega)}{|\tilde{G}_E(Q^2)|^2} d\omega. \tag{1.24}$$

The Coulomb sum rule predicts S_L be unity when $q > 2k_F$ with k_F the Fermi momentum of the nucleon. There exist a few known corrections to the Coulomb Sum Rule:

- Finite size effect: The finite size effect is due to center-of-mass motion [4][5]. In the calculation of the Coulomb Sum, the nucleon form factor should be calculated with nucleon's position relative to the center of mass. In the shell model, the subtraction of the center of mass in form factor is done by Tassie-Barker correction:

$$|F(\vec{q})|^2 = \exp\left(\vec{q}^{\,2}a^2/2A\right)|F_{SM}(\vec{q})|^2 \ , \tag{1.25}$$

  where a is the length parameter of the oscillator well, A is the number of nucleons in the nucleus, $F(\vec{q})$ is the corrected form factor, and $F_{SM}(\vec{q})$ is the usual shell model form factor from shell model wave functions. This effect becomes smaller with increasing mass number, as shown in Fig. 1-3. This correction is important for small q.

- Pauli blocking: Nucleons are fermions, and the Pauli exclusion principle requires that no two fermions can occupy the same quantum state within the same quantum system. When calculating the Coulomb sum, the result will be different if we neglect the anti-symmetrization property of the nucleons. Pauli blocking is important at small $|\vec{q}|$ and negligible at large $|\vec{q}|$. A comparison between with and without Pauli correlations was calculated by Lightbody using harmonic oscillator model for ^{12}C [7], as shown in Fig. 1-4.

- Long range correlations: In the region of low momentum transfer, the interac-

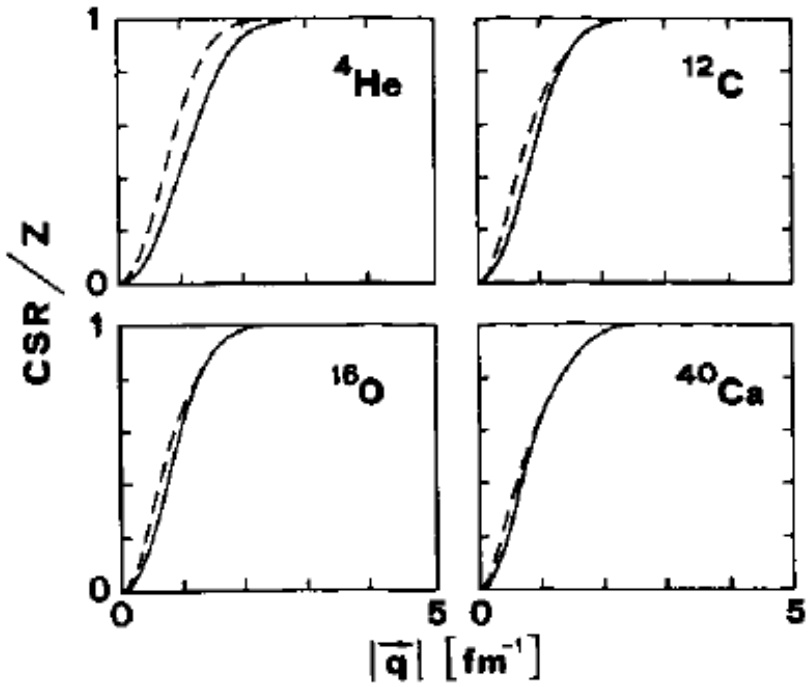

Figure 1-3: From Ref. [6]: CSR S_L divided by the proton number as a function of the three-momentum transfer, in the harmonic oscillator model, without (broken curve) and with (full curve) center-of-mass corrections.

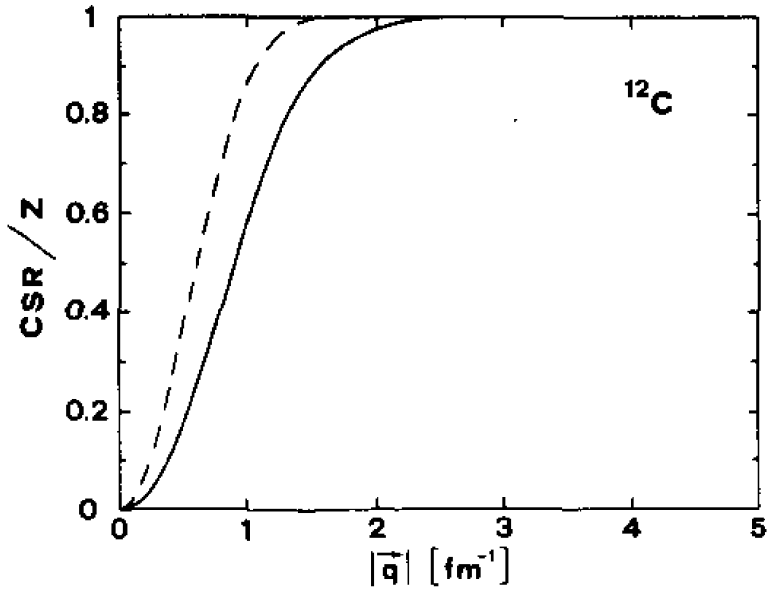

Figure 1-4: From Ref. [6]: CSR S_L divided by the proton number as a function of the three-momentum-transfer, without (broken curve) and with (full curve) Pauli correlations. The center-of-mass effect is not included in this figure.

tion between nucleons has a long range nature. The long-range correlation has been studied based on the random phase approximation (RPA) [8] [9]. The long range correlations are effective at low q and vanish at high q. The quenching (below unity) effect on the CSR produced by RPA is shown in Fig. 1-5.

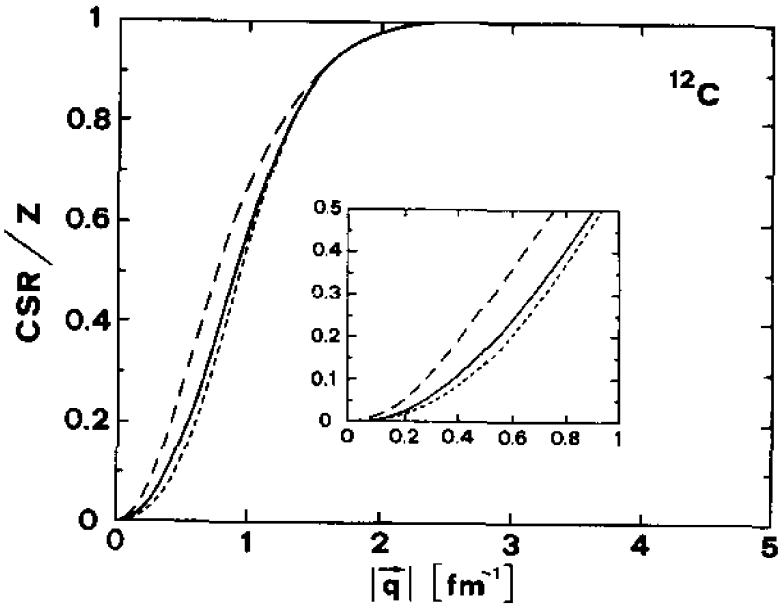

Figure 1-5: From Ref. [6]: CSR divided by the proton number as a function of the three-momentum-transfer in the harmonic oscillator model without (long broken curve) and with (full curve) center-of-mass correlations. The short broken curve represents the result including RPA correlations.

- Short range correlations: In the quasi-elastic region and when the incident electron's momentum is high enough, the virtual photon explores the medium and short inter-nucleon distances [6]. As a result, the longitudinal structure function is sensitive to the short range proton-proton correlations, and can cause the Coulomb sum to quench. Short-range correlations can be calculated, for example by modifying the short-range behaviour of the relative proton-proton wave function through a Jastrow-type correlation:

$$g(r) = 1 - e^{\gamma\alpha^2 r^2/4}, \tag{1.26}$$

where γ is a correlation parameter and α_0 is the harmonic oscillator constant,

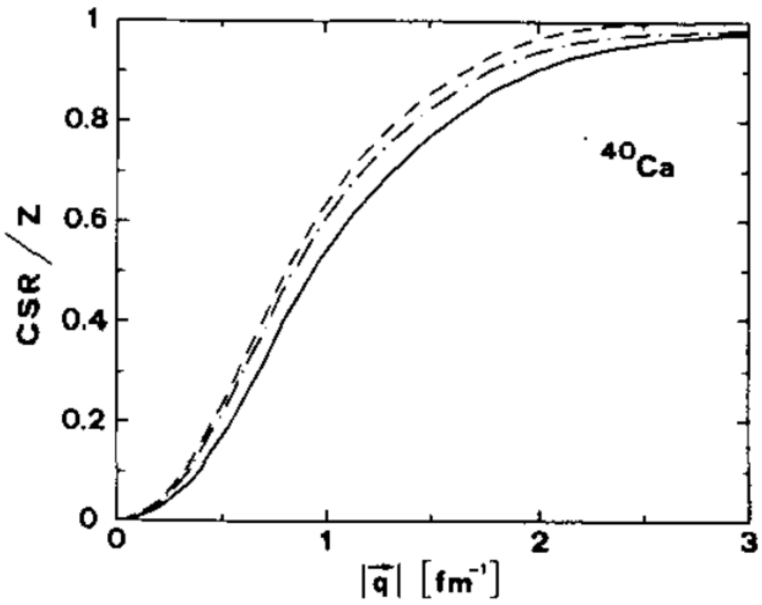

Figure 1-6: From Ref. [6]: CSR divided by the proton number as a function of the three-momentum-transfer in the harmonic oscillator model (broken curve, $\alpha_0 = 0.51$ fm^{-1}) and with short-range correlations included (chain curve, $\gamma = 56.1$; full curve: $\gamma = 24.9$).

and r is the distance between the two protons. The effect of short range correlation for ^{12}C is shown in Fig. 1-6.

1.6 World Data

In the past thirty years, a large experimental program has been carried out at Bates, Saclay and SLAC that aimed at the extraction of R_L and R_T for a variety of nuclei [10]. The Bates and Saclay data allowed Rosenbluth separation to be performed only up to $q = 600$ MeV/c due to the maximum beam energy available($\approx$ 800 MeV). At SLAC, only one measurement at $q = 1140$ MeV/c was performed due to the minimum beam energy available ($\approx$ 900 MeV). The large uncertainty of the SLAC data point makes it inconclusive. Overall, the longitudinal and transverse response functions extracted with Rosenbluth separation are available for ^{2}H, ^{3}H, ^{3}He, ^{4}He, ^{12}C, ^{40}Ca, ^{48}Ca, ^{56}Fe, ^{238}U in the range 200 MeV/c $\leq q \leq$ 600 MeV.

From previous world data, it was observed that the measured transverse response

functions R_T are generally in reasonable agreement with model predictions. In the kinematic region where contributions from processes such as elastic scattering, nuclear excitation and giant resonance are small, the agreement between theories and experiments is good. In regions where contributions from other processes – meson exchange current (MEC) and Δ excitation – are important, the situation becomes complicated. By taking into account these contributions, theorists can still reproduce the measured transverse response function well, see Figs. 1-7, 1-8, 1-10, 1-12 and 1-13.

For the longitudinal response function R_L, the agreement between calculation and experiment is reasonably good for very light nuclei such as ^{2}H, ^{3}H, and ^{3}He, see Figs. 1-7 and 1-8. For medium-weight to heavy nuclei such as ^{4}He, ^{12}C, ^{40}Ca, an obvious "quenching" – the R_L value is smaller than the calculation– is observed, see Figs. 1-7, 1-8, 1-9, 1-11, and 1-13. The quenching of R_L is observed to have a clear dependence on the nuclear mass number. Furthermore, the quenching has a dependence on the momentum transfer: the discrepancy between experimental R_L and simple Fermi gas model calculation becomes smaller when q increases. This feature may be explained by the Pauli correlation that decreases quickly when q increases.

The Coulomb Sum was extracted from the data mentioned above with three-momentum-transfer in the range 200 MeV/c $\leq q \leq$ 550 MeV/c, by integrating R_L over the experimental measured region of energy loss ω. As shown in Figs. 1-14, 1-15 and 1-16, Coulomb sum for the light nucleus ^{3}He reaches unity at increasing q quickly. On the other hand, there is a clear indication of quenching from theoretical calculation up to 40% for medium (^{56}Fe, ^{40}Ca and ^{48}Ca) and heavy nuclei (^{208}Pb).

A later analysis on Saclay and SLAC data by Jourdan [16] showed that no quenching exists by using the distorted wave Born approximation with the Coulomb corrections. The Coulomb corrections will be explained in Section 4.11.1. However, reanalysis of Saclay Data by Morgenstern and Meziani [10] with the effective momentum approximation showed that quenching still exists. The comparison between Morgenstern and Meziani's analysis and Jourdan's work is presented in Table 1.1. Two differences are identified: (a) the Coulomb corrections and (b) the use of the total error in the Saclay data but only the statistical error in the SLAC data by Jourdan.

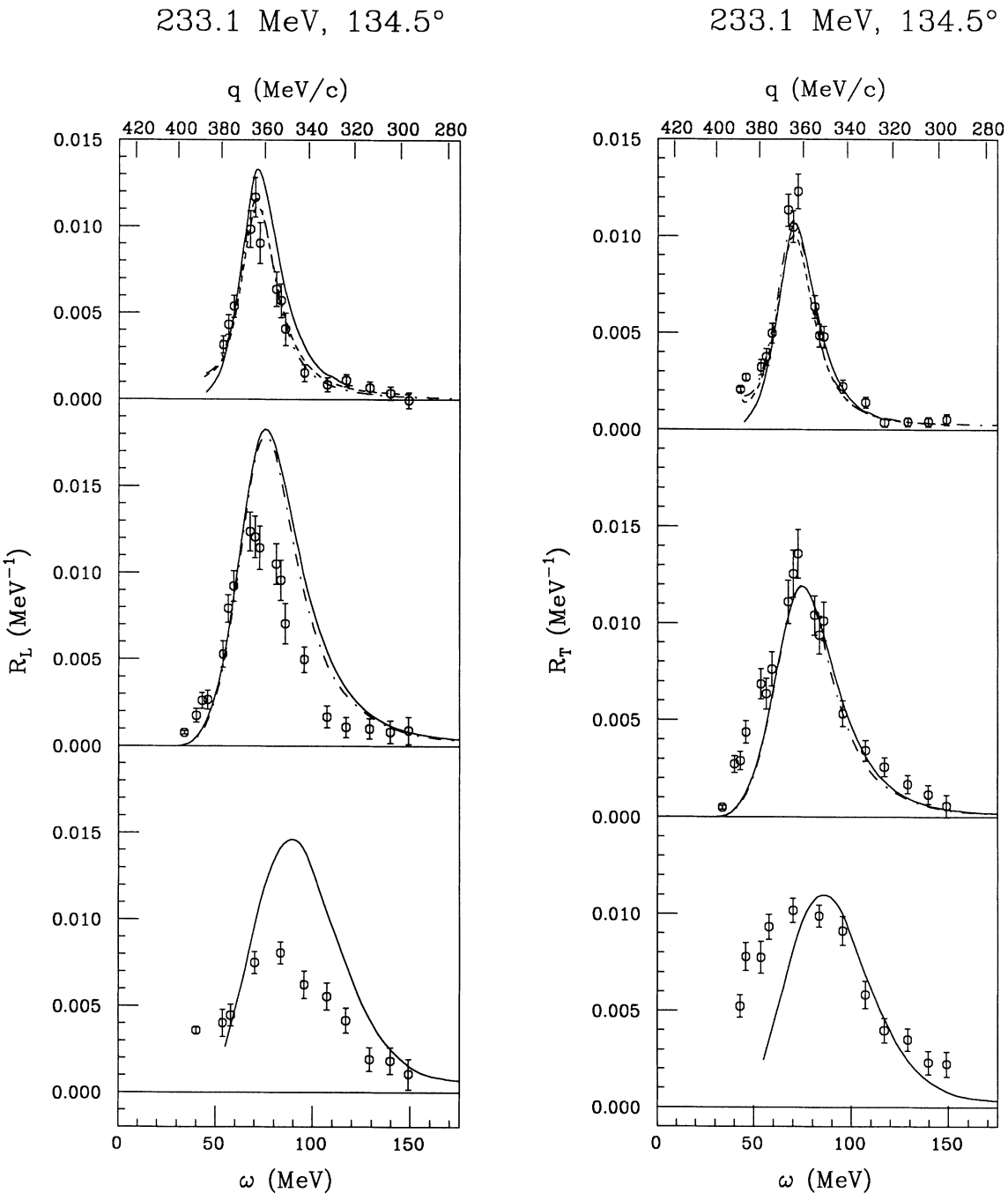

Figure 1-7: From Ref. [11]: Longitudinal and transverse response functions for $E =$ 233.1 MeV at $\theta = 134.5°$ for ^{2}H (top), ^{3}He (middle) and ^{4}He (bottom). Curves are theoretical calculations.

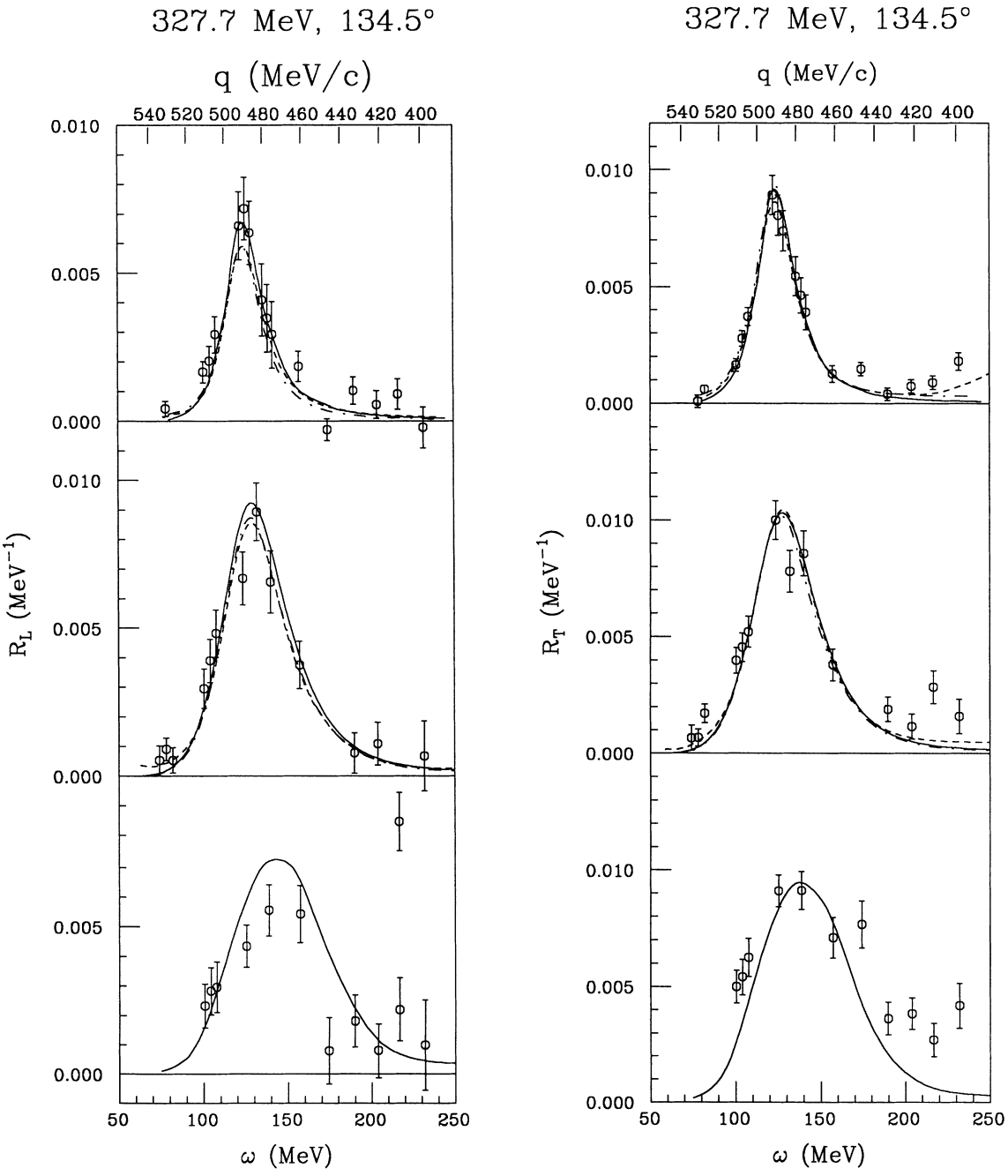

Figure 1-8: From Ref. [11]: Longitudinal and transverse response functions for $E =$ 327.7 MeV at $\theta = 134.5°$ for ^{2}H (top), ^{3}He (middle) and ^{4}He (bottom). Curves are theoretical calculations.

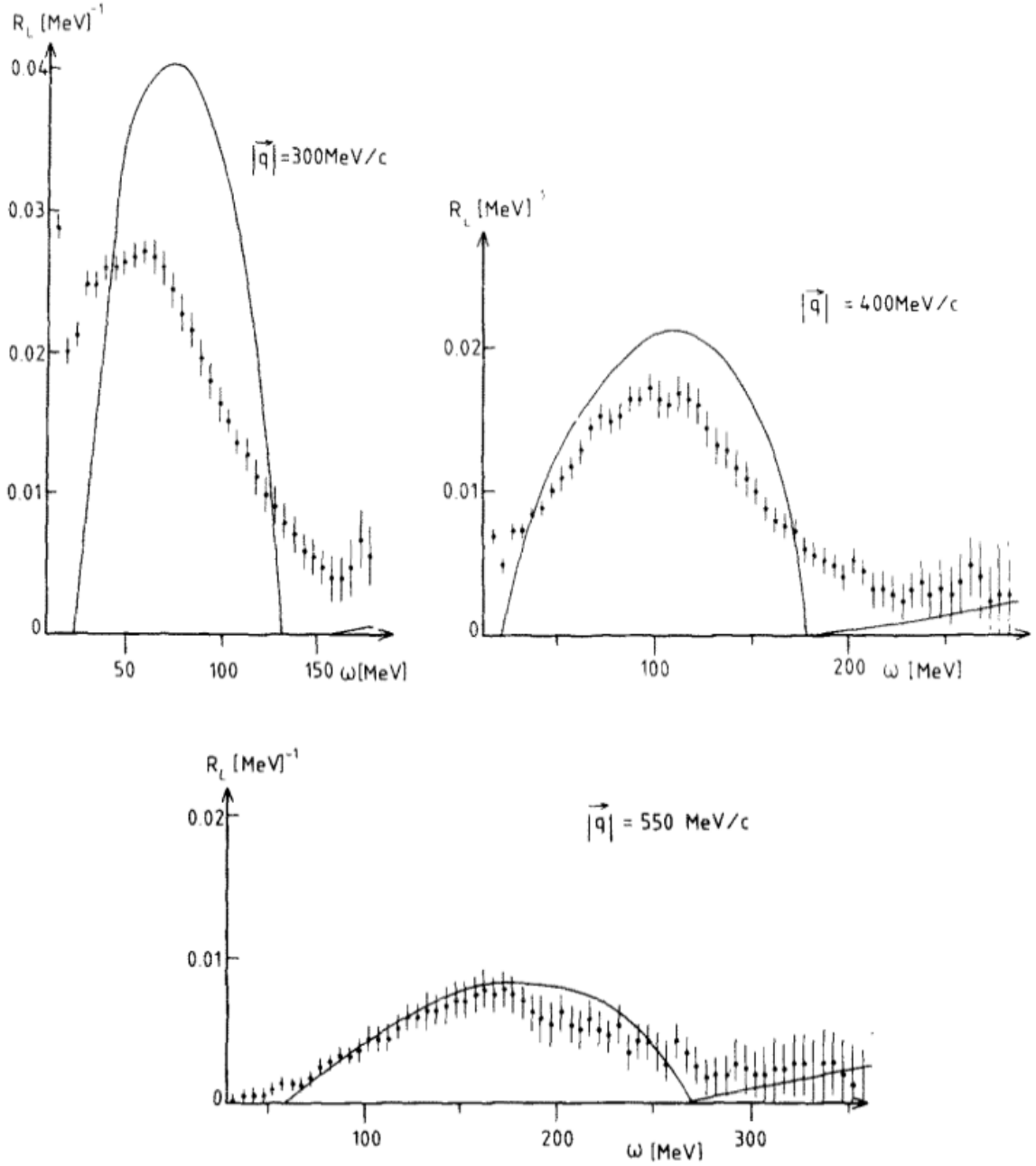

Figure 1-9: From Ref. [12]: The longitudinal response function R_L of ^{12}C versus ω for (a) $|\vec{q}| = 300$ MeV/c; (b) $|\vec{q}| = 400$ MeV/c; (c) $|\vec{q}| = 550$ MeV/c. Solid curves represent Fermi-gas calculations.

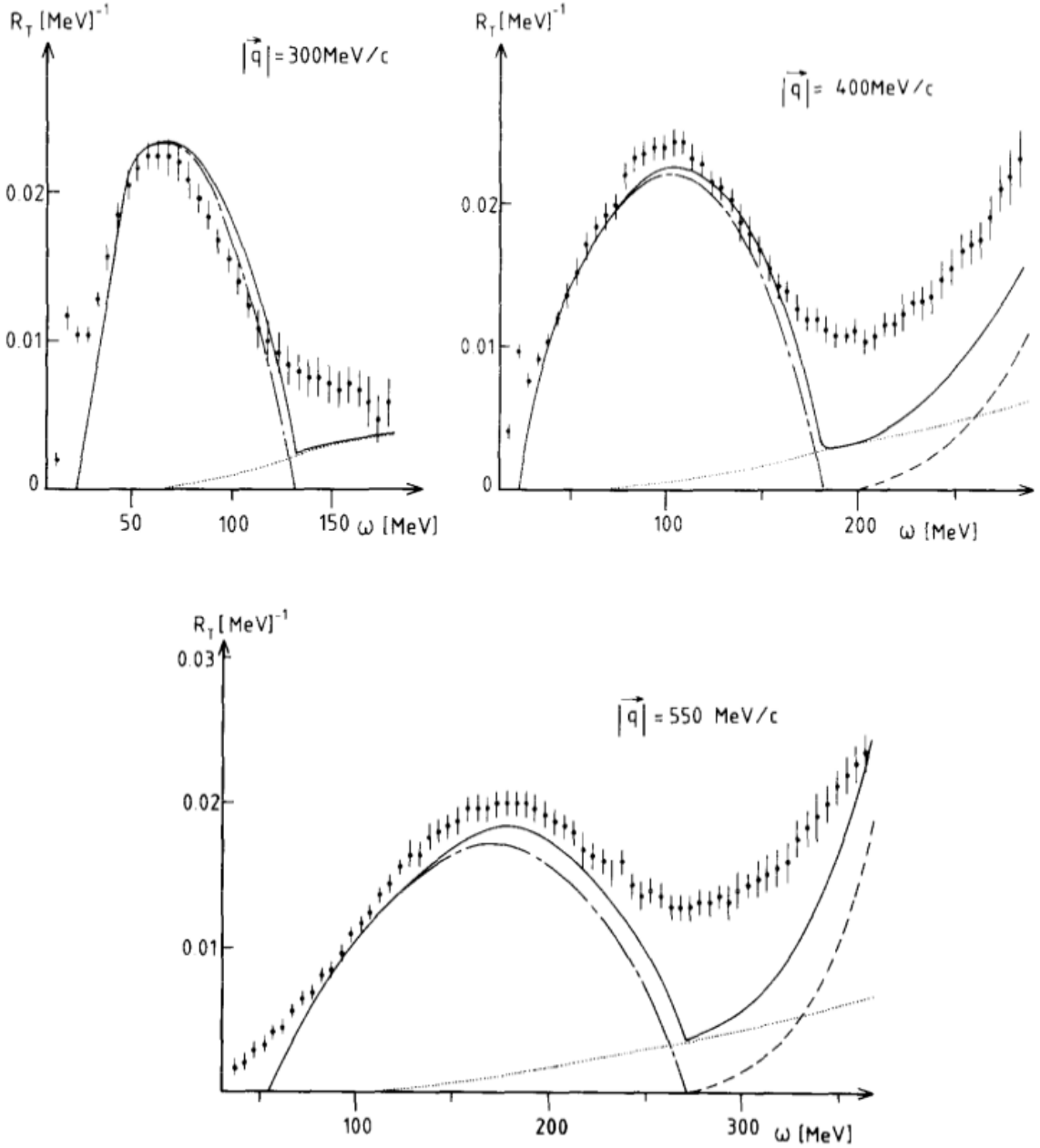

Figure 1-10: From Ref. [12]: The transverse response function R_T of ^{12}C as functions of ω for momentum transfer $|\vec{q}|$ =300 MeV/c, 400 MeV/c and 550 MeV/c. The solid curve represents the sum of the component curves: long dash curve: quasi-elastic; dot curve: MEC; short dash curve: pion production.

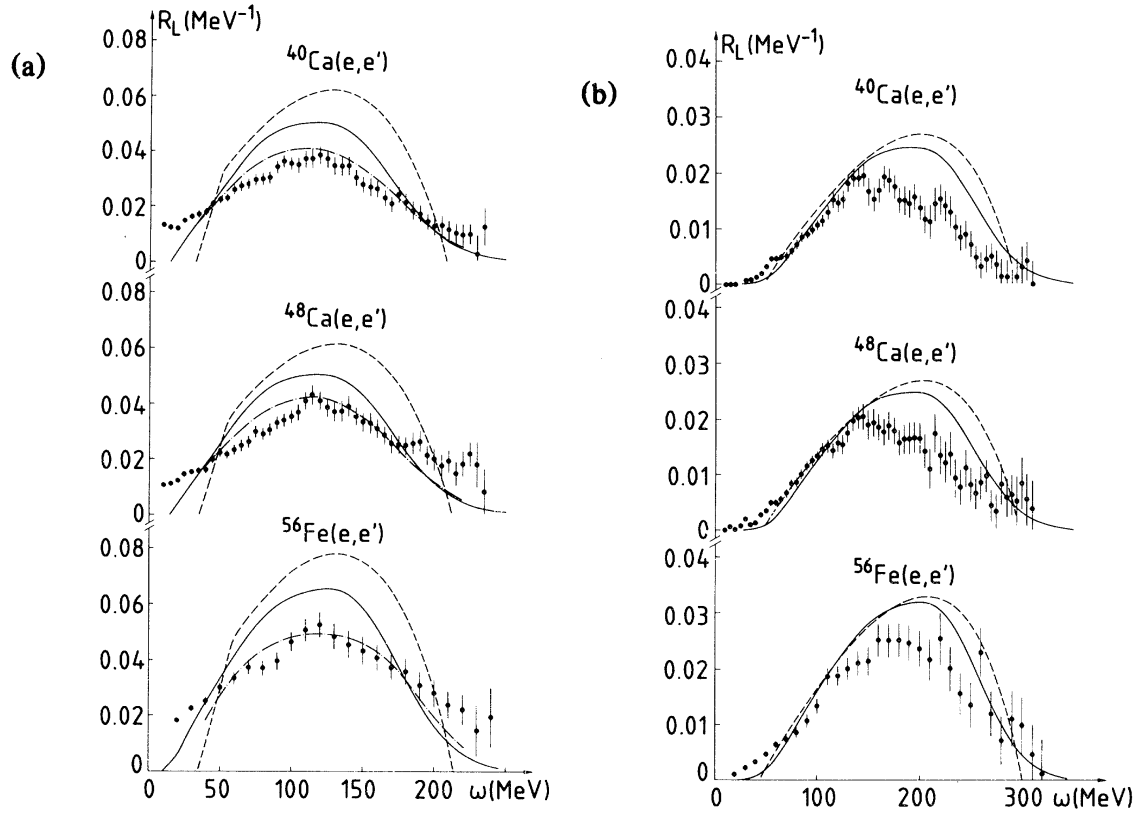

Figure 1-11: From Ref. [13]: Longitudinal response functions for ^{40}Ca, ^{48}Ca and ^{56}Fe at (a) $|\vec{q}| = 410$ MeV/c and (b) $|\vec{q}| = 550$ MeV/c. Dashed curves are Fermi gas model calculations.

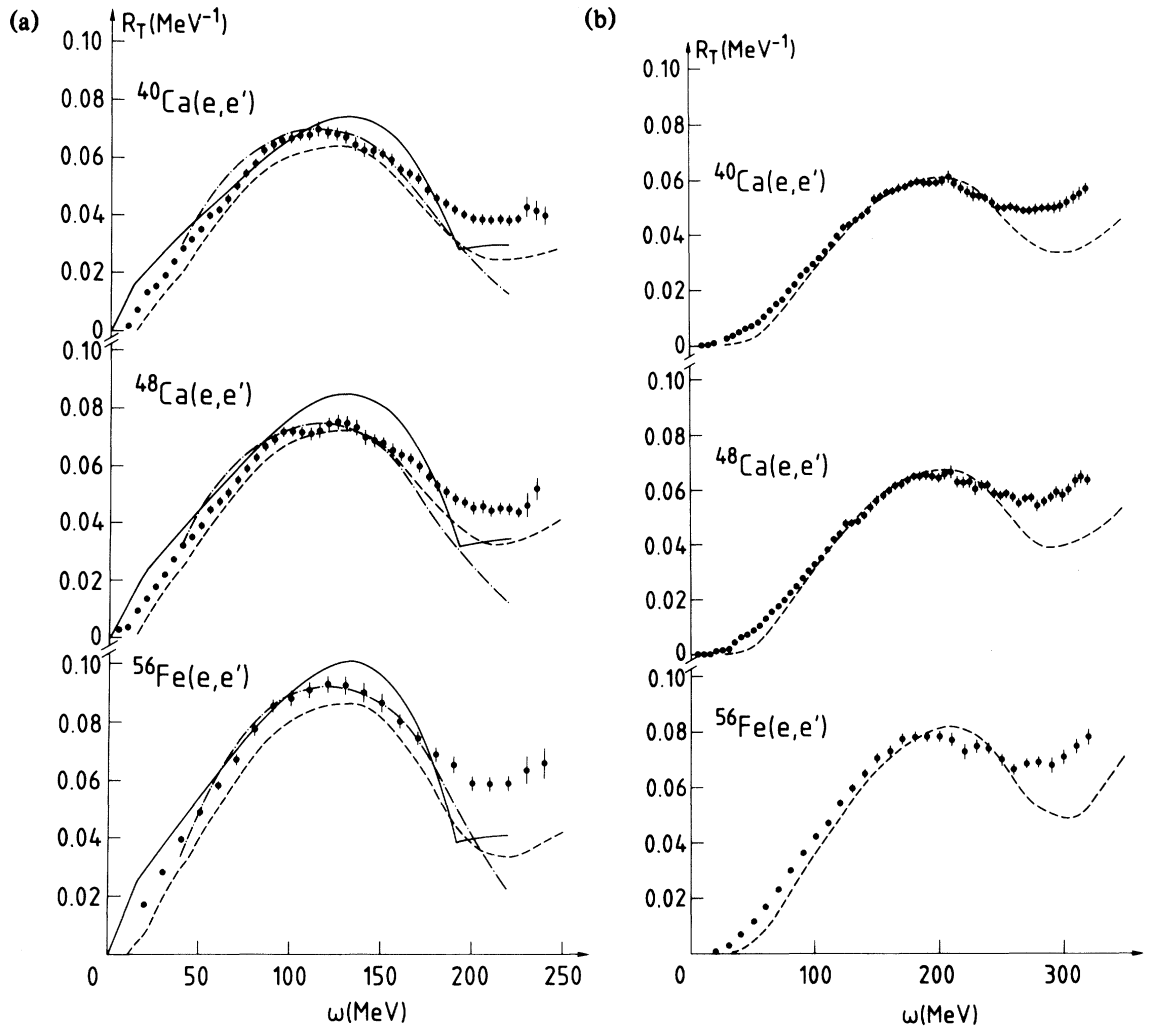

Figure 1-12: From Ref. [13]: Transverse response functions for ^{40}Ca, ^{48}Ca and ^{56}Fe at (a) $|\vec{q}| = 410$ MeV/c, (b) $|\vec{q}| = 550$ MeV/c. Dashed curves are Fermi gas calculations.

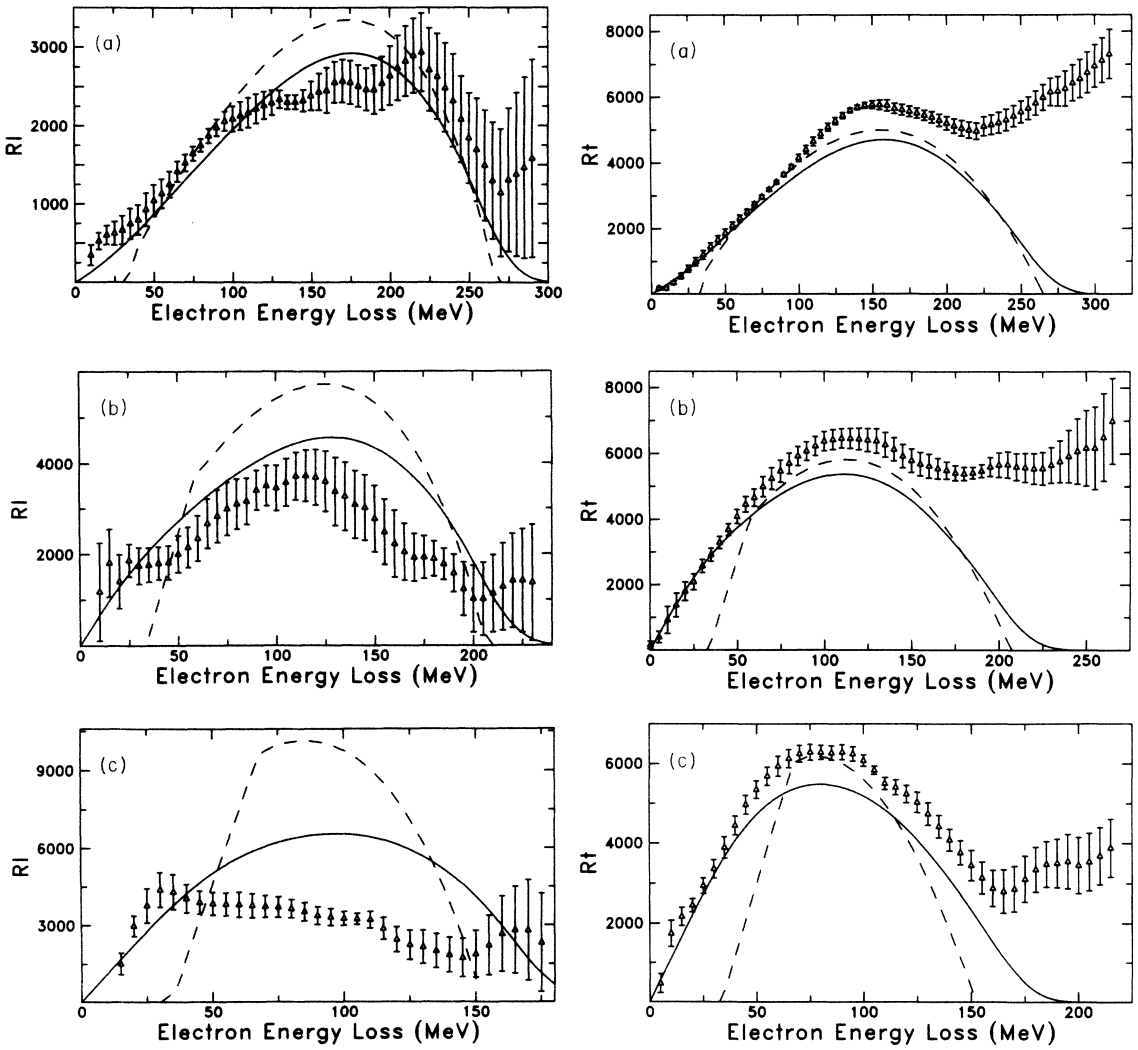

Figure 1-13: From Ref. [14]: Longitudinal (left) and transverse (right) response functions for ^{238}U at (a) $q = 300$ MeV/c, (b) $q = 400$ MeV/c, and (c) $q = 500$ MeV/c. Dashed curves are Fermi gas calculations.

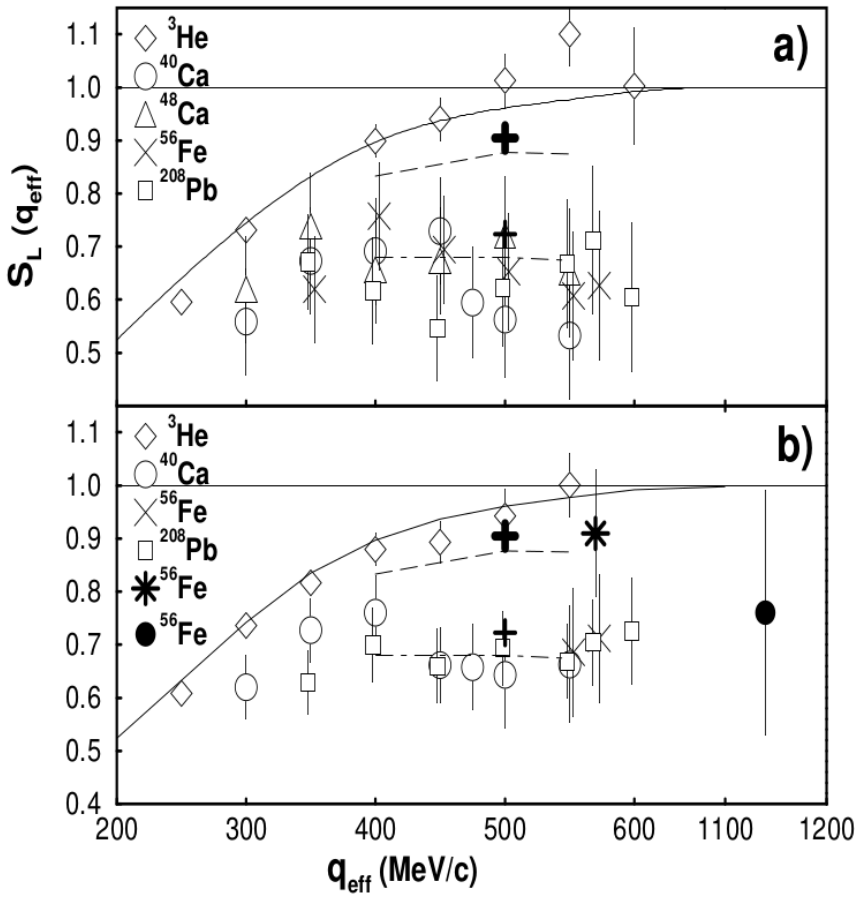

Figure 1-14: From Ref. [10]: S_L obtained in the Effective Momentum Approximation(EMA) as a function of q_{eff} (effective q, defined by Eq. 4.13 in Section 4.11.1):(a) the data shown were obtained using only cross section measured at Saclay; (b) the results by combining data from at least two different laboratories among Bates, Saclay and SLAC except for the data point from SLAC experiment NE9 at $q_{eff} = 1.14$ GeV/c [15]. In (b), filled circle: ^{56}Fe SLAC NE9 data [15]; thick star: Jourdan analysis of ^{56}Fe Saclay data [16].
Some model calculations results are shown as: Solid line: Microscopic Nuclear Matter calculations (N-M) calculations [17]; dash line: a partial NM Coulomb sum integrated only within the experimental limits at $400 \leq q_{eff} \leq 550$ MeV/c; dotted dash line: similar as dash line, but with modified form factors [18] [19]; thick right cross: partial Hartree-Fock(HF) calculations [20] in ^{208}Pb integrated within the experimental limits at $q_{eff} = 500$ MeV/c, thin right cross: similar as thick right cross, but with modified form factors.

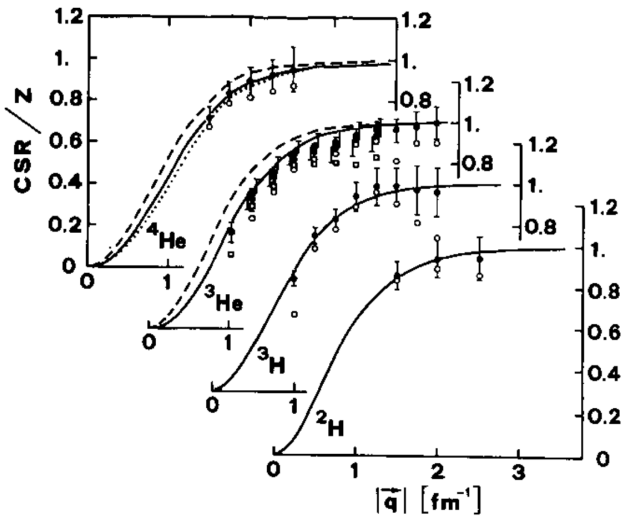

Figure 1-15: From Ref. [6]: The CSR divided by the proton number as a function of three-momentum-transfer for light weight nuclei. Continuous curves: results from Schiavilla [19]; dotted curve: correlated model. The open markers represent the experimental values, while the solid markers are the tail corrected results. Both Saclay (circles) and Bates (squares) data are shown for ^{3}He.

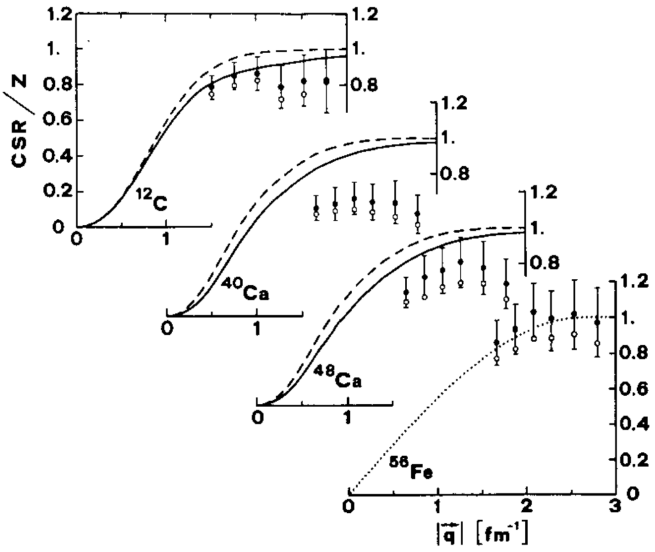

Figure 1-16: From Ref. [6]: The CSR divided by the proton number as a function of three-momentum-transfer for medium weight nuclei. Broken curves: harmonic oscillator; Continuous curves: correlated model; Dotted curve: Fermi gas model, k_F = 1.32 fm^{-1}. The open markers represent the experimental values from Saclay, while the solid markers are the tail corrected results.

Analysis	Saclay Uncertainty	SLAC Uncertainty	Coulomb Correction	S_L
Jourdan	total	statistical	No	0.86±0.12
	total	statistical	Yes	0.91±0.12
M&M	total	Not included	No	0.72±0.23
	total	Not included	Yes	0.63±0.20
	total	total	No	0.82±0.12
	total	total	Yes	0.73±0.12

Table 1.1: Comparison of the Coulomb Sum in ^{56}Fe between Jourdan and M&M analysis at $|\vec{q}| = 570$ MeV/c. Table reproduced from Ref. [10].

1.7 Theoretical Models

Since the 1980s, great efforts have been made to resolve the R_L quenching problem, also called the "missing charge problem". The traditional non-relativistic models cannot explain the problem. Some models included relativistic corrections, final state interactions, and two-body and many body correlations. These effects are important but not large enough to fully explain the quenching of R_L if the predicted R_T is to remain in agreement with the experiment data. As an example, predictions based on the Auxiliary Field Diffusion Monte Carlo method [21] are shown in Fig. 1-17.

In order to explain the missing charge puzzle, several more exotic explanations have been raised:

- Inadequate Coulomb correction: The idea of the Rosenbluth separation of the longitudinal and transverse response functions is based on the Plane Wave Born Approximation (PWBA) and one photon exchange. This approximation is not valid for medium and heavy nuclei because of the Coulomb field of the nucleus. In a large Z nucleus, the strong Coulomb field of the protons distorts the wave front of the electron and the wave function of the electron is not plane wave anymore. The electrons are accelerated when approaching the nuclei and decelerated when leaving the nuclei. This effect will modify the scattered electron's momentum and the scattering cross section as well as R_L and R_T. The effect of the Coulomb field can be calculated with the Distorted Wave Born Approximation (DWBA) [22][23]. However, DWBA cross sections cannot be written in a

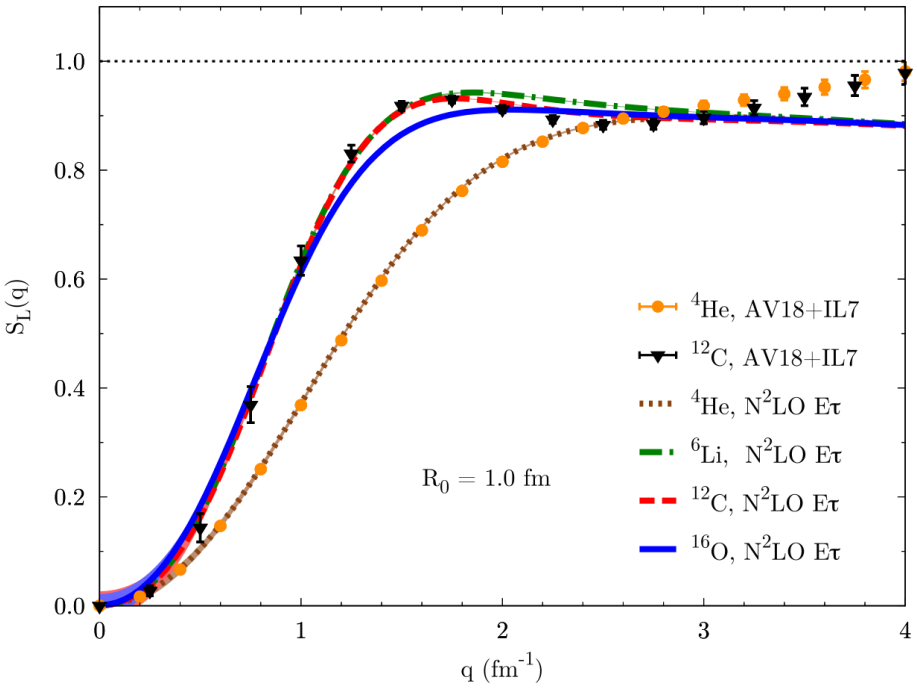

Figure 1-17: From Ref. [21]: Model prediction of Coulomb sum rule for $4 \leq A \leq 16$. Lines refer to AFDMC (Auxiliary Field Diffusion Monte Carlo) results for the N^{2}LO $E\tau$ potential with cutoff $R_0 = 1.0$ fm. Solid symbols are the GFMC (Green Function Monte Carlo) one- plus two-body results for AV18+IL7. Shaded areas indicate the statistical Monte Carlo uncertainty.

separable form, and are extremely time consuming in numerical complications. Due to these difficulties, the Effective Momentum Approximation (EMA) is developed [24][25]. As mentioned earlier, the re-analysis of Saclay and SLAC data by Jourdan [16] suggested that no quenching exists if using the distorted wave Born approximation with the Coulomb corrections.

- Swollen nucleon models: Noble first suggested another approach that there could be an effective change in the size of the nucleon in the nuclear medium [26], which is also used to explain the EMC effect [27][28]. The changing of nucleon size in the nuclear medium may relates to the partial deconfinement of quarks in the nuclear medium, which leads to modified quark distributions in the nucleus. Noble's calculations indicated a 30% increase in the nucleon charge radius. He calculated the CSR by using the Fermi gas model (FGM) with an increased charge radius. The results are shown in Fig. 1-18.

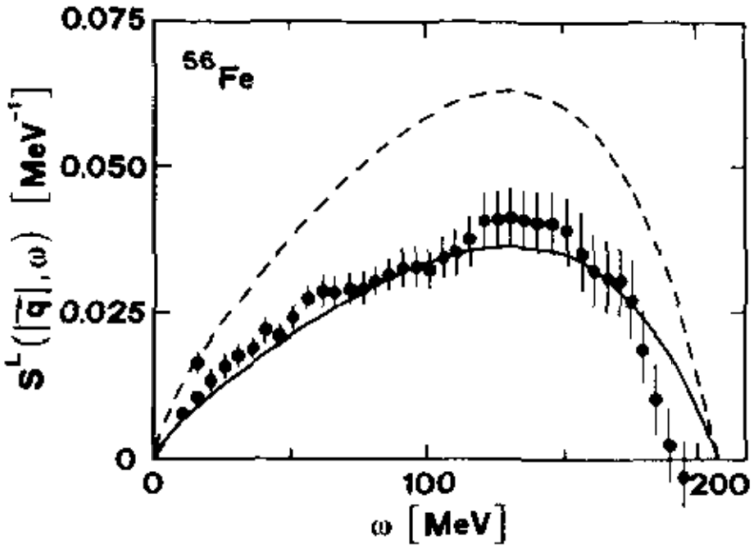

Figure 1-18: From Ref. [6]: Longitudinal structure function in the relativistic FGM calculation of Noble [26] for $|\vec{q}| = 410$ MeV/c with $k_F = 1.11$ fm^{-1}). Experimental data are from Altemus [29]. Broken curve: impulse approximation; Full curve: results with scaled root mean square radius.

Chapter 2

The CSR Experiment Setup

During experiment E05-110 that ran from October 23th 2007 to January 16th 2008 in Hall A of Thomas Jefferson National Accelerator Facility (Jefferson Lab), the Coulomb Sum Rule was tested. To determine the Coulomb Sum, both response functions R_L and R_T of four different nuclei (^{4}He, ^{12}C, ^{56}Fe, ^{208}Pb) were measured from inclusive scattering in the quasi-elastic region. In this chapter, the experiment setup and most of instrumentation are described. In Chapter 3, the optics calibration and acceptance correction for the spectrometer system will be presented. Chapter 4 covers the data analysis procedure. Finally, preliminary results on $R_{L,T}$ and S_L of ^{4}He will be presented in Chapter 5.

2.1 JLab Experiment E05-110

The purpose of JLab E05-110 experiment is to test Coulomb sum rule with three-momentum-transfer in the range 550 MeV/$c \leq |\vec{q}| \leq$ 1 GeV/c and with significantly improved precision. This is the first experiment that measured longitudinal and transverse response functions in this three-momentum-transfer range: the previous experiments performed at MIT Bates and Saclay covered 200 MeV/$c \leq q \leq$ 600 MeV/c, and SLAC NE9 had only one point at $q = 1140$ MeV/c with limited precision.

During E05-110, an unpolarized electron beam was scattered from ^{4}He, ^{12}C, ^{56}Fe and ^{208}Pb targets to measure cross-sections in the quasi-elastic region. The ^{4}He target

is a gaseous target, ^{12}C and ^{56}Fe targets are solid foil targets, and ^{208}Pb target is a solid foil target kept in liquid hydrogen. The Hall A High Resolution Spectrometer (HRS) pair was used to detect the scattered electrons at four different angles: 15°, 60°, 90° and 120°. The relatively large differences between scattering angles allowed for the largest Rosenbluth lever arm within a single experiment compared to all previous experiments. The cross section data were used to extract the R_L and R_T response functions and the Coulomb Sum.

In order to have as much coverage as possible in (q, ω) to reduce systematic uncertainties in the Rosenbluth separation procedure, data were acquired for beam energies between 400 MeV and 3679 MeV and spectrometer central momenta between 100 MeV/c and 3.6 GeV/c, see Table 2.1. The kinematic coverage is shown in Fig. 2-1. The main difficulty of the experiment is the massive number of kinematic settings and the very low momentum setting of the HRS.

15°		60°		90°		120°	
E	E'_{low}	E	E'_{low}	E	E'_{low}	E	E'_{low}
1260	810	646	187	400	100	400	100
1646	1147	740	250	528	108	528	98
2145	1605	845	305	646	127	646	107
2448	1838	957	377	740	170	740	110
2845	2135	1030	270	845	135	845	105
3249	2440	1102	333	957	267	957	237
3679	2770	1260	370	1030	100		

Table 2.1: Incident electron beam energy and the lowest scattered electron energy detected at each kinematic setting of JLab E05-110. All energies shown are in MeV and all four targets shared the same settings.

A total of six Ph.D students worked on the data analysis of the E05-110 experiment: Huan Yao [30] focused on ^{12}C and ^{56}Fe target data; Xinhu Yan [31] focused on ^{12}C and ^{56}Fe target data; Yoomin Oh [32] focused on ^{4}He and ^{12}C target data; Hamza Atac [1] focused on ^{12}C and ^{56}Fe target data; Yan Huang focused on ^{208}Pb target data; and I focused on ^{4}He target data. The analysis of ^{4}He target data is reported in this dissertation. The work presented here will also help finalizing all prior analysis performed by the other five students.

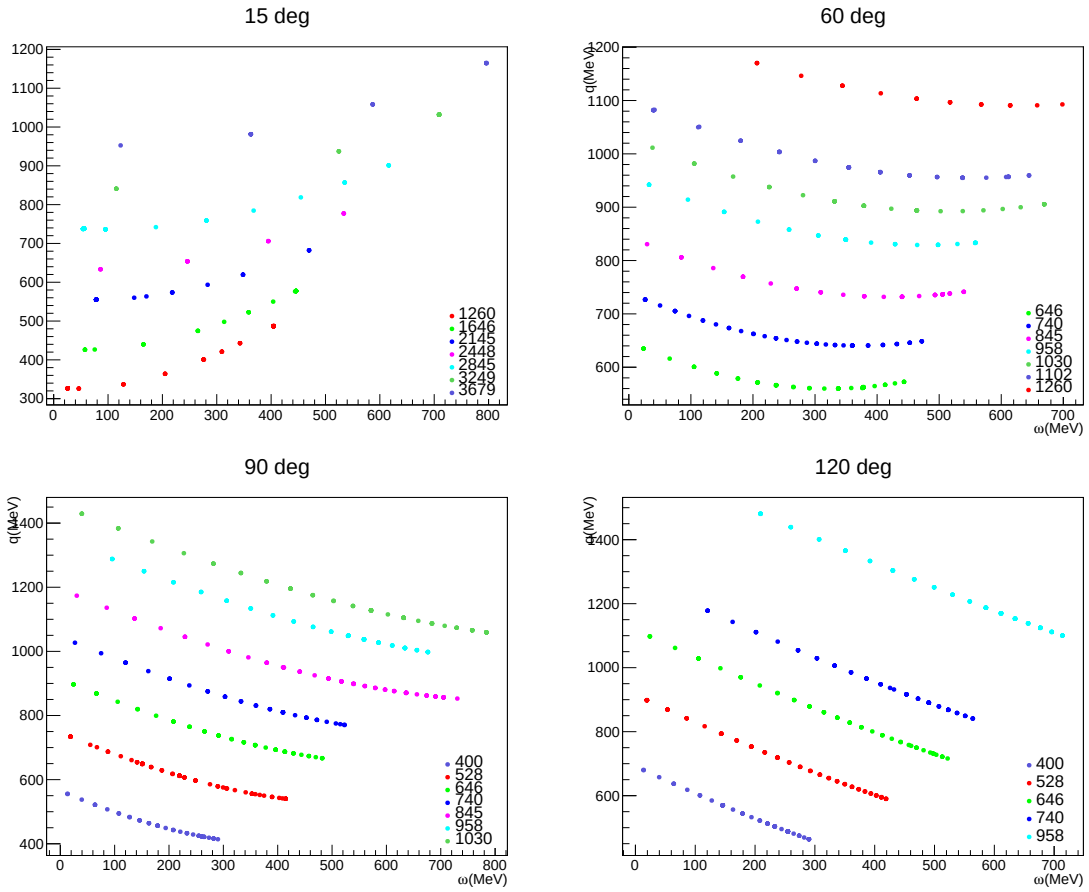

Figure 2-1: Kinematic coverage of the CSR experiment. Each graph is for one scattering angle and each color represents a beam energy in MeV. The x axis is energy loss ω (MeV), and the y axis is three-momentum-transfer q (MeV) .

In the remaining part of this chapter, I will present details of the experiment setup, including the electron beam, Hall A beamline components, the cryogenic and solid targets and the HRS system.

2.2 The Accelerator and the Electron Beam

The Continuous Electron Beam Accelerator Facility (CEBAF) at JLab was built to investigate the structure of nuclei and hadrons and the underlying fundamental interactions in the region below the high-energy "asymptotically free" regime. The accelerator consists of an electron injector, two super-conducting linear accelerators (linacs), recirculation arcs, and RF separators. The layout of the accelerator is shown in Fig. 2-2.

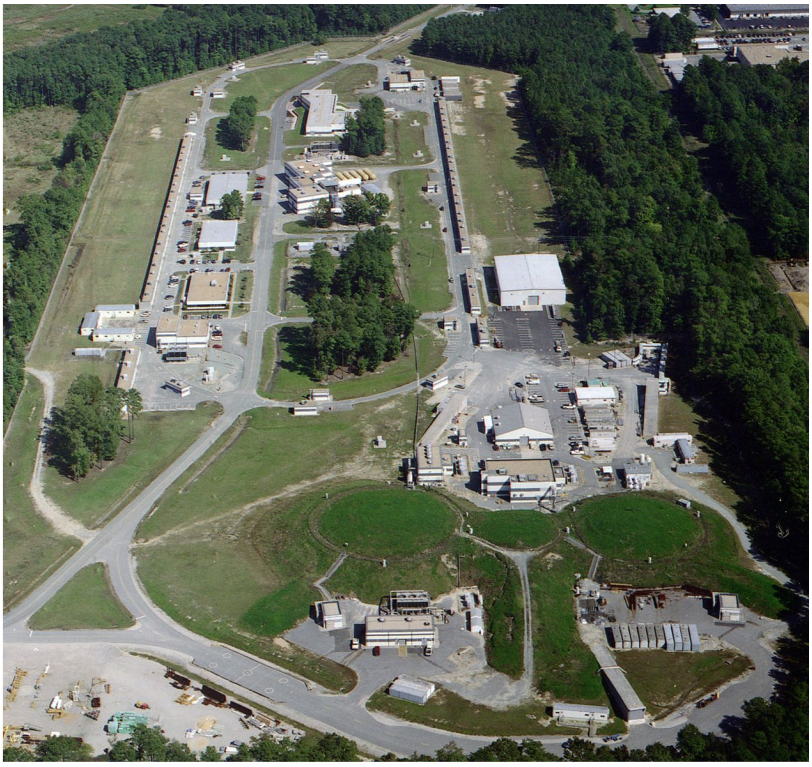

Figure 2-2: Aerial view of the JLab accelerator during the 6 GeV era.

The source of polarized electrons is a strained GaAs cathode at the injector. The cathode is illuminated by a 1497 MHz gain-switched 780 nm diode laser, and provides a polarized beam with up to 90% polarization.

The beam is first accelerated to 45-60 MeV in the injector, then is transported to the north linac. The north and the south linacs are connected by recirculation arcs with radius 80 m that can turn the beam by 180° from the south to the north linac and vice versa, forming a recycling beamline in the shape of a racetrack. Quadruple and dipole magnets in each arc provide the field that keeps the beam on a precise path and tightly focused. Each linac contained 20 cryomodules during the 6 GeV era, and 5 new cryomodules were added to each linac during the 12 GeV upgrade. There are eight super-conducting niobium RF cavities in each cryomodule, kept at a temperature of 2 K using liquid helium from the CHL (Central Helium Liquefier). The RF cavities are phased to provide maximum acceleration. During the 6 GeV era, the nominal gain of each linac is up to 400 MeV, and it can be tuned further up to 600 MeV, making it possible for the beam to reach an energy of 6 GeV.

After passing through the south linac, the beam can either go to the next recirculation arc for another pass around the accelerator, or enter one of the experiment halls using RF extraction. The designed maximum current is 200 μA, which can be split arbitrarily to three 499 MHz bunch trains, one for each of the three experimental halls, Hall A, B and C. The CSR experiment required 50 μA average current, with energies ranging from 0.4 to 4 GeV.

2.3 Beam Energy Measurement

Beam energy measurements is an important part of the experiment to ensure the accuracy of data analysis. There are two independent methods to measure the absolute beam energy: Arc measurement, which is based on measurements of the beam deflection in a known field; and eP measurement, which is based on measurement of the electron elastic scattering off a proton target. During the CSR experiment, only the Arc measurement was used.

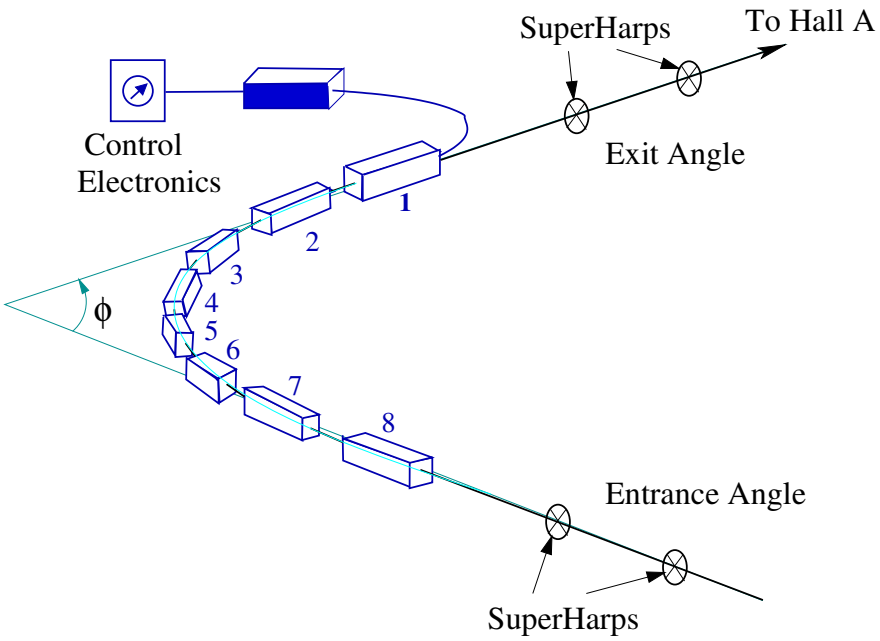

Figure 2-3: Arc section of the Hall A beamline. Figure reproduced from [33].

2.3.1 Arc Measurement

The principle of this method is that electrons in a magnetic field will move in a circular pattern, with the radius depending on the field strength and the electron's momentum. The Arc method measures the bending radius of the beam in the arc section, see Fig. 2-3.

The momentum of the beam (P in GeV/c) is related to the field integral in eight dipoles ($\int \vec{B} \times d\vec{l}$ in T$\cdot$ m) and the net bending angle through the arc section (θ in radians) by:

$$P = k \left| \frac{\int \vec{B} \times d\vec{l}}{\theta} \right| \tag{2.1}$$

where $k = 0.299792$ GeV $\cdot$ rad $\cdot$ T^{-1} $\cdot$ m $^{-1}$.

The arc measurement consists of two simultaneous measurements. One is for the bending angle of the beam measured by a set of wire scanners. Another is for the field strength integral $\int \vec{B} \times d\vec{l}$ of the eight dipoles based on the reference magnet (the 9-th dipole) field measurement. There are two operation modes in the Arc section: the dispersive (invasive) and non-dispersive (non-invasive) mode. The dispersive mode

will affect the quality of the beam, but has better precision ($\Delta E_{beam}/E_{beam} = 2\times10^{-4}$) than non-dispersive mode (5×10^{-4}). Detailed description of the Arc measurement can be found in [34].

The Arc measurement during the CSR experiment was done at a beam energy of 845 MeV. The measurement result (845.08 ± 0.2 MeV) is consistent with the so-called "Tiefenbach" energy (844.87 ± 0.4 MeV), calculated from the Hall A arc $\vec{B}d\vec{l}$ value and the Hall A beam position measured from the beam position monitor (BPM). For other energies, the Tiefenbach values are used for the analysis.

2.4 Beam Charge Measurement

The incident number of beam electrons is an essential normalization factor in the extraction of cross sections. It is proportional to the beam current measured by the Beam Current Monitor (BCM) in Hall A, which provides a stable, low-noise, non-interfering beam current measurement [34].

The BCM consists of an Unser monitor, two RF cavities, associated electronics and a data-acquisition system. The diagram of BCM is shown in Fig. 2-4. The cavities and the Unser monitor are located 25 m upstream of the target. The Unser monitor is a parametric current monitor that provides an absolute reference. The two resonant RF cavity monitors on two sides of the Unser Monitor are stainless steel cylindrical high-Q ($Q \approx 3000$) waveguides. They are tuned to the frequency of the beam (1.497 GHz), producing voltage levels at their outputs that are proportional to the beam current. Each of the RF output signals from the two cavities is split into sampled and integrated parts of the data acquisition system.

The sampled data were sent to a high-precision Digital Multi-Meter (DMM), which provides an output signal that represents the root-mean-square (RMS) of the input signal during that second. The output is proportional to the beam charge accumulated for that second. Signals from both cavities are sent to a computer through GPIB cables, and are recorded every 1-2 seconds in the Experimental Physics and Industrial Control System (EPICS) database.

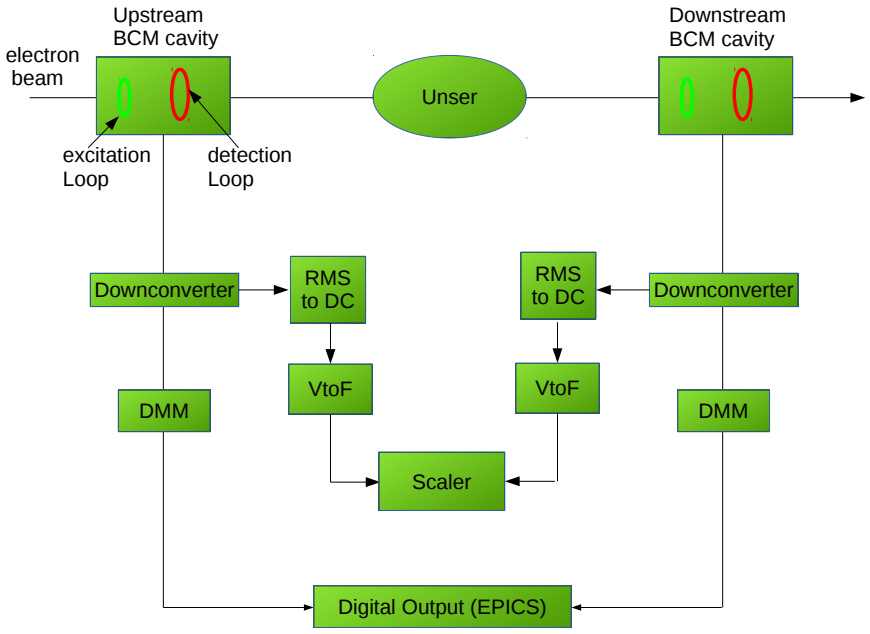

Figure 2-4: Beam current monitor diagram. Figure reproduced from [34].

The integrated data are sent to an RMS-to-DC converter to generate an analog DC voltage level. The voltage level is sent to a Voltage-To-Frequency (VtoF) converter whose output frequency is proportional to the input. The frequency signal is fed to 200 MHz VME scalers and stored in the data stream with other scaler information every 4 seconds. The scaler value accumulates during the run and is proportional to the time-integrated voltage level. The regular RMS to DC output is linear for currents from 5 μA to 200 μA. A set of amplifiers with different gain factors ($\times 1$, $\times 3$, $\times 10$) can extend the linear region to lower currents. The six signals for each spectrometer (U1, U3, U10 and D1, D3, D10, corresponding to the three gain factors and the up and downstream cavities respectively) are sent to scalers and provide the charge information with redundancy.

The beam charge can be derived from BCM scaler reading $\text{Scaler}_{bcm\times n}$ as

$$Q_{bcm\times n}(\mu C) = \frac{\frac{\text{Scaler}_{bcm\times n}}{T} - \text{Offset}_{bcm\times n}}{\text{Constant}_{bcm\times n}} T \ , \tag{2.2}$$

where $n = 1, 3, 10$ is the gain factor of the amplifiers and T is the clock time for each

Gain	Upstream Calibration Constants	Upstream Offsets	Downstream Calibration Constants	Downstream Offsets
1	2372.38	362.5	24727.91	160.1
3	7294.51	350.2	7517.37	126.7
10	22067.11	442.6	23485.15	321.1

Table 2.2: BCM calibration constants and offsets for the CSR experiment.

run (in seconds). The $\text{Offset}_{bcm\times n}$ and $\text{Constant}_{bcm\times n}$ are determined in the BCM calibration procedure. The values calibrated for the CSR experiment are given in Table 2.2.

2.5 Beam Position Monitor and Beam Raster

The beam produced by the accelerator typically has a Gaussian distribution across the cross-sectional area with full width at half maximum (FWHM) $\sigma \approx 100$ μm. To avoid damaging the target, the beam is rastered to a few millimeters in size. The raster is a pair of horizontal (X) and vertical (Y) air-core dipoles located 23 m upstream of the target. There are two modes of the raster: sinusoidal and amplitude modulated. In the sinusoidal mode, both X and Y dipoles are driven by pure sine waves with relative 90° phase difference and a frequency which do not produce a closed Lissajous pattern. In the amplitude modulated mode, both X and Y dipoles are driven at 18 kHz with a phase difference between X and Y producing a circular pattern. The radius of this pattern is changed by amplitude modulation at 1 kHz. The radius modulation is controlled by a function generator and creates a uniform distribution of the area swept out by the beam motion. In the CSR experiment, a 2 mm $\times$ 2 mm sinusoidal mode was used on both the cryogenic targets and solid targets. The beam spot is 2 mm $\times$ 2 mm with a square shape.

The beam position is an important parameter for the optics calibration and acceptance calculation of the spectrometers. Two Beam Position Monitors (BPMs) located at 7.524 m and 1.286 m upstream of the target are used to determine the position and direction of the beam at the target. Each BPM consists of four wire antennas perpendicular to the beam direction, which are tuned to the beam RF frequency 1.497

GHz. They are placed symmetrically around the beam pipe in a vacuum chamber. When a electron passes through the BPM, it will induce signals in antennas. The amplitude of the signal in each antenna is inversely proportional to the distance between the antenna and the beam. The absolute position of the BPMs can be calibrated with respect to the harps near each of the BPMs. The beam position information measured by the BPMs is stored in two ways:

1. The average beam position data over a 0.3 s time period are recorded in EPICS database and injected asynchronously into the data stream every 3-4 s.

2. The event-by-event beam position information is recorded in the CODA data stream from each of the 8 BPM antennas, and are also recorded in the data stream.

The beam position and direction at the target are reconstructed from BPM information $x_{bpma,b}$ and $y_{bpma,b}$ as:

$$x_{beam} = \frac{x_{bpma} \cdot z_{bpmb} - x_{bpmb} \cdot z_{bpma}}{z_{bpmb} - z_{bpma}} \tag{2.3}$$

$$y_{beam} = \frac{y_{bpma} \cdot z_{bpmb} - y_{bpmb} \cdot z_{bpma}}{z_{bpmb} - z_{bpma}} \tag{2.4}$$

$$\theta_{beam} = \frac{x_{bpmb} - x_{bpma}}{z_{bpmb} - z_{bpma}} \tag{2.5}$$

$$\phi_{beam} = \frac{y_{bpmb} - y_{bpma}}{\sqrt{(x_{bpmb} - x_{bpma})^2 + (z_{bpmb} - z_{bpma})^2}} \tag{2.6}$$

where $z_{bpma} = -7.345$ m, $z_{bpmb} = -2.214$ m are the location of BPMA and BPMB along the beamline, x_{beam} and y_{beam} are the horizontal and vertical positions and θ_{beam} and ϕ_{beam} are the vertical and horizontal angles of the beam at the target, respectively.

Since the beam is spread by a 18 kHz "fast" raster, the BPMs can not provide the beam position event by event due to the time delay effect. The BPMs are only used to measure the center and shape of the raster pattern, and the raster current information is combined with the BPM readout to provide the beam position for

each event. The magnet currents of the rasters are calibrated to provide the absolute values of the deviation with respect to the center of the raster pattern. More details can be find in Ref. [35].

2.6 Target System

2.6.1 Target Chamber

The standard target vacuum chamber is used in the CSR experiment, see Fig. 2-5. The vacuum chamber is constructed out of a 1037-mm diameter ring supported on a 607-mm diameter central pivot post. The stainless-steel base ring has one vacuum pump-out port and other ports for viewing and electrical feed-through. The aluminum middle ring is located at the beam height with 152-mm high vertical cutouts on each side of the beam over the full angular range. The cutoff can accommodate scattering angles within $12.5^\circ \leq \theta \leq 167.5^\circ$, and are covered with a pair of flanges with thin (0.38 mm) aluminum foils. It also has entrance and exit beam ports. The top part of the target chamber is used to house the cryotarget, and the bottom part is used to house solid targets.

2.6.2 Target Configuration of the CSR Experiment

The CSR experiment used targets from light to heavy nuclei in order to study medium dependence of the Coulomb Sum. Several targets: ^{2}H, ^{4}He, ^{12}C, ^{23}Al, Empty, BeO, ^{56}Fe and ^{208}Pb — were used in this experiment. These targets were installed on a target ladder in the target chamber and can be controlled remotely.

The target ladder is oriented vertically and is controlled by three servo motors, each connected to its own motion controller. Two of the motion controller units are configured as “Slaves” and are controlled by the third, the “Master”. During the running of the experiment, the target can be moved by controlling the Master motion controller through Input-Output Controllers (IOCs). The various target positions are stored as 15 encoder values on the control computer. An encoder that is attached to

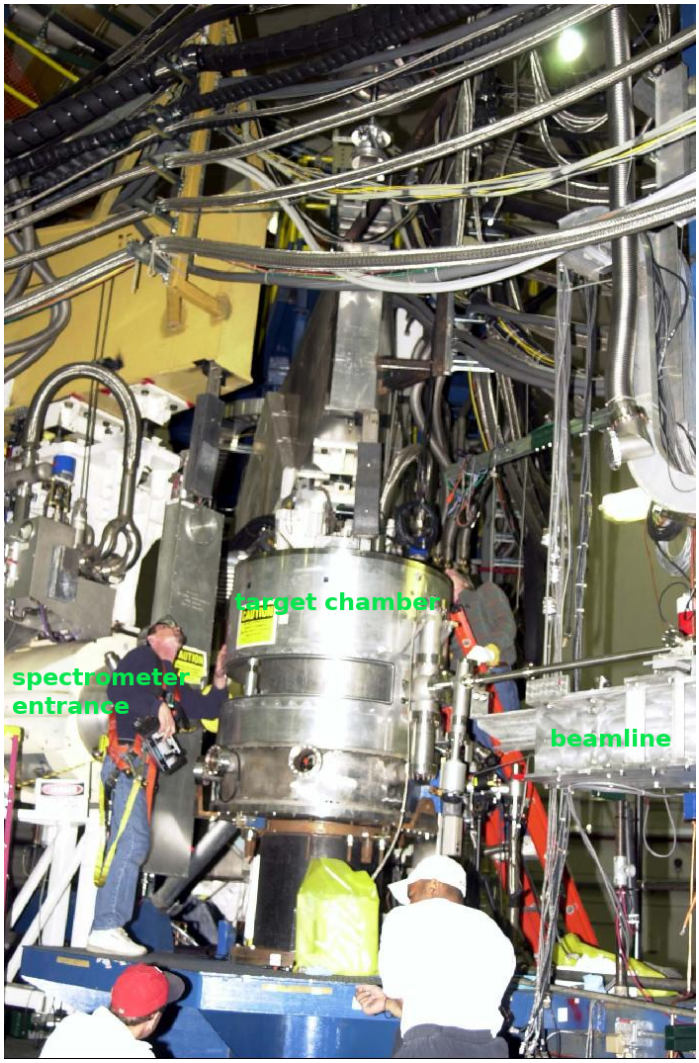

Figure 2-5: Hall A target chamber.

the Master's servo motor determines the target encoded position. The target positions used in the CSR experiment are listed in Table 2.3.

The cryogenic targets are mounted on the top layer of the target ladder inside the target chamber with sub-systems for cooling, gas handling, and temperature and pressure monitoring. The cryogenic target has three independent target loops: one gaseous helium loop (Loop 1), one liquid helium loop (Loop 2) and one liquid hydrogen loop (Loop 3).

The Loop 1 target is a vertical "racetrack" shape cell, it is 10 cm long and 2cm wide, see Fig. 2-6. This ^{4}He target is not static: ^{4}He gas flowed vertically to recycle and cool the target.

Target	Material	Encoded Position
Loop 1 10cm	High Pressure He	32932800
Loop 2 15 cm + Pb	He + Pb	26954176
Loop 2 10 cm	He	23377856
Loop 3 15 cm + Pb	H_2 + Pb	19802560
Loop 3 15 cm	H_2	16241600
Optics	7 carbon foils	12760000
10 cm dummy	2 Al foils	10092480
15 cm dummy	2 Al foils	9370560
Empty	N/A	8653760
BeO	BeO	6406480
Beam right carbon	Carbon	4321550
Beam right iron	Iron	2692366
Beam left carbon	Carbon	585998
Beam left iron	Iron	-1040625

Table 2.3: Target materials and encoded positions used during the CSR experiment.

Figure 2-6: Loop 1 and part of loop 2 of the cryogenic target.

Cryogenic Target	Entrance Window (mm) ± 0.005	Exit Window (mm) ± 0.005	Lead thickness (g/cm^2)	Beam left wall (mm)	Beam right wall (mm)
Loop1 10 cm	0.263 ± 0.008	0.280 ± 0.005	N/A	0.245 ± 0.002	0.239 ± 0.007
Loop2 15 cm	0.128 ± 0.002	0.194 ± 0.009	0.1057 ± 0.0001	0.194 ± 0.009	0.194 ± 0.009
Loop2 10 cm	0.257 ± 0.005	0.120 ± 0.070	N/A	0.120 ± 0.070	0.120 ± 0.070
Loop3 15 cm	0.129 ± 0.001	0.207 ± 0.005	0.3187 ± 0.0004	0.207 ± 0.005	0.207 ± 0.005
Loop3 15 cm	0.217 ± 0.003	0.115 ± 0.001	N/A	0.115 ± 0.001	0.115 ± 0.001

Table 2.4: Cryotargets window and lead target thicknesses.

The Loop 2 target has two aluminum cylindrical target cells filled with liquid ^{4}He. The upper cell is 15 cm long with a ^{208}Pb foil held at the center and tilted 50.0 ± 2.00° to the beam right. The ^{208}Pb is kept in ^{4}He for cooling purpose. The lower cell is 10 cm long filled with liquid ^{4}He only. Similarly, Loop 3 has two aluminum cylindrical 15-cm long target cells filled with liquid hydrogen. The upper cell has a ^{208}Pb foil at the center, also tilted 50.0 ± 2.00° to the beam right. The lower cell is 15 cm long filled with liquid hydrogen only. Loop 2 and Loop 3 cryogenic targets are shown in Fig. 2-7. Table 2.4 shows thickness of the cell window and wall and the lead foil. The cryo targets are cooled with helium supplied by the End Station Refrigerator (ESR).

The ^{4}He gas target was operated at 7.0 K and about 170 psi, with a density about 0.12 g/cc. The nominal operating conditions of liquid targets are: 6.3 K at 1.4 MPa for ^{4}He in Loop 2, and 19.0 K at 0.17 MPa for H_2 in Loop 3. The uncertainty in the target density is minimized by monitoring the pressure and temperature with pressure transducers.

Next on the target ladder are optics, dummy and empty targets, see Fig. 2-8. The optics target consists of seven carbon foils cut from the same 99.5% chemically pure 0.042 ± 0.001 g/cm^2 thick carbon sheet. The foils are separated by 4 cm along the beam direction. The dummy targets are two pairs of aluminum foils with thickness 0.259 ± 0.001 g/cm^2. The two foils of one pair are separated by 10 cm (called "10 cm dummy target"), and those of the second pair are separated by 15 cm (called "15 cm dummy target") in the beam direction direction. The dummy targets are for measuring scattering contribution from the cryogenic target windows. In addition, there is a hole on each foil of the second dummy target, and the position that allows the beam to pass through all holes (no material along the beam path) is called the

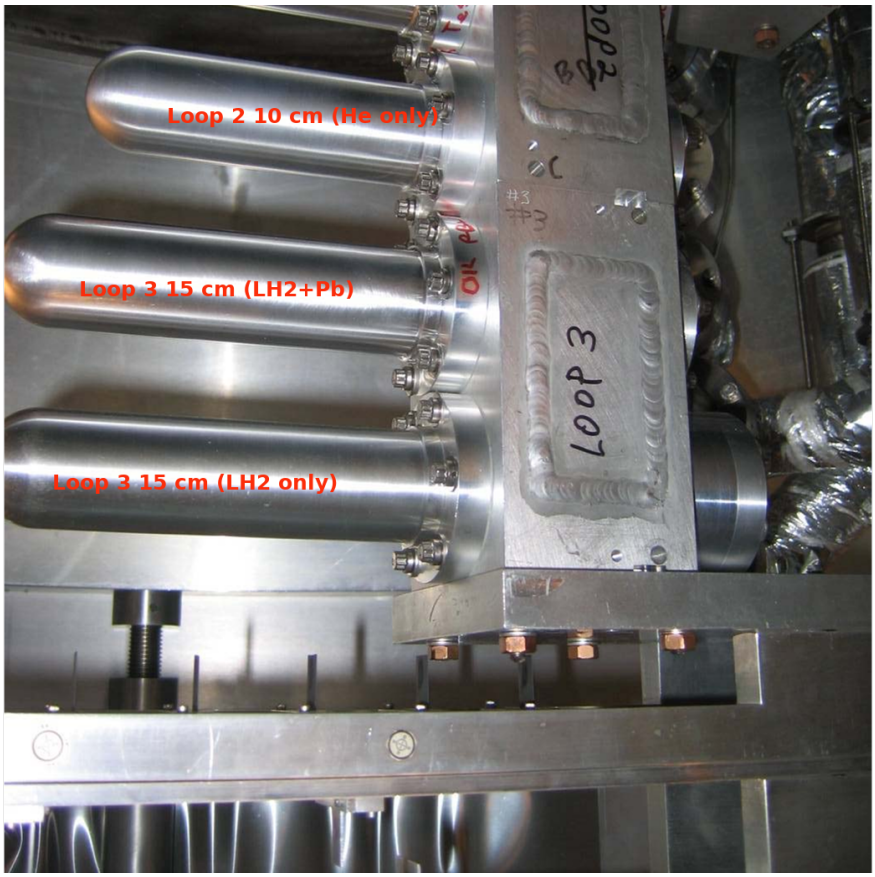

Figure 2-7: Loop 2 and Loop 3 cryogenic target.

"empty target".

The last on the target ladder are solid targets. The upper position is for BeO which is perpendicular to the beam. The second two positions are for carbon and iron targets and they are tilted 51.78° clockwise when viewed from top, so the beam hits the right side of foils ("Beam right"). The bottom two positions are also for carbon and iron targets, but tilted 48.56° counterclockwise, and the beam hit the foils from the left side ("Beam left"). The configuration of the left and right titled solid target are shown in Fig. 2-9. The tilting angles are optimized so electron's average passing length in the target material T is small, in particular for electrons with scattering angle 90°. The solid targets are shown in Fig. 2-10, with foil positions, thicknesses and chemical purity shown in Table 2.5.

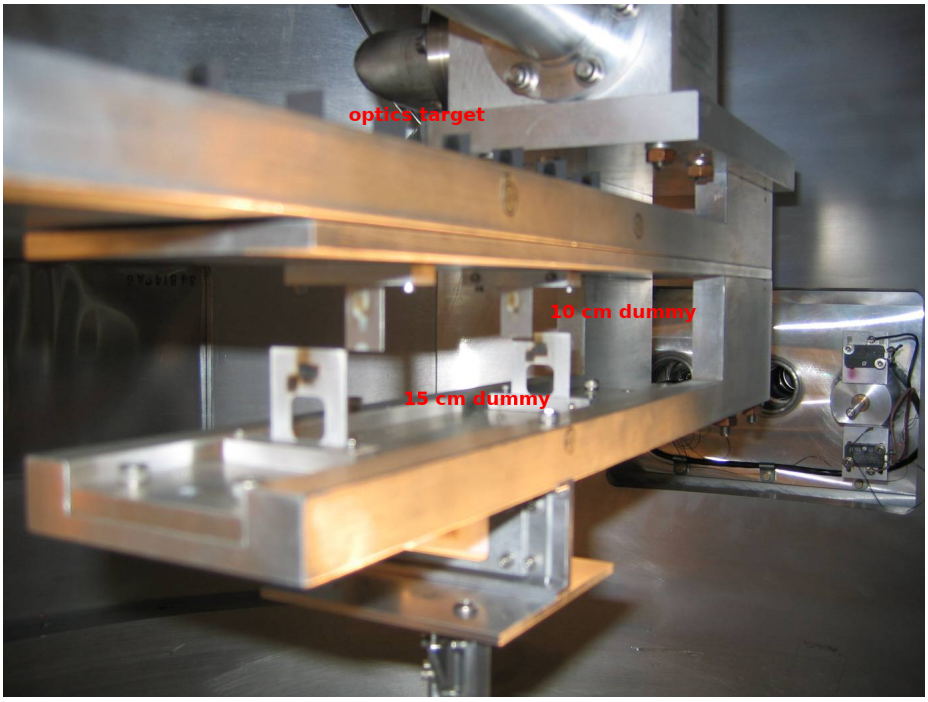

Figure 2-8: Optics, dummy and empty target.

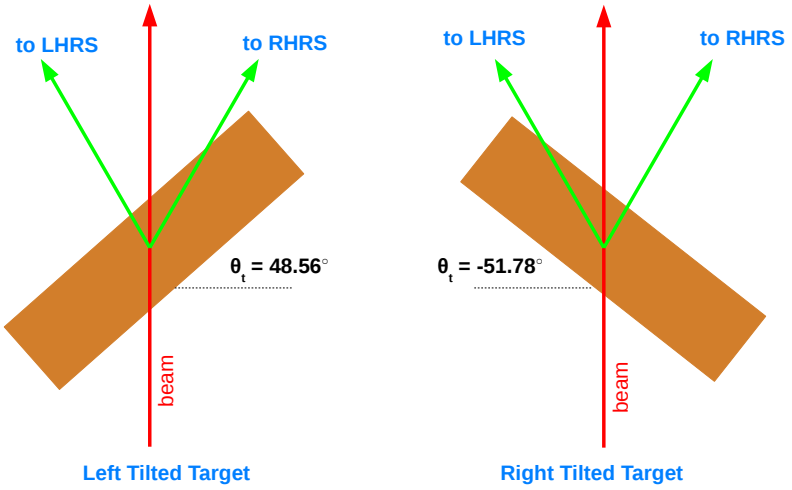

Figure 2-9: Configuration of left and right tilted carbon and iron targets (viewed from the top).

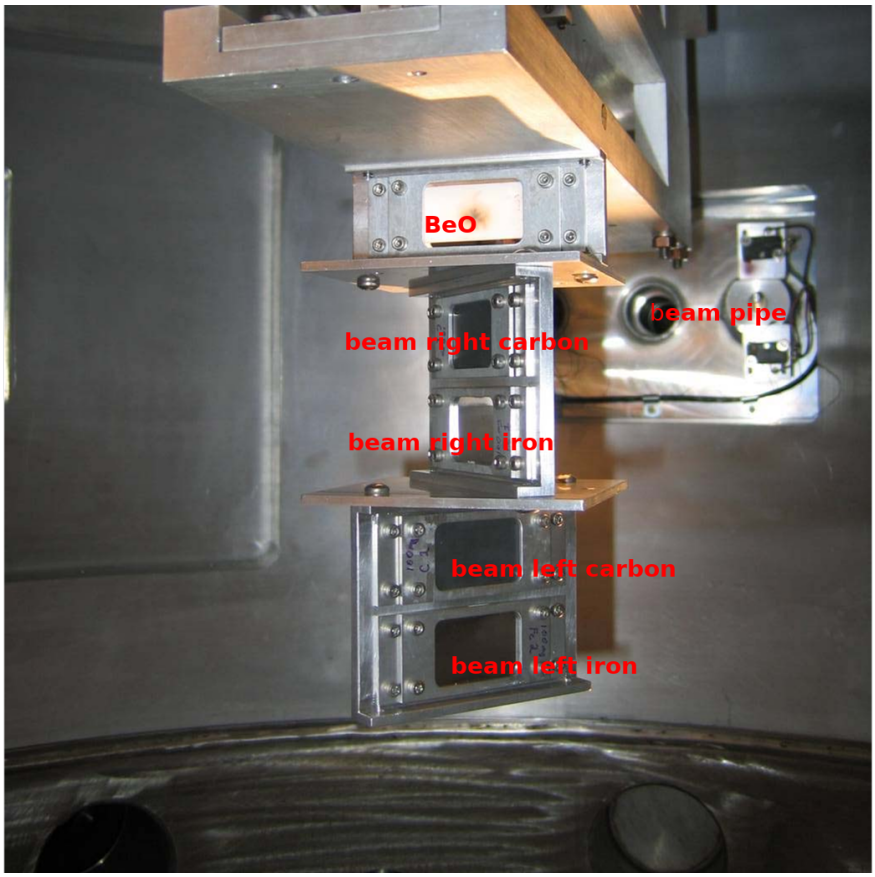

Figure 2-10: Solid targets ladder.

Purity	Target Position	Material	Thickness (g/cm^2)
99%	BeO	BeO	0.149 ± 0.001
99.95%	Beam right carbon	Carbon	0.0894 ± 0.0001
99.99%	Beam right iron	Iron	0.1027 ± 0.0001
99.95%	Beam left carbon	Carbon	0.0895 ± 0.0001
99.99%	Beam left iron	Iron	0.1023 ± 0.0001

Table 2.5: Solid target purity and thickness.

2.7 Hall A High-Resolution Spectrometers

The core of the Hall A equipment is a pair of nearly identical High Resolution Spectrometers (HRS) designed to study electromagnetic interactions and hadronic structure with high precision, see Fig. 2-11. Viewing along the beam direction, the two HRSs are called Left HRS (LHRS) and Right HRS (RHRS), respectively. Important design characteristics of the HRSs are shown in Table 2.6.

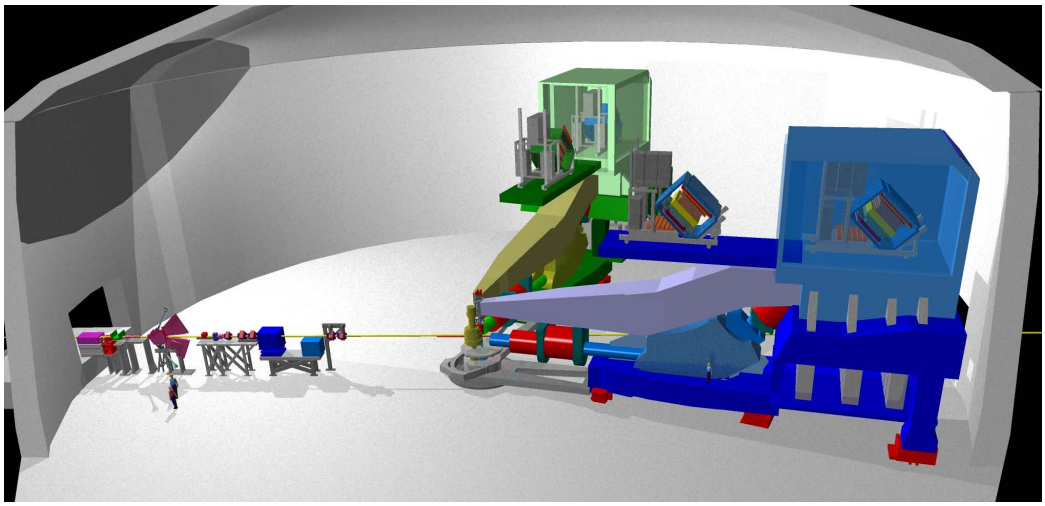

Figure 2-11: The Hall A high resolution spectrometers. Figure reproduce from [34].

Configuration	QQDQ vertical bend
Bending angle	45°
Optical length	23.4 m
Momentum range	$0.1 - 4.0$ GeV/c
Momentum acceptance	$-4.5\% < \delta p/p < +4.5\%$
Momentum resolution	1×10^{-4}
Dispersion at the focus (D)	12.4 m
Radial linear magnification (M)	-2.5
D/M	5.0
Angular range	
HRS-L	$12.5 - 150°$
HRS-R	$12.5 - 130°$
Angular acceptance	
Horizontal (ϕ)	$\pm$30 mrad
Vertical (θ)	$\pm$60 mrad
Angular resolution	
Horizontal ($\Delta\phi/\phi$)	0.5 mrad
Vertical ($\Delta\theta/\theta$)	1.0 mrad
Solid angle at δp/p=0, y_0=0	6 msr
Transverse length acceptance	$\pm$ 5 cm
Transverse position resolution	1 mm

Table 2.6: Main design characteristics of the Hall A high resolution spectrometers. Table reproduced from [34].

2.7.1 Design and Characteristics of the HRS Magnets

Each HRS has four superconducting magnets: three quadrupoles (Q) and one dipole (D). The QQDQ magnet configuration (see Fig. 2-12) is used because of a few requirements: a high momentum resolution at the 10^{-4} level over the 0.8 to 4.0 GeV/c momentum range, a large acceptance in both angle and momentum, good position and angular resolution in the scattering plane, and extended target acceptance [34]. The first two quadrupoles are used to focus the scattered electrons vertically and horizontally, respectively, to achieve the desired angular acceptance and avoid particles to collide with the magnets. The dipole is mainly used to bend the electron trajectory by 45° upward and to achieve a good momentum resolution. The third quadrupole further focuses the particles horizontally.

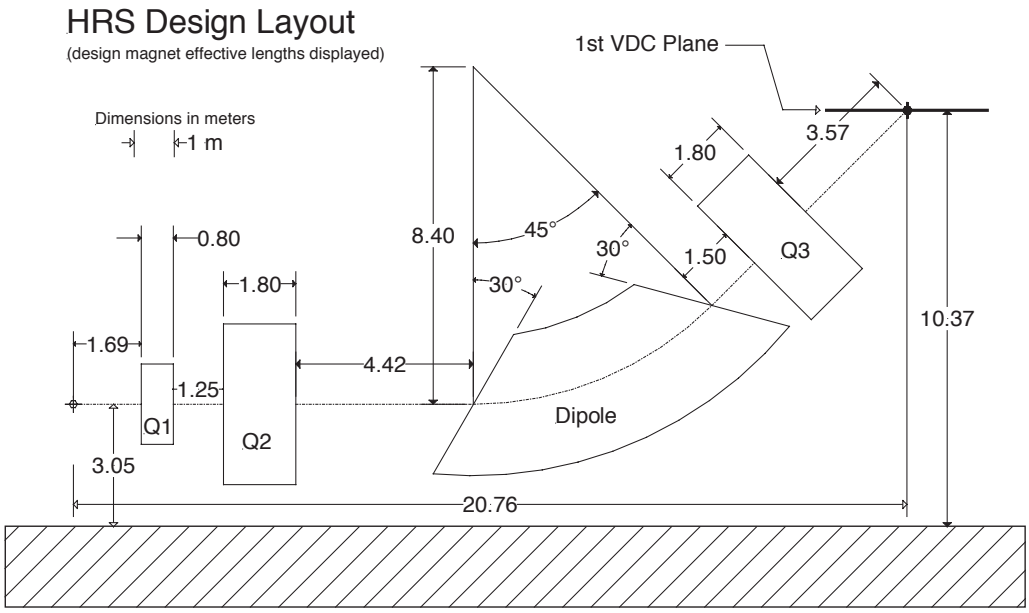

Figure 2-12: The Hall A high resolution spectrometers magnets layout (sideview).

2.7.2 HRS Collimator

Each HRS has a collimator box carefully aligned and rigidly attached to the entrance flange of the first quadrupole. In each collimator box, there are a set of collimators and a sieve slit. Only one collimator or sieve slit is selected and used at

a single time.

The first two collimators are made of 80 mm thick tungsten, positioned around 1109 mm away from the target. The first collimator has an aperture of 121.8(Vertical) × 62.9(Horizontal) mm at the entrance and 129.7(V) × 66.8(H) mm at the exit. The second collimator is smaller and with an aperture of 50.0(V) × 21.3(H) mm at the entrance and 53.2(V) × 22.6(H) mm at the exit. The third collimator is called "sieve slit", which is used to determine the angular information during optics calibrations. It is made of a 5 mm thick stainless steel sheet, positioned 1165.3 mm for LHRS (1192.5 mm for RHRS) away from the Hall A center. There are 49 holes (arranged in a 7×7 array) on each sieve slit sheet, spaced 25 mm apart vertically and 12.5 mm apart horizontally. Two of these holes have a diameter of 4 mm, and all other holes are 2 mm in diameter. Details of the sieve slits will be presented in Chap. 3.

2.7.3 HRS Detector Package

Following the third quadrupole is the detector package. The detector package is designed for various functions in the characterization of charged particles that come through the spectrometer. The layout of the LHRS and RHRS detector packages used in the CSR experiment are shown in Figs. 2-13 and 2-14, respectively, and included:

- A pair of Vertical Drift Chambers (VDCs) to determine the tracking information (momentum and trajectory);
- Two scintillator planes, S1 and S2, to provide triggers that activate the data acquisition (DAQ) electronics;
- A gas Cerenkov detector to provide particle identification (PID) information;
- On the LHRS, a NaI calorimeter was used to check the background especially at low momentum. The information from NaI confirmed that the background level is under control. Unfortunately, some NaI blocks were unresponsive during the experiment due to problems during installation, and the NaI was used only to cross check other detectors and not for defining the PID cuts.

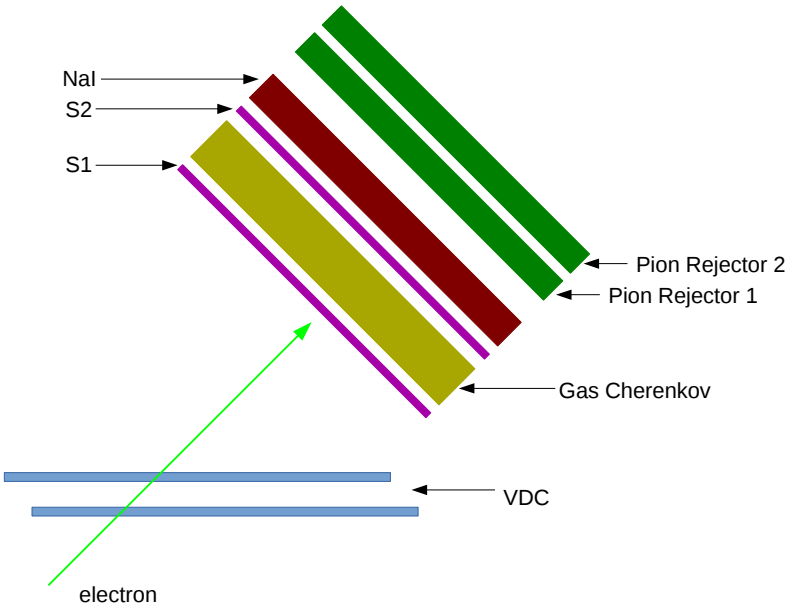

Figure 2-13: The LHRS detector package.

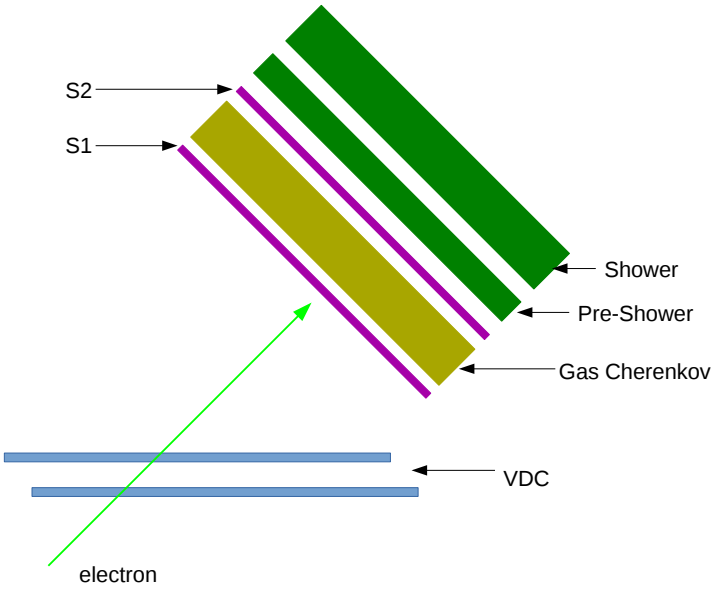

Figure 2-14: The RHRS detector package.

- A set of lead glass calorimeter for additional PID.

Details of each detector are explained below.

Vertical Drift Chamber

Each HRS uses a pair of Vertical Drift Chambers (VDC) to provide particle tracking information. The layout of the VDC is shown in Fig. 2-15.

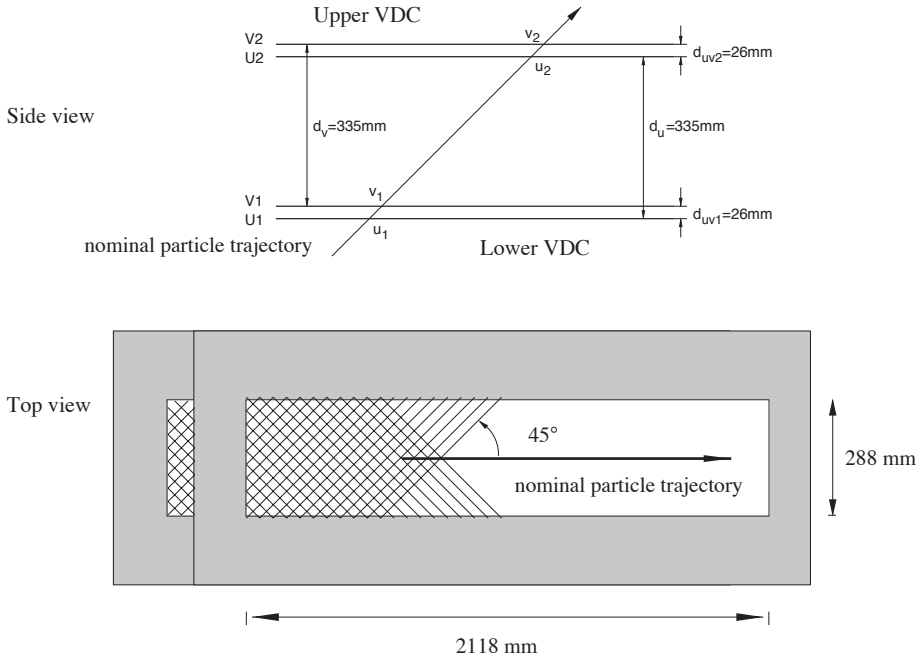

Figure 2-15: Schematic layout of a pair of Vertical Drift Chambers.

The two VDCs are positioned 335 mm away from each other. Each VDC has a standard U-V plane configuration: the wires of one plane are at 90° w.r.t. the wires of the other plane, and all lie in the laboratory horizontal plane. All wires are inclined at an angle of 45° w.r.t. the dispersive (vertical) and the non-dispersive (horizontal) directions of the HRS. The particle's central trajectory crosses the wire planes at an angle of 45° vertically. The distance between U and V planes is 26 mm. There are 368 sense wires in each plane, the spacing between two adjacent wires is 4.243 mm.

There are three high voltage gold-plated Mylar planes at about -4 kV in each VDC, one between U and V wire planes and two on opposite sides. The wires are kept at ground voltage. The electric field between the wires and the cathode planes

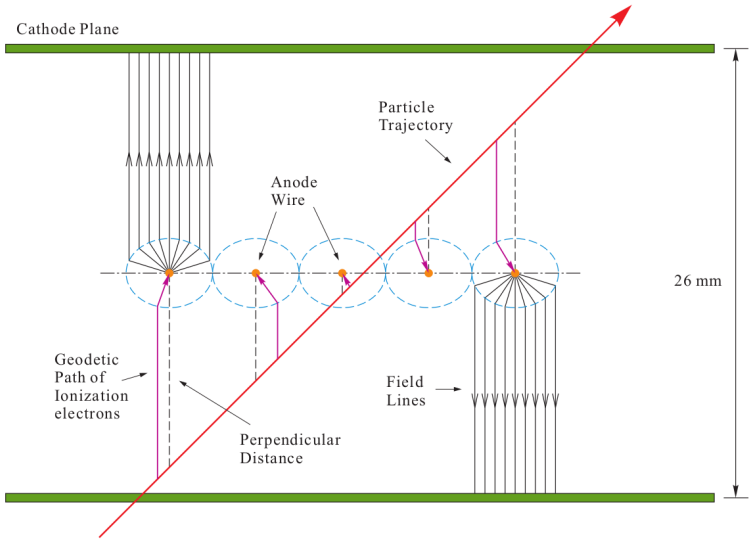

Figure 2-16: Electric fields between the wires and the cathode planes in the VDC.

is show in Fig. 2-16. The gas supply to the VDCs is a mixture of 62% argon and 38% ethane, which is bubbled through cooled alcohol to reduce aging effects on the sense wires [34].

When a charged particle passes through the VDC, it ionizes the gas inside the chamber and leaves behind ions and generated electrons on its track. The generated electrons initially drift towards sense wires with a constant velocity (50 μm/ns) along the path of the least time, and accelerate rapidly when approaching the wires, producing a shower of secondary ionization. This generates an electric signal on the sense wires. The timing information of the signal is measured by the Time-To-Digital Converter (TDC), which is started by a triggered wire and stopped by the event trigger supervisor. Since the ionization electron's drift velocity is constant for most of the flight path, the drift distance from the trajectory to the wire can be extracted from the TDC output. The trajectory can be reconstructed by combining drift distances of all fired wires of the two VDC planes. By design, charged particles that cross the VDCs at the nominal angle of 45° typically trigger 5 wires. Considering the inefficiency of sense wires, signals with 3 or 4 hits on a plane are also accepted as good tracks. The position and angular reconstruction resolution of the particle trajectory at the focal plane are approximately 100 μm and 0.5 mrad, respectively.

Scintillators and Trigger Definition

Two scintillator planes separated by 2 meters, S1 and S2, are used to generate the trigger for the DAQ system. The active volumes of S1 and S2 are 36.0 cm (transverse or horizontal direction) $\times$ 29.3 cm (dispersive or vertical direction) $\times$ 0.5 cm (thickness), and 60.0 cm (horizontal) $\times$ 37.0 cm (vertical) $\times$ 0.5 cm (thickness), respectively. Each scintillator plane consists of 6 overlapping thin plastic scintillator paddles. Two photomultipliers (PMT) are attached to each scintillator paddle, one on the left side and another on the right side. The timing resolution of each plane is around 0.3 ns.

Charged particles passing through a scintillator paddle generate scintillating light which travels towards PMTs on both sides. A paddle is called "fired" if both PMTs on its two sides have signals. Signals from PMTs are used to generate triggers which control the signal readout of all other detectors and the DAQ system. Each event recorded by the DAQ is assigned an event type based on the scintillator signal pattern as follows:

- A T1(T3) event for the right (left) HRS is formed if all the following conditions are satisfied:

  1. The N_1^{th} paddle of S1 and the N_2^{th} paddle of S2 are "fired" within a specific time window;
  2. $N_2 = N_1$ or $N_2 = N_1 \pm 1$. This means the angle formed by the particle trajectory and the central ray of the spectrometer is very small. In other words, the particle trajectory is at approximately 45° w.r.t. the Hall floor.

  T1(T3) events are often considered to be "good events".

- A T2(T4) event for the right (left) arm is formed if *one of* the following conditions is satisfied:

  1. The $N_1{}^{th}$ of S1 and $N_2{}^{th}$ of S2 are fired within a specific time window, but $N_2 \neq N_1$ and $N_2 \neq N_1 \pm 1$;

2. Either a S1 paddle or a S2 paddle is fired, and at the same time the Gas Cerenkov is fired.

T2(T4) events are either cosmic ray events, or particles on the edge of the acceptance.

- A T5 event is defined as a coincidence event of T1 and T3. It was not used during the CSR experiment.

Triggers T1-T4 are counted by scalers and are sent to the trigger supervisor. The trigger supervisor synchronizes all the detector read-outs and sends them to the DAQ system. Because of hardware limitations, the DAQ cannot record all events when the event rate is high. A quantity called livetime (LT) is defined as the fraction of events recorded by DAQ:

$$LT = \frac{\text{number of events that are recorded by DAQ}}{\text{number of events that are fed to the DAQ}}. \tag{2.7}$$

If the event rate is very high, events can be prescaled by an integer prescale factor $p_{1(2,3,4)}$ for $T_{1(2,3,4)}$ at the trigger supervisor to decrease the load of the DAQ system. Only one event is sent to the DAQ system for each set of $p_{1(2,3,4)}$ events. Livetime is event type dependent. It can be found by comparing the number of triggers $T_{1(2,3,4)}$ recorded by scalers and the total number of triggers accepted by the DAQ system, $T_{DAQ,1(2,3,4)}$:

$$LT_{1,(2,3,4)} = \frac{p_{1,(2,3,4)} T_{DAQ,1(2,3,4)}}{T_{1(2,3,4)}}. \tag{2.8}$$

Similarly, we can define a quantity called trigger inefficiency which describes the fraction of "good events" miscounted as T2(T4) events. To minimize the dilution from cosmic events, we usually choose a high rate run to determine the inefficiency as

$$\text{Inefficiency} = \frac{T_{2(4)}}{T_{1(3)} + T_{2(4)}} \tag{2.9}$$

and the trigger efficiency as

$$\eta_{trig} = 1 - \text{Inefficiency} = \frac{T_{1(3)}}{T_{1(3)} + T_{2(4)}}. \tag{2.10}$$

The trigger inefficiencies for both left and right HRS were below 1% during the CSR experiment and are considered negligible.

Gas Cerenkov Detector

The Gas Cerenkov detector is used for particle identification during the CSR experiment. The Gas Cerenkov detector is based on the Cerenkov effect: The speed of light in medium, c/n with n the medium index of refraction, is always smaller than the speed of light in vacuum c. When a high energy particle travels in a medium with high enough speed, $v > c/n$, the disturbance accumulates in the medium due to the limited response speed (speed of light in the medium) and causes a radiation in a cone with aperture angle θ_c with respect to the particle's trajectory.

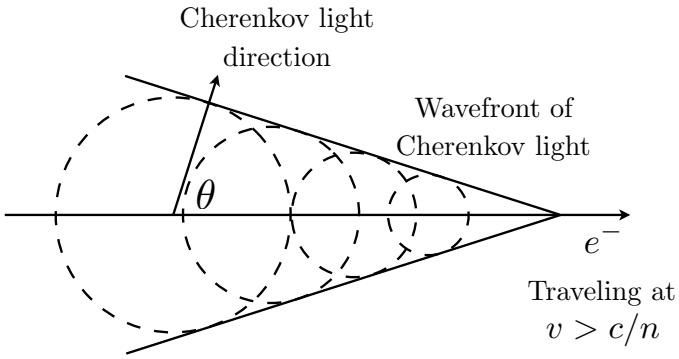

Figure 2-17: The geometry of the emission of Cerenkov radiation when an electron (or any charged particle) passes through a dielectric medium at speed $v > c/n$.

The threshold velocity and momentum for the production of Cerenkov light of a charged particle of mass m are

$$\beta_{min} c = \frac{c}{n}, \tag{2.11}$$

$$p_{min} = \frac{mc}{\sqrt{n^2 - 1}} \ . \tag{2.12}$$

The threshold angle θ_c is given by:

$$\cos\theta_c = \frac{1}{\beta_{min} n}. \tag{2.13}$$

By detecting if a particle emits Cerenkov light, one can determine if this particle's velocity is larger than the threshold velocity in the medium.

The main background during the CSR experiment is from pions. The Cerenkov detector can be used to separate electrons from pion background. The gas Cerenkov detector is filled with CO_2 at atmospheric pressure. With a refraction index $n = 1.00041$, the threshold momentum of electrons and pions are:

$$p_{e,min} = 17 \text{ MeV}/c, \text{ and } p_{\pi,min} = 4.8 \text{ GeV}/c. \tag{2.14}$$

Because the beam energy of CSR experiment varied from 0.4 to to 4 GeV, only electrons generate signals in the Cerenkov and pions do not. The Gas Cerenkov detector can achieve a very high efficiency in identifying electrons.

The Gas Cerenkov detector for each HRS is located between the two scintillator planes S1 and S2. It is made of steel with thin entrance and exit windows made of tedlar. There are ten spherical mirrors installed as a 5 (vertical) $\times$ 2 (horizontal) array that reflect the Cerenkov light onto ten PMTs. The mirrors have a radius of curvature of 90 cm, and the PMTs are placed at $f = 90/2 = 45$ cm from the mirrors, such that parallel incident light can be focused on PMTs. Signals from PMTs are sent to ADCs and summed together.

Even though pions cannot produce Cerenkov light, they can still ionize the gas medium and thus generate secondary electrons. These secondary electrons may have high enough energy to trigger Cerenkov detector and leave a background signal that lies near the single-photon-electron peak. These electrons are called knock-on electrons. This background can be removed in the analysis using ADC cuts which will be explained in Chap. 4.

Electromagnetic Calorimeters

The electromagnetic calorimeters provide an additional way of particle identification (PID). For the two HRS, the electromagnetic calorimeters are made of leadglass blocks. When a high energy charged particle of light mass travels through lead glass, it creates a cascade of photons and e^-/e^+ pairs and loses nearly all its energy in to such "electromagnetic shower". The photons created in this process are collected by PMTs and the signal intensity is linearly proportional to the energy deposit of the incoming particle. On the other hand, high energy charged particles of heavier mass (such as pions) do not produce electromagnetic shower and lose energy more slowly. There are therefore typically two peaks in the output spectrum: one peak with higher energy deposit for electrons and another peak with lower energy deposit for pions, and one can separate electrons from pions by applying a cut on the spectrum. A double-layer configuration further separates electrons from contamination of pions.

The configurations of the electromagnetic calorimeter on the LHRS and RHRS are slightly different, see Fig. 2-18. The calorimeter on LHRS is composed of two layers of leadglass blocks with the same geometry. Each layer is called a "pion rejector" and consists of 17 long blocks and 17 short blocks of dimension 14.5 cm $\times$ 14.5 cm $\times$ 30 and 35 cm, respectively, forming a 17 (dispersive) $\times$ 2(transverse) array. The 30-cm and the 35-cm long blocks are arranged interchangeably in the dispersive direction for each row.

On the RHRS, the two layers are called "preshower" and "shower" respectively. The preshower layer consists of leadglass blocks of dimension 35 cm $\times$ 10 cm $\times$ 10 cm, arranged in a 24 (dispersive) $\times$ 2 (transverse) array. The preshower blocks are oriented perpendicular to the direction of incoming particles. The shower layer consists of 16 (dispersive) $\times$ 5 (transverse) blocks of dimension 35 cm $\times$ 15 cm $\times$ 15 cm, with the 35-cm long side oriented parallel to the particle trajectory.

The main difference between LHRS and RHRS lead-glass calorimeters is that the RHRS calorimeter is thick enough that electrons will deposit all their energies, while the calorimeter on LHRS is not a full energy absorber because of its reduced thickness.

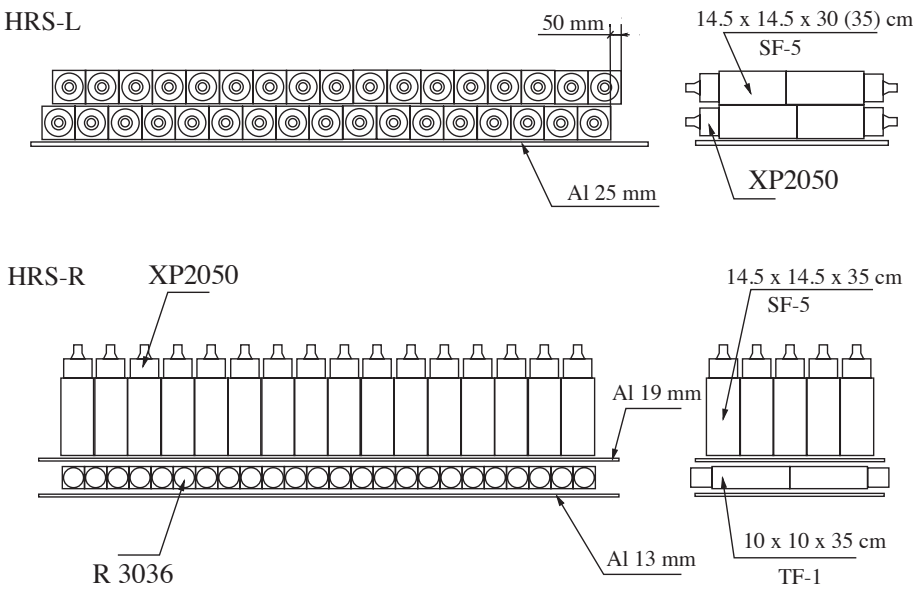

Figure 2-18: Schematic layout of electromagnetic calorimeters in the left (top) and the right (bottom) HRS. Figure reproduced from [34].

2.8 Data Acquisition System

The Data Acquisition system is used to collect event information from the detectors and beamline apparatus and store the raw data. The Hall A DAQ system is built on the CEBAF Online Data Acquisition System (CODA), a software package specifically developed for nuclear physics applications by the JLab data-acquisition group, see Fig. 2-19.

CODA is composed of a set of software packages which can control DAQ hardwares such as front-end Fastbus VME digitization devices (ADCs, TDCs, scalers), the VME Interface to Fastbus, single-board VME computers, and mass storage system (MSS). The raw data are divided into different runs for specific kinematics settings. The data of each run consists of several parts of information:

- A header consists of information such as run number, timestamp, event size and prescale factors.
- CODA events which contain detectors and helicity information.
- EPICS events which contain information about beamline apparatus, spectrom-

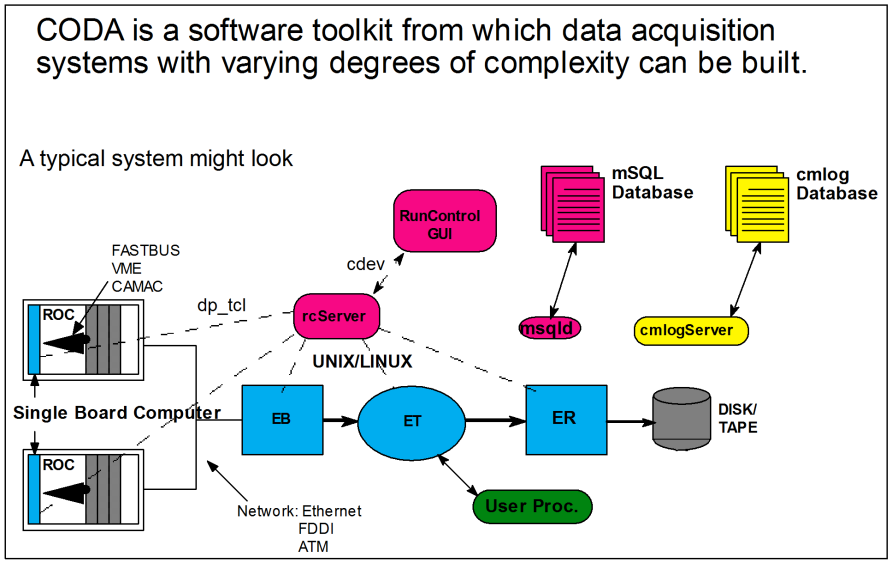

Figure 2-19: DAQ system diagram.

eter magnets setting and angle, and information on the target and other slow control device.

- Scaler events which contain numbers of triggers and the accumulated charge of the run.

The data are first written to a local disk, then moved to the MSS. The total volume of data accumulated during the CSR experiment was about 3.0 TBytes.

Chapter 3

HRS Optics and Acceptance

For the CSR experiments, most of the momentum settings of the HRS were below the range specified by the HRS design. As a result, calibration of the HRS optics and acceptance were challenging. This chapter will focus on presenting the procedure and the results of optics calibration and acceptance analysis.

3.1 Optics Calibration

The Hall A HRS are two spectrometers each with an identical group of superconducting magnets: three quadrupoles and a dipole in a QQDQ configuration as mentioned in the previous chapter. The optics of the QQDQ magnets determines how charged particles move once they enter the magnets. An optics matrix can be used to describe how particles move forward from the target to the HRS focal plane, and a reverse optics matrix is typically used to reconstruct the kinematic variables at the target interaction vertex using coordinates of the particle detected at the HRS focal plane. In this section I will describe the optics calibration procedure in which dedicated data are used to determine the optics matrix elements.

3.1.1 Coordinate Systems

In this section, coordinate systems used in the optics calibration are introduced. More details of these coordinate systems can be found in [36]. Note that all angular coordinates used in optics calibration refer to the tangent of the angle.

Hall Coordinate System (HCS)

The origin of HCS is the center of Hall A, which is the intersection of the beamline and the vertical symmetric axis of the target system. The $\hat{z}$ axis is along the beamline and pointing to the beam dump, the $\hat{x}$ axis is pointing to the left of the beam, and the $\hat{y}$ axis is pointing up vertically, see Fig. 3-1.

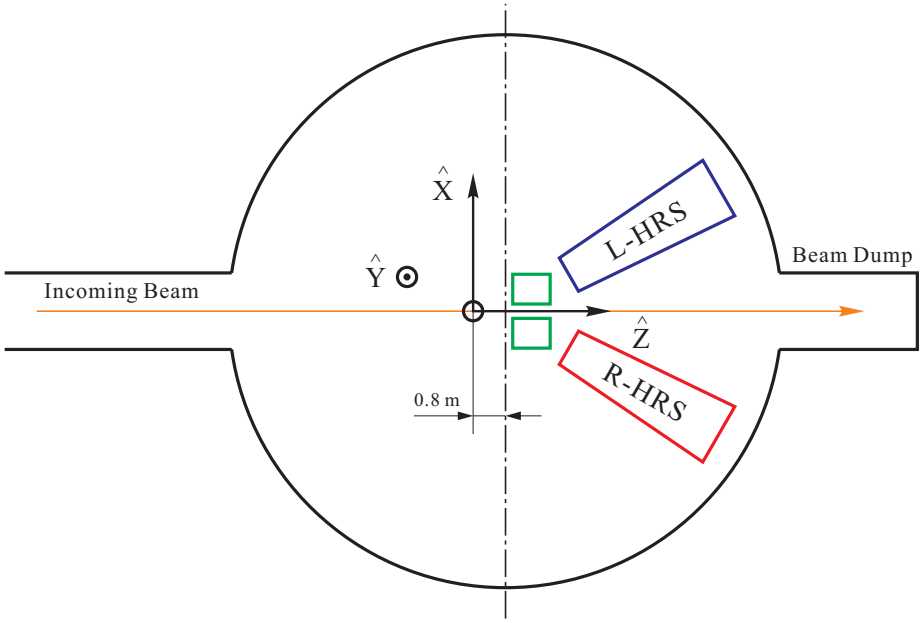

Figure 3-1: Top view of hall coordinate system (HCS). Figure reproduced from [37].

Target Coordinate System (TCS)

Each of the spectrometers has its own TCS coordinates, see Fig. 3-2. The $\hat{z}$ axis of TCS is along the spectrometer center line and is perpendicular to the sieve slit surface, pointing away from the target. The $\hat{y}$ axis is pointing to the left side of $\hat{z}$ axis, and the $\hat{x}$ axis is pointing down vertically. In the ideal case, the origin of TCS

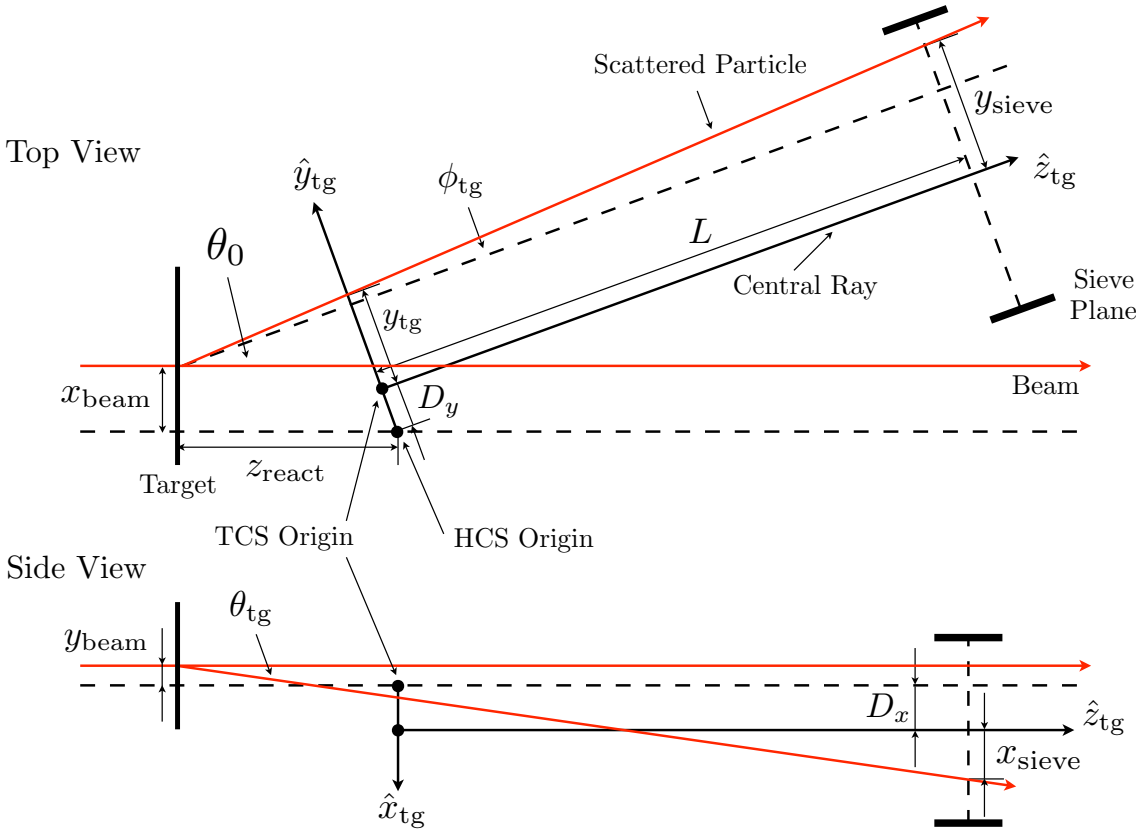

Figure 3-2: Top and side view of target coordinate system (TCS). Figure reproduced from [38].

is at the Hall center and coincide with the HCS origin. In reality, the HRS central ray is not pointing exactly at the Hall center, and there can be a horizontal shift D_y and a vertical shift D_x that can be measured in surveys. In the TCS, the distance from the origin to the center of the collimator is defined as a constant L. If a particle trajectory intersects with the sieve slit plane at (x_{sieve}, y_{sieve}), one can calculate its in-plane angle $\theta_{tg} = \frac{x_{sieve}}{L}$ and the out-of-plane angle $\phi_{tg} = \frac{y_{sieve}}{L}$.

Detector Coordinate System (DCS)

The origin of DCS is defined by wire 184 of the VDC U1 plane and the projection of wire 184 of the VDC V1 plane on the U1 plane. The $\hat{z}$ axis is perpendicular to the VDC plane and the $\hat{x}$ axis is along the long symmetry axis and pointing to the dispersive direction, see Fig. 3-3. The coordinate of the detector vertex (x_{det}, y_{det},

θ_{det}, ϕ_{det}) in DCS can be calculated from the intersection points of the trajectory on four VDC planes (U1, V1, U2, V2):

$$\tan(\eta_1) = \frac{p_{U2} - p_{U1}}{d_2}, \tag{3.1}$$

$$\tan(\eta_2) = \frac{p_{V2} - p_{V1}}{d_2}, \tag{3.2}$$

$$\theta_{det} = \frac{1}{\sqrt{2}}(\tan(\eta_1) + \tan(\eta_2)), \tag{3.3}$$

$$\phi_{det} = \frac{1}{\sqrt{2}}(-\tan(\eta_1) + \tan(\eta_2)), \tag{3.4}$$

$$x_{det} = \frac{1}{\sqrt{2}}p_{U1} + p_{V1} - d_1 \tan(\eta_2), \tag{3.5}$$

$$y_{det} = \frac{1}{\sqrt{2}} - p_{U1} + p_{V1} - d_1 \tan(\eta_2), \tag{3.6}$$

where p_{U1}, p_{V1}, p_{U2}, p_{V2} are the trajectory's intersection point positions in U-V coordinates, on U1, V1, U2 and V2 planes, respectively. η_1 and η_2 are angles between the trajectory and the U and the V axis, respectively. d_1 is the distance between U1 and V1 plane, and d_2 is the distance between U1 and U2 plane.

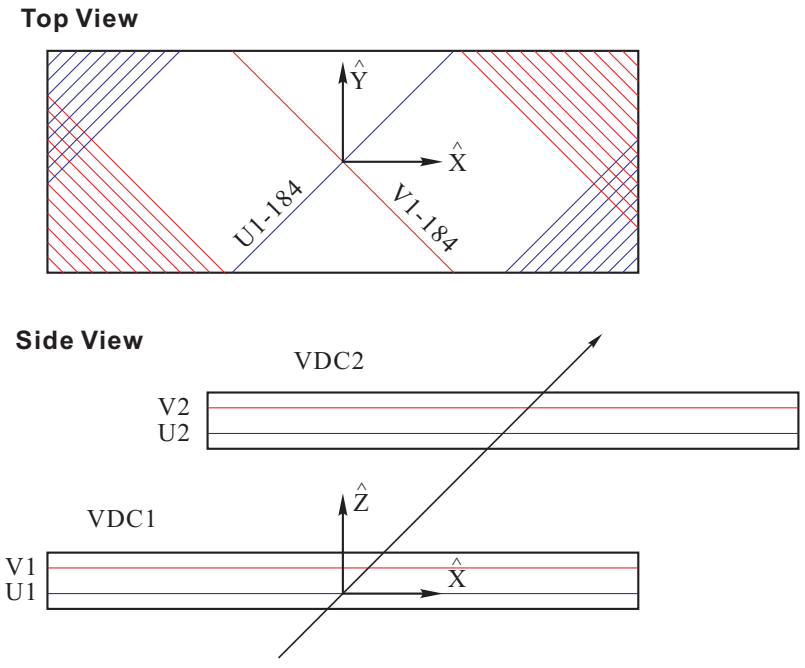

Figure 3-3: Top and side view of detector coordinate system (DCS). Figure reproduced from [37].

Target Transport Coordinate System (TRCS)

The TRCS is generated by rotating DCS clockwise along its $\hat{y}$ axis by 45°, see Fig. 3-4). The $\hat{z}$ axis of TRCS coincides with the central trajectory of the spectrometer in the ideal case. TRCS is a middle step from DCS to Focal Plane Coordinate System (FCS) which will be described in the next section. The transform from DCS variables (x_{det}, y_{det}, θ_{det}, ϕ_{det}) to TRCS variables (x_{tra}, y_{tra}, θ_{tra}, ϕ_{tra}) can be expressed as:

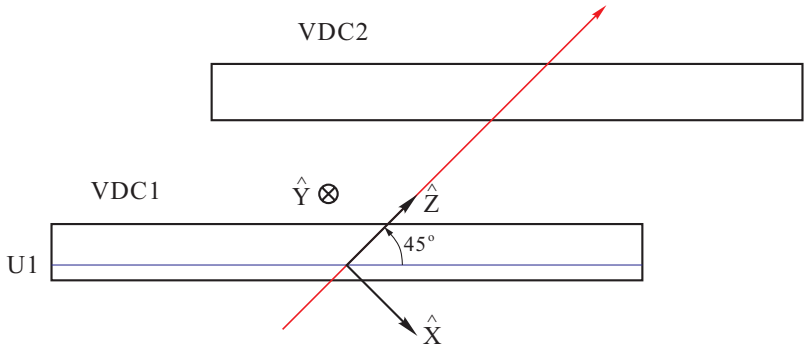

Figure 3-4: Target transport coordinate system (TRCS). Figure reproduced from [37].

$$x_{tra} = x_{det}\cos(\rho_0)(1 + \theta_{tra}\tan(\rho_0)) \tag{3.7}$$

$$\theta_{tra} = \frac{\theta_{det} + \tan(\rho_0)}{1 - \theta_{det}\tan(\rho_0)} \tag{3.8}$$

$$y_{tra} = y_{det} + \sin(\rho_0)\phi_{tra}x_{det} \tag{3.9}$$

$$\phi_{tra} = \frac{\phi_{det}}{\cos(\rho_0)(1 - \theta_{det}\tan(\rho_0))} \tag{3.10}$$

where $\rho_0 = 45°$ is the rotation angle.

Focal Plane Coordinate System (FCS)

Because of the focusing feature of the HRS magnet system, particles from different scattering angles are focused on the focal plane. The relative momentum δ (sometimes written as dp), defined as $\delta = \frac{p-p_0}{p_0}$ with p_0 the nominal momentum setting of the HRS, depends mostly on the location in the dispersive direction, x_{det}.

The FCS is a rotated coordinate system. It is generated by rotating the DCS by a varying angle $\rho(x_{tra})$ such that the new FCS $\hat{z}$ axis is always along the local central ray that has $\theta_{tg} = 0$ and $\phi_{tg} = 0$, see Fig. 3-5. With this rotation, θ_{fp} is small for all points on the focal plane and is approximately centered around θ_{fp}=0. This ensures the expansion of the optics matrix will converge fast during the optimization procedure.

The FCS variables can be expressed a

$$x_{fp} = x_{tra}\tan(\rho) = \Sigma t_{i000} x^i_{fp} \ , \tag{3.11}$$

$$y_{fp} = y_{tra} - \Sigma y_{i000} x^i_{fp} \ , \tag{3.12}$$

$$\theta_{fp} = \frac{x_{det} + \tan(\rho)}{1 - \theta_{det}\tan(\rho)} \ , \tag{3.13}$$

$$\phi_{fp} = \frac{\phi_{det} - \Sigma p_{i000} x^i_{fp}}{\cos(\rho_0) - \theta_{det}\sin(\rho_0)} \ , \tag{3.14}$$

where t_{i000}, y_{i000} and p_{i000} are important optics matrix elements and will be discussed later.

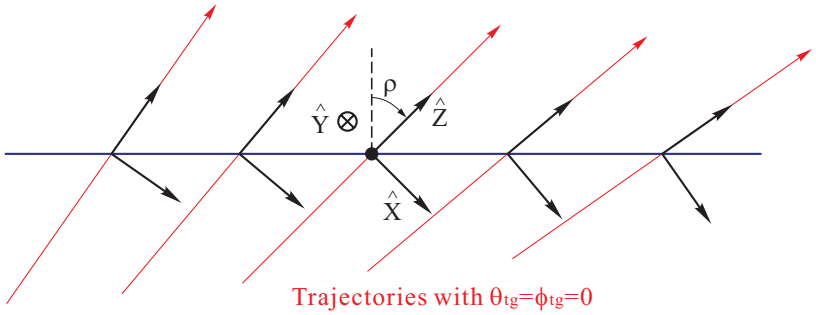

Figure 3-5: Focal coordinate system. Figure reproduced from [37].

3.1.2 Optimization Procedure

The DCS variable $(x_{det}, \theta_{det}, y_{det}, \phi_{det})$ are directly measured in experiment, and are transformed to focal plane variables $(x_{fp}, \theta_{fp}, y_{fp}, \phi_{fp})$. The optics matrix provides a point-to-point mapping between focal plane variables and the target variables $(\delta, \theta_{tg}, y_{tg}, \phi_{tg})$. In the optics calibration, the x_{tg} is always set to be zero, and an

extended target correction that depends on x_{beam} is applied to θ_{tg} and δ in the reconstruction process.

To the first order the optics matrix can be expressed as:

$$\begin{pmatrix} \delta \\ \theta \\ y \\ \phi \end{pmatrix}_{\text{tg}} = \begin{pmatrix} \langle\delta|x\rangle & \langle\delta|\theta\rangle & 0 & 0 \\ \langle\theta|x\rangle & \langle\theta|\theta\rangle & 0 & 0 \\ 0 & 0 & \langle y|y\rangle & \langle y|\phi\rangle \\ 0 & 0 & \langle\phi|y\rangle & \langle\phi|\phi\rangle \end{pmatrix} \begin{pmatrix} x \\ \theta \\ y \\ \phi \end{pmatrix}_{\text{fp}} . \tag{3.15}$$

The optics matrix used in the experiment has a more complicated form: a set of tensors D_{jkl}, T_{jkl}, Y_{jkl} and P_{jkl} transform the focal plane variables to target plane variables as:

$$\delta = \sum_{j,k,l} D_{jkl} \theta_{fp}^{j} y_{fp}^{k} \phi_{fp}^{l}, \tag{3.16}$$

$$\theta_{tg} = \sum_{j,k,l} T_{jkl} \theta_{fp}^{j} y_{fp}^{k} \phi_{fp}^{l}, \tag{3.17}$$

$$y_{tg} = \sum_{j,k,l} Y_{jkl} \theta_{fp}^{j} y_{fp}^{k} \phi_{fp}^{l}, \tag{3.18}$$

$$\phi_{tg} = \sum_{j,k,l} P_{jkl} \theta_{fp}^{j} y_{fp}^{k} \phi_{fp}^{l}, \tag{3.19}$$

where the tensors D_{jkl}, T_{jkl}, Y_{jkl} and P_{jkl} are polynomials in x_{fp}. For example:

$$D_{jkl} = \sum_{i=0} C^{D}_{i,j,k,l} x_{fp}^{i}, \tag{3.20}$$

where $C^{D}_{i,j,k}$ are called the optics matrix elements of δ. All the optics matrix elements are up to the third order in powers of x_{fp}, θ_{fp}, y_{fp} and ϕ_{fp}, that is, each of the summations of index in Eqs. 3.16-3.20 is up to $i, j, k, l = 3$. The optics optimization is a method to determine the optics matrix elements using dedicated optics calibration data. The optimization procedure is described in the next section.

3.1.3 Experimental and Optimization Procedure

The optics calibration requires sets of dedicated data with wide coverage over the entire acceptance of the spectrometer, including δ for momentum, θ_{tg} and ϕ_{tg} for solid angle and y_{tg} for reaction position. The target variables of calibration data are precisely determined by methods including: survey of the sieve-slit collimator and spectrometer angle for θ_{tg} and ϕ_{tg}, survey of foil targets for y_{tg}, and well-known physics process such as elastic scattering for δ.

To optimize θ_{tg}, ϕ_{tg} and y_{tg}, a multi-foil optics (carbon) target is used with a fixed energy, unrastered electron beam. The seven carbon foils of the optics target are aligned along the beam line to cover the y_{tg} acceptance from $z = -12$ cm to $z = +12$ cm, with a separation of 4 cm between foils. The z_{react} can be determined by $\hat{z}$ coordinates of the survey result of target foils. The x_{beam} and y_{beam} of interaction point in HCS can be determined by BPM. The sieve slit collimator is inserted before the entrance of the first quadrupole of the spectrometer. The sieve slit pattern is shown in Fig. 3-6. The holes on the sieve slit are placed in a grid pattern, and two large holes are used to determine the orientation of the image at the focal plane. The in-plane angle ϕ_{tg} and out-of-plane angle θ_{tg} for each sieve-slit hole can be expressed as:

$$\phi_{tg} = \frac{y_{sieve} + D_y - x_{beam}\cos\theta_0 + z_{react}\sin\theta_0}{L - z_{react}\cos\theta_0 - x_{beam}\sin\theta_0}, \tag{3.21}$$

$$\theta_{tg} = \frac{x_{sieve} + D_x + y_{beam}}{L - z_{react}\cos\theta_0 - x_{beam}\sin\theta_0}, \tag{3.22}$$

where (x_{sieve}, y_{sieve}) are the position of the hole on the sieve slit plate, z_{react} is the position of the target foil from which the event originates, θ_0 is the spectrometer central angle, D_x and D_y are the vertical and horizontal mis-pointing distances of the spectrometer central ray from the HCS origin, L is the distance from the TCS origin to the sieve slit (see Fig. 3-2). Values of θ_0, L, D_x and D_y can be determined from surveys of the spectrometer and the sieve slit. The spatial coordinates x_{tg} and y_{tg}

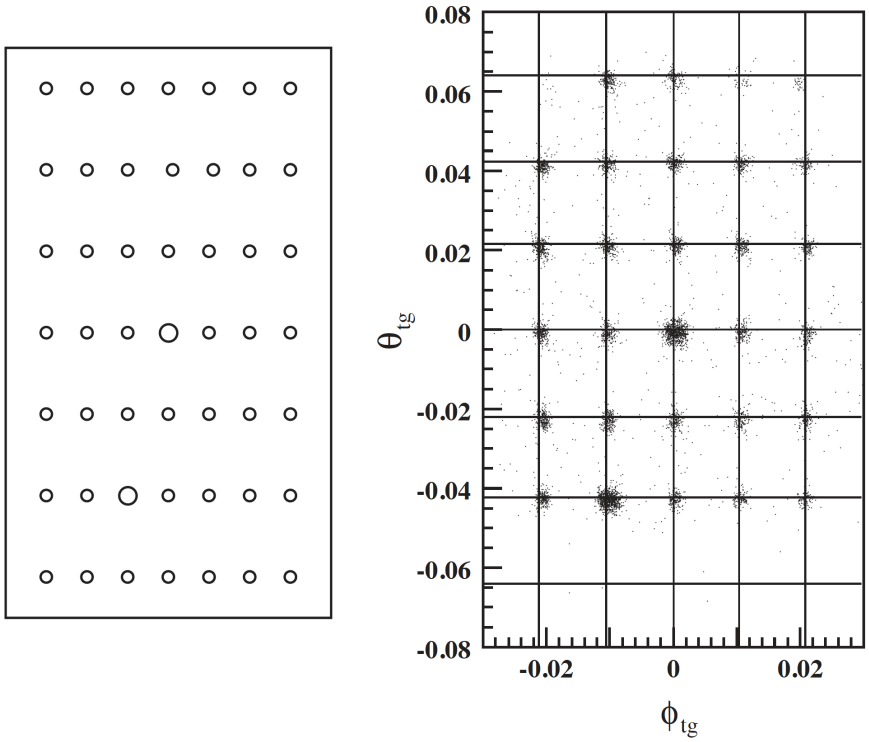

Figure 3-6: Geometric (left) and reconstructed (right) configurations of the sieve slit. Figure reproduced from [34].

can be expressed by:

$$x_{tg} = x_{sieve} - L\theta_{tg}, \tag{3.23}$$

$$y_{tg} = y_{sieve} - L\phi_{tg}. \tag{3.24}$$

The momentum calibration typically uses carbon elastic scattering to determine the momentum of the detected particle. It requires precise measurements of the spectrometer central momentum and beam energy. The momentum of the elastically scattered electron can be expressed as:

$$P(M,\theta) = E' = \frac{E}{1 + \frac{E}{M}(1 - \cos\theta)}, \tag{3.25}$$

where E is the beam energy, M is the target mass and θ is the scattering angle. Because the solid angle acceptance covers a wide θ_{tg} and ϕ_{tg} range, the scattering angles of electrons passing through different sieve holes are different. The elastic peak

is broadened and this effect becomes larger for lighter target nucleus. To remove the angular dependence of δ, a new variable δ_{kin} is defined as:

$$\delta_{kin} = \delta - \frac{P(M, \theta_{scat}) - P(M, \theta_0)}{P_0}, \tag{3.26}$$

where the θ is the scattering angle and θ_0 is the central angle of the spectrometer. To cover the δ acceptance of the spectrometer, several different central momentum P_0 values are typically during the optics calibration. Such runs are called the "delta scan". The scattered particles will pass through target foils and several windows before entering the spectrometer, and the energy loss of the scattered electrons due to radiative effect is considered as a correction to δ.

For optimization of the optics matrix, the target variables δ, θ_{tg}, ϕ_{tg} and y_{tg} calculated from survey or elastic scattering peaks are taken as the true value. Then a minimization is carried out on:

$$\sigma^2(x) = \sum_{s=1}^{N} (x^{recon} - x^{true})^2, \tag{3.27}$$

where N is total number of events measured for optics calibration, x can be any of the target variables δ, θ_{tg}, ϕ_{tg} or y_{tg}, x^{recon} is the target variable reconstructed by the optics matrix, and x^{true} is the true target variable calculated from survey results and Eqs. 3.21-3.24 or elastic scattering peak using Eq. 3.25. The optimization begin with an initial optics matrix generated by the magnetic field simulation tool SNAKE. The core of the optimization package is the TMinuit package of ROOT [39]. The package also contains scripts to make graphic cuts and select events to be used for optimization.

3.1.4 Optics Results

In the CSR experiment, two sets of optics calibrations were done: one with E_b = 1.1 GeV and θ_0 = 14.6°, and another with E_b = 399 MeV and θ_0 = 35°. The optimization results of these optics calibrations are discussed.

The angular components of the optics matrix were optimized first. The reconstructed sieve pattern for the 1.1 GeV data is shown in Fig. 3-7, obtained by projecting the reconstructed θ_{tg} and ϕ_{tg} from the interaction point to the sieve slit plane. The nominal position of the sieve holes are indicated by the cross points of the grids in the plots. As can be seen from the figure, the agreement between reconstructed θ_{tg} and ϕ_{tg} and their expected values is quite good. The resolution in θ_{tg} and ϕ_{tg} are 1×10^{-4} mrad and 0.5×10^{-4} mrad, respectively.

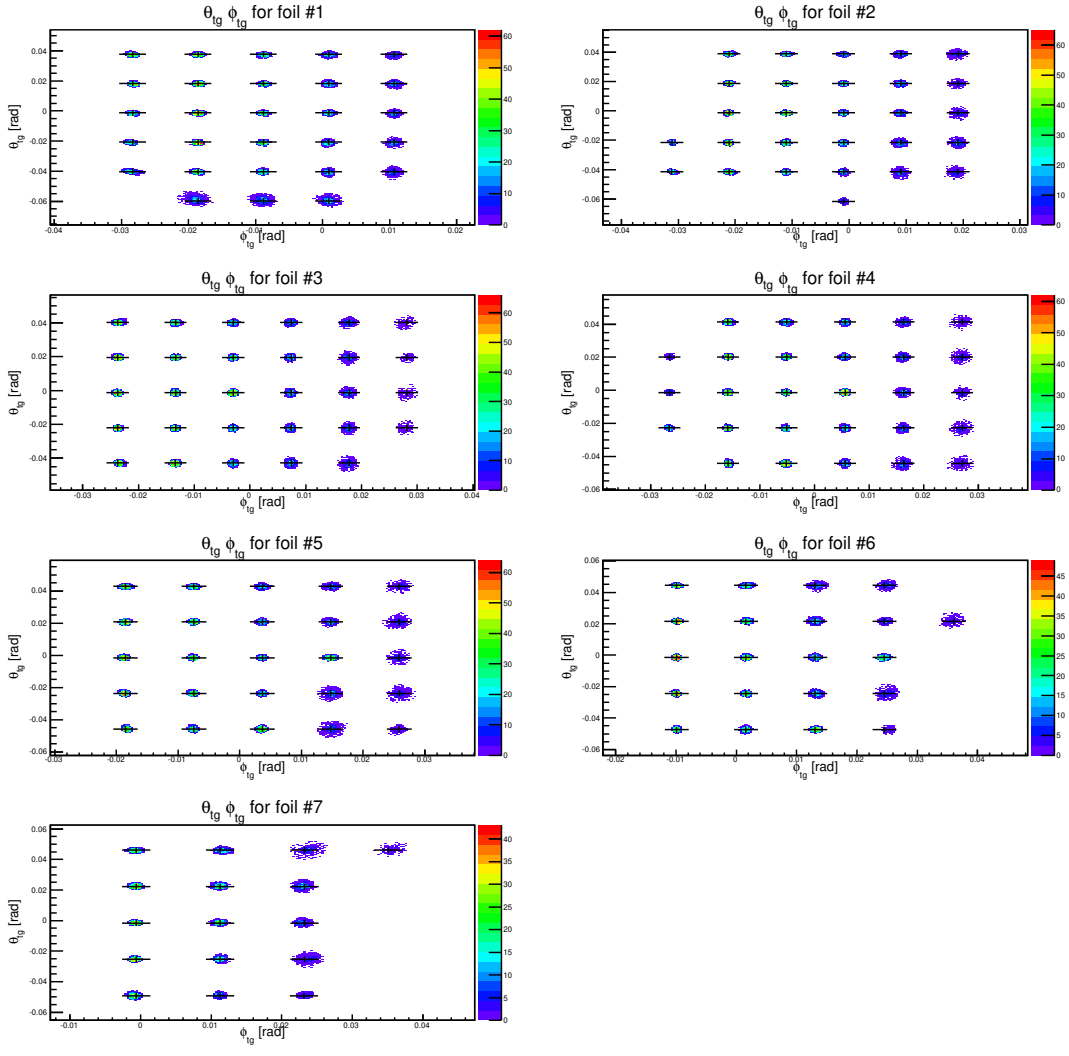

Figure 3-7: 1.1 GeV optics θ_{tg} and ϕ_{tg} reconstruction for each of the seven carbon foils. From left to right, top to bottom, the foil targets are from downstream to upstream. For each panel, x axis is ϕ_{tg}, y axis is θ_{tg}. The black crossing shows the reference (true) θ_{tg}, ϕ_{tg} position for each sieve slit hole.

The next step is momentum calibration. To optimize the matrix elements of δ, measurements of runs with five different central momentum P_0 of the HRS were used, with $\frac{P_{el}-P_0}{P_0} = -2.7\%, -1.2\%, 0.2\%, 1.8\%, 3.3\%$ where P_{el} is the elastic peak momentum. The δ_{kin} calibration results for 1.1 GeV data are shown in Fig. 3-8. The nominal positions of δ_{kin} are indicated by magenta lines for each delta scan run. The resolution of each δ_{kin} peak is $\approx 2 \times 10^{-4}$.

The y_{tg} is related to the foil target position along the $\hat{z}$ direction in Hall coordinate system. It is optimized by minimizing the difference between the reconstructed foil target position and the real foil target position. The y_{tg} calibration for 1.1 GeV data results are shown in Fig. 3-9. The nominal position of the optics foils are indicated by red lines for each foil. The resolution of y_{tg} of the foils is ≈ 1 mm.

The 399 MeV optics calibration results are also presented here: the θ_{tg}, ϕ_{tg} optimization results are shown in Fig. 3-10, the δ optimization results in Fig. 3-11, and y_{tg} optimization results in Fig. 3-12.

Due to several reasons, the target variables resolution at 399 MeV are much worse than 1.1 GeV: First, spectrometer pointing survey was not performed for the 399 MeV optics calibration because of limited beam time; Second, while the HRS central momentum is typically measured by a NMR probe, the NMR probe does not work below $P_0 = 450$ MeV (see 3.2.3). Thus the measurement of the HRS momentum for the 399 MeV optics calibration was performed only by a Hall probe and the precision is 10 times worse than the NMR probe; Third, multiple scatterings that smear the target variables distributions are much stronger at 399 MeV than 1.1 GeV.

3.2 HRS Acceptance

Because of the limited aperture of the HRS, the spectrometer can only detect scattered electrons in a certain range of θ_{tg}, ϕ_{tg}, δ and y_{tg}. The acceptance of the spectrometer can be defined as a window in θ_{tg}, ϕ_{tg}, δ and y_{tg} (the foil target has only acceptance in the first three variables, the y_{tg} acceptance is used only for extended target) in which scattered electrons can pass through all magnets of the spectrometer

and be detected at the focal plane. In the ideal case, the spectrometer would accept all the particles if they are inside the aperture of the spectrometer and reject particles outside the aperture. But in reality, the spectrometer's geometrical aperture is more complicated than a hypercube of the five target variables (x_{tg}, y_{tg}, ϕ_{tg}, θ_{tg}, δ), and multiple scatterings and the resolution of the VDC will smear out the boundaries.

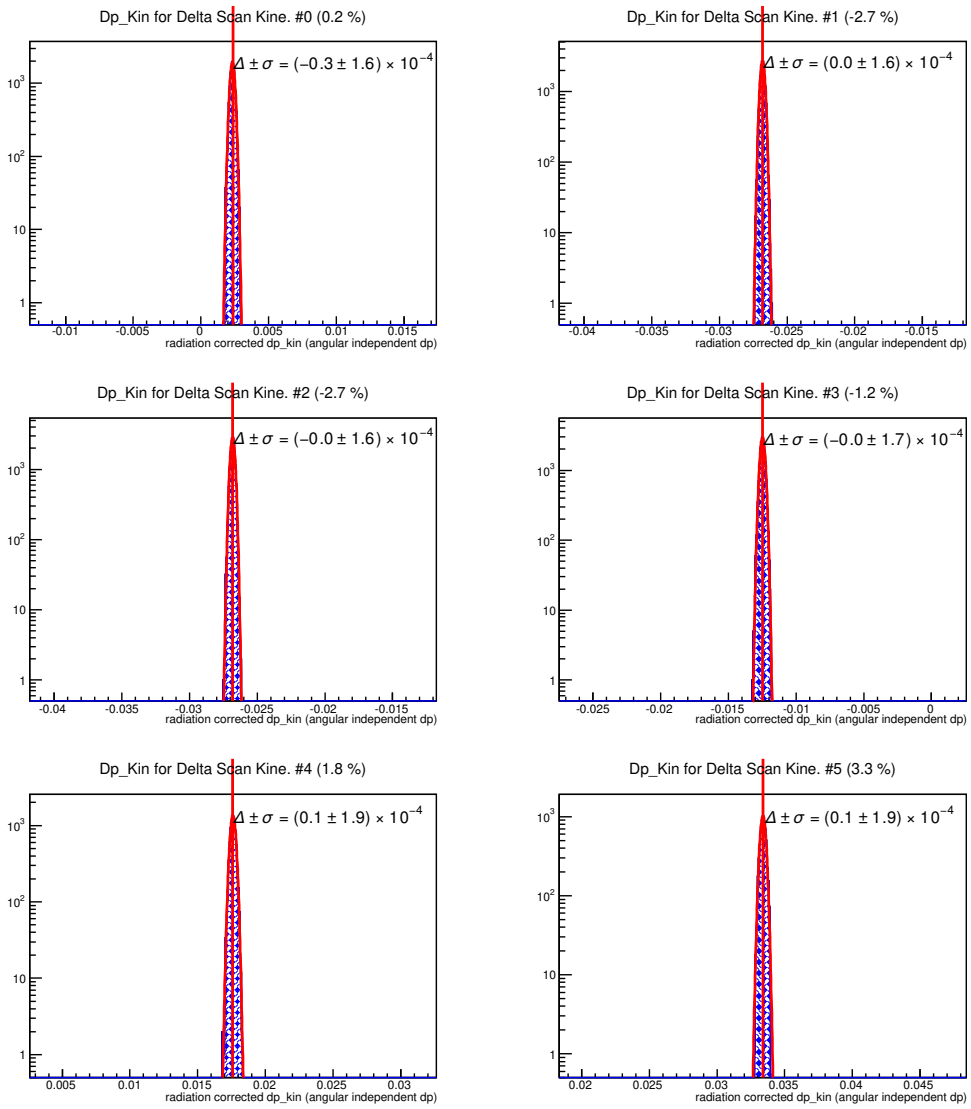

Figure 3-8: The δ optimization result of 1.1 GeV optics calibration. Each figure is for a delta scan run and the expected δ_{kin} is shown as the red line. The δ values are -2.7%, -1.2%, 0.2%, 1.8%, 3.3% (there are two runs with same δ value). The difference between the reconstructed and the expected (true) δ_{kin} is fitted and the results are shown in each panel, with Δ the mean and σ the root-mean-square (RMS) of the difference.

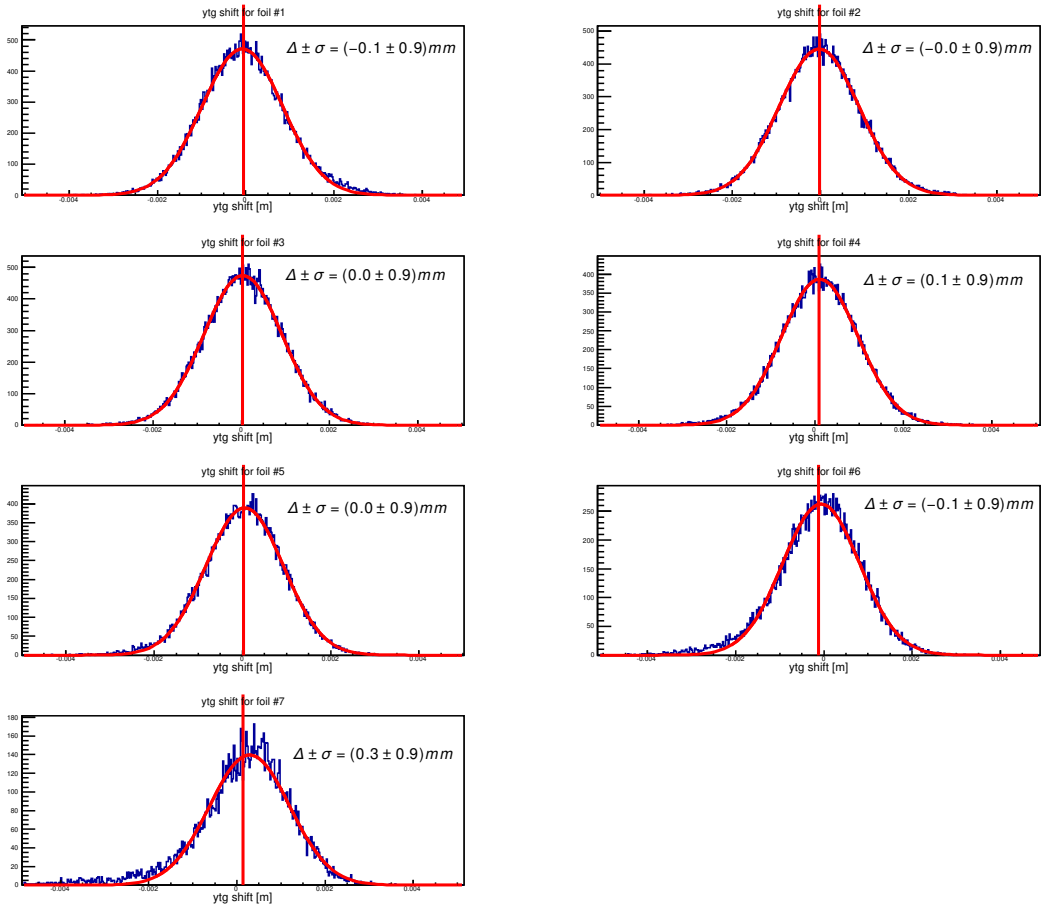

Figure 3-9: Results for 1.1 GeV optics y_{tg} optimization. From left to right, top to bottom, the foil targets are from downstream to upstream. The blue is the reconstructed y_{tg} for each foil and the red line shows the expected (true) value. The difference between the reconstructed and the true values are fitted with a Gaussian function (red curve) and the results shown in each panel with Δ the mean and σ the RMS values.

A more proper definition of the acceptance is a probability function that depends on target variables, acc(θ_{tg}, ϕ_{tg}, δ, y_{tg}) (x_{tg} is not included but an extended target correction is applied to correct the effect from x_{tg}, see [40]). The value of this function is the probability for a scattered electron with certain target variables to reach the focal plane, and can be obtained from simulations described below.

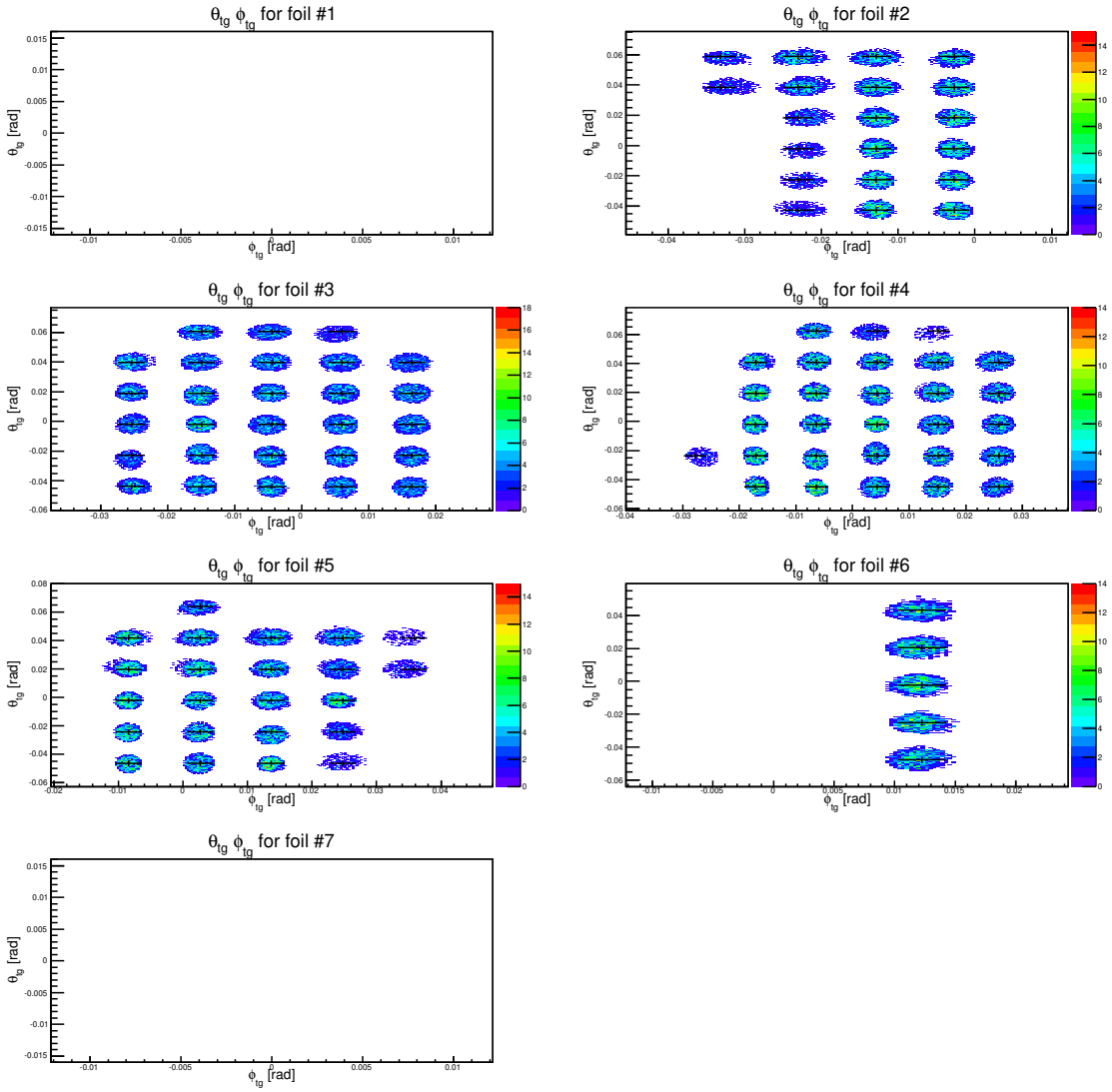

Figure 3-10: 399 MeV optics θ_{tg} and ϕ_{tg} reconstruction for each foil. From left to right, top to bottom, the foil targets are from downstream to upstream. For each panel, x axis is ϕ_{tg}, y axis is θ_{tg}. The black crossing is the reference θ_{tg}, ϕ_{tg} position for each sieve slit hole. Because the 399 MeV optics calibration data were collected at a scattering angle of 35°, the first and last foil are outside HRS spectrometer's acceptance. Overall, we also see much less holes than 1.1 GeV optics data.

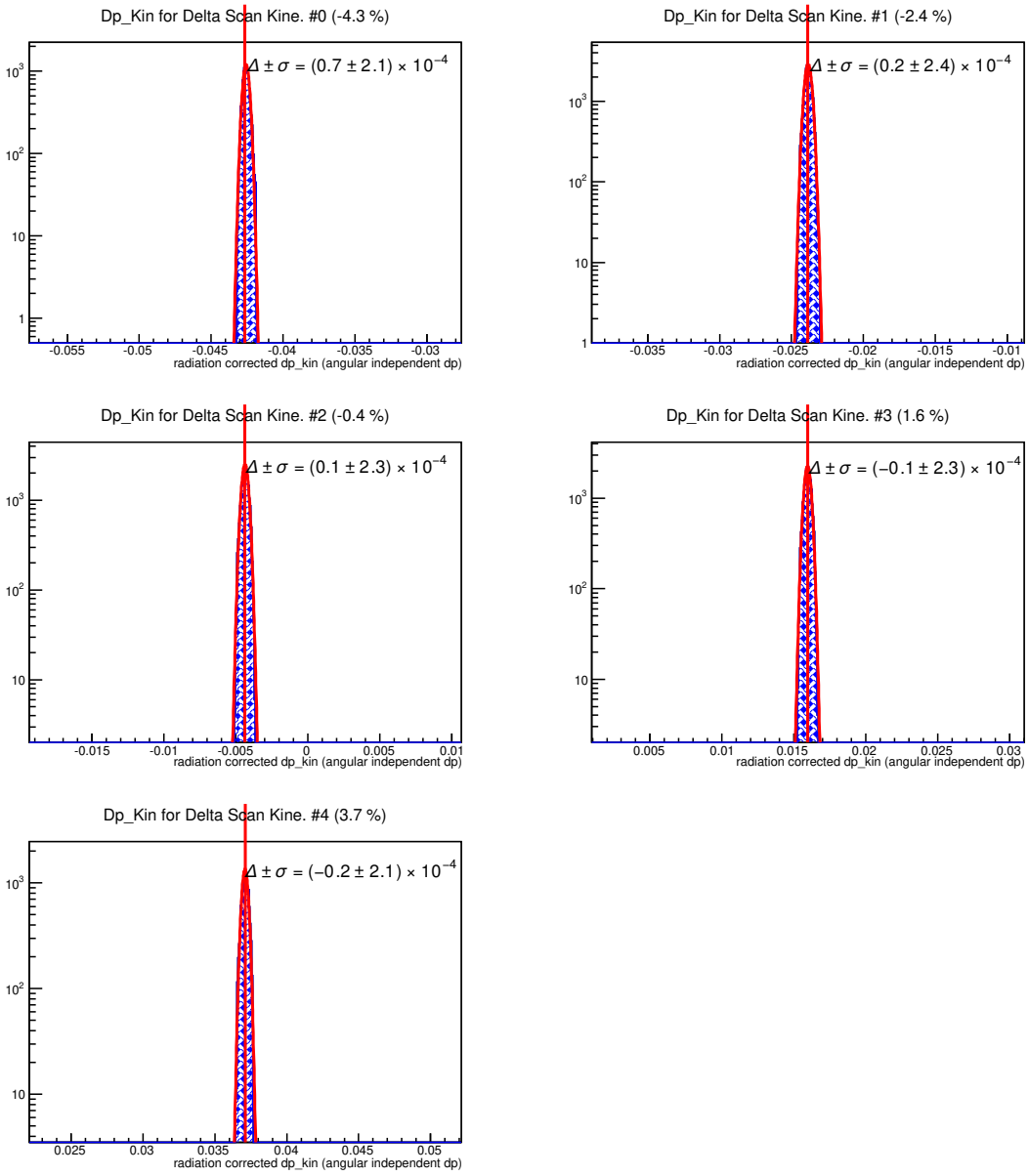

Figure 3-11: The δ optimization result of 399 MeV optics calibration. Each figure for a delta scan run. The δ value are -4.3%, -2.4%, -0.4%, 1.6%, 3.7%. The difference between the reconstructed and the true values are fitted and the results are shown in each panel with Δ the mean and σ the RMS values.

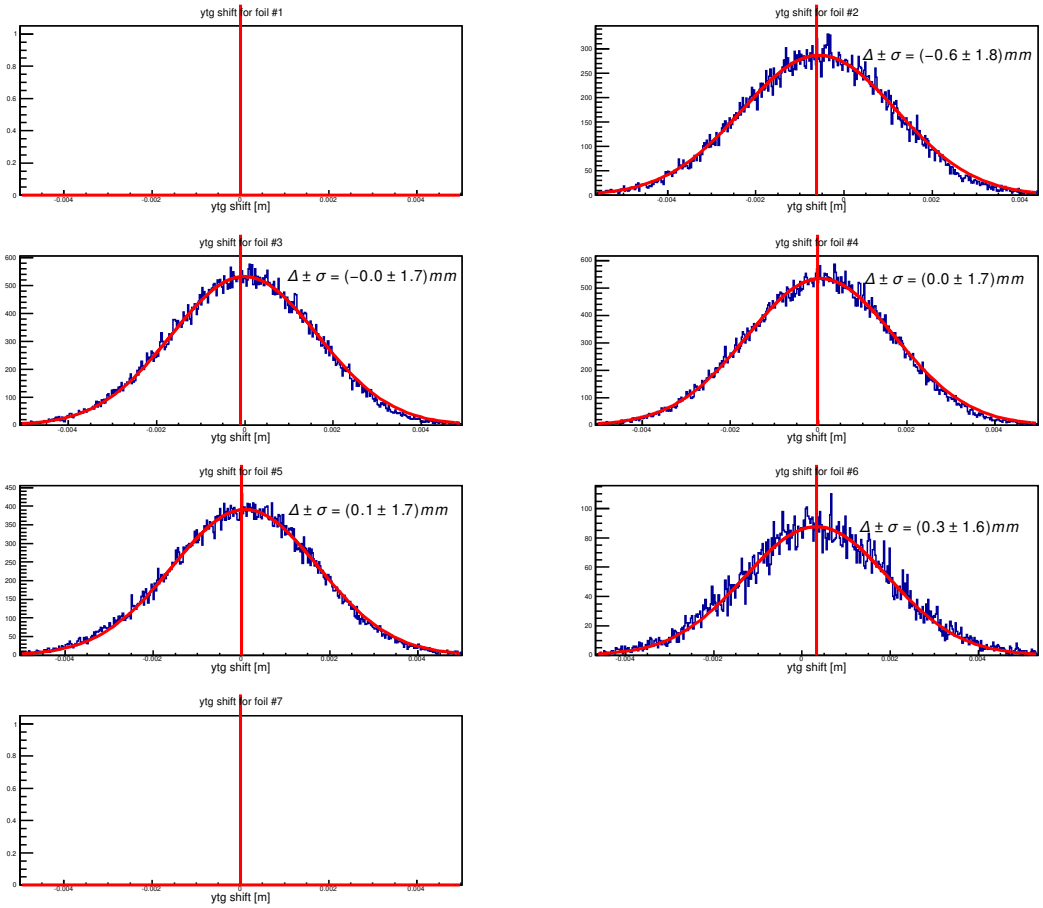

Figure 3-12: Results for 399 GeV optics y_{tg} optimization. From left to right, top to bottom, the foil targets are from downstream to upstream. The red lines indicate the real foil target positions. The difference between reconstructed and expected y_{tg} is fitted and the fitting results are shown in each panel, with Δ the mean and σ the RMS value. Because the 399 MeV optics calibration data were collected at 35°, the first and last foil are outside the HRS spectrometer's acceptance.

3.2.1 SAMC simulation

A Monte Carlo simulation package called Single Arm Monte Carlo (SAMC) [41] is used to study the acceptance of the spectrometer. SAMC was originally written in Fortran by A. Deur and converted into ROOT/C++ by Huan Yao. A detailed description of SAMC is given below:

- Trial events are generated at the target with a uniform distribution in $(\delta, \theta_{tg}, \phi_{tg}, y_{tg})$, within ranges that are (much) larger than the HRS acceptance.

- When scattered electrons pass through target and a few windows, the radiative

Name	Material	Z	A(g/mol)	Length(cm)	Density (g/cm^3)	Radiation Length X_0 (g/cm^2)
Target chamber exit window	Al	13	26.982	4.064×10^{-2} (Left HRS)	2.70	24.01
Target chamber exit window	Al	13	26.982	3.048×10^{-2} (Right HRS)	2.70	24.01
Air between target chamber and spectrometer	Air	7	14.028	≈ 65	1.2×10^{-3}	36.66
Spectrometer entrance window	Kapton	5	9.80	1.778×10^{-2}	1.42	40.61
Spectrometer exit window	Titanium	22	47.867	1.016×10^{-2}	4.54	16.16

Table 3.1: List of materials that scattered electrons pass through in SAMC (same for LHRS and RHRS unless specified) for the CSR experiment.

effects due to ionization and multiple scatterings are calculated. The windows and other materials for the CSR experiment are listed below in Table 3.1.

- Scattered electrons are then transported forward into the spectrometer using a set of forward propagation matrix generated by SNAKE simulation and the MUDIFI fitting package. The position of each event is checked at each aperture of the spectrometer. An event is discarded if it falls outside an aperture. Apertures of the HRS magnets are listed in Table 3.2.

- Events that pass through all the aperture cuts in the spectrometer are transported to VDC wire planes. They are randomly smeared according to VDC resolutions $\sigma_x = \sigma_y = 100\ \mu m$ and $\sigma_\theta = \sigma_\phi = 0.3$ mrad.

- All events reaching the focal plane are reconstructed back to the target coordinates with the reverse matrix fitted from the SNAKE simulation.

Position	Aperture(unit in meter)
Q1 Entrance/Exit	$\sqrt{x^2+y^2} < 0.15$
Q2 Entrance/Exit	$\sqrt{x^2+y^2} < 0.15$
Dipole Entrance/Exit	$\lvert x\rvert$<0.4 and $\lvert y\rvert < 0.125(1 - 1.25 \cdot x/8.40)$
Q3 Entrance/Exit	$\sqrt{x^2+y^2} < 0.30$

Table 3.2: HRS magnet apertures used in SAMC simulation (same for LHRS and RHRS). x and y are hit position of the event at that aperture.

3.2.2 Acceptance functions from SAMC

A 3-dimensional (3D) acceptance function that depends on δ, θ_{tg}, ϕ_{tg} is used for foil targets like ^{12}C and ^{56}Fe. To avoid most of the pions and low energy electrons scattered by the inner boundary of the spectrometer, we define a tight acceptance cut for the acceptance simulation and the same cut is also used for raw cross section extraction: $|\theta_{tg}| < 40$ mrad, $|\phi_{tg}| < 20$ mrad and $|dp| < 0.035$. The 3D acceptance is integrated over θ_{tg} and ϕ_{tg}, and projected on δ, as shown in Fig. 3-13. Because of the tight cuts, the acceptance inside the cuts is very close to unity.

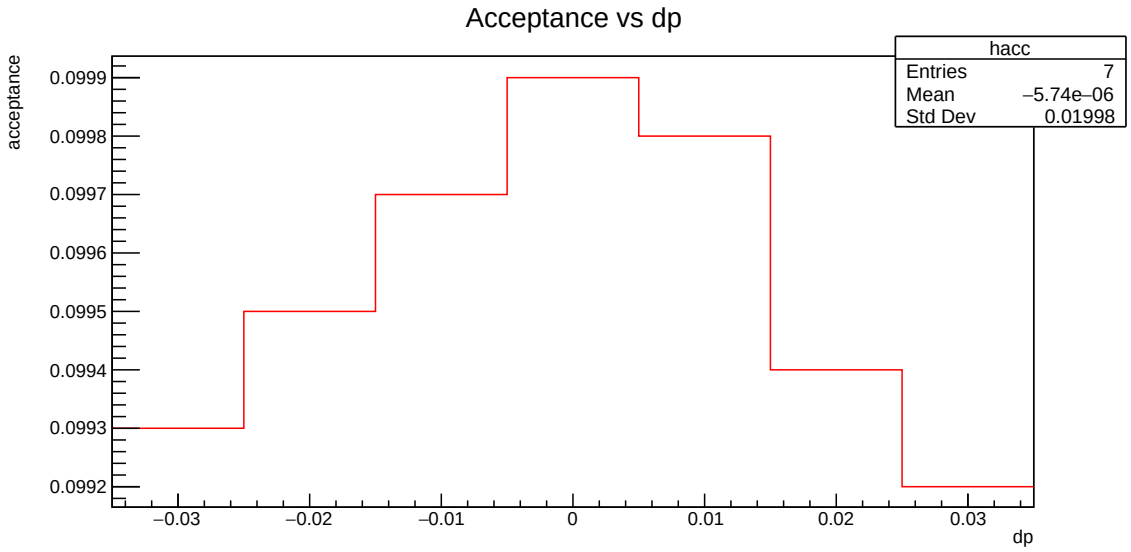

Figure 3-13: 3D acceptance function for foil targets, integrated over θ_{tg} and ϕ_{tg}, projected on dp from SAMC simulation.

For extended targets (^{4}He and ^{1}H), a 4D acceptance function that also depends on y_{tg} is necessary. The acceptance is integrated over θ_{tg} and ϕ_{tg}, and projected onto y_{tg} for different dp separately, as shown in Fig. 3-14. The acceptance falls below 1.0

for events scattered from the up- or down-stream part of the target.

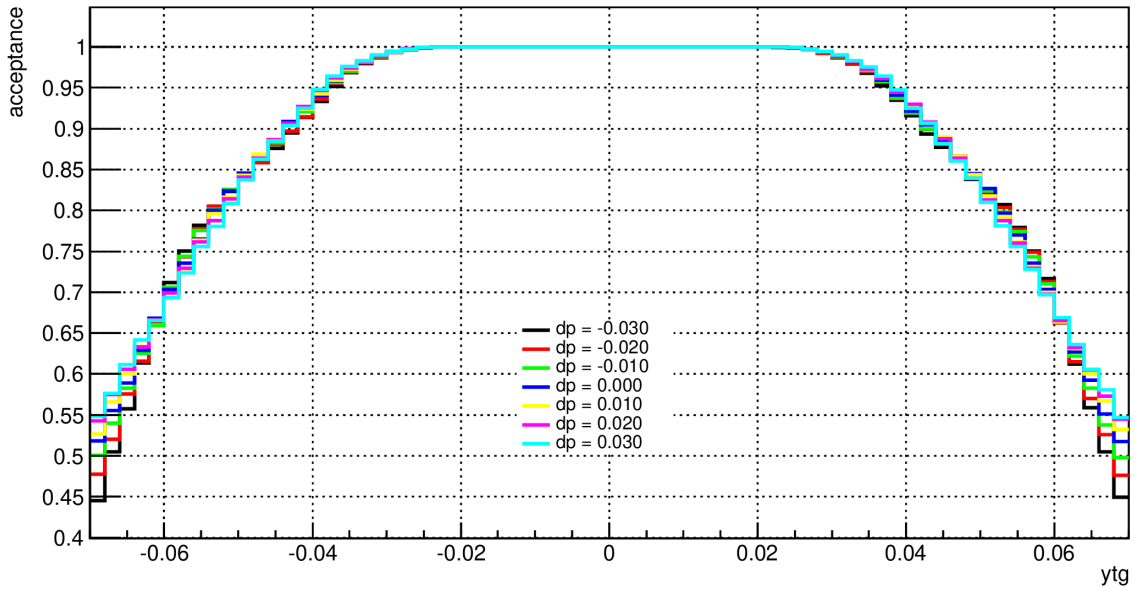

Figure 3-14: 4D acceptance function for extended targets (^{4}He and ^{1}H), integrated over θ_{tg}, ϕ_{tg}, projected on y_{tg} for different dp separately, from SAMC simulation.

3.2.3 Low momentum (<450 MeV) acceptance simulation

As mentioned in Chapter 2, the HRS spectrometer has a QQDQ magnet configuration. The functionality of the dipole magnet is bending the scatted particles upward by 45°. The central momentum of the HRS spectrometer P_0 is related to the magnetic field B_0 of the dipole with a constant Γ [42]:

$$P_0 = \Gamma B_0. \tag{3.28}$$

When the central momentum is above 450 MeV, the magnetic field in each dipole is measured and monitored by two arrays of three NMR field probes each, that work for a field range from 0.17 to 2.10 T [43]. The probes are connected through a multiplexer to a PT 4025 Teslameter. The system has a precision at the 10^{-4} level. But below 0.17 T ($\approx$ 450 MeV for the particle momentum) the NMR probes do not work, and the field in the dipole is measured by a Hall probe. The Hall probe is read out

with a Model 450 Gaussmeter which has a precision at the 10^{-3} level. The field in quadrupoles are always measured by Hall probes and Model 450 Gaussmeters.

The central momentum of the HRS can be changed by adjusting the dipole's power supply until the field in the dipole is close enough to the desired value $B_0 = \Gamma^{-1} P_0$. Power supplies of quadrupoles are also changed at the same time to keep the ratio between quadrupole fields and the dipole field almost constant. This ensures that the optics property of HRS spectrometer is independent of the central momentum and the same optics matrix can be used to analyze runs with different central momenta. Fields in the dipole and quadrupoles above 450 MeV are shown in Fig. 3-15 and are fitted as functions of the central momentum as:

$$\begin{aligned}
B_{Q1}^{P_0>450}(P_0) &= 7.05631 \times 10^{-5} - 6.3525 \times 10^{-5} P_0, \\
B_{Q2}^{P_0>450}(P_0) &= 0.000733 + 0.000226 P_0 + 3.293 \times 10^{-10} P_0^2 - 1.075 \times 10^{-13} P_0^3, \\
B_{Q3}^{P_0>450}(P_0) &= 0.000167 - 0.000202 P_0 + 5.623 \times 10^{-11} P_0^2 + 3.894 \times 10^{-14} P_0^3, \\
B_{Dipole}^{P_0>450}(P_0) &= -0.000580 - 0.000356 P_0 - 1.332 \times 10^{-9} P_0^2 + 2.864 \times 10^{-13} P_0^3,
\end{aligned} \tag{3.29}$$

where B is in unit of Tesla and P_0 is in unit of MeV/c. The ratio between quadrupole fields and the dipole field with central momentum above 450 MeV is shown in Fig. 3-16.

For the CSR experiment, a significant fraction of the large angle (90° and 120°) data were collected with central momenta below 450 MeV. By comparing the y_{det} (focal plane variable in DCS coordinate) of data with central momentum below and above 450 MeV, I found that y_{det} has an abrupt change near 450 MeV, as shown in Fig. 3-17: This abrupt change indicates the optics property is changed near 450 MeV. I found that the reason is the ratio between dipole field and quadrupole field has a "jump" near 450 MeV, see Fig. 3-18.

A further study shows that, the fields in quadrupoles and dipole have a different momentum dependence below 450 MeV. The fields are again fitted as functions of the central momentum for $P_0 < 450$ MeV, see Fig. 3-19. The fitted results are:

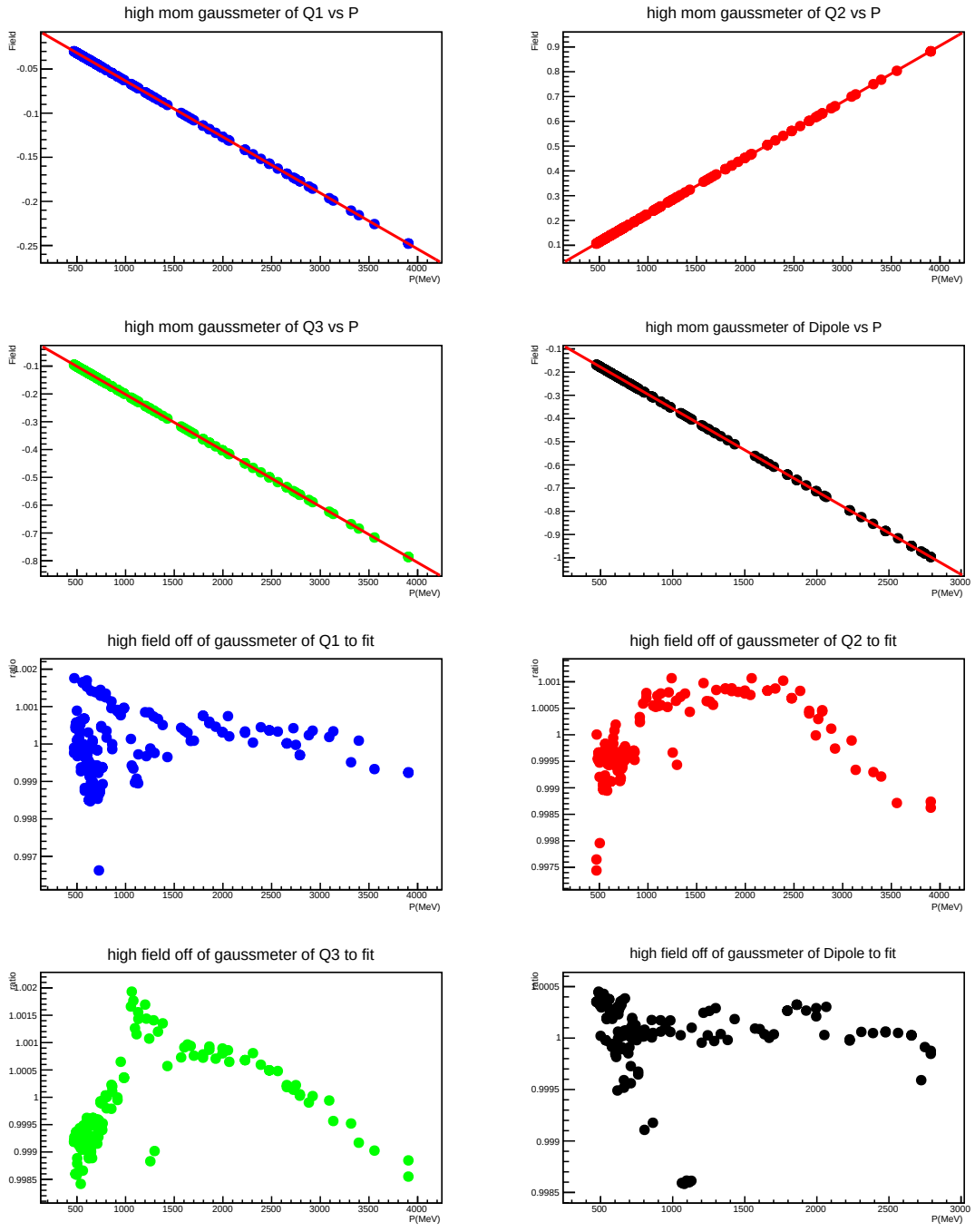

Figure 3-15: Top: measured magnetic fields in the dipole and quadrupoles with central momentum above 450 MeV. Bottom: deviation of the fields from the fitting functions of Eqs. 3.29.

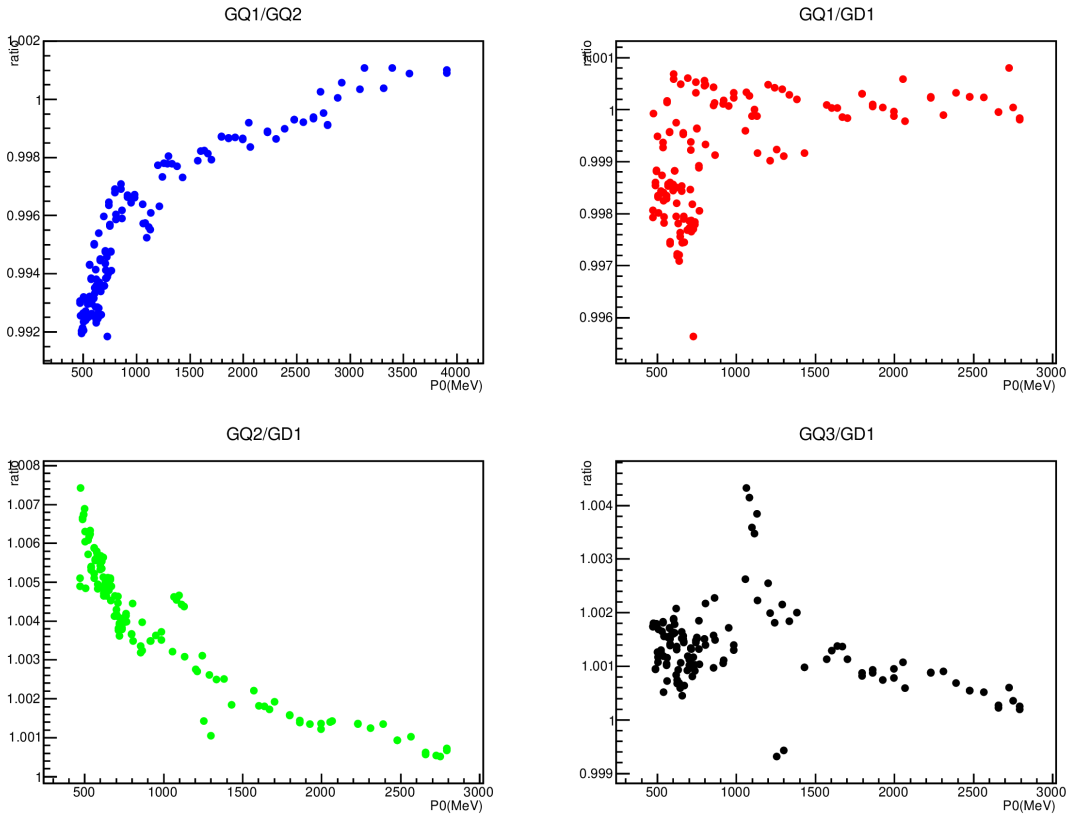

Figure 3-16: Field ratios between HRS magnets for $P_0 > 450$ MeV: Top left: Q1 field/Q2 field; top right: Q1 field/dipole field; bottom left: Q2 field/dipole field; bottom right: Q3 field/dipole field. All the ratios are normalized by ratios of fields calculated from Eqs. 3.29 for $P_0 = 3000$ MeV/c. The ratio is within $\pm 1\%$ of unity.

$$
\begin{aligned}
B_{Q1}^{P_0<450}(P_0) &= 3.101 \times 10^{-4} - 6.356 \times 10^{-5} P_0, \\
B_{Q2}^{P_0<450}(P_0) &= 9.556 \times 10^{-5} + 2.262 \times 10^{-4} P_0, \\
B_{Q3}^{P_0<450}(P_0) &= 7.937 \times 10^{-4} - 1.988 \times 10^{-4} P_0, \\
B_{Dipole}^{P_0<450}(P_0) &= -2.963 \times 10^{-7} - 3.573 \times 10^{-4} P_0.
\end{aligned}
\tag{3.30}
$$

I also calculated the ratio between dipole field and quadrupole fields, as shown in Fig. 3-20. The ratio between dipole field and Q1 (or Q3) field changed by ∼3% when the central momentum P_0 decrease from 450 MeV to 100 MeV. This change in field ratio means the optics property changes continuously with momentum when $P_0 <$

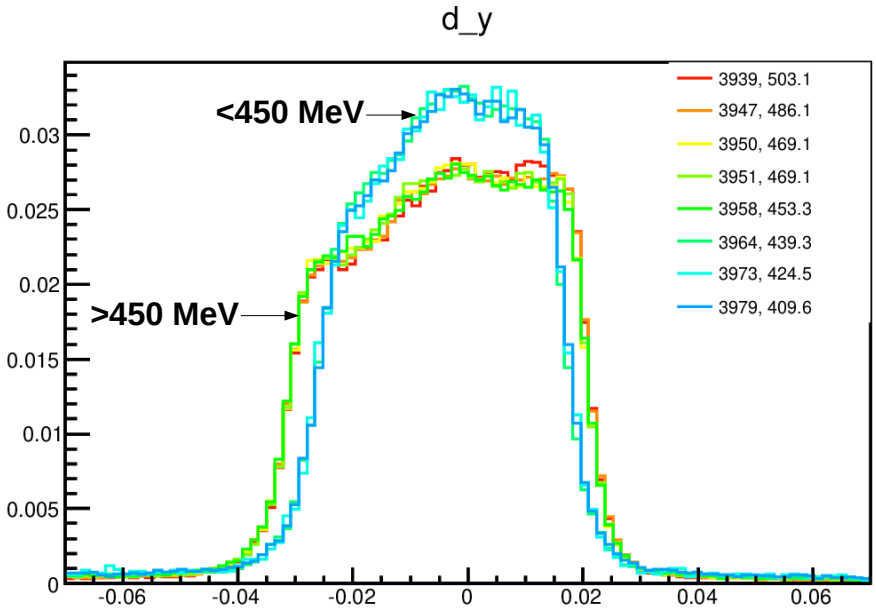

Figure 3-17: y_{det} distribution of run. Each colored line is for a run, with the run number and the HRS central momentum (in MeV) shown on the right. Runs below 450 MeV have narrower y_{det} peaks.

450 MeV. But we only had one optics calibration below 450 MeV at $P_0 = 399$ MeV. The optics matrix optimized based on this optics calibration will not work very well at momenta below 250 MeV.

To solve this issue, I implemented an acceptance correction as follows:

- For each central momentum P_0, calculate the field in quadrupole and dipole using Eqs. 3.30. Feed these field values into SNAKE simulation;
- Use MUDIFI to fit the forward matrix at P_0 based on SNAKE simulation result;
- Run an SAMC simulation using the forward matrix fitted in the previous step to propagate events from the target to the focal plane. Then use 399 MeV optics matrix to reconstruct target variables of all survived events;
- Calculate 3D acceptance for foil target or 4D acceptance for extended target as the high momentum case.

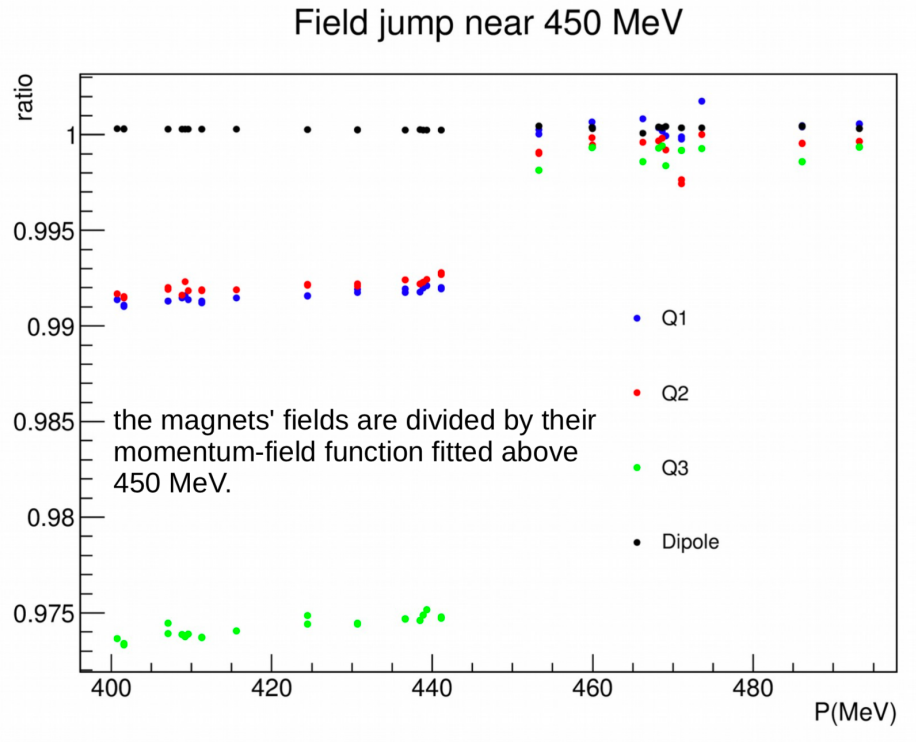

Figure 3-18: Magnetic fields of quadrupoles and dipole divided by the functions fitted with field data above 450 MeV (Eqs. 3.29). The field of Q1 and Q2 change by 0.8% while field of Q3 changes by 2.5% near 450 MeV, while the dipole field is consistent with Eqs. 3.29 for all P_0 values. Since Q3 focus electrons in the y direction, the abrupt change in y_{det} distribution shown in Fig. 3-17 is consistent with the finding here. The low momentum ($P_0 < 450$ MeV) fields are shown in a wider P_0 range in Fig 3-19.

Please note step 3 above differs from the typical simulation of acceptance (where the reverse matrix from SNAKE is used for reconstruction). This method ensures the simulation follows the same process as the real physics events and the resulting acceptance function is accurate.

3.2.4 Check of Forward Matrix

Acceptance used in this analysis was based on SAMC simulation, which used forward propagation matrix generated by SNAKE simulation and MUDIFI fitting package. Because the forward matrix is crucial to the acceptance calculation, we need to check it with experimental data.

The forward matrix were checked with 1.1 GeV and 399 MeV optics calibration

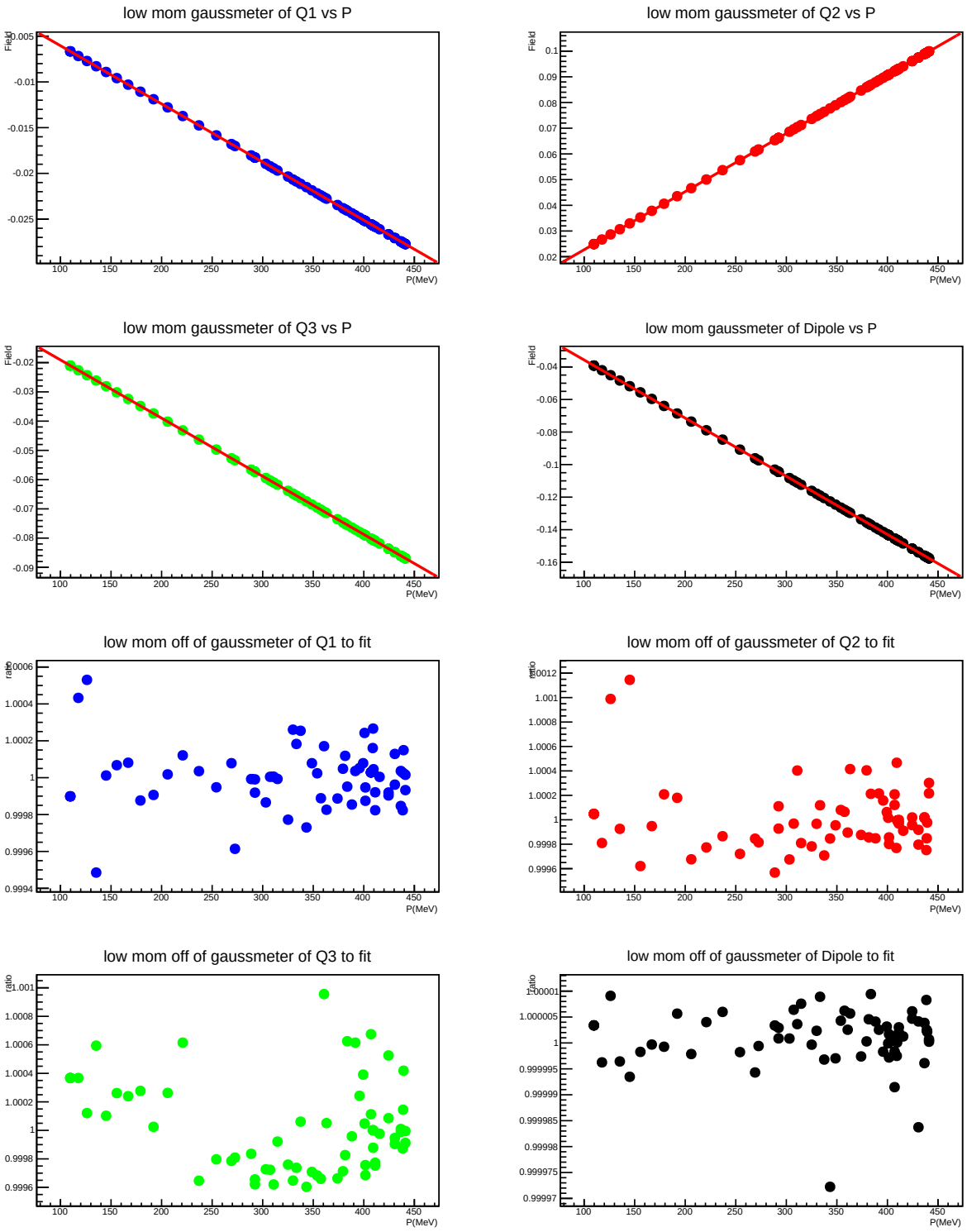

Figure 3-19: Top: field in dipole and quadrupoles with central momentum below 450 MeV. Bottom: deviation of dipole and quadrupoles field from the fitting of Eqs. 3.30.

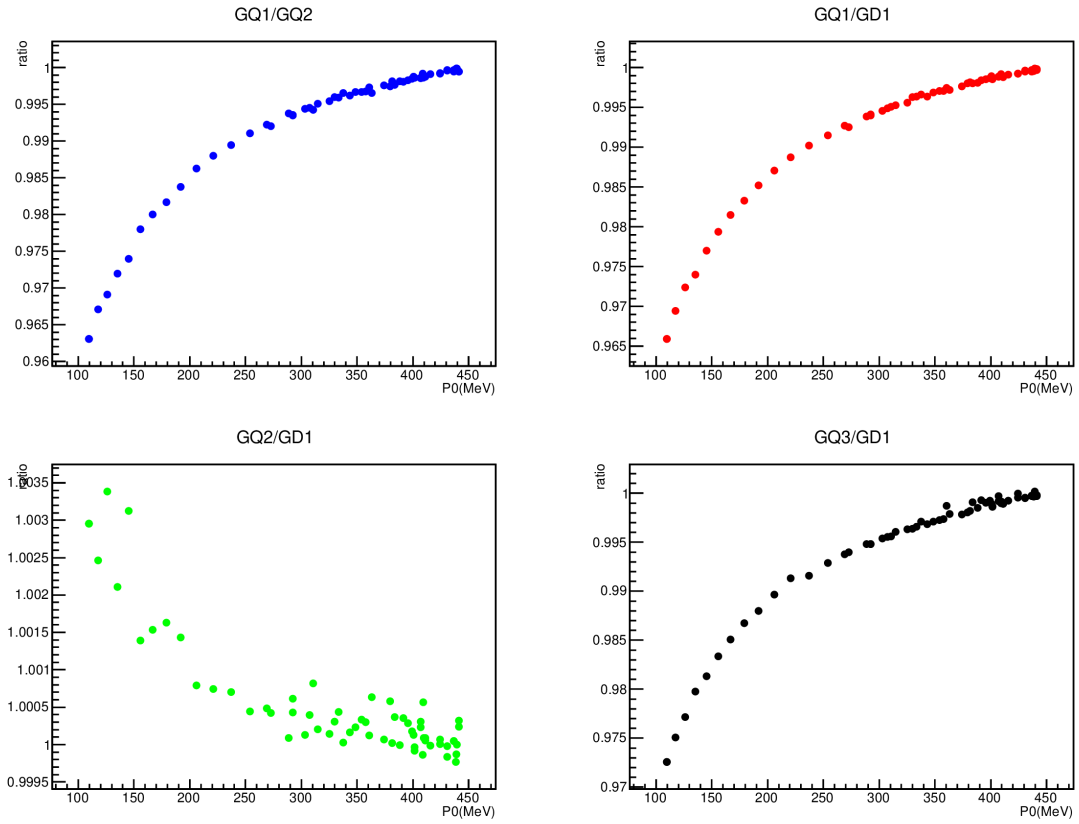

Figure 3-20: Field ratio between HRS magnets for $P_0 < 450$ MeV/c: Top left: Q1 field/Q2 field; top right: Q1 field/dipole field; bottom left: Q2 field/dipole field; bottom right: Q3 field/dipole field. All the ratios are normalized by ratios between fields calculated from Eqs. 3.30 at 450 MeV. The ratio differs from unity by up to 3%.

data: the reconstructed target variables (θ_{tg}, ϕ_{tg}, δ, y_{tg}) of events from optics calibration data (clean carbon elastic scattering events) were fed into forward matrix fitted from MUDIFI to propagate these events to focal plane. The focal plane variables (x_{det}, y_{det}, θ_{det}, ϕ_{det}) of these events are compared with their real focal plane variables from optics data, seee Figs. 3-21 and 3-22.

From Fig. 3-21, the y_{det} variable has a ≈ 2 mm difference between simulation and optics data at $y_{det} \approx 18$ mm. This difference shows a difference between the real fields in magnets and fields measured by NMR probes/Hall probes. To correct this difference, a tuning of fields in quadrupoles and dipole was performed: Numerous field settings were generated by changing the fields in quadrupoles and dipole individually

from 99% to 101%, with a step size 0.1%. For each field setting, a forward matrix was fitted from a SNAKE simulation and implemented into a SAMC simulation using optics calibration data as described above. Focal plane variable differences between simulation and optics calibration data were plotted for each field setting. The optimal field setting was found as: Q2 field increased to 100.1% and Q3 field increased to 100.3% of original values, while keeping Q1 and dipole field unchanged, as shown in Fig. 3-23. This field adjustment was applied to all field settings above 450 MeV.

The same procedure was performed on forward matrix at 399 MeV, but due to limited resolution in the optics calibration data, it was not clear how to identify the optimal field setting. Therefore the field settings below 450 MeV were not changed.

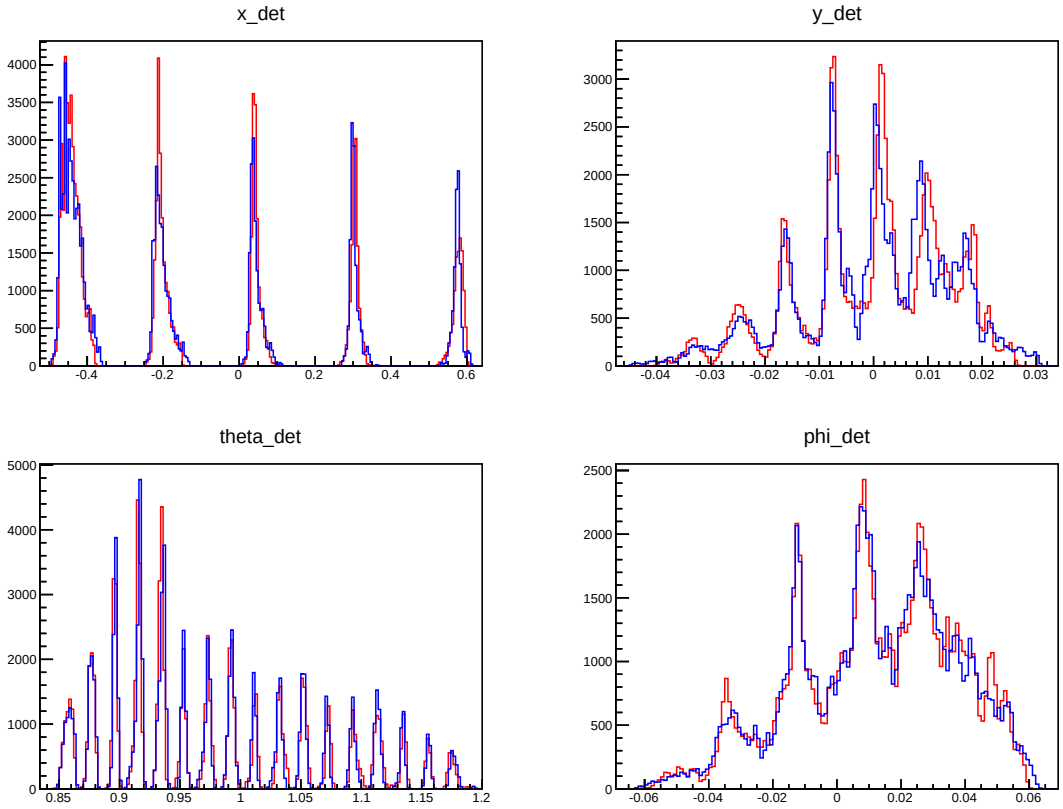

Figure 3-21: Focal plane variables (x_{det}, y_{det}, ϕ_{det}, θ_{det}) from SAMC simulation using 1.1 GeV forward matrix fitted by MUDIFI (blue) and from 1.1 GeV optics calibration data (red) are compared.

Because the ratio between dipole field and quadrupoles field change with momentum when central momentum $P_0 < 450$ MeV, optics below 450 MeV has a momentum

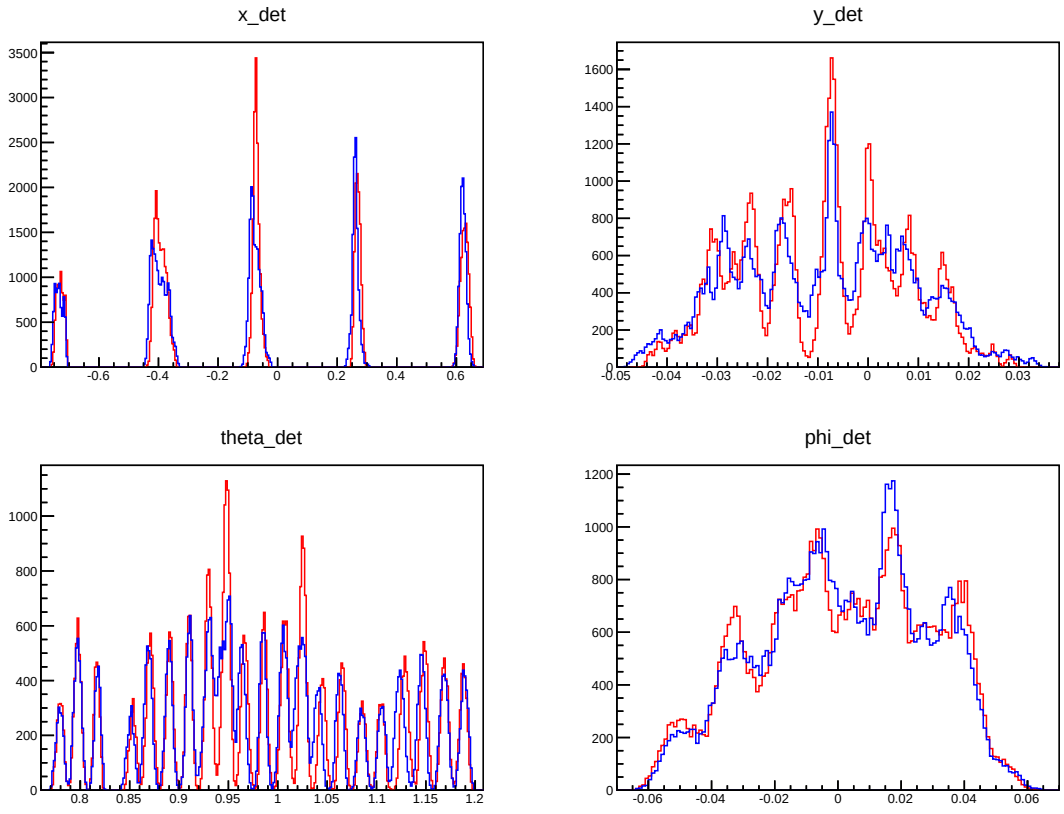

Figure 3-22: Focal plane variables (x_{det}, y_{det}, ϕ_{det}, θ_{det}) from SAMC simulation using 399 MeV forward matrix (blue) and from 399 MeV optics calibration data (red) are compared.

dependence, therefore the forward matrix below 450 MeV also changes with momentum. To check the performance of low momentum forward matrix, several SAMC simulations were run and compared with hydrogen elastic runs. Information including beam energy E, spectrometer angle θ_0, central momentum P_0, beam position and beam size of a hydrogen elastic run was fed into SAMC simulation, and the forward matrix at P_0 was also put into the simulation. The simulation result was then weighted by hydrogen elastic cross section calculated from:

$$\frac{d^2\sigma}{d\Omega} = \sigma_{Mott}\left(\frac{G_E^2(Q^2)+\tau G_M^2(Q^2)}{1+\tau} + 2\tau G_M^2(Q^2)\tan^2\frac{\theta}{2}\right), \tag{3.31}$$

where

$$\tau = \frac{Q^2}{4M_p}. \tag{3.32}$$

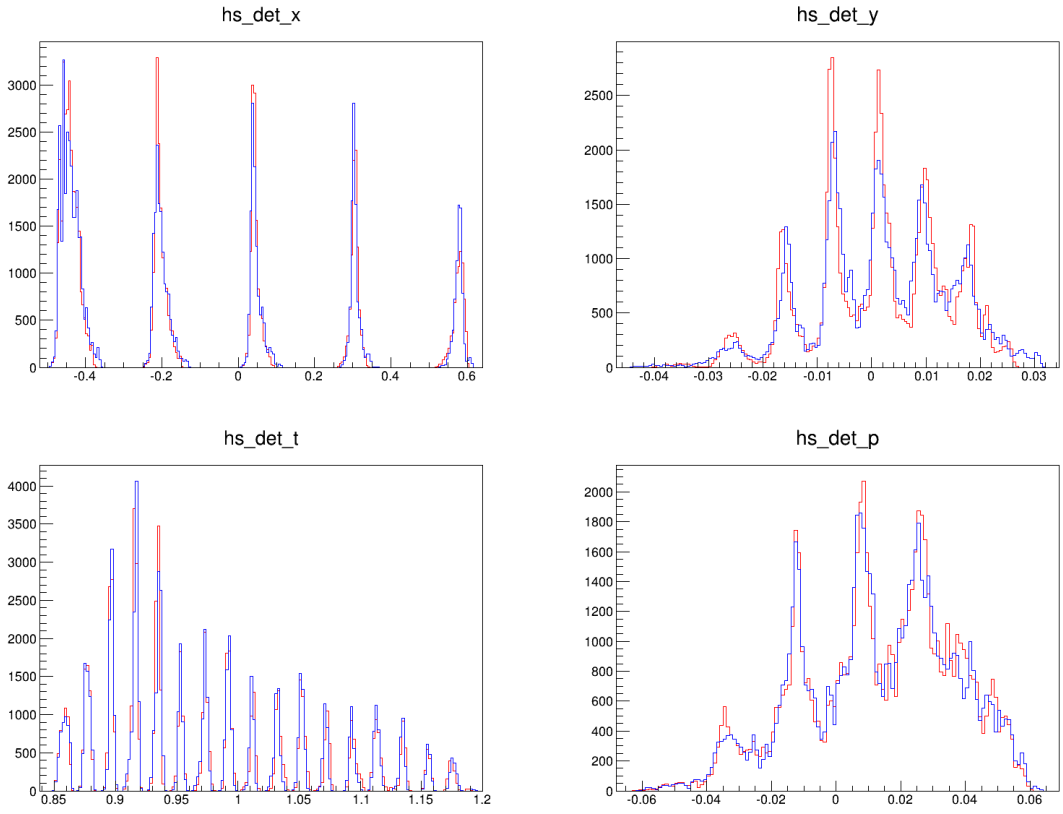

Figure 3-23: Focal plane variables (x_{det}, y_{det}, ϕ_{det}, θ_{det}) using 1.1 GeV forward matrix with optimal field setting (blue) and from 1.1 GeV optics calibration data (red) are compared.

For the proton's form factors $G_E(Q^2)$ and $G_M(Q^2)$, Zhihong Ye's nucleon electromagnetic form factor fitting parametrizations [44] were used.

Target variables of three 90° hydrogen elastic runs and corresponding simulation are compared in Figs. 3-24, 3-25, and 3-26. These hydrogen elastic runs are at P_0 = 433.7 MeV, 341.3 MeV, 272.0 MeV, respectively. Despite the difference in dp, The simulation and data agree very well. This indicates the acceptance calculation works for low momentum settings until 272.0 MeV.

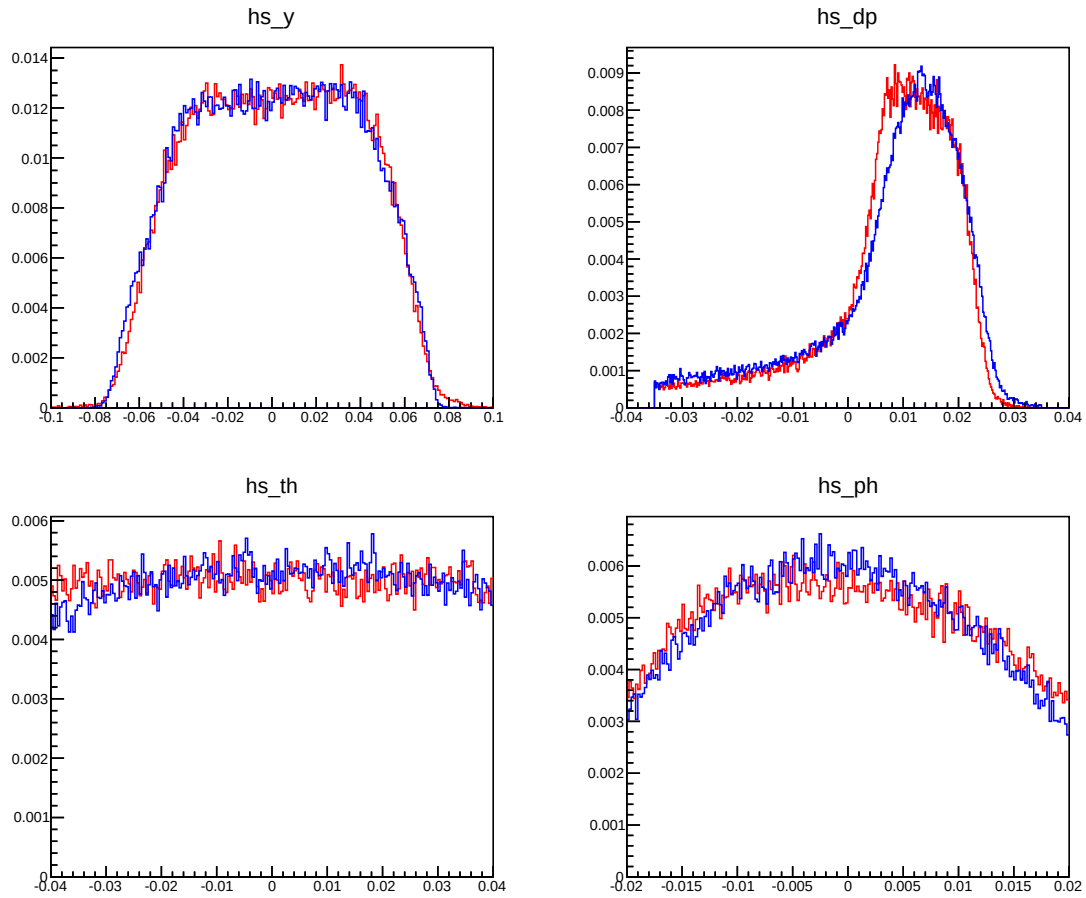

Figure 3-24: Target variables y_{tg}, dp, θ_{tg}, ϕ_{tg} (from left to right, top to bottom) of SAMC simulation (blue) and hydrogen elastic data (red) are compared. The hydrogen elastic data is from run 2659, with $E = 845.0$ MeV, $P_0 = 433.7$ MeV, $\theta_0 = 90°$.

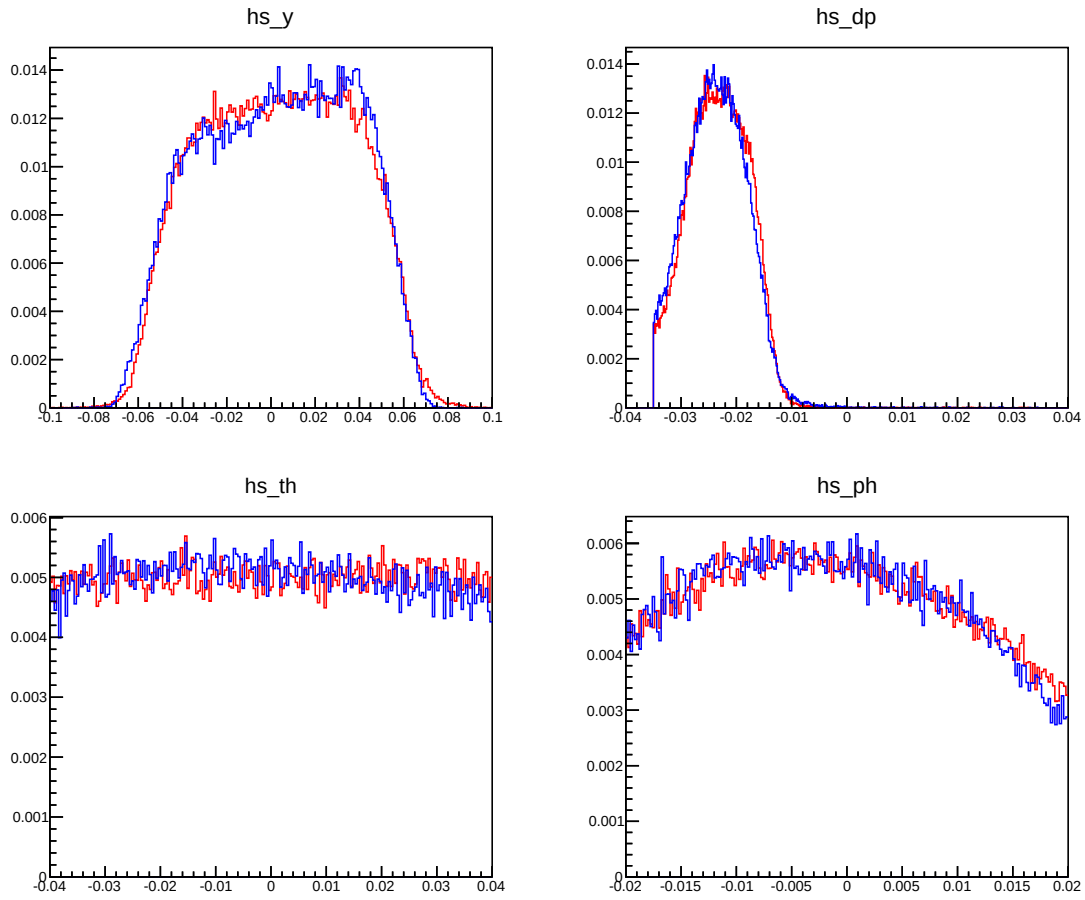

Figure 3-25: Target variables y_{tg}, dp, θ_{tg}, ϕ_{tg} (from left to right, top to bottom) of SAMC simulation (blue) and hydrogen elastic data (red) are compared. The hydrogen elastic data is from run 1754, with $E = 528.3$ MeV, $P_0 = 341.3$ MeV, $\theta_0 = 90°$.

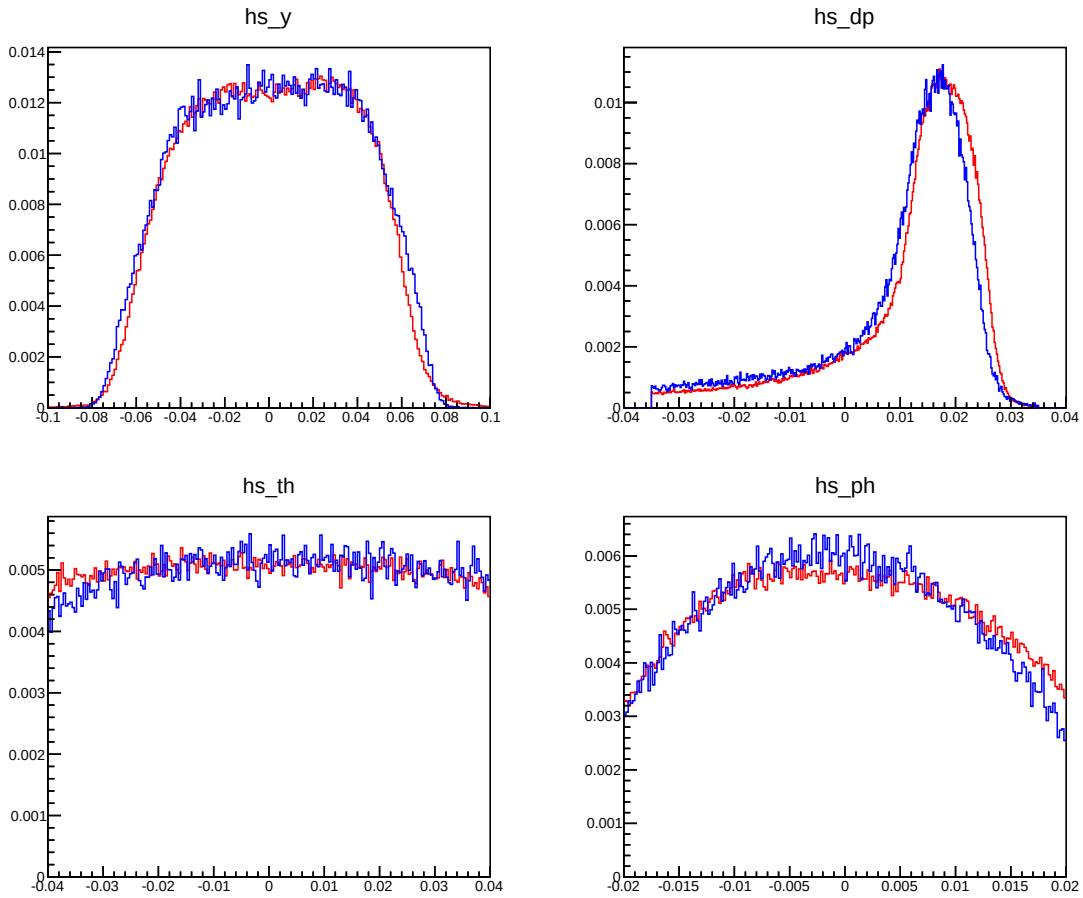

Figure 3-26: Target variables y_{tg}, dp, θ_{tg}, ϕ_{tg} (from left to right, top to bottom) of SAMC simulation (blue) and hydrogen elastic data (red) are compared. The hydrogen elastic data is from run 4876, with $E = 399.4$ MeV, $P_0 = 272.0$ MeV, $\theta_0 = 90°$.

Chapter 4

Data Analysis

In this chapter I will discuss the data analysis procedure of the CSR Experiment.

4.1 Particle Identification Efficiency

For Hall A experiments using the standard HRS detector package, particle identification (PID) is achieved by a Cerenkov detector and a double-layered lead glass calorimeter. For the CSR experiment, a NaI calorimeter was installed on LHRS in front of the double-layered lead glass calorimeter in order to have a better control of background particles at low momentum settings. However, some of the blocks were unresponsive during the experiment, which made the NaI Calorimeter very difficult to use in the analysis, and thus only Cerenkov was used for PID. In this analysis, we define PID cuts only by Cerenkov cuts. PID analysis on RHRS was done with the aid of shower/preshower detectors.

The PID efficiencies of left and right arm HRS were fairly close. The PID efficiency is usually characterized by the electron efficiency η_e and the pion rejection factor η_π. Electron efficiency η_e is defined as the ratio between number of electrons identified by the detector and the total number of electrons that enter the detector. The pion rejection factor η_π is defined as the ratio between number of pions rejected by the detector and the number of pions that are mis-identified as electrons by the detector.

Figure 4-1 shows a spectrum of summed ADC signal of the LHRS gas Cerenkov

detector. The ADC signal of the Cerenkov detector has two peaks: the peak around 1400 ADC channels for LHRS (and 1800 ADC channels for RHRS) is the multiple photo-electron peak triggered by electrons. The peak centered around 250 ADC channels is the single photo-electron peak triggered mostly by background particles.

A Cerenkov ADC cut at ADC channel $\geqslant 350$ was used to select scattered electrons and reject background particles such as pions and knock-on electrons (see Section 2.7.3). Pions usually cannot fire the Cerenkov detector, but the knock-on electrons produced by pions still can.

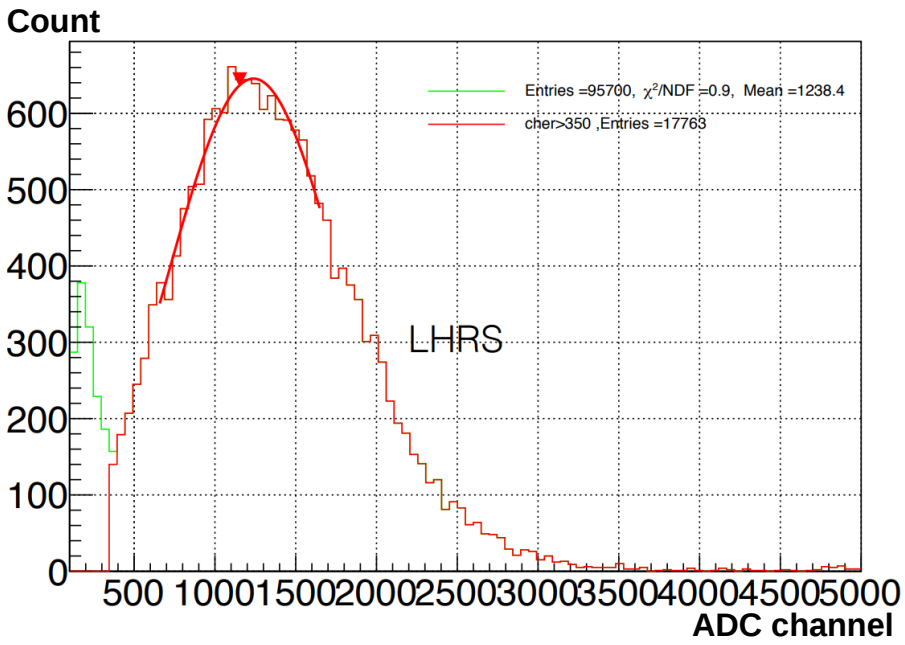

Figure 4-1: LHRS Cerenkov spectrum, both total (green) and those pass the PID cut (red). The x axis is the sum of all ADC channels of the Cerenkov, while y axis is event count.

To study the electron efficiency and pion rejection factors of the Cerenkov detector, we first use RHRS shower and preshower calorimeters to select clean samples of electrons and clean sample of background. Once clean electrons and background samples were selected, their RHRS Cerenkov ADC spectra are plotted and fitted separately using Poisson distributions. The parameters from the fitting of clean electron and background samples were used to fit the multiple photo-electron peak and one photo-electron peak. Because part of the clean electron sample is below the Cerenkov

ADC channel $\geqslant$ 350 cut, the cut will remove some of the good electrons. The cut efficiency can be calculated by estimating the electrons below the Cerenkov ADC channel $\geqslant$ 350 cut using the multiple photo-electron peak fit. A similar Poisson distribution fit was applied to the LHRS Cerenkov ADC spectra, but without using lead glass calorimeters to select clean electron/pion samples.

The electron cut efficiency for both LHRS and RHRS can be defined as:

$$\varepsilon_{\text{Cerenkov}} = \frac{A_1}{A_1 + A_2} \tag{4.1}$$

where A_1 is the area above the Cerenkov ADC channel 350 cut, and A_2 is the area below that cut, as shown in Fig. 4-2. Here areas (instead of number of electron or pion entries) are used in the definition because the LHRS has no calorimeters to select clean electron or pion samples.

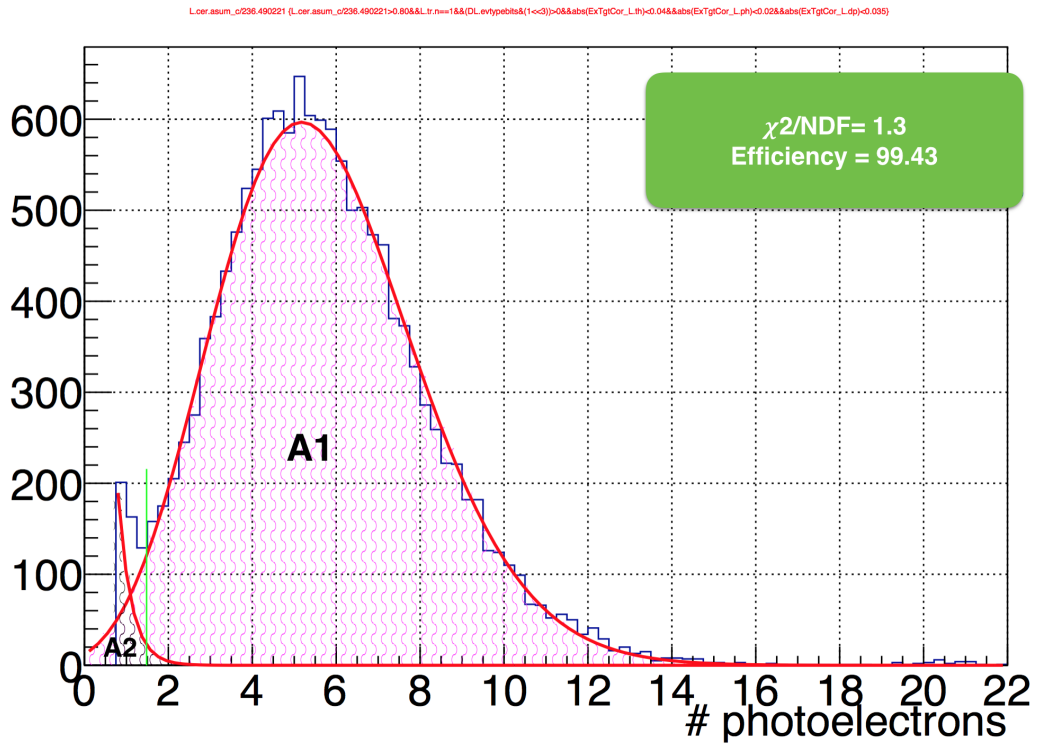

Figure 4-2: LHRS Cerenkov ADC signal as a function of the number of photoelectrons. The green vertical line is the position of the Cerenkov ADC cut at channel 350. A_1 is the area above the cut and A_2 is the area below the cut. The left red curve is the fitting of one-photoelectron peak and the right curve is the fitting of main peak. Figure reproduced from [1].

The Cerenkov electron efficiency was studied for each run. It was found to be 99.6 $\pm$ 0.003% for the LHRS (see Fig. 4-3) and 99.9$\pm$0.003% for the RHRS (see Fig. 4-4). The RHRS Cerenkov is longer than LHRS and is thus slightly more efficient.

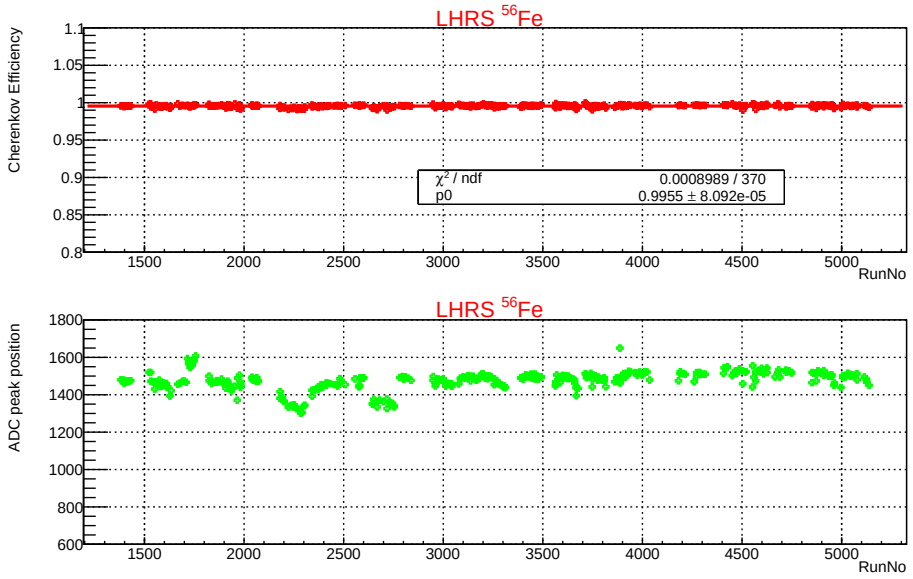

Figure 4-3: Cerenkov electron efficiency (top) and ADC peak position (bottom) results for LHRS as function of run numbers. Figure reproduced from [1].

Similarly, part of the pion background is above the Cerenkov ADC 350 cut. To study the pion rejection factor, we use shower/preshower of RHRS to get a clean pion sample. $N_{\pi^- sample}$ is the total number of pions in the clean pion sample and $N_{\pi^- leak}$ is the number of π^- that is above the Cerenkov ADC channel 350 cut. The pion rejection factor is defined as:

$$\pi^-_{rej} = \frac{N_{\pi^- sample} - N_{\pi^-_{leak}}}{N_{\pi^- sample}}, \tag{4.2}$$

Because the backward angle and high beam energy runs have the most background, the 120° and E=957 MeV runs were used for the pion rejection study. The pion rejection factor was found to be 99.7 $\pm$ 1.1% for RHRS (see Fig. 4-5). This factor was applied on LHRS data too because the LHRS calorimeter (or the NaI detector) cannot be used to define clean pion samples.

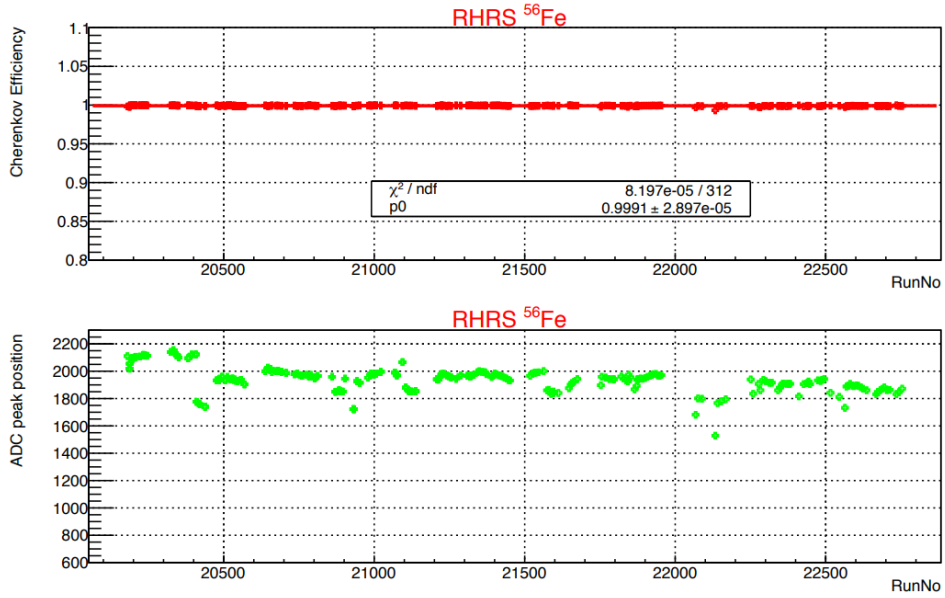

Figure 4-4: Cerenkov electron efficiency (top) and ADC peak position (bottom) results for RHRS as function of run numbers. Figure reproduced from [1].

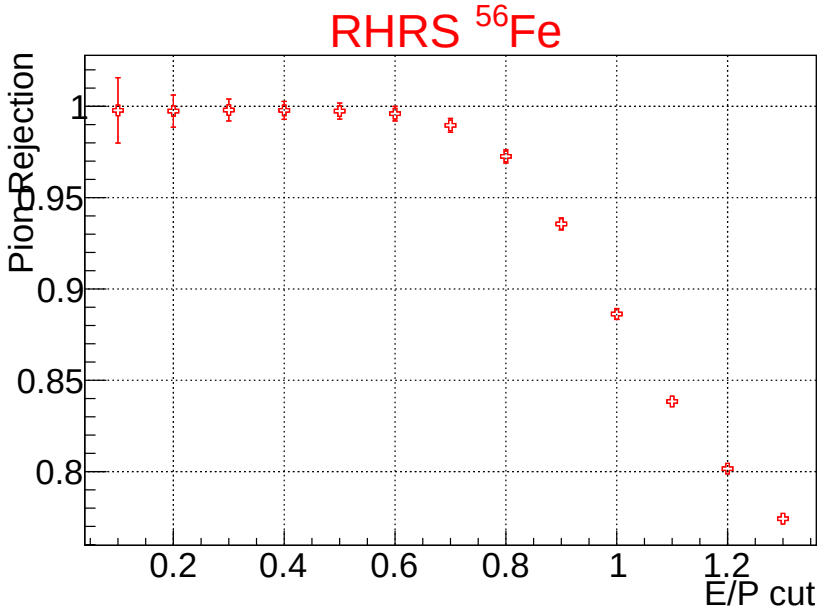

Figure 4-5: The pion rejection factor as a function of calorimeter E/P cut. The calorimter E/P cut is used to define the clean pion samples. Figure reproduced from [1].

4.2 Tracking Efficiency

The Vertical Drift Chambers (VDC) detect hits of scattered particles and reconstruct tracks through the track reconstruction algorithm. Under normal conditions, each event leaves only one track in the VDC, but in certain cases an event can have zero track or multiple tracks. The inefficiency of VDC wires or failure of track reconstruction may result in zero track events. In most cases, the wire inefficiency is less than 0.1%. The wire inefficiency cannot be separated from the tracking inefficiency and is convoluted into the multi-track efficiency. A multi-track event means two or more tracks are reconstructed by the VDC for a single event. It can happen when several particles generated by secondary processes are passing through VDC simultaneously, or when there is noise in the VDC.

For most of runs in the CSR experiment, the event rate was below 10 kHz and only a small fraction of events had multiple tracks. For kinematic settings with higher trigger rates, the fraction of multi-track events is also higher: there are some runs with trigger rates higher than 10 kHz, and multi-track events contribute more than a few percent to total events. A strict treatment is therefore necessary for these runs: Multi-track events must be examined carefully to determine whether there is a good track among all the reconstructed tracks.

The tracking efficiency can be defined as the ratio:

$$\varepsilon_{\mathrm{VDC}} = \frac{N_{\mathrm{good}}}{N_{\mathrm{total}}}, \tag{4.3}$$

where N_{good} is the number of events with successful track reconstruction and are confirmed by the energy deposit in the leadglass calorimeter and also pass all acceptance cuts and PID cuts, N_{total} is the number of events that pass all acceptance and PID cuts. The PID cuts used for tracking analysis are Cerenkov cut and shower/preshower cuts (the shower/preshower cuts are only available for RHRS, and this tracking efficiency is done on RHRS and applied on LHRS).

Because checking the multi-track event is very time consuming, in the analysis of production runs, we usually use only events with a single track, and a correction for

the loss of multi-track events is applied: We redefine the multi-track efficiency as:

$$\varepsilon_{\rm VDC} = \frac{N_{\rm goodsingletrack}}{N_{\rm goodsingletrack} + N_{\rm goodmultitrack}}, \tag{4.4}$$

where $N_{\rm goodsingletrack}$ is the number of events with good single-track reconstruction in the sample and $N_{\rm goodmultitrack}$ is the number of multi-track events with at least one good track in the same sample.

A multi-track event is considered a good event if: (a) at least one track resides inside the normal acceptance cuts used for the analysis: $|dp| \leq 3.5\%$, $|\theta_{tg}| \leq 40$ mrad, $|\phi_{tg}| \leq 20$ mrad; and (b) the energy deposited in the calorimeter of this track satisfies the PID cuts.

To obtain the energy deposition of an event in the calorimeter, we need to project forward the track onto the calorimeter. Because some of the blocks of the NaI calorimeter in LHRS were not responsive during the experiment, this tracking efficiency is studied only for RHRS, and then applied to LHRS since the left and right HRS VDCs are identical.

Figure 4-6 shows the distribution of energy deposition in 2 layers of the RHRS calorimeter (sum of shower and preshower) for two-tracks events. We can divide these events into four distinct types, depending on the total energy deposits, E_1 and E_2, of the two tracks:

- Region A: $E_1 < E_{PID}$ and $E_2 < E_{PID}$, where E_{PID}=620 MeV is the PID cut for total energy deposited in the preshower and shower calorimeter. None of the tracks can pass the PID cut, therefore none of the tracks is considered good.

- Region B: $E_{PID} \leq E_1 < 2E_{PID}$ and $E_2 < E_{PID}$, if track #1 passes acceptance cut and its energy deposited in the preshower also satisfies the PID energy cut, track # 1 is considered good and track # 2 not good.

- Region C: $E_1 < E_{PID}$ and $E_2 \geq E_{PID}$, similar to Region B, track # 2 is considered good and track # 1 not good.

- Region D: $E_1 > 2E_{PID}$ or $E_2 > 2E_{PID}$, if one track can pass acceptance cut

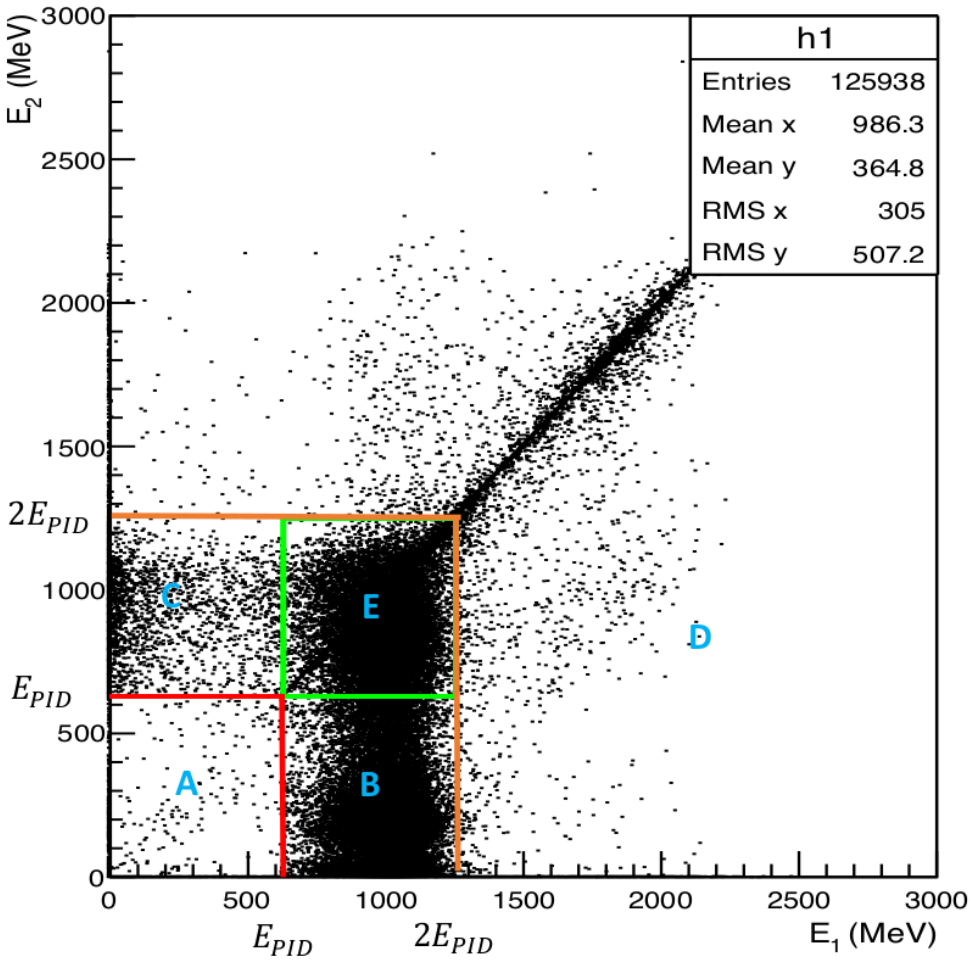

Figure 4-6: Energy deposit summed over in shower and preshower for two track events. x axis: E_1 is energy deposit of the first track; y axis: E_2 is energy deposit of the second track.

and its energy deposited in the preshower also satisfies the PID energy cut, at least one good track is expected.

- Region E: $E_{PID} < E_1, E_2 < 2E_{PID}$. There can be two good tracks, or one good track and one bad track, or two bad tracks. More study is necessary to further identify good events in this region, as follows:

  1. If there is at least one block distance between the pointed blocks of the two tracks at lead glass, then at least one track is considered good in this event (one good track in the event is enough to identify this event as good multi-track event).

2. If the distance between the pointed blocks of the two tracks at lead glass is smaller than one block width, the two tracks overlapped in the energy deposition. If one cluster energy subtracts the energy deposited in the overlapping block still satisfying the PID cut, we can expect at least one good track in this event.

The multi-track efficiency is plotted as a function of the trigger rate and fitted to a first order polynomial, as shown in Fig. 4-7. This fitted function was used to calculate the tracking efficiency of each run using the run's trigger rate.

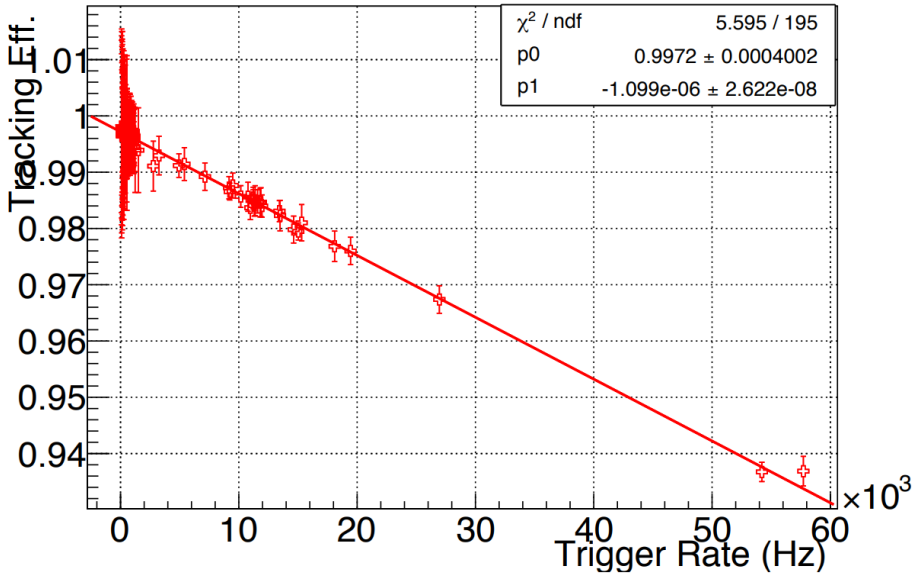

Figure 4-7: Tracking efficiency as a function of trigger rate.

4.3 Window Background Subtraction

As mentioned in Chapter 2, the cryogenic targets (gaseous or liquid ^{4}He or liquid hydrogen) are made of aluminium. Therefore, data from cryotargets contain electrons scattered from aluminium walls, which form a background. To extract experimental cross sections, the background must be subtracted properly. For this reason, data were taken on the aluminium dummy target with the same kinematic settings as the ^{4}He and ^{1}H data, including the same beam energy E_{beam}, spectrometer central

momentum P_0 and scattering angle θ.

To subtract aluminium background from cryogenic target data, the yield from pure ^{4}He or H_2 is calculated as:

$$Y_{\text{corrected}} = Y_{\text{cryot}} - Y_{\text{dummy}} \frac{T_{\text{wall}}}{T_{\text{dummy}}} \frac{R_{\text{wall}}}{R_{\text{dummy}}} \ , \tag{4.5}$$

where Y_{cryot} and Y_{dummy} are yields of the cryogenic target runs and dummy runs. The yield is defined as the amount of scattered electron events normalized by the incident beam charge. T_{wall} and T_{dummy} are aluminum wall thicknesses of the cryogenic and the dummy target, and R_{wall} and R_{dummy} are the radiation factors of the cryogenic target and the dummy target, respectively. The radiation factor term is included because electrons scattered off entrance/exit window of the cryotarget target pass through gaseous or liquid ^{4}He or H_2 both before and after scattering, which is different from the situation of the dummy target. Two sets of SAMC simulations were used to calculate this factor: one contains the material of the cryotarget target, another contains the material of the dummy target. The ionization and Bremsstrahlung are properly included for both conditions. The simulation used the aluminium cross section from F1F209 model [45]. The yield ratio between two sets of simulations is used as the radiation factor ratio $R_{\text{wall}}/R_{\text{dummy}}$. The SAMC simulation of ^{4}He target and dummy target are shown in Fig. 4-8. The wall background subtraction of ^{4}He run 1881 at 90° is shown in Fig. 4-9.

Besides using dummy target to subtract window background, another method to remove the window background was used independently as a cross check. In this second method, a y_{tg} cut was used to remove the background from entrance and exit windows: a cut $|y_{tg}| \leq 5$ mm was applied for 15° data, and a cut $|y_{tg}| \leq 2.5$ cm was applied to other angles. A comparison of the cross section extracted using these two methods is shown in Fig. 4-10. The difference is below 1% for 60° data.

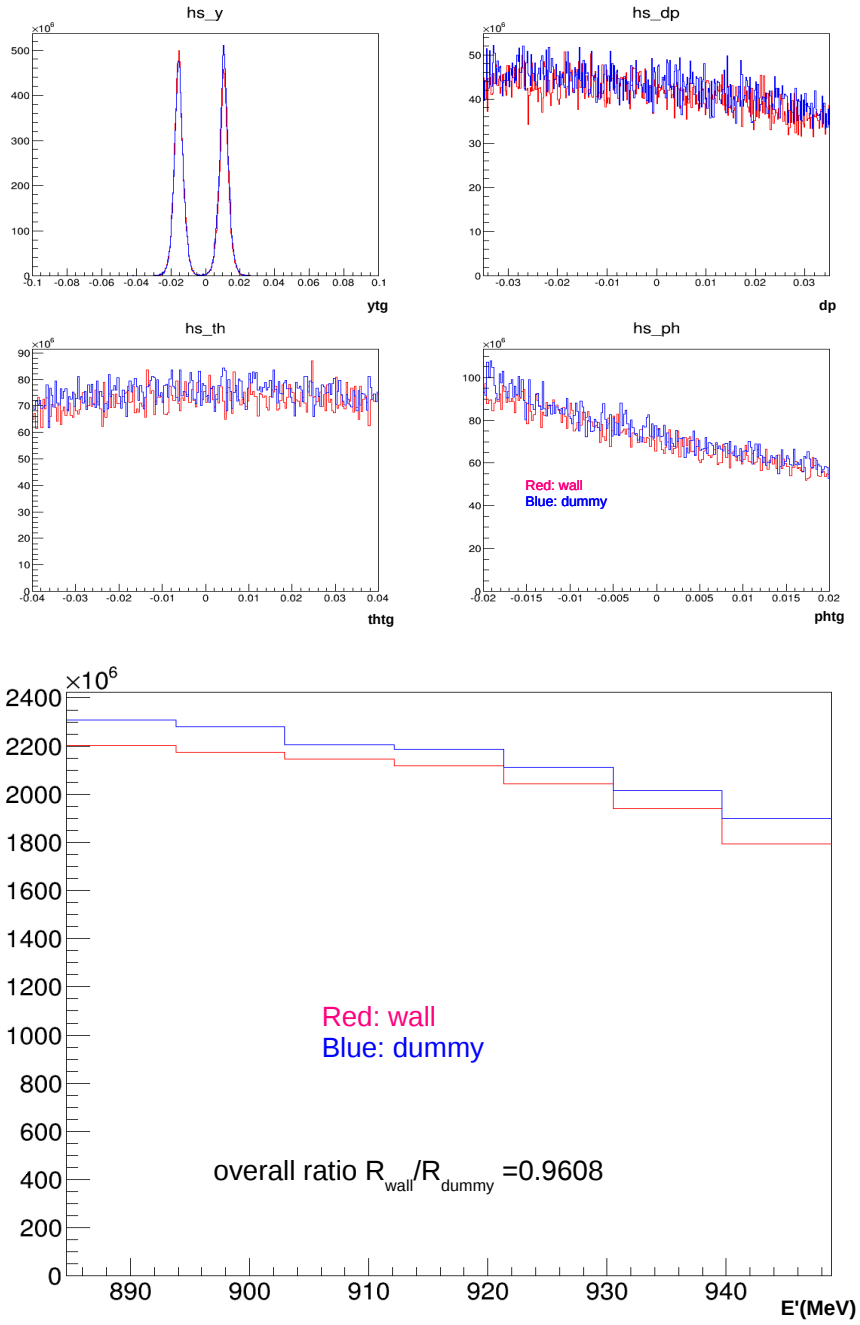

Figure 4-8: Top: SAMC simulation of electrons scattered on aluminum windows of ^{4}He target (red) and electrons scattered on aluminium foils of dummy target (blue), from left to right, top to bottom, the figures are for y_{tg}, dp, θ_{tg} and ϕ_{tg}. Bottom: E' spectrum of electron scattered on aluminium windows of ^{4}He target (red) and on aluminium foils of dummy target (blue).

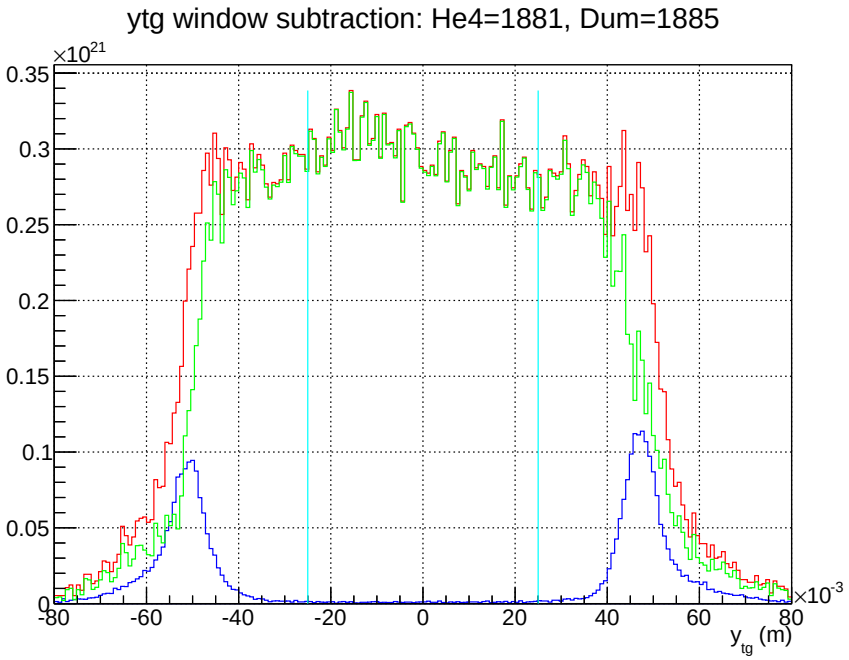

Figure 4-9: Yield for cryogenic ^{4}He target run 1881 (red), aluminium background calculated (blue) from dummy target run 1885, and clean ^{4}He contribution (green). The y_{tg} cut at 2.5 cm is marked as teal colored lines. The kinematic setting for this run is E_b=1030.5 MeV, θ=90°, and E'=301.2 MeV.

4.4 Center-of-bin Correction

With angular cuts of $|\theta_{tg}| \leq 40$ mrad and $|\phi_{tg}| \leq 20$ mrad as mentioned previously, the cross section measured at a certain central spectrometer angle is the average of cross sections within the range of acceptance. Because the cross section varies non-linearly within the bin size of the acceptance, the measured cross section is not the value at the bin center and a center-of-bin correction must be applied.

For the carbon/proton elastic cross section, we can use Phaseshift.f program to calculate the cross section based on world data of elastic scattering and form factors. The center-of-bin factor C_a can be calculated as:

$$C_a = \frac{\sigma_c}{\frac{\int \sigma(\delta,\theta,\phi)\cdot Acc(\delta,\theta,\phi) d\delta d\theta_{tg} d\phi_{tg}}{\int_{\theta,\phi,\delta} Acc(\theta,\phi,\delta) d\delta d\theta_{tg} d\phi_{tg}}}, \tag{4.6}$$

where σ_c and $\sigma(\delta,\theta,\phi)$ are the calculated cross sections at the center and at a certain bin (δ,θ,ϕ) of the acceptance.

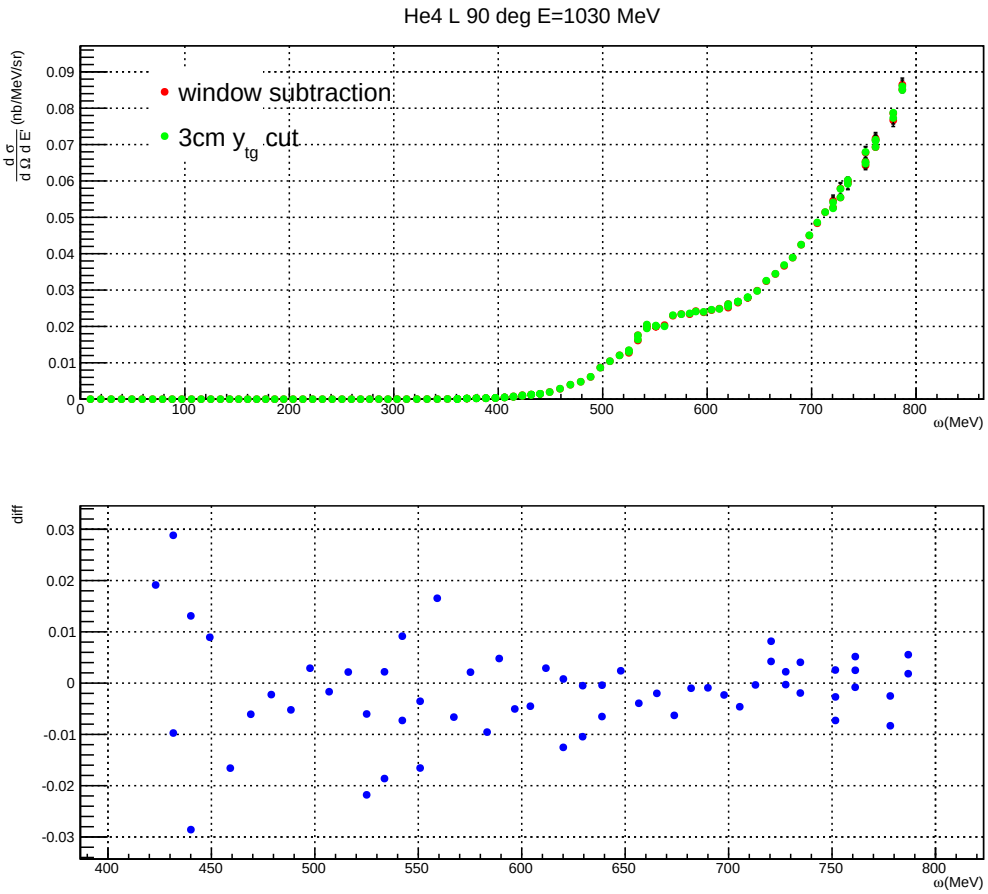

Figure 4-10: Comparison of cross sections using two methods of window background subtraction: Top: cross section spectrum of 90°, E = 1030 MeV using $|y_{tg}| < 3$ cm cut (green) and dummy subtraction (red). Bottom: relative difference between cross sections using these two methods (0.01 in the y axis means 1%).

For the case of quasi-elastic scattering, we don't known the exact cross section, and the correction is performed based on calculations using the F1F209 fitting [45].

4.5 e^- Background from e^+e^- Pair Production

One major source of background is e^+e^- pair production resulting from the decay of π^0. π^0 particles are generated at the target and the main decay mode of π^0 is $\pi^0 \rightarrow 2\gamma$. These photons then decay into e^+e^- pairs, and electrons from the e^+e^- pair production become a background for this experiment. To evaluate and subtract this background, the magnetic filed of the HRS magnets are reversed at θ =90°, E=

Angle	Constant
90°	1042
120°	1346.6

Table 4.1: Constants that bring the experimental and calculated e^+ cross sections to agreement. They were used as scale factors to calculate positron cross sections for unmeasured kinematic regions.

845 MeV and θ =120° E= 740 MeV to measure e^+ cross sections. Because the number of e^- generated from the pair production is equal to the number of e^+, the e^+ cross section can be used to subtract the e^- background due to pair production.

Unfortunately, because of the limited beam time, the e^+ spectrum was not measured at all kinematic settings. To evaluate e^+ spectra at unmeasured kinematics, a Fortran program EPC [46] and J.P Chen's calculation [47] were used: EPC is used to produce the π^0 cross sections at the desired kinematic setting, then the π^0 cross sections were used as an input to J.P Chen's calculation to give the e^+ cross sections.

The measured positron spectra were used to extract the positron cross sections with the similar procedure as electron data, except a β cut was used to reject the knocked out proton background. The measured positron cross sections were compared with J.P Chen's calculation results, as shown in Fig. 4-11. A scale factor that makes the Chen's calculation results agree with measured cross sections was extracted. This scale factor was then applied to the calculated positron spectra at unmeasured kinematic settings. One scale factor was evaluated for each angle, see Table 4.1. The background from e^+e^- pair production is found to be negligible at high momentum and increases at low momentum settings.

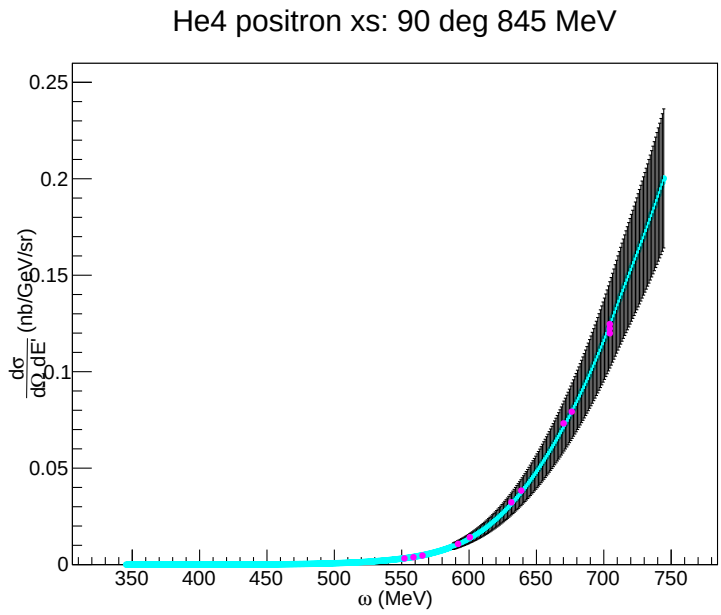

(a) ^{4}He positron cross section at θ=90°, E=845 MeV.

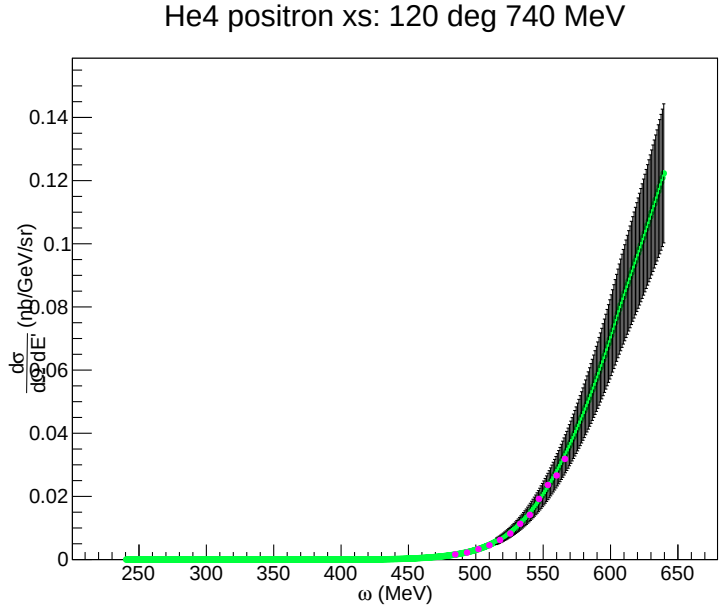

(b) ^{4}He positron cross section at θ=120°, E=740 MeV.

Figure 4-11: ^{4}He positron cross sections. The colored line are from EPC and J.P Chen's calculation with the uncertainty of the calculation shown as the black band. The purple data point are from CSR measured positron spectra. The scaling factor of Table 4.1 is already applied to the calculation.

4.6 Extraction of Experimental Cross Section

The goal of experiment E05-110 is to measure the longitudinal and transverse response functions, and extract the Coulomb sum to test the Coulomb Sum Rule(CSR). To obtain the Coulomb sum with high precision, it is important to extract the cross sections while minimizing the uncertainties. The raw experimental cross section can be extracted from data as:

$$\frac{d\sigma}{d\Omega d\omega} = \frac{N_{cut}}{(Q/e)\cdot t_{LT}\cdot Acc\cdot \varepsilon \cdot N_{tg}}\frac{1}{\Delta E'\Delta\Omega}, \tag{4.7}$$

where

- N_{cut} is the number of events that pass all electron cuts in one bin.
- Q/e is the number of incident beam electrons. Q is the total charge read from BCM scalers and e is the magnitude of the charge of a single electron.
- $t_{LT} = T_{1(3)}/T_{1(3)raw}$ is the Livetime of the detector. $T_{1(3)}$ is the count of main trigger event type 1(3) for right(left) HRS.
- Acc is the spectrometer's acceptance determined from SAMC simulation, see Section 3.2.
- ε is the total detector efficiency, $\varepsilon \equiv \prod_i \varepsilon_i$, that includes efficiencies of the VDC, scintillators and the gas Cerenkov;
- N_{tg} is the number of the target particles calculated as:

$$N_{tg} = \frac{L\rho N_a}{A}, \tag{4.8}$$

  where $L\rho$ is the target thickness in unit of g/cm^2 (the target thickness is listed in Section 2.6; if a y_{tg} cut is applied, a shorter target thickness L' is used in Eq. 4.8), $N_a = 6.02\times10^{23}$ is Avagadro's number, and A is the mass number of the target. The target density effect on ρ will be presented in Section 4.7.

- $\Delta E = P_0 dp$ is the width (in unit of MeV) for the given momentum bin.

- $\Delta\Omega = \Delta\theta\Delta\phi$ is the solid angle defined by the acceptance cuts used in θ_{tg} and ϕ_{tg}: $\Delta\theta = 80$ mrad and $\Delta\phi = 40$ mrad for this analysis.

4.7 Density effect

The gaseous ^{4}He target is in a high pressure gas state, and the liquid helium and the liquid hydrogen targets are in a liquid state. For fluid targets, the local heating generated by beam current will result in lower density along the beam trajectory that cannot be detected by sensor devices. This density fluctuation effect was measured by investigating the linearity between the event yield and the beam current using elastic scattering data.

The density fluctuation depends on two parameters: beam current and beam size. A higher beam current or smaller beam size will cause a larger decrease in the target density. Due to the configuration of the cryogenic target that the cooling flow enters the target at the top and exits at the bottom, the vertical beam size has less effect on target density than horizontal beam size.

This density effect was extracted from two groups of calibration runs with different beam sizes, see Fig. 4-12 for the gaseous (loop 1) ^{4}He target: For beam with size 2 mm $\times$ 2 mm, the density effect causes the yield to drop by 5.4% per 100 μA, and for beam with size 3.5 mm $\times$ 2 mm, this effect is 4.1% / 100 μA. Similar data on the (loop 3) liquid hydrogen target are shown in Fig. 4-13. No study was done on the loop 2 liquid helium target. On the other hand, most ofthe ^{4}He data were collected on the loop 1 target.

It is interesting to see the difference between the two kinds of cryogenic target: the density of the gaseous ^{4}He target decreases linearly as beam current grows, while the liquid hydrogen target has a changing slope. The density fluctuation is found to be less than 5% for both targets, and is corrected for in cross section extractions.

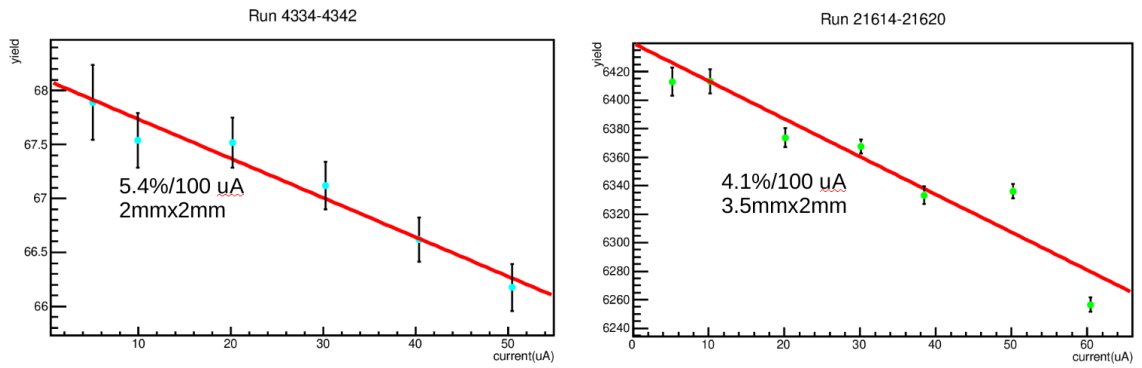

Figure 4-12: Density effect: ^{4}He elastic scattering yield vs beam current for loop 1 target with beam size 2 mm $\times$ 2 mm (left) and 3.5 mm $\times$ 2mm (right). The kinematic settings are E_{beam} = 1260 MeV, θ_{LHRS}=15° (left), E_{beam} = 2845 MeV, θ_{RHRS}=15° (right).

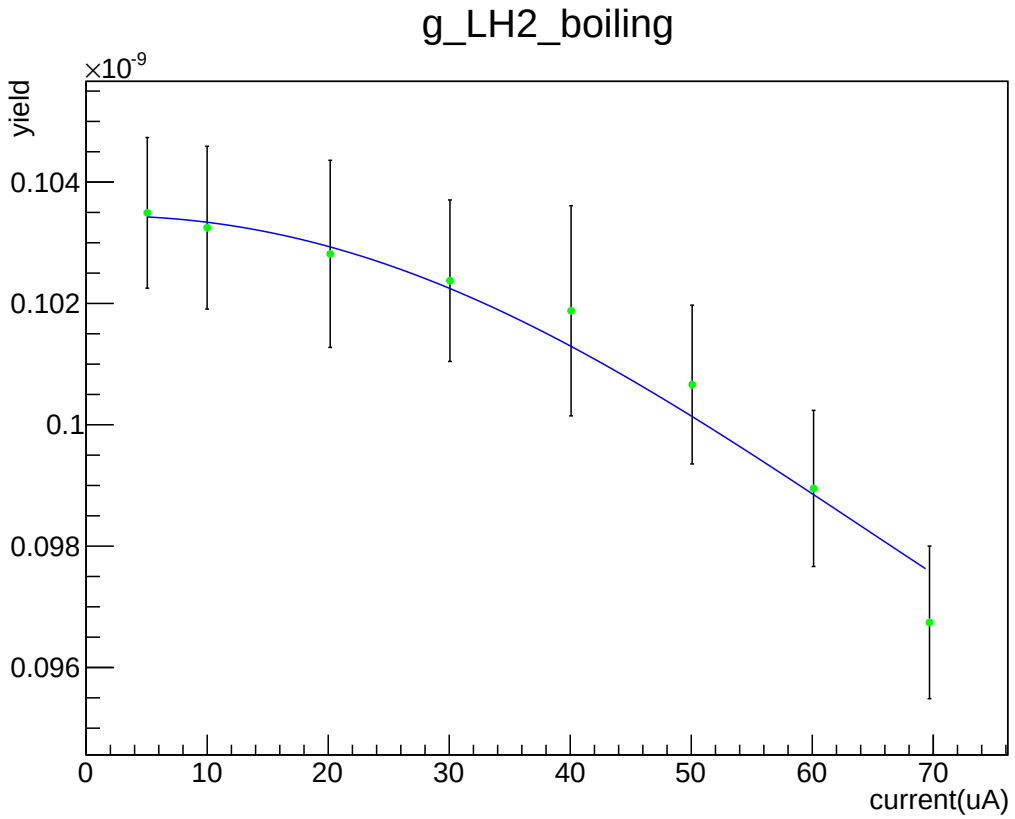

Figure 4-13: Density effect: liquid hydrogen elastic scattering yield vs beam current for 2 mm $\times$ 2 mm beam size. The kinematic setting is E_{beam} = 739 MeV, θ_{LHRS}=45°.

4.8 Radiative Corrections

The cross section in the Rosenbluth Eq. 1.10 was derived to the lowest order in fine-structure constant α, which includes only the amplitude from the exchange of a single virtual photon between the incident electron and the nucleon. This is known as Born approximation. Cross sections measured in actual experiments have large contributions from higher order processes and the straggling effect (ionization and bremsstrahlung energy loss before and after the main scattering). Therefore the raw measured cross section needs to be corrected to extract the Born cross section. This process is called "radiative correction" for the next to leading order (in α) (if we ignore 2-γ contribution). Details of radiative corrections are explained in Appendix B.

There are several steps in the radiative corrections. The first is to remove the radiative tail of elastic scattering from the measured cross section. The radiative elastic tail was calculated using Fortran code rosetail.f. The material thickness passed through by electrons are taken into account in the program, with elastic cross sections calculated based on form factors from a phase shift calculation [48]. The radiative elastic tail for 60° and E = 1260 MeV is given in Fig. 4-14.

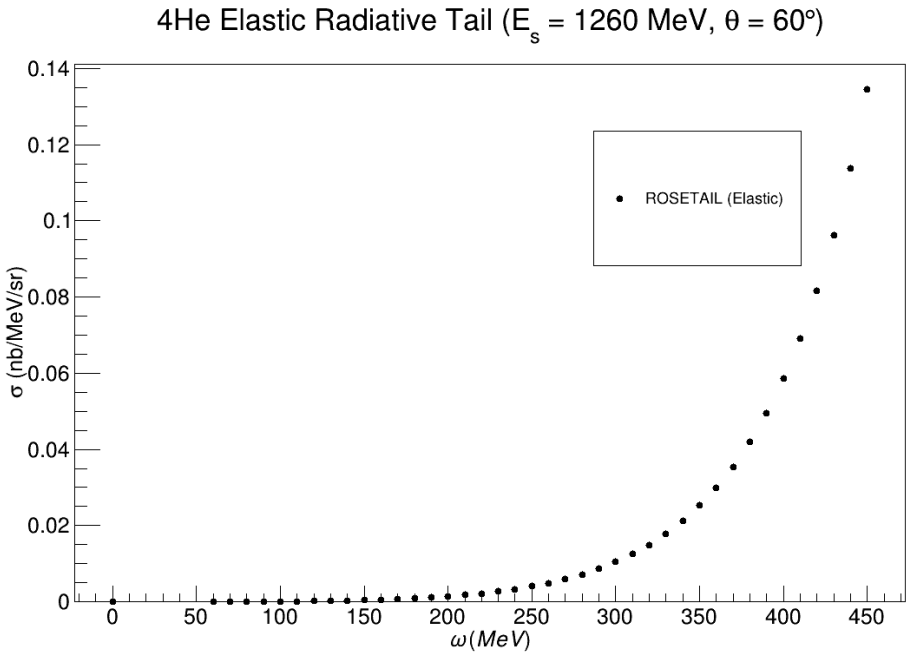

Figure 4-14: Elastic radiative tail of ^{4}He with E=1260 MeV, θ = 60°.

After the radiative elastic tail was subtracted, radiative corrections of quasi-elastic scattering were calculated separately for each scattering angle.

Additionally, the electron scattering cross section measured in the experiment is not the cross section at the scattering vertex: electrons pass through target material and windows before and after main scattering with straggling effects. Therefore the incident beam energies and the detected scattered energies of electrons are different from the actual values at the scattering vertex, and interpolation or extrapolation is needed to obtain the cross section at the vertex energy values. This is called external radiative correction. The external radiative corrections needs measured cross sections with many beam energies. For 15°, 60° and 90° angles, data were taken with 7 different incident energies during CSR experiment. For the 120° data, spectra were measured for 6 incident energies. These data were still not enough to cover the full range needed for radiative corrections, and the F1F209 fit [45] was used below the lowest beam energy for each angle. Fortran code radcor.f was used to do the unfolding procedure for the CSR experiment analysis.

4.9 ^{12}C Elastic Cross Sections

Elastic scattering of ^{12}C has been well studied in many experiments, thus the elastic form factors and cross sections are known to a very good precision. The ^{12}C elastic cross sections measured during the CSR experiment are compared with world data to check the quality of optics and acceptance corrections. The ^{12}C elastic cross sections were extracted similar to the extraction of quasi-elastic cross section, Eq. 4.7, as:

$$\left(\frac{d\sigma}{d\Omega}\right)_{elastic} = \frac{N_{cut}}{(Q/e)\cdot t_{LT}\cdot Acc\cdot \varepsilon \cdot N_{tg}}\frac{1}{\Delta\Omega}. \tag{4.9}$$

The measured elastic cross sections represent the average of elastic cross sections over the acceptance range $|\theta_{tg}| < 40$ mrad and $|\phi_{tg}| <$20 mrad. Because the elastic form factor changes rapidly with q^2, as shown in Fig. 4-15, a finite acceptance correction was applied as follows: the acceptance was divided into small bins, then

the phaseshift program was used to calculate cross sections and form factors in each bin based on world data and an average was taken over the whole acceptance. The finite acceptance correction factor is the ratio of the average cross section to the cross section at the center of acceptance.

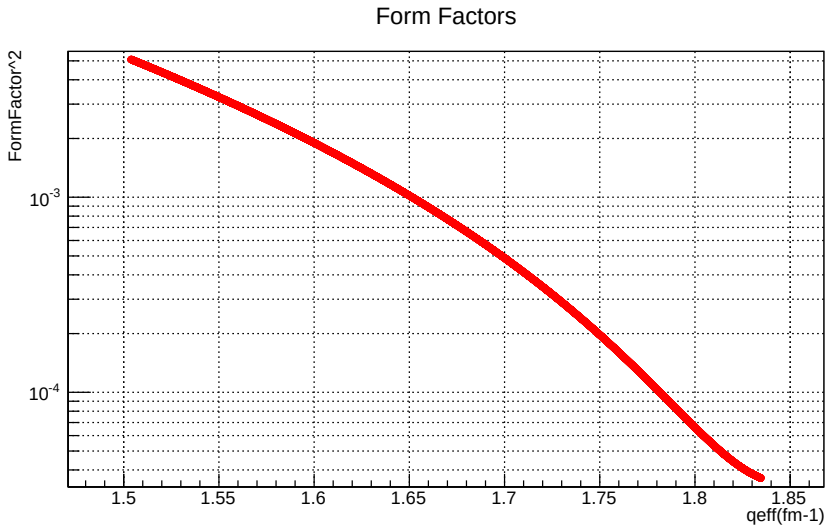

Figure 4-15: ^{12}C form factor as a function of q_{eff}.

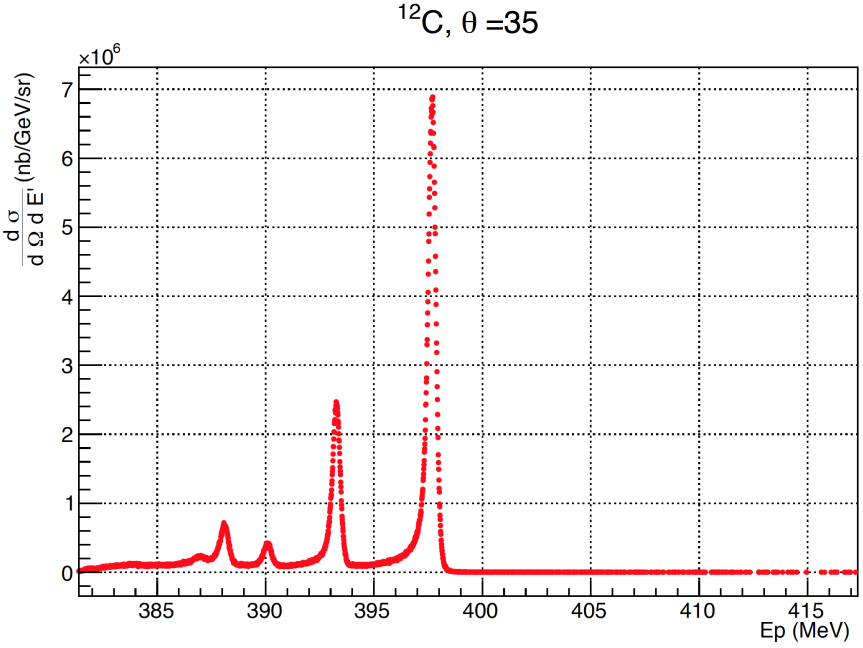

Figure 4-16: ^{12}C elastic scattering spectrum extracted from this experiment using data taken with E=400 MeV at 35°.

Radiative corrections for elastic scattering were applied by using Mo and Tsai formula [49]. The procedure is given in Appendix B. After ^{12}C elastic cross sections were extracted, form factors were also calculated. The results were plotted as function of q^2 and compared with world data, see Fig. 4-17 for the comparison at 15° and E = 1260 MeV. As one can see, the ^{12}C elastic results have fairly good agreement with world data. The difference observed from most of the elastic runs is less than 3%.

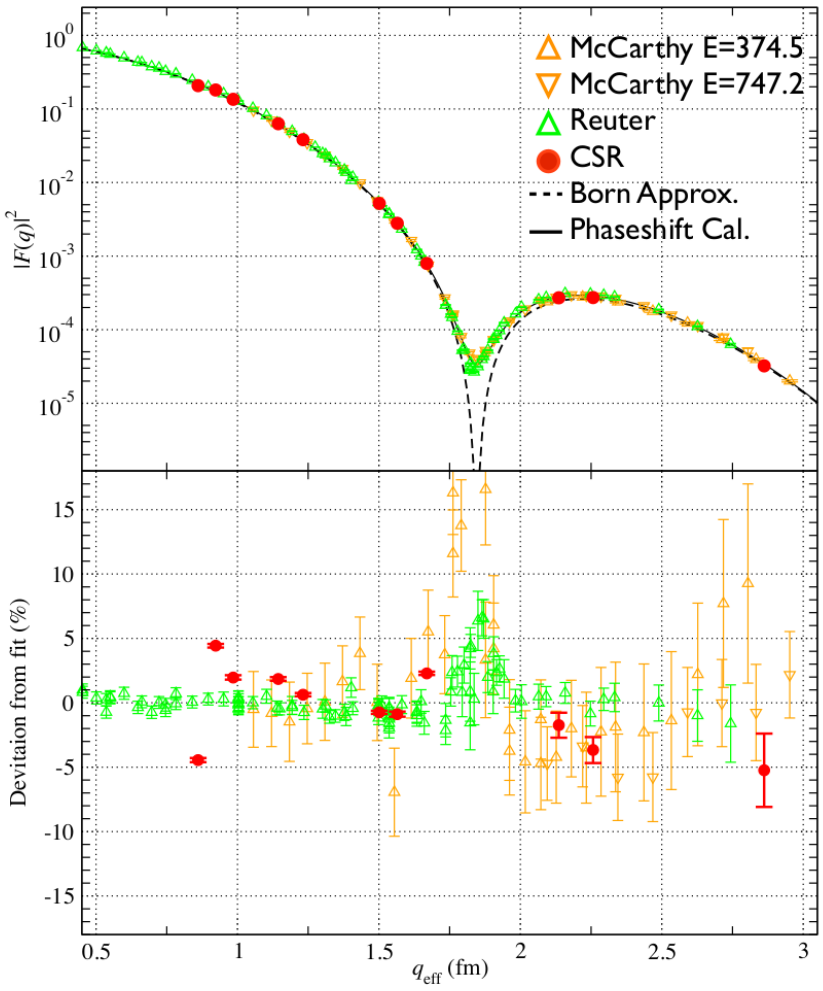

Figure 4-17: ^{12}C elastic form factors extracted from this experiment (red solid circles) and comparison with world data [50] [51]. The solid curve in the top panel is a calculation from phase shift program [48]. The bottom panel shows the experiment data's deviation from the phase shift calculation.

4.10 Systematic Uncertainties

Systematic uncertainties of the cross section include:

- Beam energy: the uncertainty in beam energy is $\Delta E_b/E_b < 5 \times 10^{-4}$. Its contribution to the uncertainty in cross section $\Delta\sigma/\sigma$ is less than 0.6% for 15° and less than 0.1% for other angles.

- Scattered electron energy: the uncertainty in the HRS central momentum is $\Delta P_0/P_0 = 5 \times 10^{-4}$. Its contribution to the cross section uncertainty $\Delta\sigma/\sigma$ is less than 0.5% for 15° and less than 0.1% for other angles.

- Scattering angle: the uncertainty in the scattering angle is 0.2 mrad. Its contribution to the cross section uncertainty $\Delta\sigma/\sigma$ is less than 0.5% for 15° and less than 0.1% for other angles.

  The F1F209 cross section fitting [45] was used to estimate the uncertainties due to the above three kinematics variables as follows: a Gaussian distribution was generated for each variable with the width being the uncertainty of that variable. The cross section was calculated using F1F209 for all events in the input Gaussian distribution, and the resulting cross section also follows a Gaussian distribution. The width of the resulting cross section distribution is used as the uncertainty in the cross section contributed from the uncertainty of that input variable. Figure 4-18 shows how the uncertainty due to beam energy is estimated using this procedure.

- Beam charge: the cross section uncertainty due to beam charge is less than 0.3% [30].

- Acceptance: The uncertainty in the acceptance was estimated by changing the acceptance cut size from 90% to 110% of the nominal value. The cross section uncertainty due to acceptance is found to be less than 1%.

- Detector efficiency: the uncertainty due to detector efficiency is less than 0.2% [30].

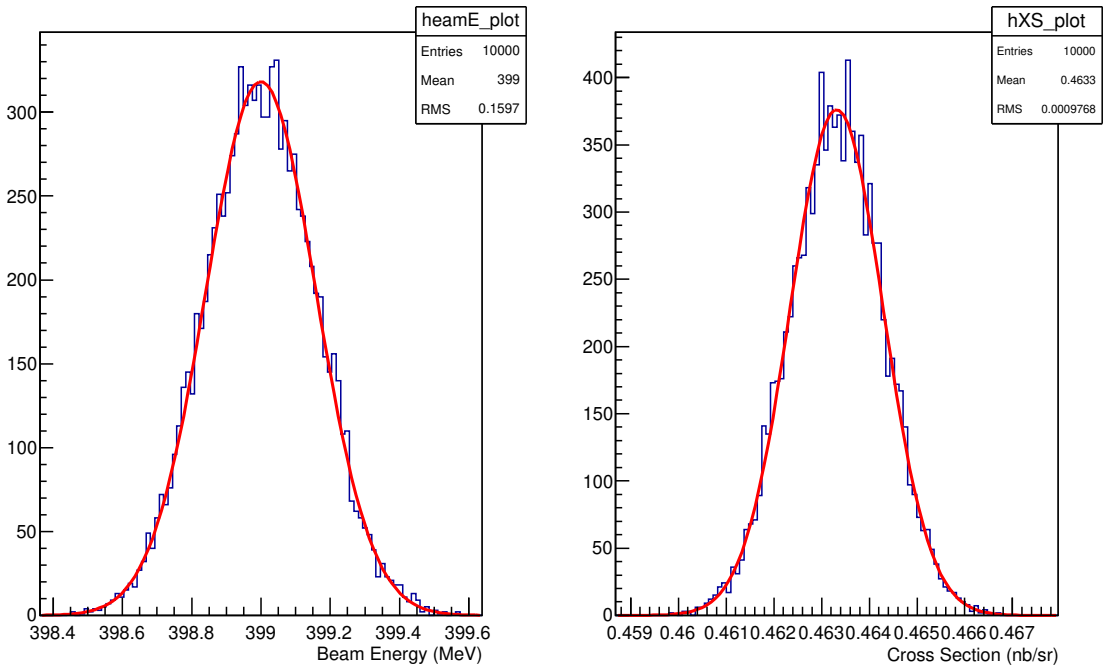

Figure 4-18: Using F1F209 fitting to calculate the cross section uncertainty due to beam energy uncertainty. Left: Gaussian distribution of beam energy, blue is distribution of beam energy, red is a Gaussian fit of this distribution. Right: Gaussian distribution of the generated F1F209 cross section, blue is the calculated distribution of cross section from the input beam energy distribution, red is a Gaussian fit of this distribution. The width of the cross section distribution is used as the uncertainty.

- Livetime: the uncertainty due to electronic and detector livetimes is less than 0.2% [30].

- Target thickness: the uncertainty in the target thickness is mainly from target density, and is 0.5% for this experiment.

- Radiative corrections: the uncertainty due to radiative corrections is studied by using different interpolation variables y,W and ω/E, the uncertainty in the cross section $\delta\sigma/\sigma$ is estimated to be around 1% for most kinematic settings.

- e^-e^+ background: The uncertainty due to e^-e^+ background is less than 5% for 90° and 120°. This uncertainty is 0 at 15° (not applied at 15°) and less than 1% at 60°.

Systematic uncertainties in the cross section extraction are summarized in Table 4.2. The total systematic uncertainty are calculated as the quadratic sum of all uncertainties.

Source	15°	60°	90°	120°
Beam Energy	<0.6%	<0.1%	<0.1%	<0.1%
Scattered Electron Energy	<0.5%	<0.1%	<0.1%	<0.1%
Scattering Angle	<0.5%	<0.1%	<0.1%	<0.1%
Beam Charge	<0.3%	<0.3%	<0.3%	<0.3%
Dead Time	<0.2%	<0.2%	<0.2%	<0.2%
Detector Efficiency	<0.2%	<0.2%	<0.2%	<0.2%
e^+e^- Background	negligible	<0.1%	<2%	<2%
π Background	<0.1%	<0.5%	<0.5%	<0.5%
Target Density	<0.2%	<0.2%	<0.2%	<0.2%
Radiative Corrections	<1%	<1%	<1%	<1%
Density Effect	<0.5%	<0.5%	<0.5%	<0.5%
Acceptance	<1%	<1%	<1%	<1%
Total	<1.82%	<1.66%	<2.59%	<2.59%

Table 4.2: Summary of all systematic uncertainties on the cross section extraction.

4.11 Rosenbluth Separation

4.11.1 Coulomb Corrections

The Rosenbluth Formula Eq. 1.10 is derived under the plane-wave Born approximation (PWBA). The PWBA assumes that the wave function of both incident and scattered electrons can be described by plane waves, and only one virtual photon

is exchanged between the target nucleus and the electrons. However, PWBA is only valid for $Z\alpha \ll 1$. For light and medium nuclei, the interaction between electrons and the charge of the nucleus must be included. The effective momentum approximation can be used to include the Coulomb correction due to the nuclear Coulomb field in the PWBA. The effective momentum approximation requires changes to the energy of the incoming and outgoing electrons due to the nuclear Coulomb potential:

$$E_{s\,\mathrm{eff}} = E_s - V_C, \tag{4.10}$$

$$E_{p\,\mathrm{eff}} = E_p - V_C, \tag{4.11}$$

where V_C is the mean value of the Coulomb potential of the nucleus,

$$V_C = \frac{3Z\alpha}{2R} \tag{4.12}$$

with $R = (5/3)^{1/2}\langle r^2\rangle^{1/2}$ and $\langle r^2\rangle^{1/2}$ the nuclear RMS radius [52]. The effective momentum transfer is:

$$q_{\mathrm{eff}} = q\left(1 - \frac{V_C}{E_s}\right). \tag{4.13}$$

Therefore, Q^2 needs to be replaced by $Q^2_{\mathrm{eff}} = 4E_{s\,\mathrm{eff}}E_{p\,\mathrm{eff}}\sin^2(\theta/2)$ and q needs to be replaced by q_{eff}. Since E_s and E_p change by an equal amount, ω remains unchanged.

4.11.2 Interpolation

To extract the Coulomb Sum, we need to integrate longitudinal response function along a constant $|\vec{q}_{\mathrm{eff}}|$ value. However the experiment cross sections were measured with constant incident beam energies at each angle, not along constant $|\vec{q}_{\mathrm{eff}}|$, as shown in Fig. 2-1. In order to do Rosenbluth separation at a constant $|\vec{q}_{\mathrm{eff}}|$, it is necessary to interpolate between measured cross section spectra in the ($|\vec{q}_{\mathrm{eff}}|$, ω) plane to obtain spectra along constant $|\vec{q}_{\mathrm{eff}}|$ values.

The interpolation needs to follow paths which can align corresponding features (quasi-elastic peak and dip region) of each spectrum. Two scaling variables were used to determine the interpolation paths: invariant mass W and quasi-elastic scaling

variable y. The quasi-elastic scaling variable y satisfies the equation [53]:

$$\omega + M_A = (y^2 + 2y\vec{q} + M^2 + \vec{q}^2)^{1/2} + (y^2 + M_{A-1}^2)^{1/2}. \tag{4.14}$$

where M_A is the nucleus mass, M is the nucleon mass and M_{A-1} is the mass of nucleus with $A-1$ nucleons. The y scaling variable changes from negative to positive, with $y = 0$ corresponding to the location of quasi-elastic peak. When the spectra are plotted as a function of y, the quasi-elastic peaks are aligned.

The interpolation is done on the total response, which is the experimental cross section divided by the Mott cross section:

$$R = \frac{\frac{d\sigma}{d\Omega}}{\sigma_M} = \frac{Q^4}{\vec{q}^4} R_L(Q^2, \omega) + \frac{Q^2}{2\vec{q}^2 \varepsilon} R_T(Q^2, \omega) \tag{4.15}$$

The spectra of four different angles plotted in W and y scaling are shown in Figs. 4-19 and 4-20. We can see the y scaling aligns the quasi-elastic peak quite well, and W scaling aligns the dip region and the Δ resonance peak better. In this analysis, y scaling is used up to quasi-elastic peak and W scaling is used above the quasi-elastic peak.

The interpolation is performed using the following procedure:

- Each measured spectrum is interpolated along ω;
- For a certain ($|\mathbf{q}|$,ω) point, calculate corresponding y and W;
- Find points with same y and W in the measured spectra;
- The total response at the given point is interpolated using a spline of ω from the points on the measured spectra.

Figures 4-21 and 4-22 show the interpolation at 15°, $|\mathbf{q}|$=650 MeV and ω=200 MeV and 60°, $|\mathbf{q}|$=750 MeV and ω=200 MeV. The difference between the two interpolation methods is used as an estimate of the systematic uncertainty. The typical uncertainty is around 1%.

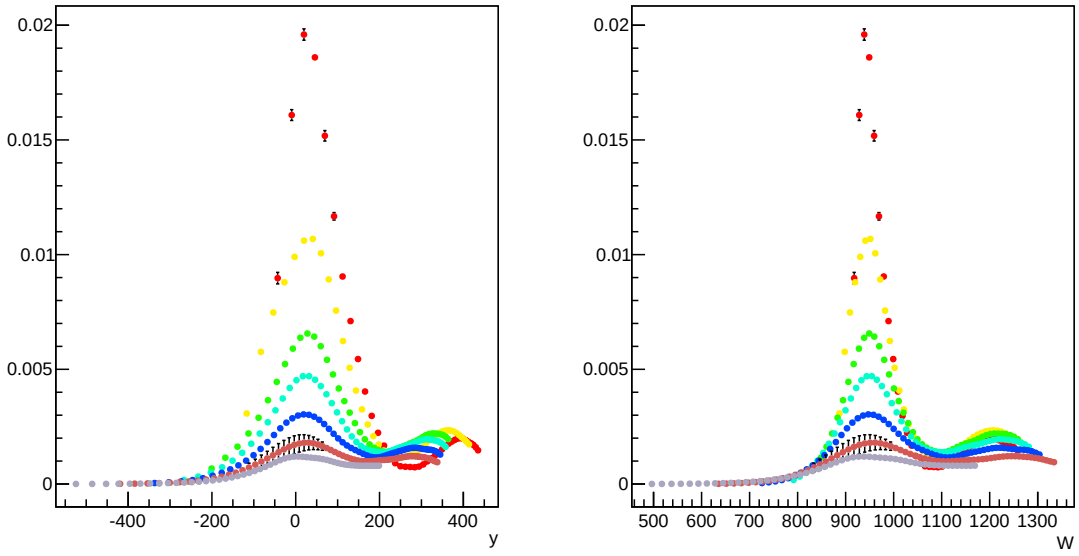

(a) $\theta = 15°$

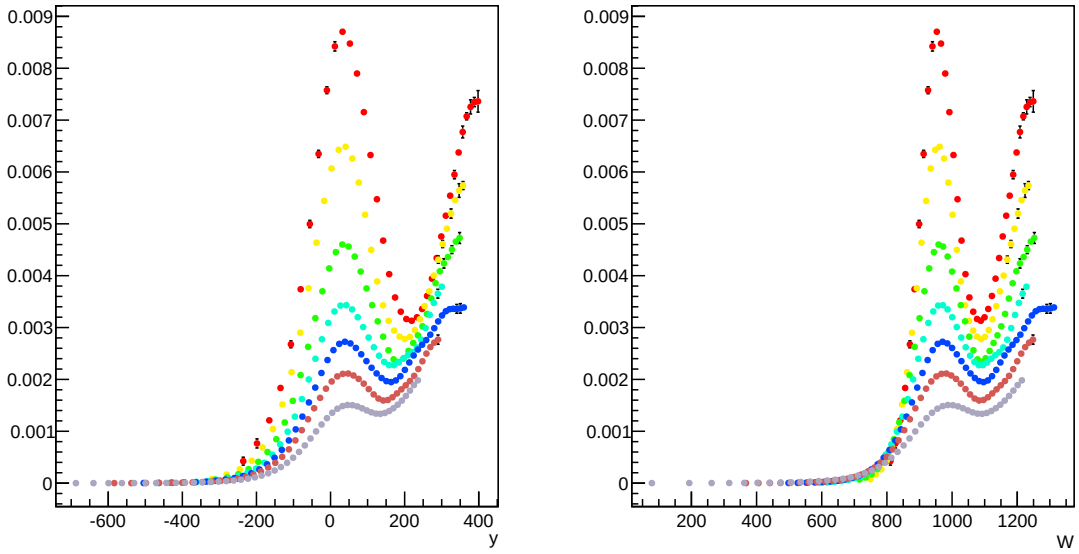

(b) $\theta = 60°$

Figure 4-19: Total response function of ^{4}He at 15° and 60° aligned in constant y (left) and constant W (right). Different colors are for different beam energies.

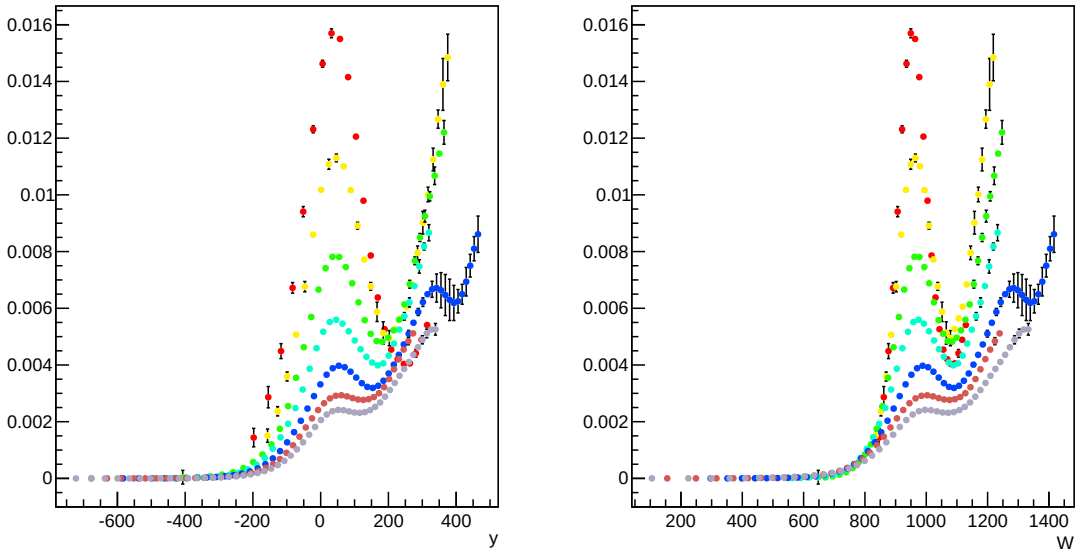

(a) $\theta = 90°$

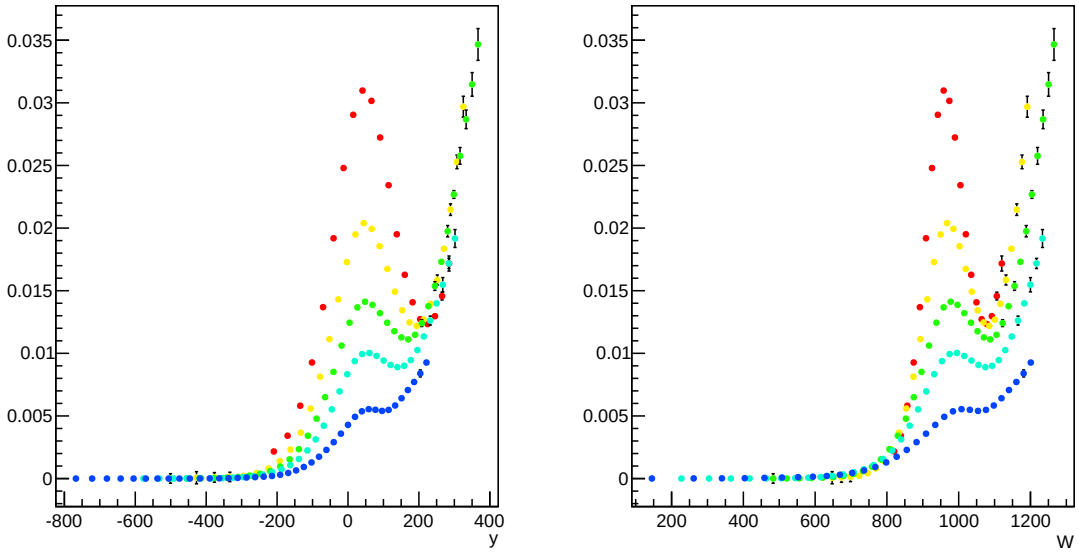

(b) $\theta = 120°$

Figure 4-20: Total response function of ^{4}He at 90° and 120° aligned in constant y (left) and constant W (right). Different colors are for different beam energies.

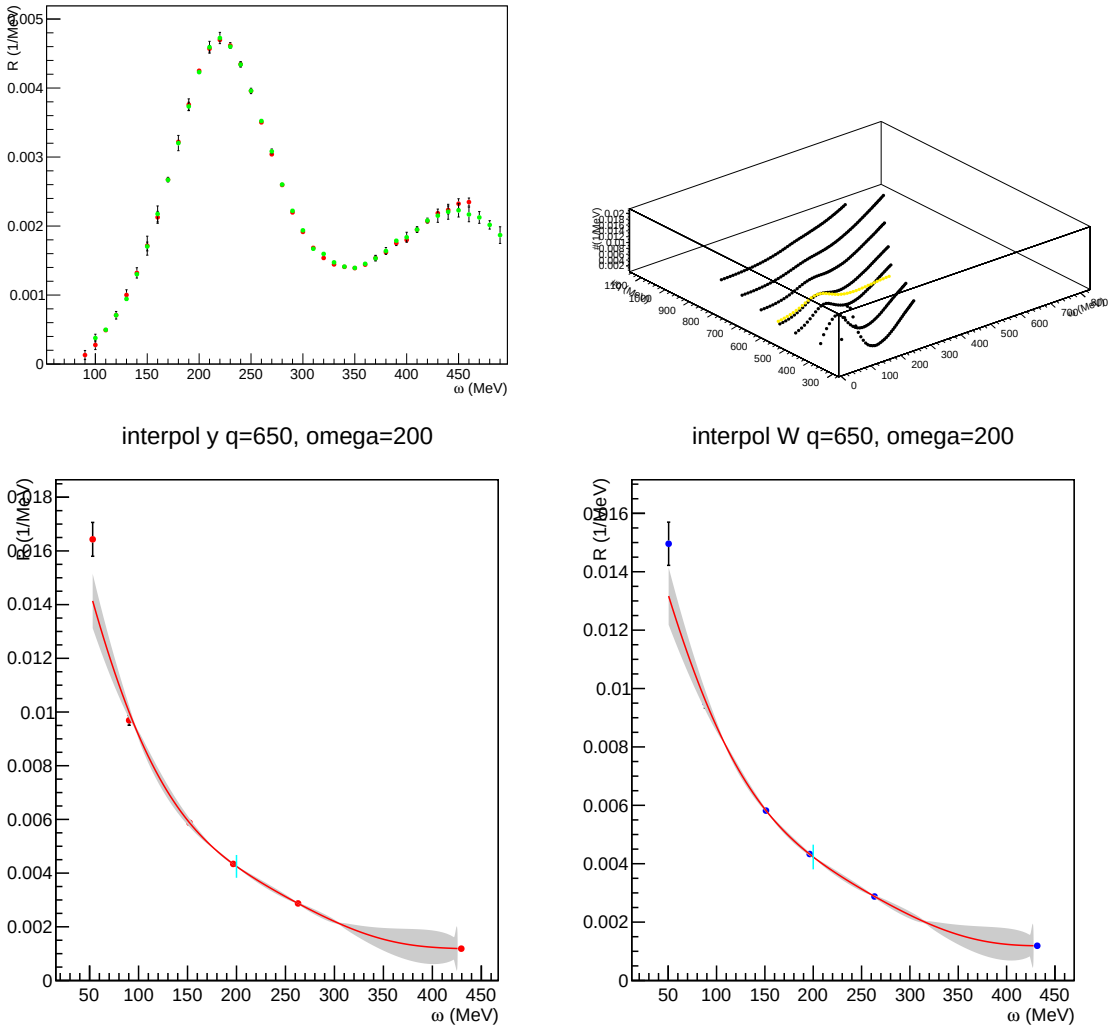

Figure 4-21: y and W interpolation of ^{4}He data at $\theta = 15°$, q=650 MeV, $\omega = 200$ MeV. Top left: Comparison of y (green) and W (red) interpolation; Top right: interpolation path (yellow) in 3D view, black points are the measured spectra; Bottom: y (left) and W (right) interpolation with spline functions. The red lines are the interpolation line, the grey bend is the uncertainty, the teal line indicates the target interpolation point.

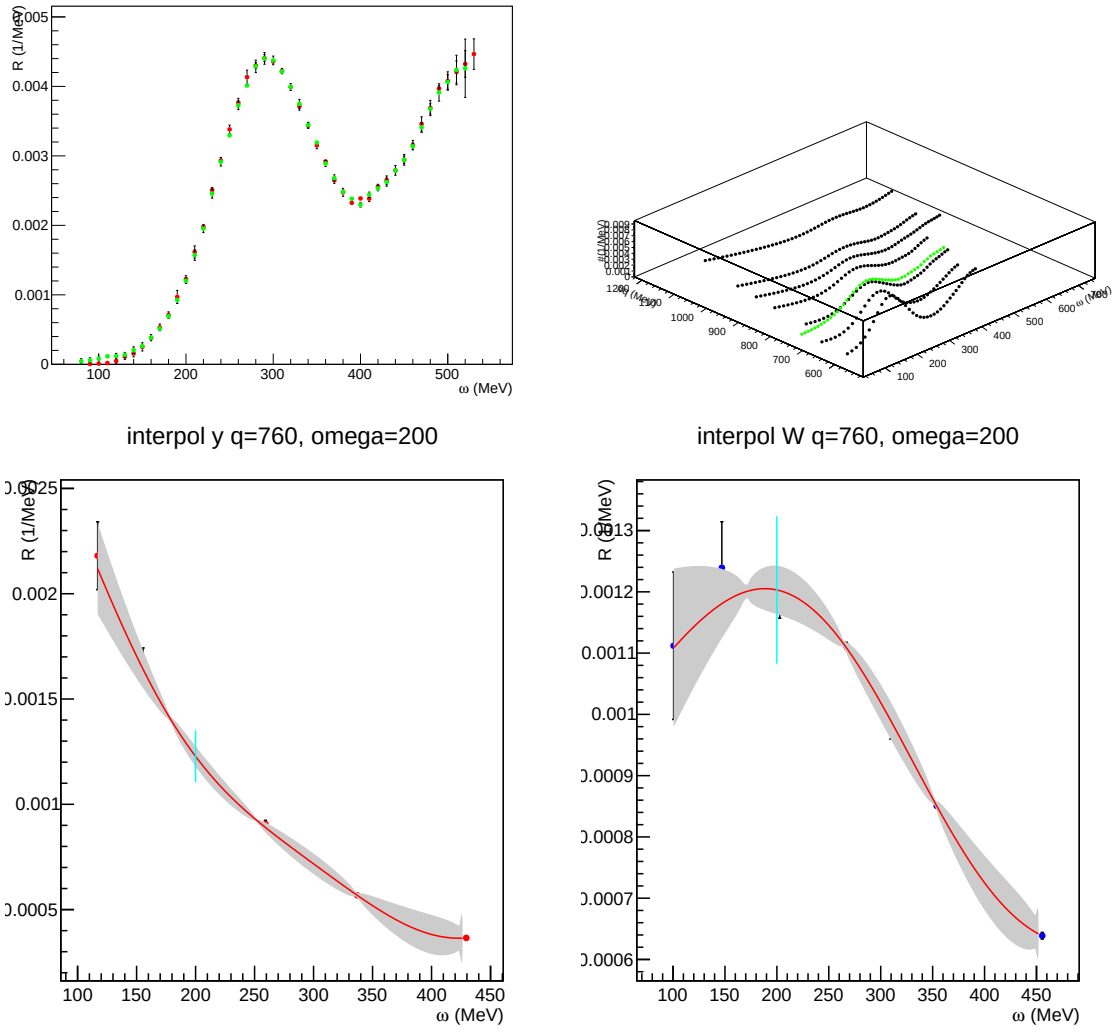

Figure 4-22: y and W interpolation at $\theta = 60°$, q=750 MeV, $\omega = 200$ MeV. Top left: Comparison of y (green) and W (red) interpolation; Top right: interpolation path (yellow) in 3D view, black points are the measured spectra; Bottom: y (left) and W (right) interpolation with spline functions. The red lines are the interpolation line, the grey bend is the uncertainty, the teal line indicates the target interpolation point.

The interpolated total response of ^{4}He in the ($|\mathbf{q}|$,ω) plane are shown in Figs. 4-23 through 4-26.

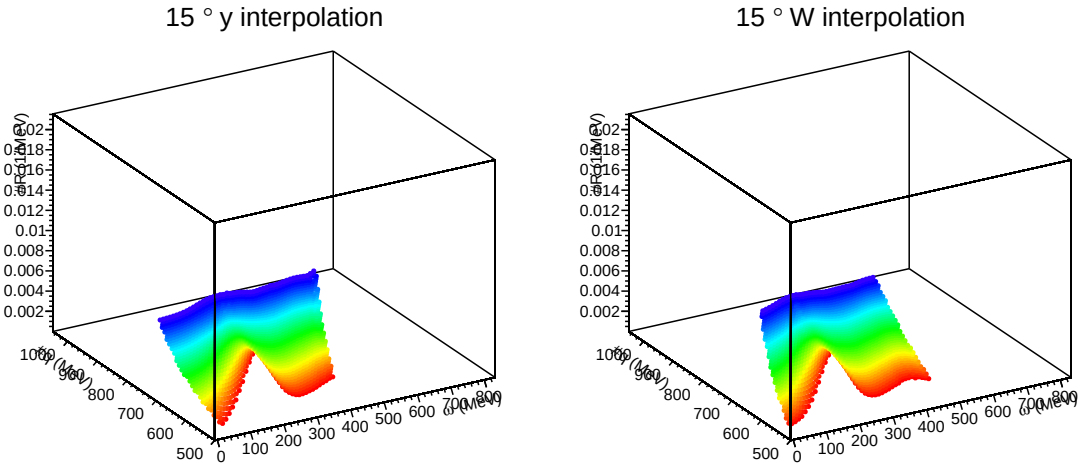

Figure 4-23: Interpolated total response function of ^{4}He at 15°.

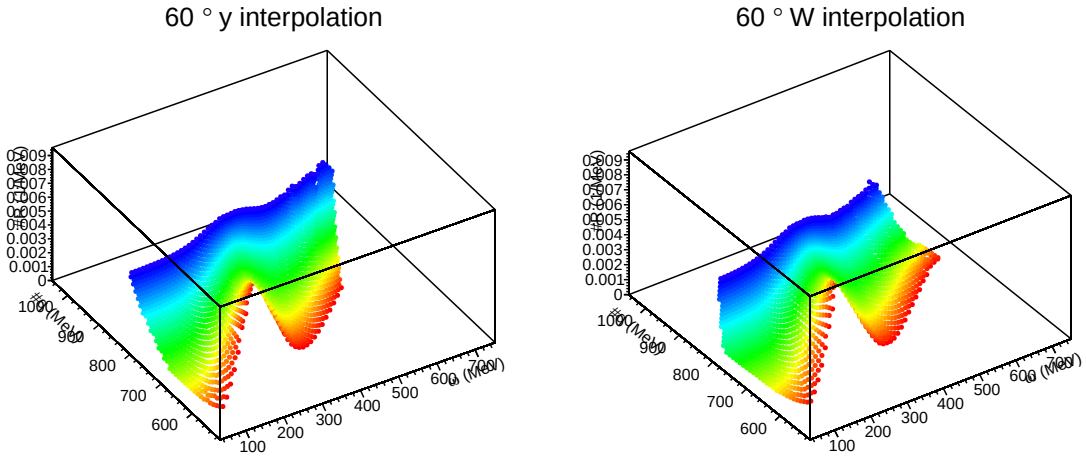

Figure 4-24: Interpolated total response function of ^{4}He at 60°.

4.11.3 Rosenbluth Separation

In Rosenbluth formula, Eq. 1.10, if one divides out the Mott cross section σ_M and multiplies virtual photon polarization ε on both sides, the formula can be re-written

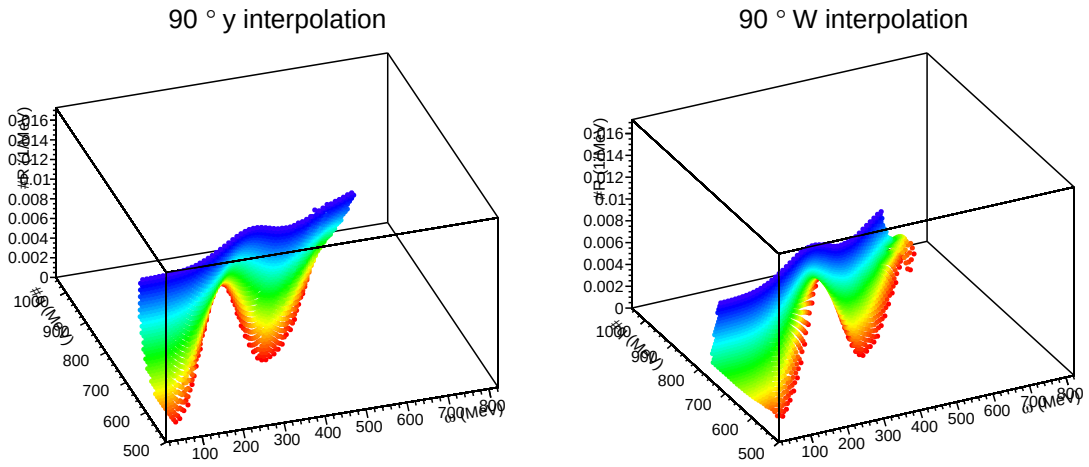

Figure 4-25: Interpolated total response function of ^{4}He at 90° and 120°.

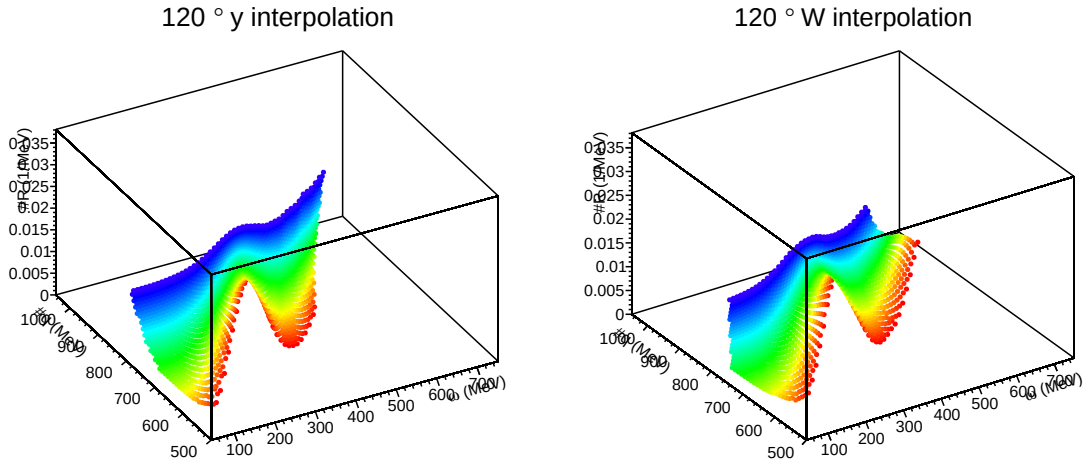

Figure 4-26: Interpolated total response function of ^{4}He at 90° and 120°.

as:

$$\begin{aligned} \varepsilon R &= \varepsilon \frac{\frac{d\sigma}{d\Omega}}{\sigma_M} \\ &= \varepsilon \frac{Q^4}{\mathbf{q}^4} R_L + \frac{Q^2}{2\vec{q}^2} R_T \end{aligned} \tag{4.16}$$

The Rosenbluth separation method can be used to extract R_L and R_T from Eq. 4.16. Because the virtual photon polarization ε has an angle dependence, one can use the plot of εR versus ε. The data point for each angle should lie in a straight line, the slope and intercept of which are $Q^4/\mathbf{q}^4 R_L$ and $Q^2/2\mathbf{q}^2 R_T$, respectively.

Figure 4-27 shows the Rosenbluth separation at $\mathbf{q}$ = 650 MeV, ω = 150, 200, 250 and 300 MeV as examples. Because the separation is done by linear fitting, the error of data points can affect the fitting results and the systematic and statistical uncertainties cannot be treated separately. The total uncertainty of data points are calculated by adding the systematic and statistical uncertainty in quadrature. The separation is performed for all ($|\mathbf{q}|$,ω) data points with more than two angles' data. The uncertainties in R_L and R_T are from the linear fitting.

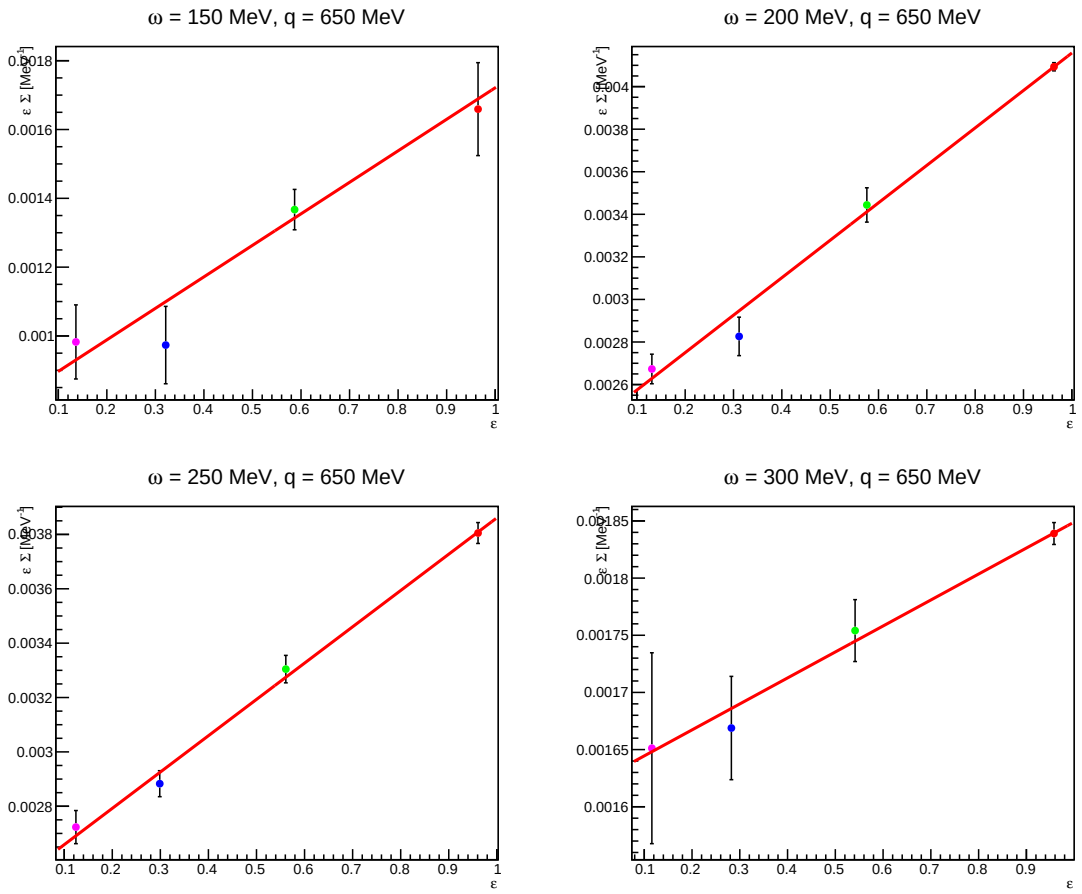

Figure 4-27: Rosenbluth separation for ^{4}He data at $|\mathbf{q}|$ = 650 MeV, ω = 150, 200, 250 and 300 MeV. In each panel, the different colors of the data points represent different scattering angles: 15°(red), 60°(green), 90°(blue), 120°(purple).

As one can see from Eq. 4.16 and Fig. 4-27: at high ω, $|\mathbf{q}|^2/Q^2$ is small, the R_L contribution decreases and the R_T contribution increases and the uncertainty in R_L can be large from the fitting procedure. Thus the Coulomb sum at large ω must be calculated carefully.

4.11.4 Coulomb Sum

The Coulomb Sum Rule is defined in Eq. 1.24, and is repeated here:

$$S_L(|\mathbf{q}|) = \frac{1}{Z}\int_{0^+}^{\infty} \frac{R_L(|\mathbf{q}|,\omega)}{\tilde{G}_E^2} d\omega$$

As shown above, the Coulomb Sum is defined to be the integral of the ratio of R_L to the nucleon electric form factor over the energy loss ω. The upper limit of the integral goes to infinity. However, it is impossible to measure $\omega > |\mathbf{q}|$ in experiments. Moreover, due to radiative corrections, falling detector efficiencies and other technical issues, the data near $\omega \approx |\mathbf{q}|$ cannot be collected. Besides, as explained in the previous section, the coefficient $|\mathbf{q}|^4/Q^4$ in Rosenbluth separation will cause large uncertainty in R_L at high ω and the Coulomb sum must be calculated carefully.

In order to extract the Coulomb sum at a given $|\mathbf{q}|$, R_L needs to be separated for all ω first, then the R_L spectrum can be integrated and the Coulomb sum can be extracted. For the nucleon electric form factor in the denominator of Eq. 1.24, Zhihong Ye's parameterization [44] was used. I will present all preliminary results on ^{4}He in the next Chapter.

Chapter 5

Results

For experiment E05-110, quasi-elastic cross sections were measured for ^{4}He, ^{12}C, ^{56}Fe, ^{208}Pb target at four angles: 15°, 60°, 90° and 120°. In this chapter, preliminary results of ^{4}He cross sections, response functions and the Coulomb sum are presented.

5.1 Cross Sections

5.1.1 Raw Cross Sections

The raw cross sections measured at 15°, 60°, 90° and 120° for the ^{4}He target are plotted versus energy loss in Figs. 5-1 through 5-8. Only statistical uncertainties are shown. The acceptance correction, center-of-bin correction, density effect correction and window background subtraction were already applied on these spectra.

The $e^{-}e^{+}$ background and radiative elastic tail were subtracted before the radiative correction was applied. The $e^{-}e^{+}$ background and radiative elastic tail are also plotted in Figs. 5-1 through 5-8. The radiative elastic tail and $e^{-}e^{+}$ background are small at forward angles 15° and 60°.

At 15°, the quasi-elastic peak is the dominant feature of the cross section at all incident energies. At 60°, the quasi-elastic peak is dominant at incident energies from 646 MeV to 1030 MeV. At $E_{beam} = 1102$ MeV the quasi-elastic peak becomes broader and eventually disappears into a background of delta excitation, meson exchange, and

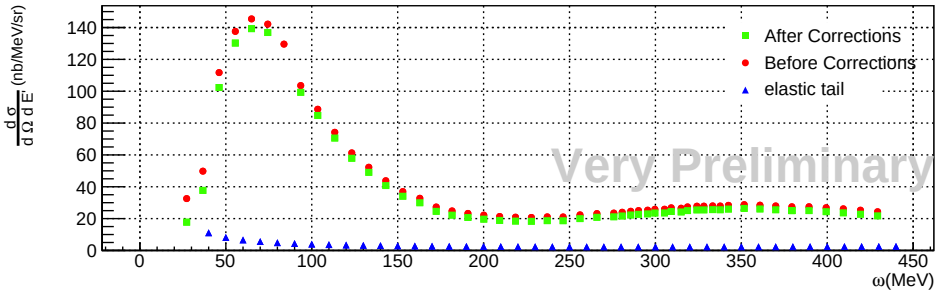

(a) E=1260 MeV, $\theta = 15°$

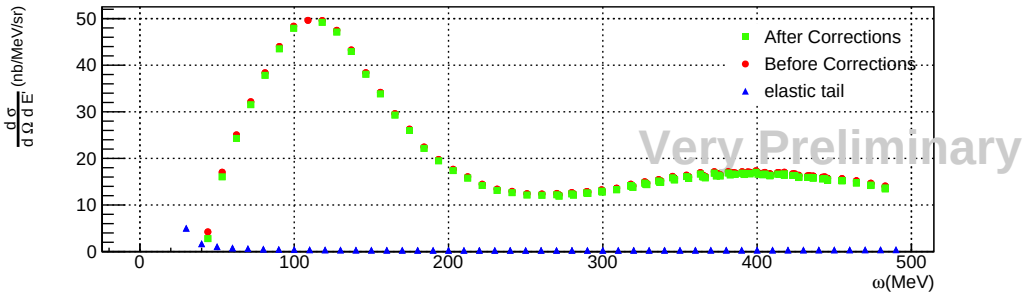

(b) E=1646 MeV, $\theta = 15°$

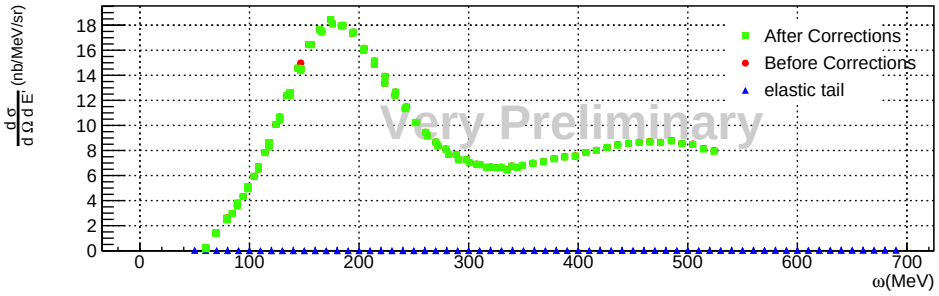

(c) E=2145 MeV, $\theta = 15°$

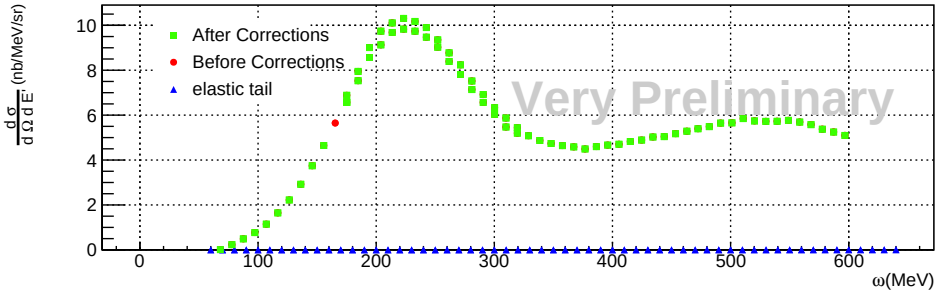

(d) E=2448 MeV, $\theta = 15°$

Figure 5-1: Raw cross sections measured by the LHRS as a function of the electron's energy loss ω (MeV) at $\theta = 15°$, before (red) and after (green) subtraction of elastic tail (blue) and e^+ background (black, too small to be seen).

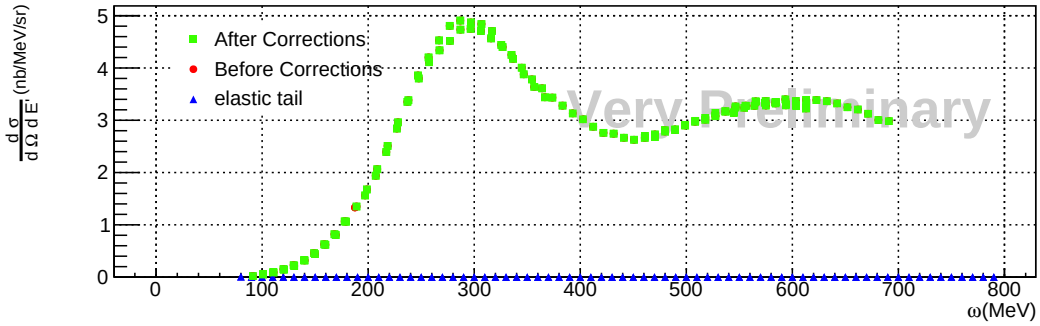

(a) E=2845 MeV, $\theta = 15°$

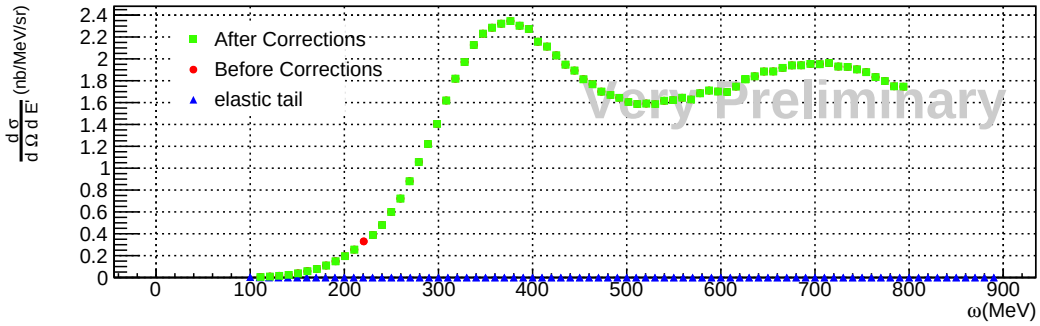

(b) E=3249 MeV, $\theta = 15°$

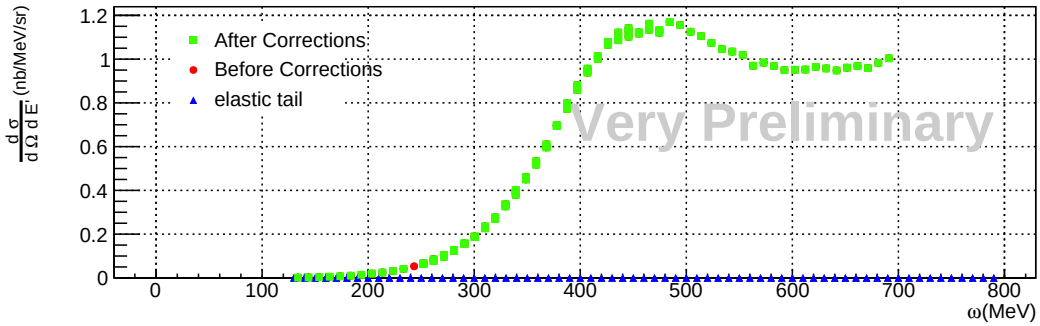

(c) E=3679 MeV, $\theta = 15°$

Figure 5-2: Raw cross sections measured by the LHRS as a function of the electron's energy loss ω (MeV) at $\theta = 15°$, before (red) and after (green) subtraction of elastic tail (blue) and e^+ background (black, too small to be seen).

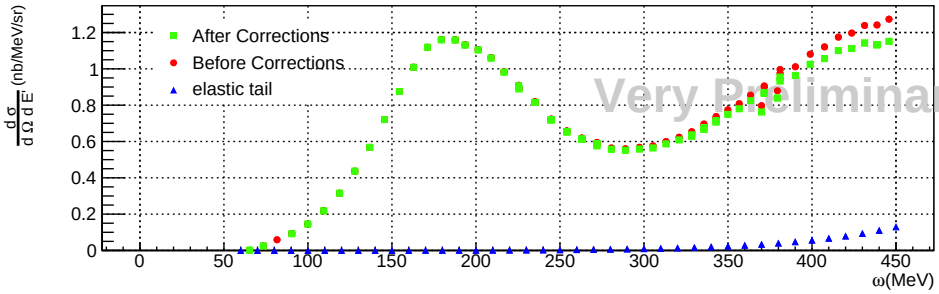

(a) E=646 MeV, $\theta = 60°$

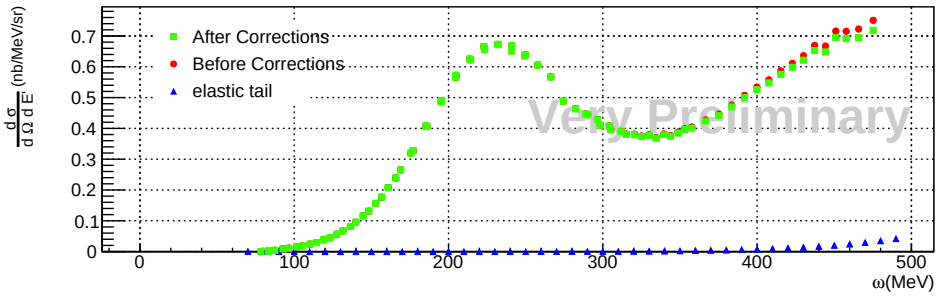

(b) E=740 MeV, $\theta = 60°$

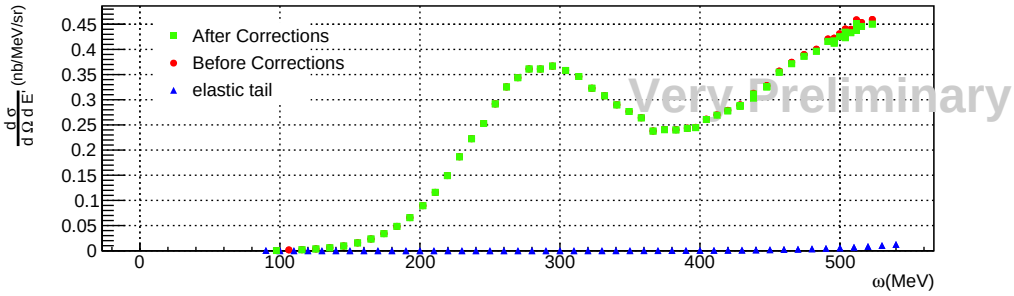

(c) E=845 MeV, $\theta = 60°$

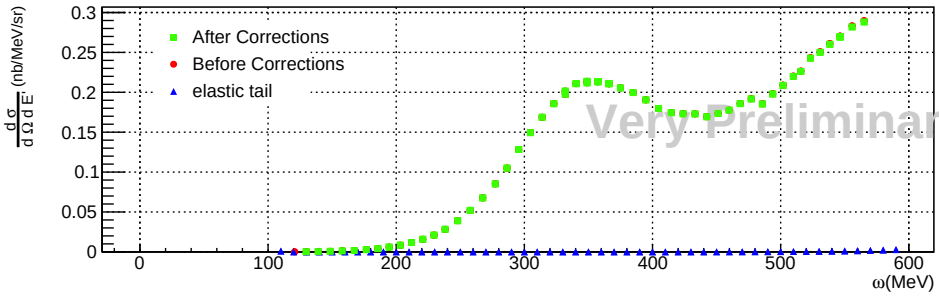

(d) E=958 MeV, $\theta = 60°$

Figure 5-3: The raw cross sections measured by the LHRS as a function of the scattered electron energy (MeV) at $\theta = 60°$, before (red) and after (green) subtraction of elastic tail (blue) and e^+ background (black, too small to be seen).

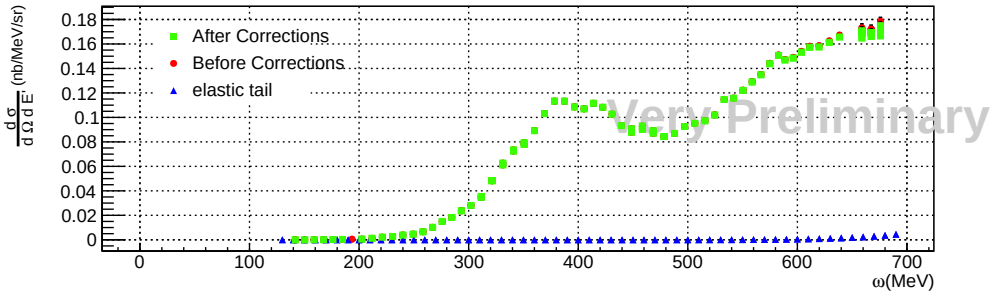

(a) E=1030 MeV, $\theta = 60^{\circ}$

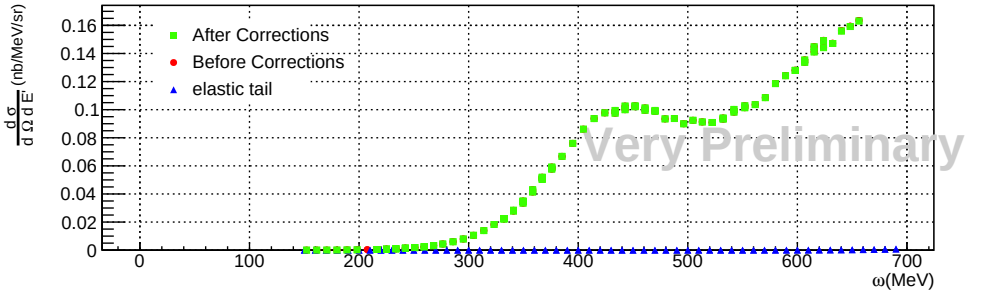

(b) E=1102 MeV, $\theta = 60^{\circ}$

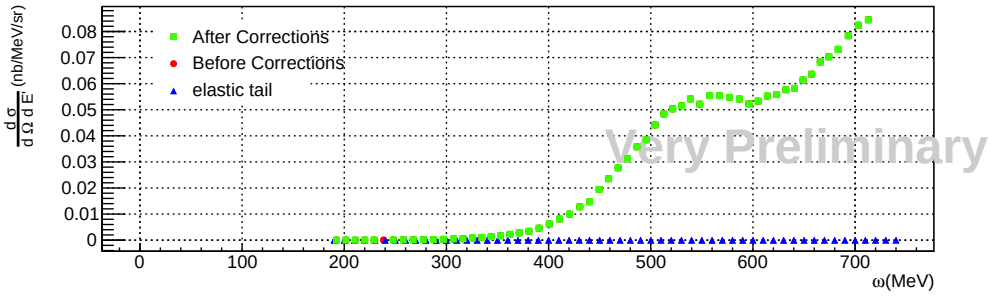

(c) E=1260 MeV, $\theta = 60^{\circ}$

Figure 5-4: The raw cross sections measured by the LHRS as a function of the scattered electron energy (MeV) at $\theta = 60^{\circ}$, before (red) and after (green) subtraction of elastic tail (blue) and e^{+} background (black, too small to be seen).

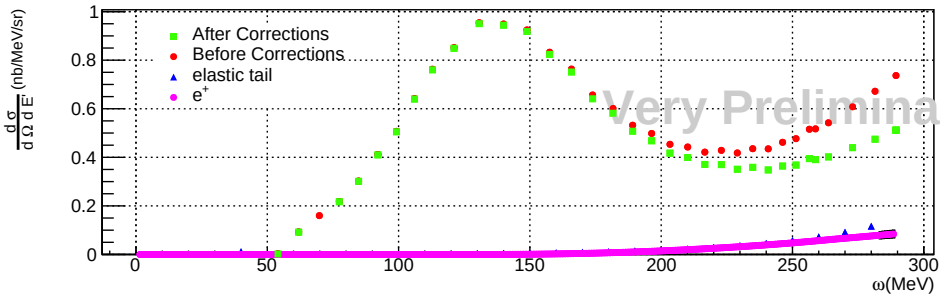

(a) E=399 MeV, $\theta = 90°$

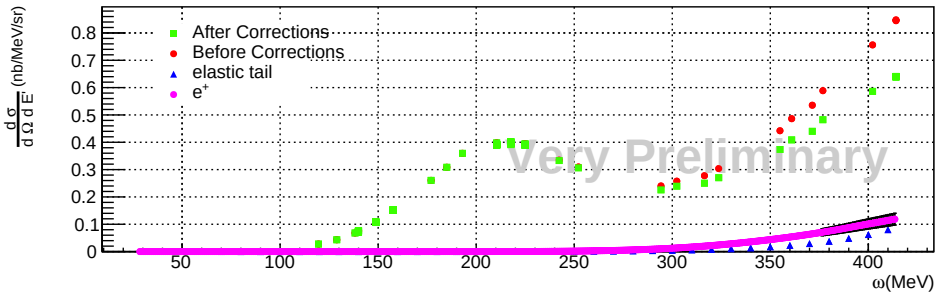

(b) E=528 MeV, $\theta = 90°$

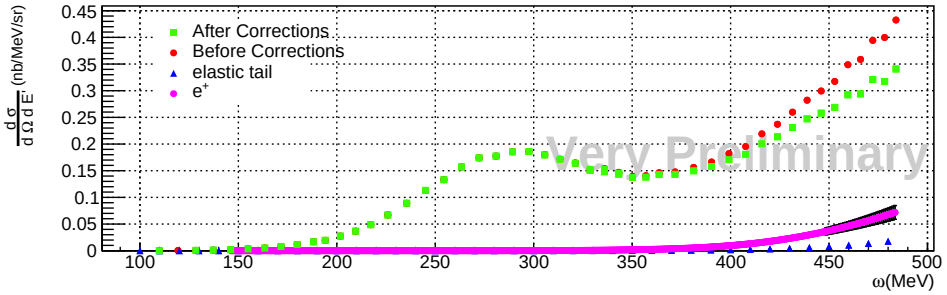

(c) E=646 MeV, $\theta = 90°$

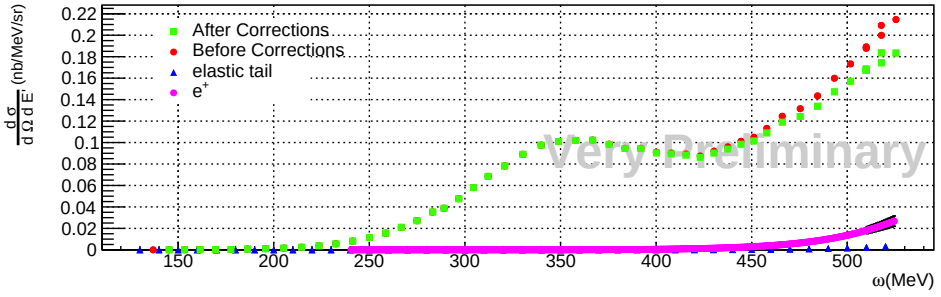

(d) E=740 MeV, $\theta = 90°$

Figure 5-5: The raw cross sections measured by the LHRS as a function of the scattered electron energy (MeV) at $\theta = 90°$, before (red) and after (green) subtraction of elastic tail (blue) and e^+ background (purple with black band as its uncertainty).

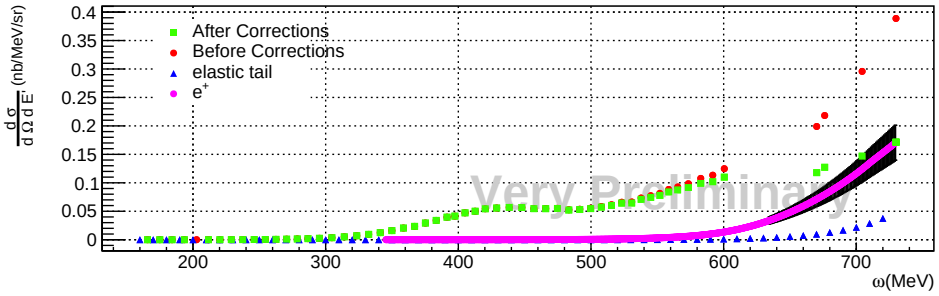

(a) E=845 MeV, $\theta = 90°$

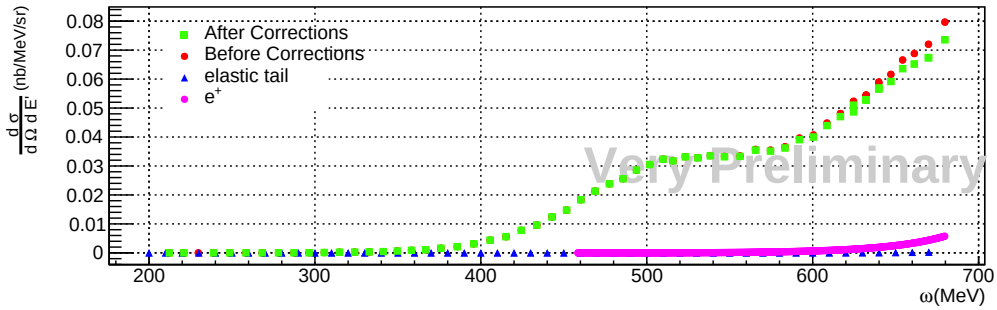

(b) E=958 MeV, $\theta = 90°$

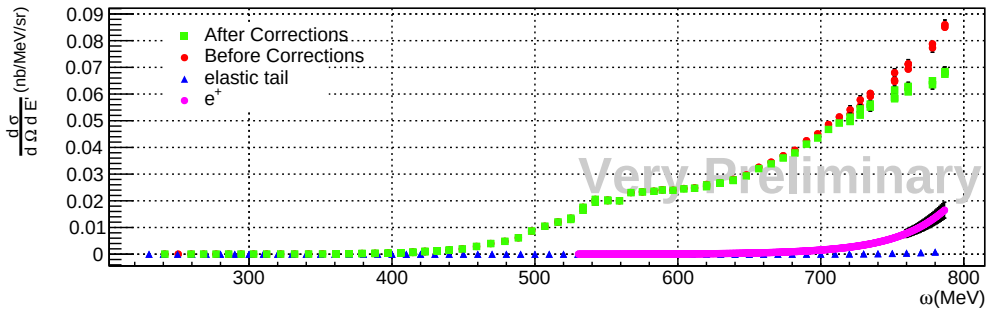

(c) E=1030 MeV, $\theta = 90°$

Figure 5-6: The raw cross sections measured by the LHRS as a function of the scattered electron energy (MeV) at $\theta = 90°$, before (red) and after (green) subtraction of elastic tail (blue) and e^+ background (purple with black band as its uncertainty).

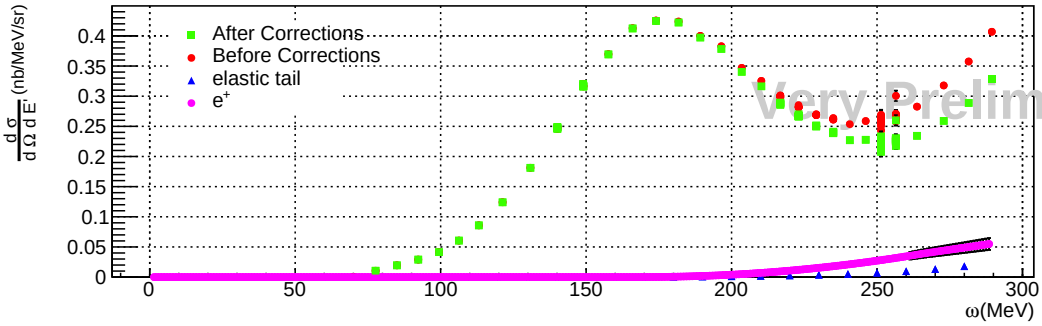

(a) E=399 MeV, θ = 120°

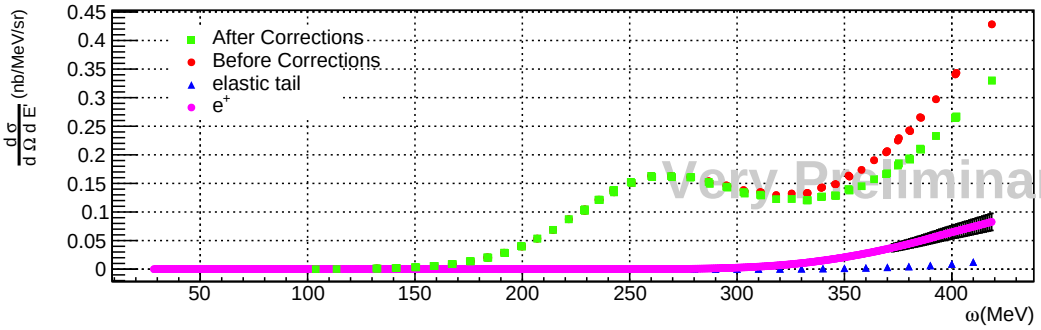

(b) E=528 MeV, θ = 120°

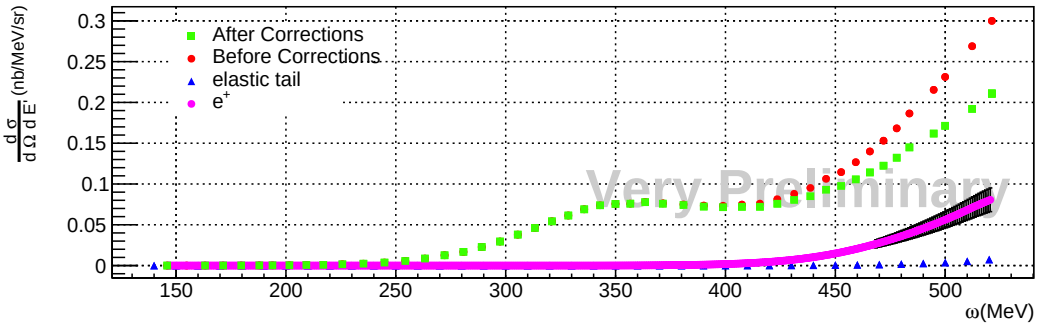

(c) E=646 MeV, θ = 120°

Figure 5-7: The raw cross sections measured by the LHRS as a function of the scattered electron energy (MeV) at $\theta = 120°$, before (red) and after (green) subtraction of elastic tail (blue) and e^+ background (purple with black band as its uncertainty).

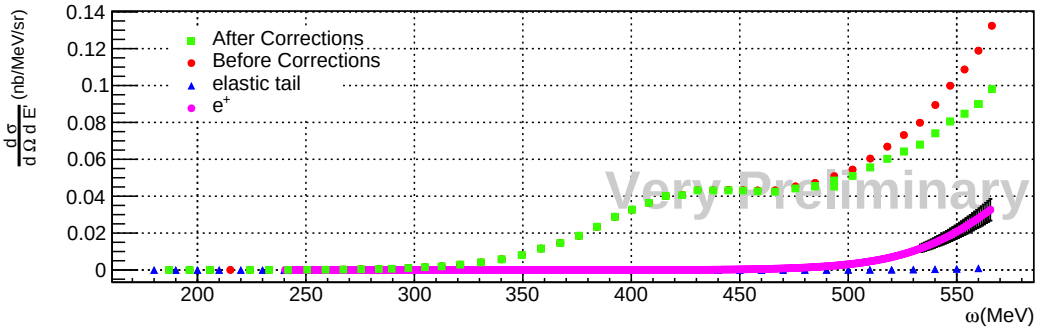

(a) E=740 MeV, θ = 120°

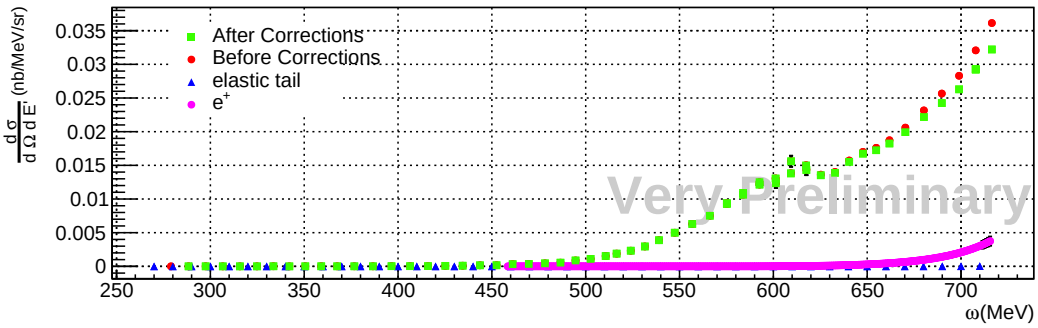

(b) E=958 MeV, θ = 120°

Figure 5-8: The raw cross sections measured by the LHRS as a function of the scattered electron energy (MeV) at $\theta = 120°$, before (red) and after (green) subtraction of elastic tail (blue) and e^+ background (purple with black band as its uncertainty).

deep inelastic scattering. At 90°, the quasi-elastic peak is visible from E_{beam} = 399 MeV to 740 MeV, and disappears into the background above 845 MeV. At 120°, the quasi-elastic peak disappears into the background above E_{beam} = 646 MeV.

5.1.2 Born Cross Sections

After the radiative elastic tail and e^-e^+ background were subtracted, the radiative correction was applied. The raw cross sections and Born cross sections after radiaitve corrections are shown in Figs. 5-9 through Figure 5-16 for 15°, 60°, 90° and 120°.

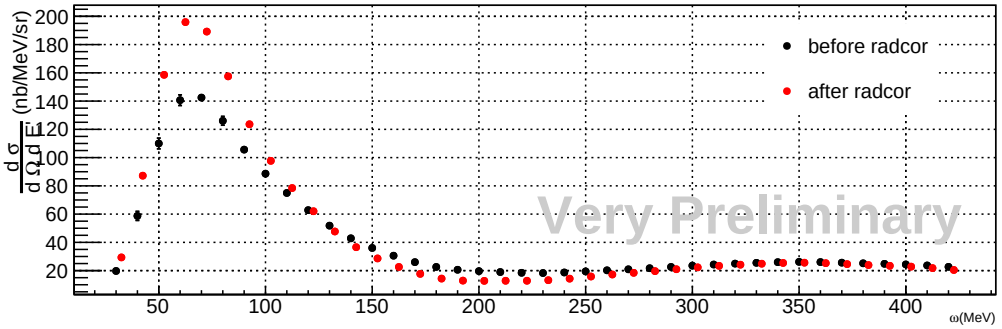

(a) E=1260 MeV, $\theta = 15°$

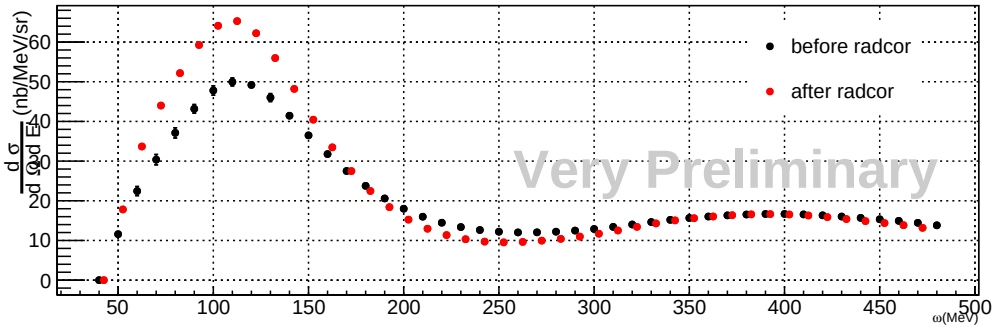

(b) E=1646 MeV, $\theta = 15°$

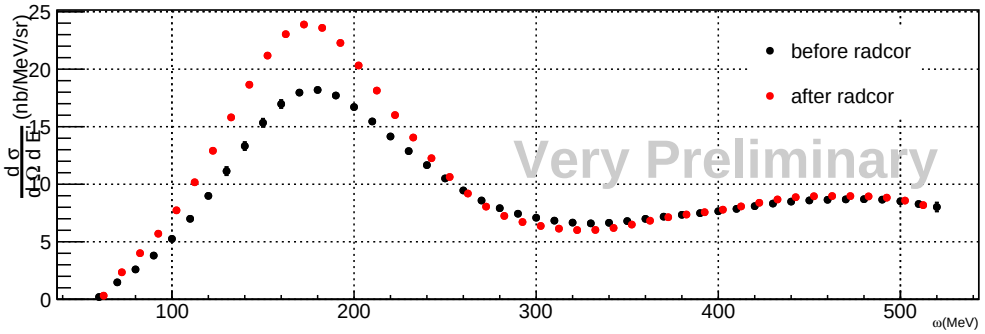

(c) E=2145 MeV, $\theta = 15°$

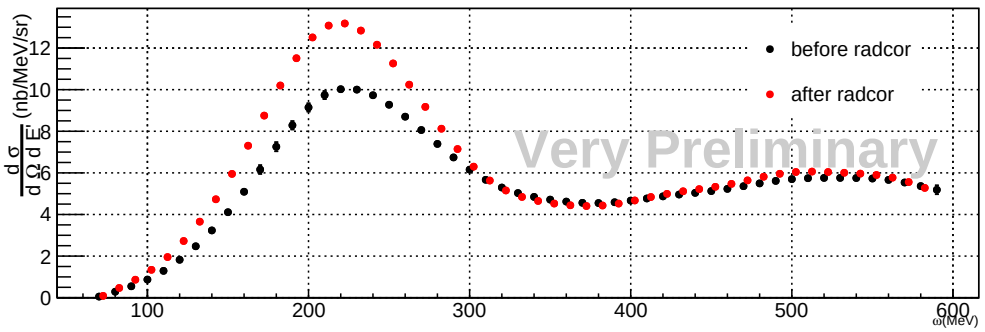

(d) E=2448 MeV, $\theta = 15°$

Figure 5-9: The Born cross section after radiative correction on 15° data. Black: raw cross section before radiative correction; red: Born cross section after radiative correction.

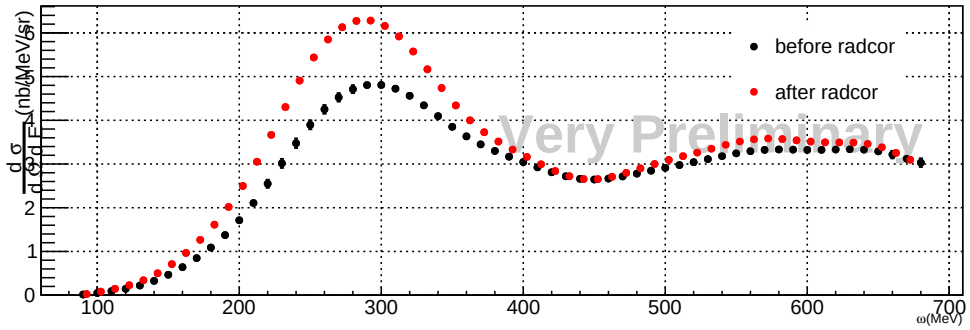

(a) E=2845 MeV, $\theta = 15°$

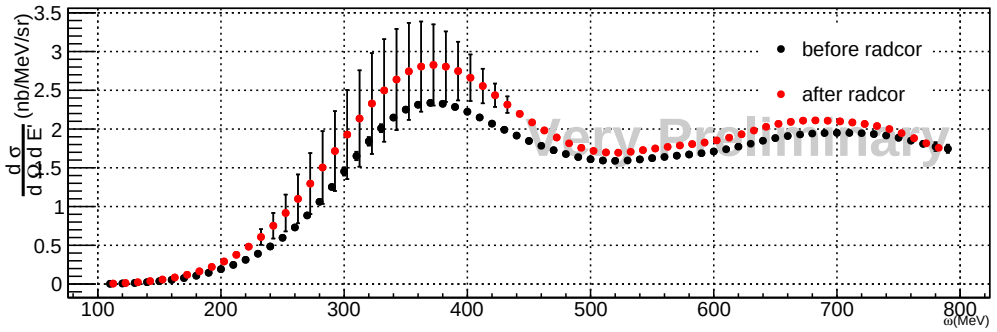

(b) E=3249 MeV, $\theta = 15°$

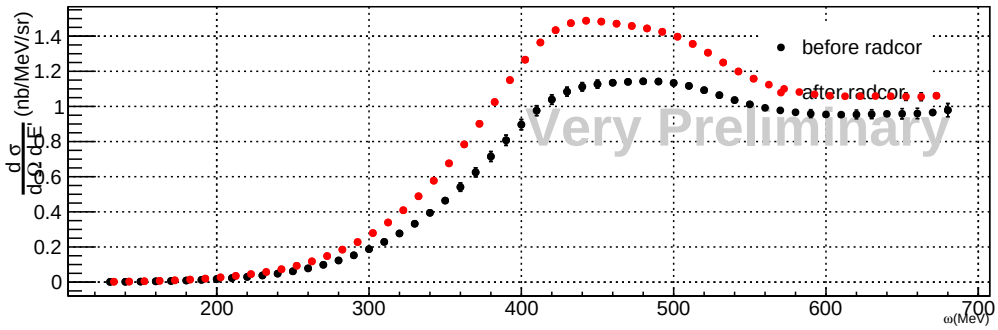

(c) E=3679 MeV, $\theta = 15°$

Figure 5-10: The Born cross section after radiative correction on 15° data. Black: raw cross section before radiative correction; red: Born cross section after radiative correction.

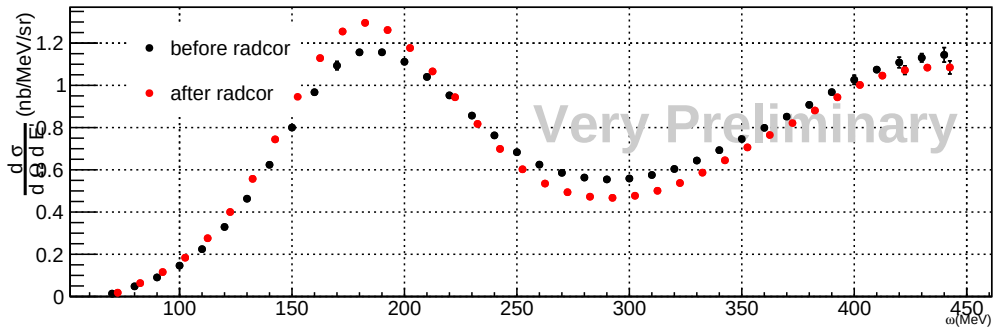

(a) E=646 MeV, $\theta = 60°$

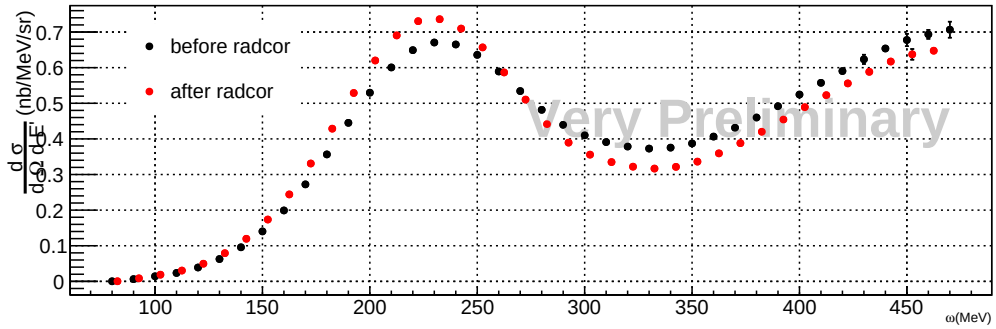

(b) E=740 MeV, $\theta = 60°$

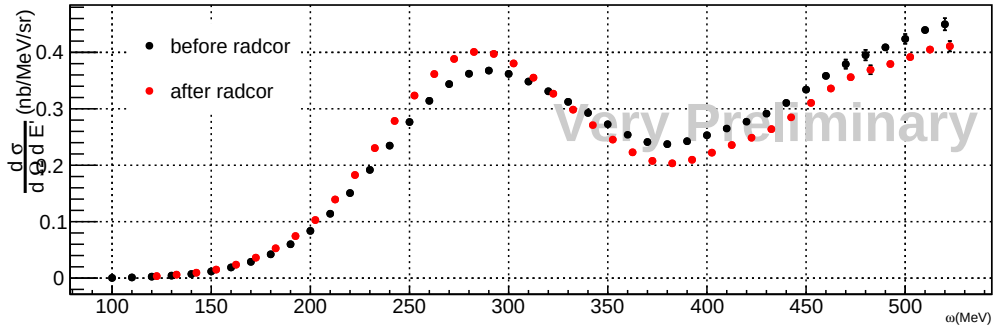

(c) E=845 MeV, $\theta = 60°$

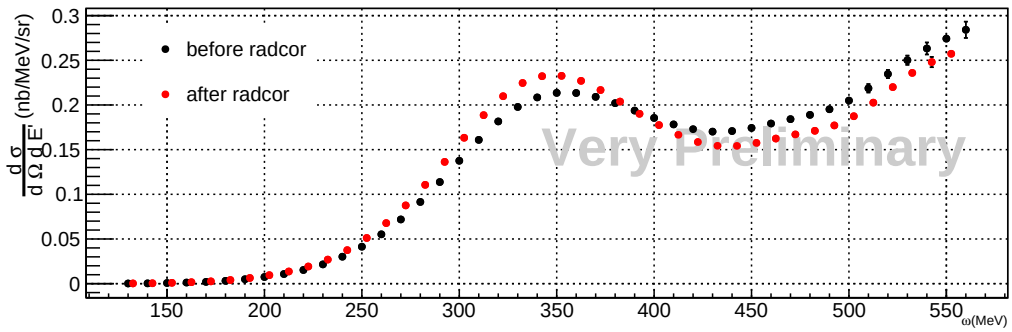

(d) E=958 MeV, $\theta = 60°$

Figure 5-11: The Born cross section after radiative correction on 60° data. Black: raw cross section before radiative correction; red: Born cross section after radiative correction.

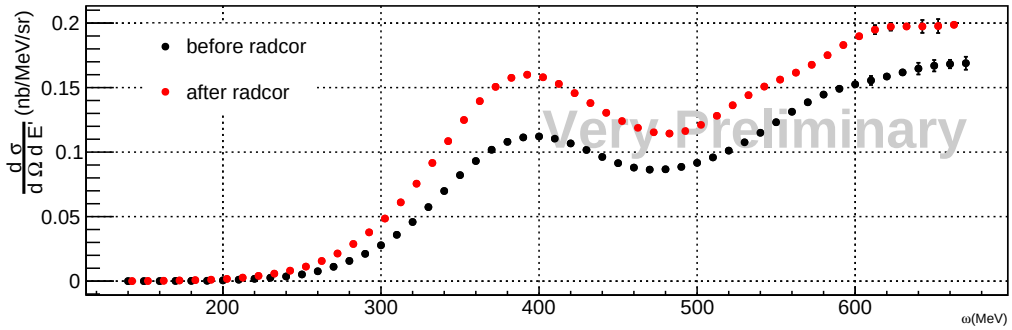

(a) E=1030 MeV, $\theta = 60°$

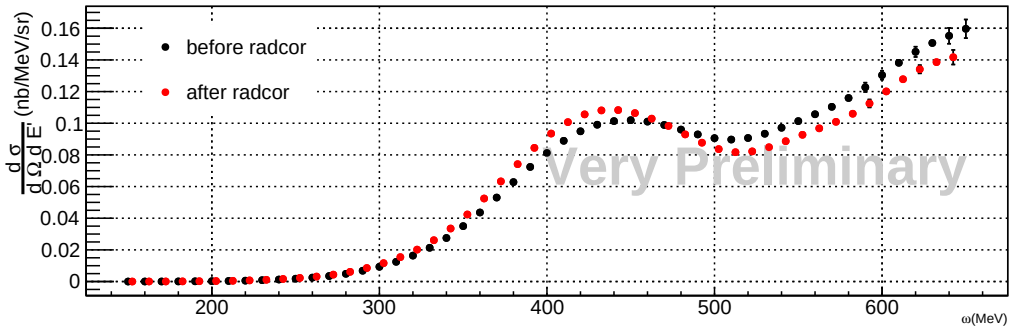

(b) E=1102 MeV, $\theta = 60°$

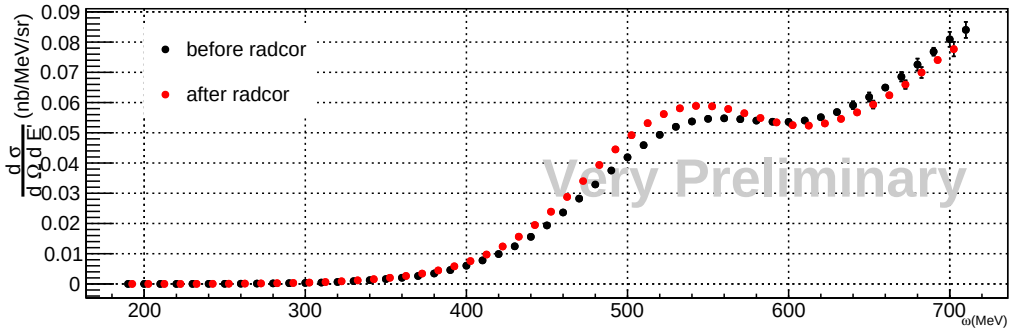

(c) E=1260 MeV, $\theta = 60°$

Figure 5-12: The Born cross section after radiative correction on 60° data. Black: raw cross section before radiative correction; red: Born cross section after radiative correction.

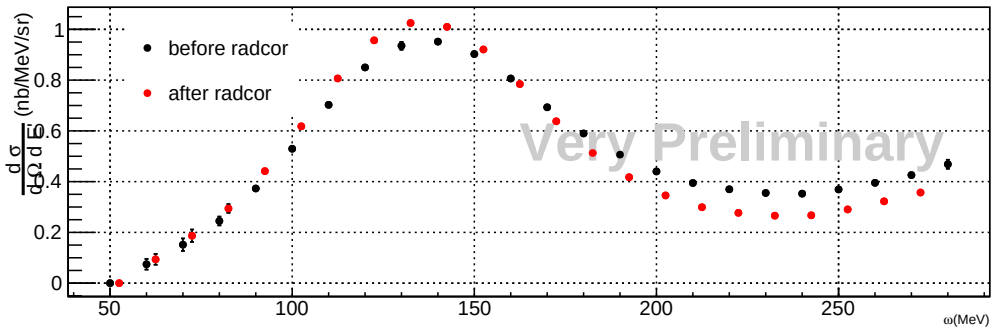

(a) E=399 MeV, $\theta = 90°$

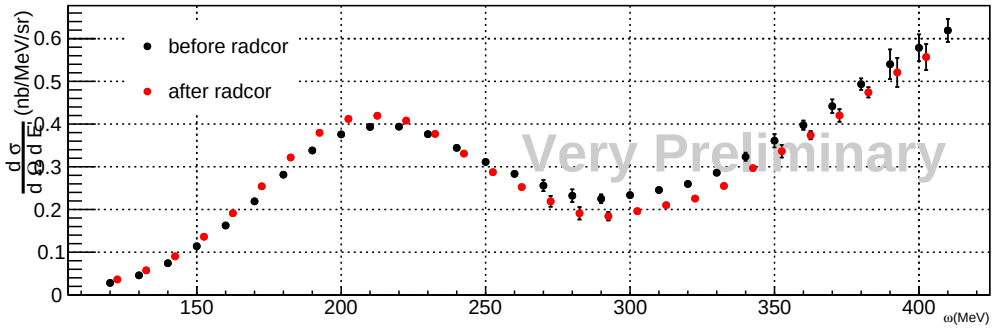

(b) E=528 MeV, $\theta = 90°$

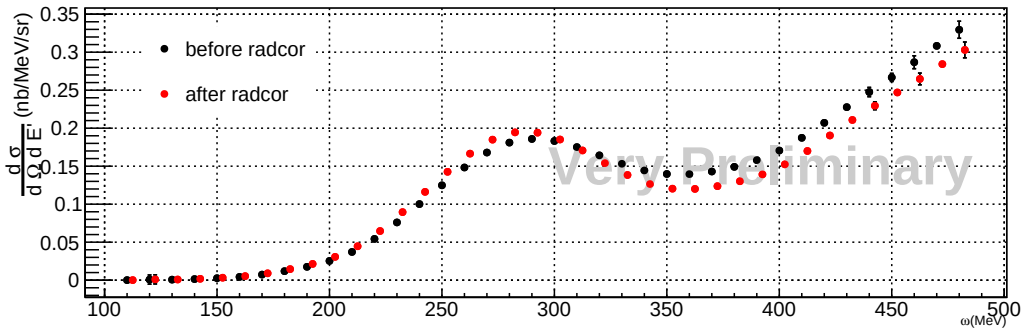

(c) E=646 MeV, $\theta = 90°$

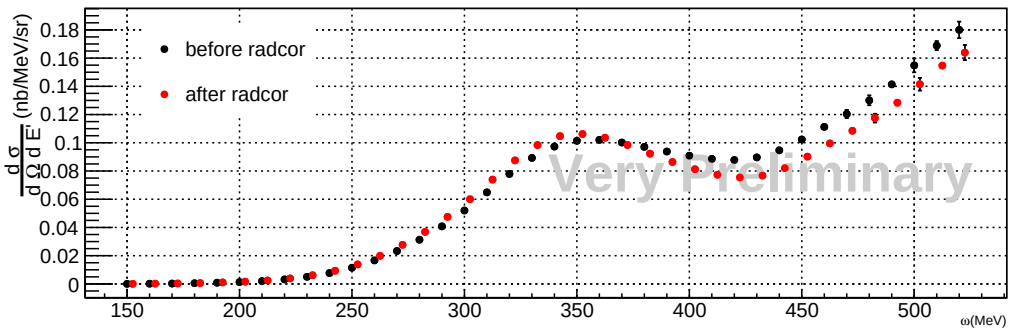

(d) E=740 MeV, $\theta = 90°$

Figure 5-13: The Born cross section after radiative correction on 90° data. Black: raw cross section before radiative correction; red: Born cross section after radiative correction.

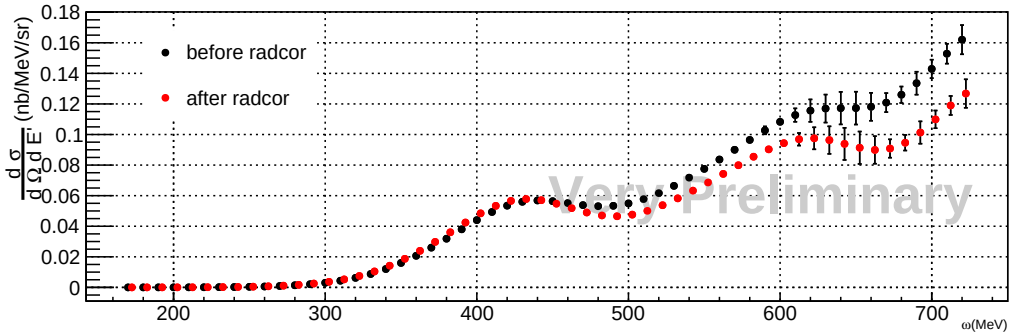

(a) E=845 MeV, $\theta = 90°$

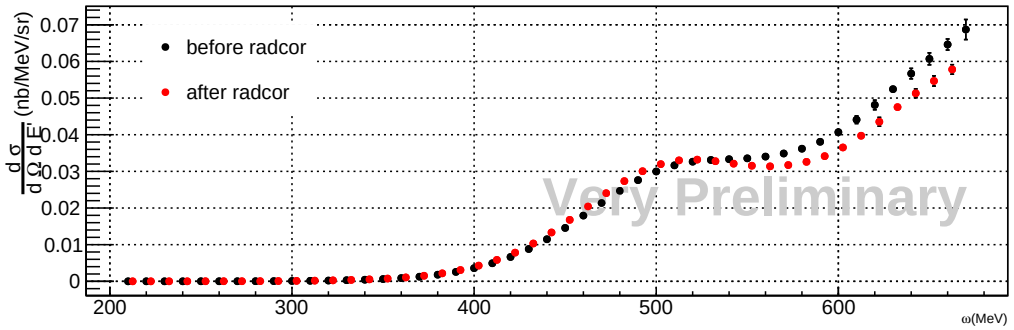

(b) E=958 MeV, $\theta = 90°$

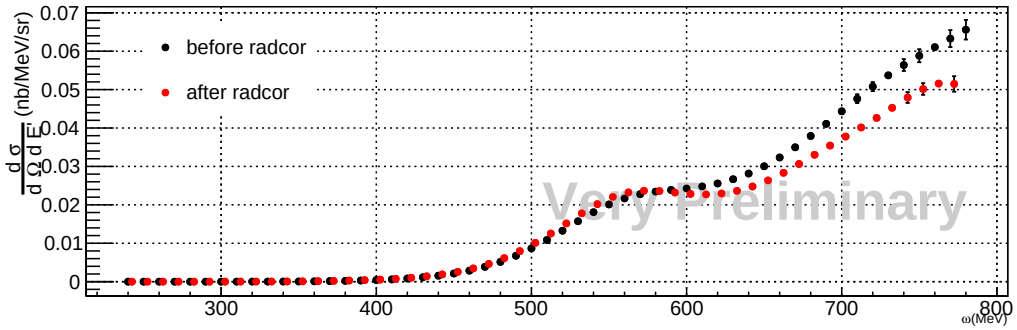

(c) E=1030 MeV, $\theta = 90°$

Figure 5-14: The Born cross section after radiative correction on 90° data. Black: raw cross section before radiative correction; red: Born cross section after radiative correction.

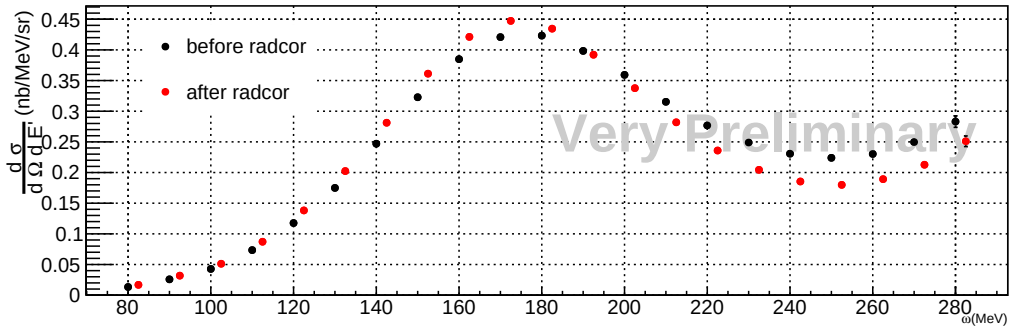

(a) E=399 MeV, θ = 120°

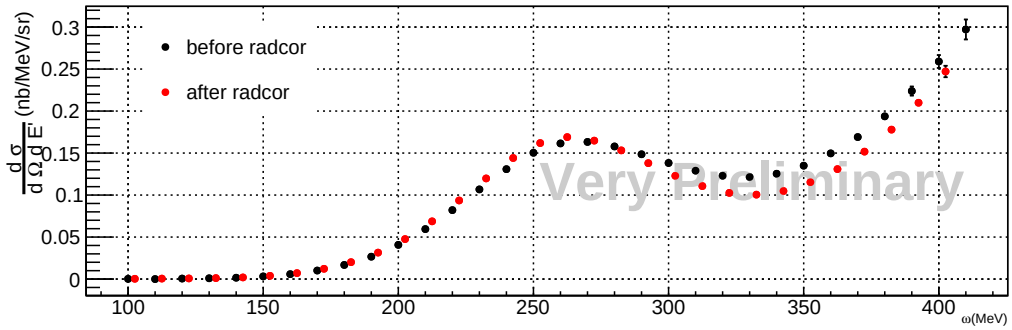

(b) E=528 MeV, θ = 120°

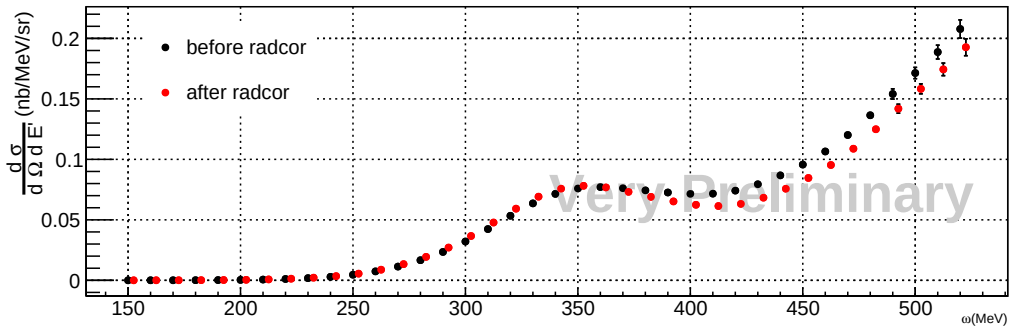

(c) E=646 MeV, θ = 120°

Figure 5-15: The Born cross section after radiative correction on 120° data. Black: raw cross section before radiative correction; red: Born cross section after radiative correction.

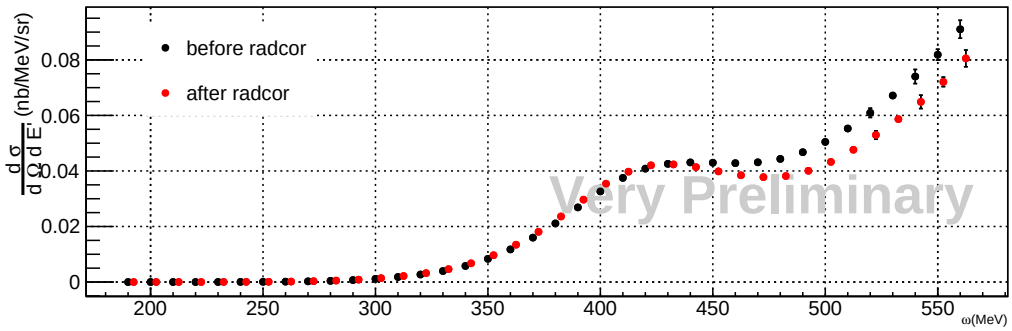

(a) E=740 MeV, θ = 120°

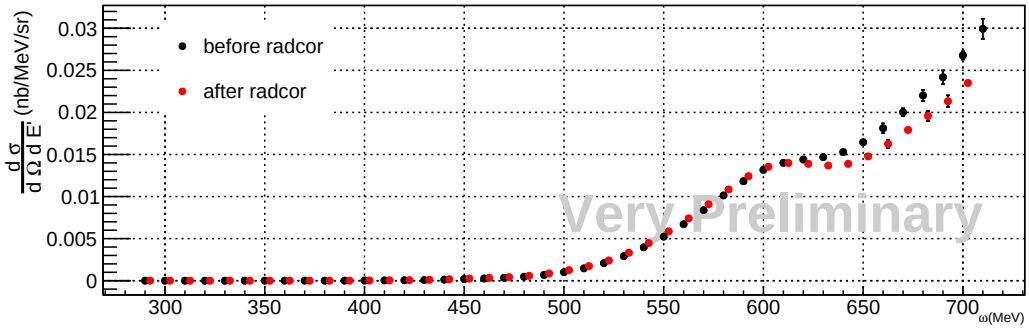

(b) E=958 MeV, θ = 120°

Figure 5-16: The Born cross section after radiative correction on 120° data. Black: raw cross section before radiative correction; red: Born cross section after radiative correction.

5.2 Rosenbluth Separation

5.2.1 R_L and R_T

The longitudinal and transverse response functions R_L and R_T of ^{4}He were extracted using Eq. 1.10 at constant three-momentum-transfer $|\vec{q}|$. The results are shown in Figs. 5-17, 5-18, 5-19, and 5-20.

As one can see from these figures: at low $|\mathbf{q}|$, all of R_L decrease to zero or even go below zero at large ω, while the transverse response function R_T keeps rising after the quasi-elastic peak. This is because the R_L has most of the contribution from quasi-elastic scattering, but the R_T has contributions from other processes such as meson exchange currents (MEC), Δ excitation, higher resonances and deep inelastic scattering. One can also see that as $|\mathbf{q}|$ increases, the uncertainties of R_L and R_T increase. This is because the difference between total response function εR of Eq. 4.16 of forward and backward angles become small, and thus the uncertainties of the linear fitting become large. Another reason for the large uncertainty in R_L is because at high $|\mathbf{q}|$, R_L contributes only a small term to the total cross section while R_T dominates the total cross section.

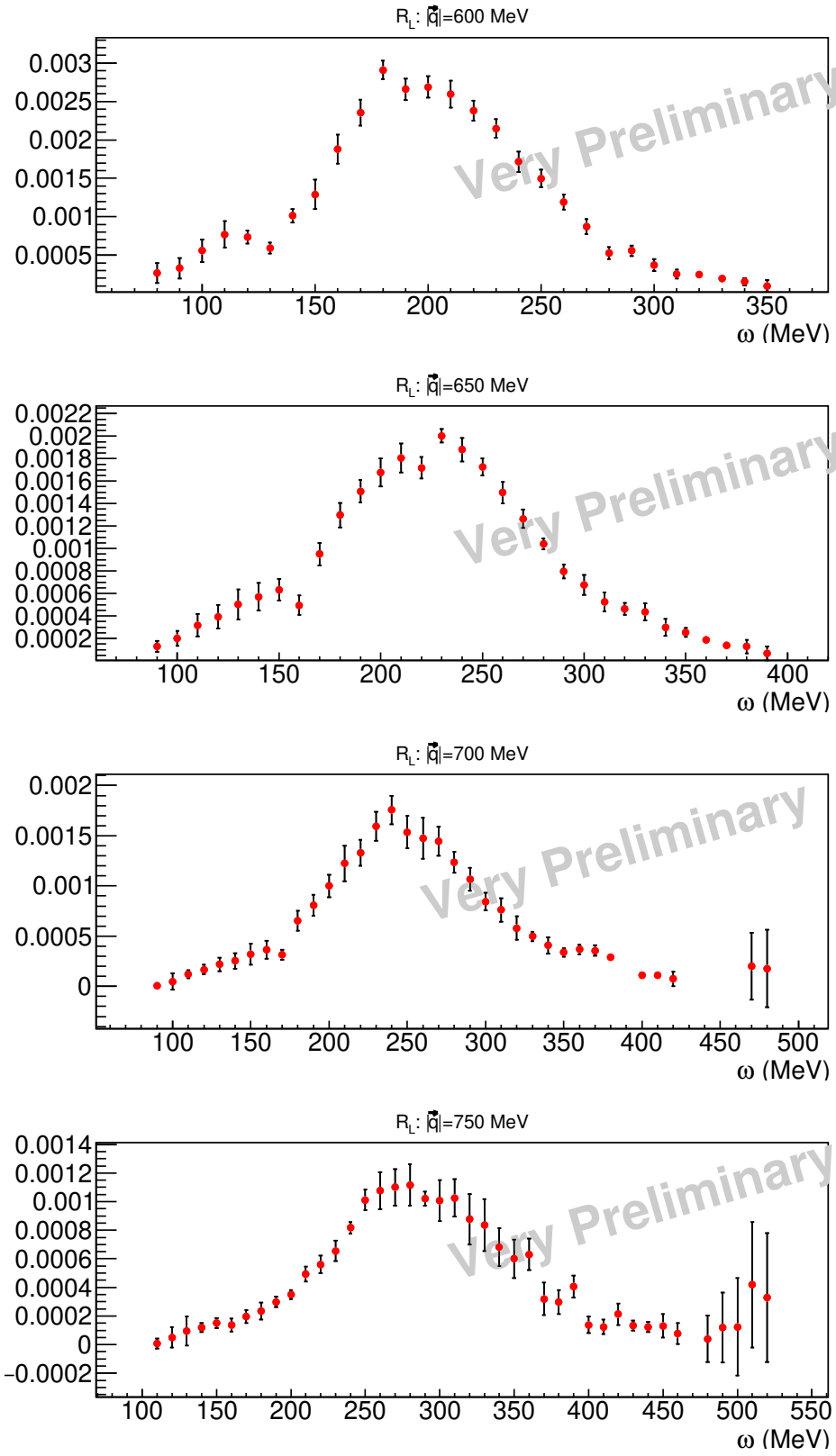

Figure 5-17: Longitudinal response function R_L of ^{4}He (in 1/MeV) at constant $|\mathbf{q}|$. From top to bottom: $|\mathbf{q}| = 600$, 650, 700 and 750 MeV.

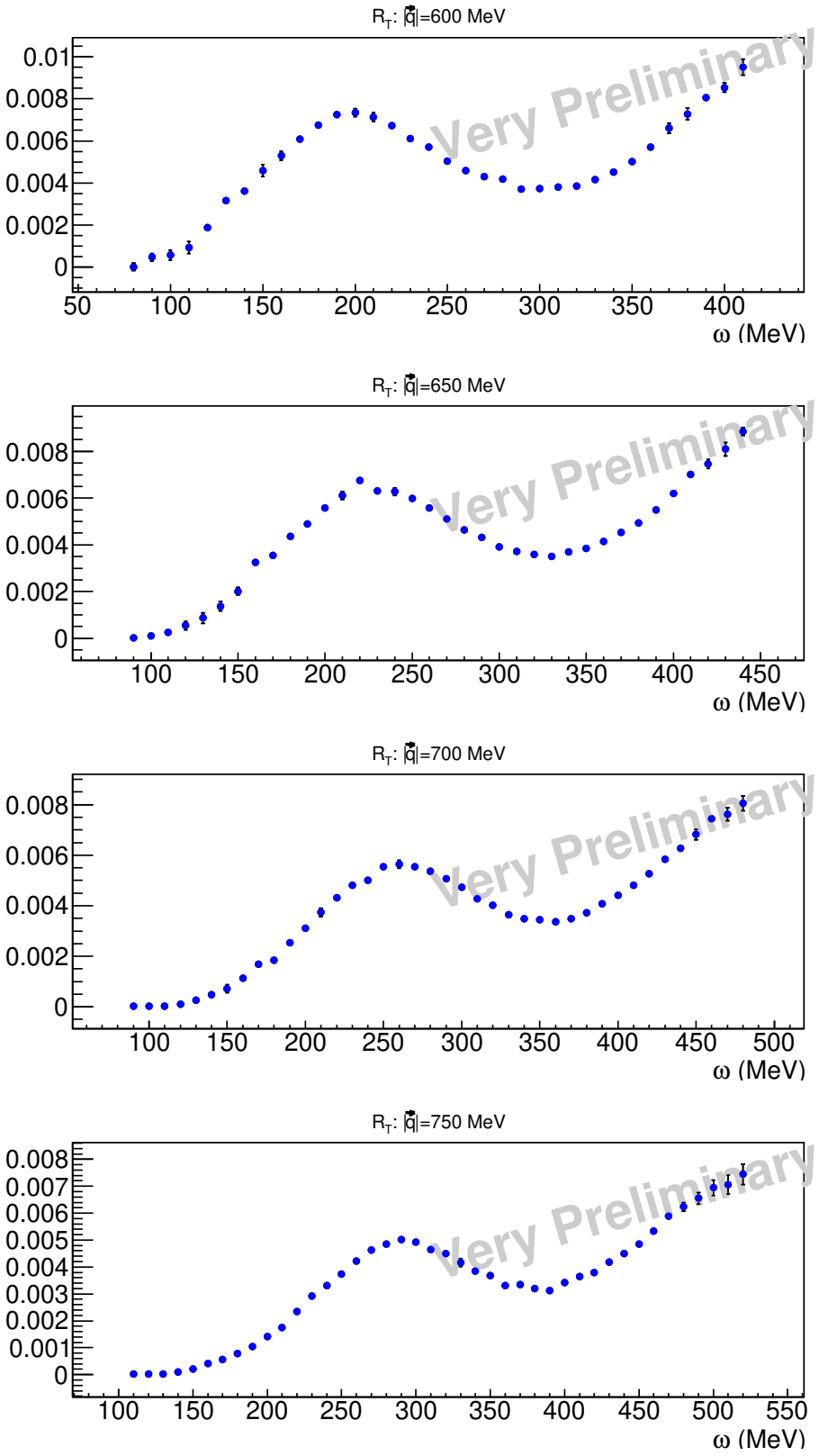

Figure 5-18: Transverse response function R_T of ^{4}He (in 1/MeV) at constant $|\mathbf{q}|$. From top to bottom: $|\mathbf{q}| = 600$, 650, 700 and 750 MeV.

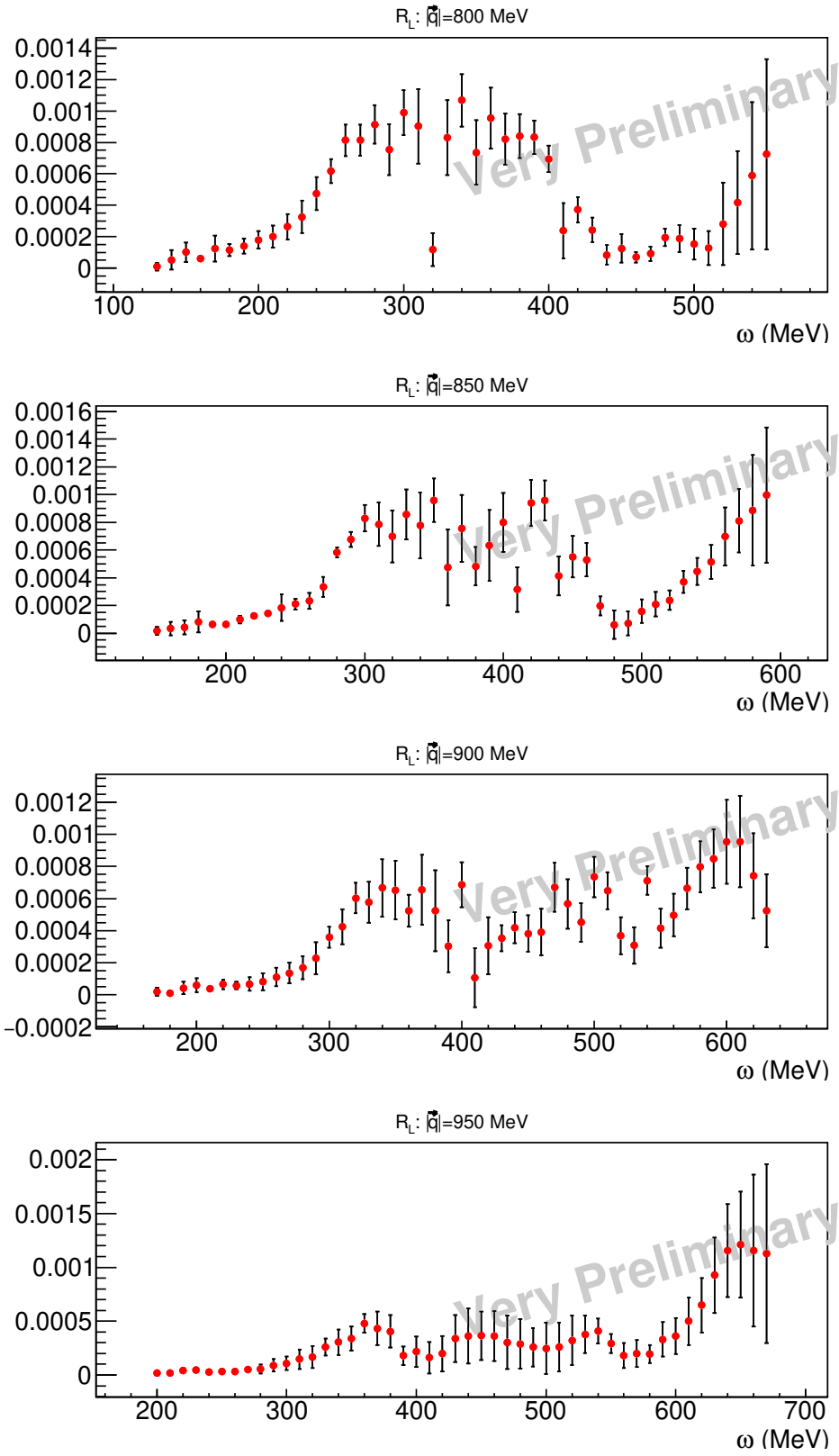

Figure 5-19: Longitudinal response function R_L of ^{4}He (in 1/MeV) at constant $|\mathbf{q}|$. From top to bottom: $|\mathbf{q}| = 800$, 850, 900 and 950 MeV.

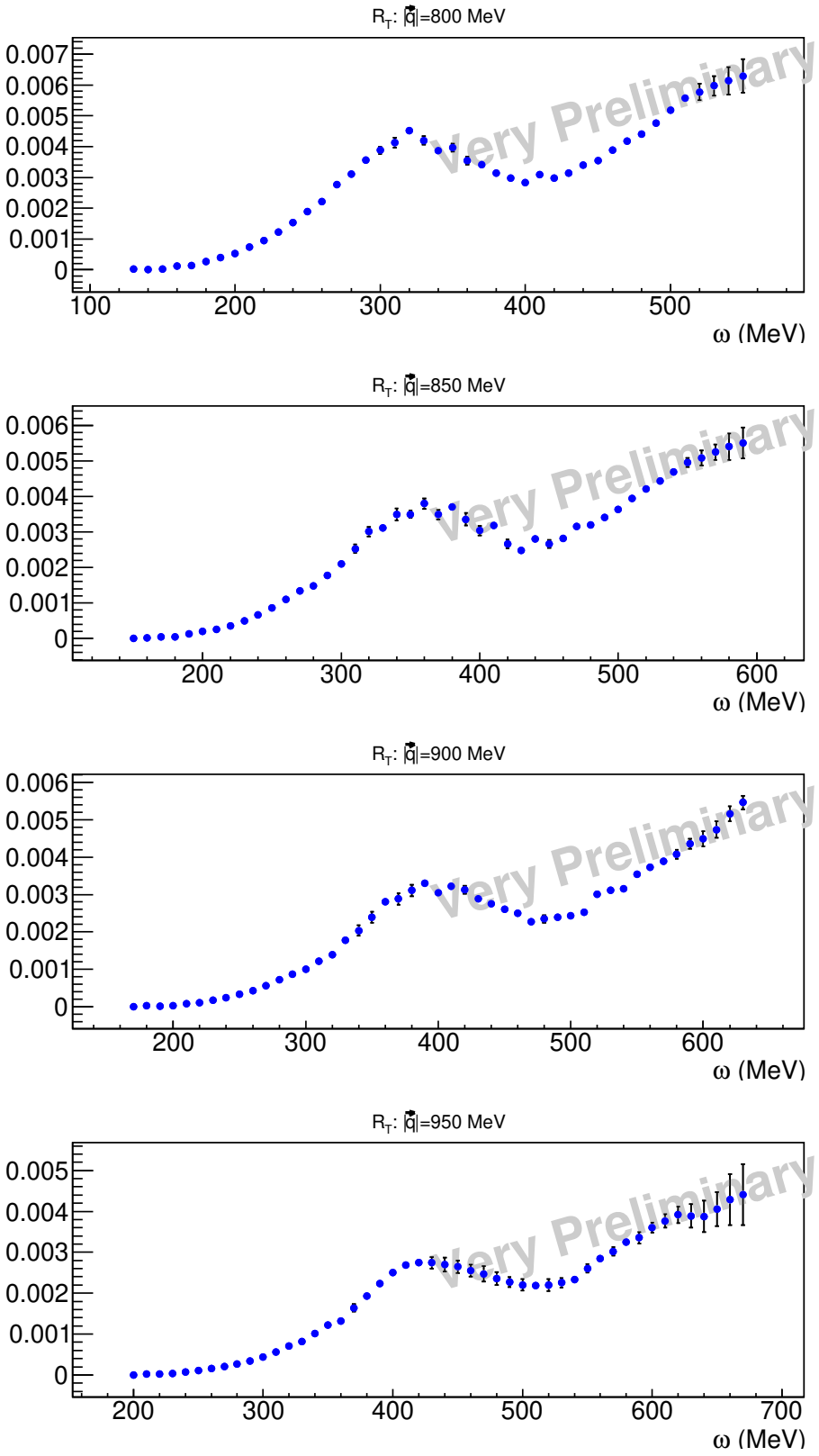

Figure 5-20: Transverse response function R_T of ^{4}He (in 1/MeV) at constant $|\mathbf{q}|$. From top to bottom: $|\mathbf{q}| = 800$, 850, 900 and 950 MeV.

5.2.2 Comparison with Existing Data

The longitudinal response function R_L extracted from this analysis at q=600 and 640 MeV/c are compared with existing data from Saclay [54], see Fig. 5-21. The agreement is very good overall.

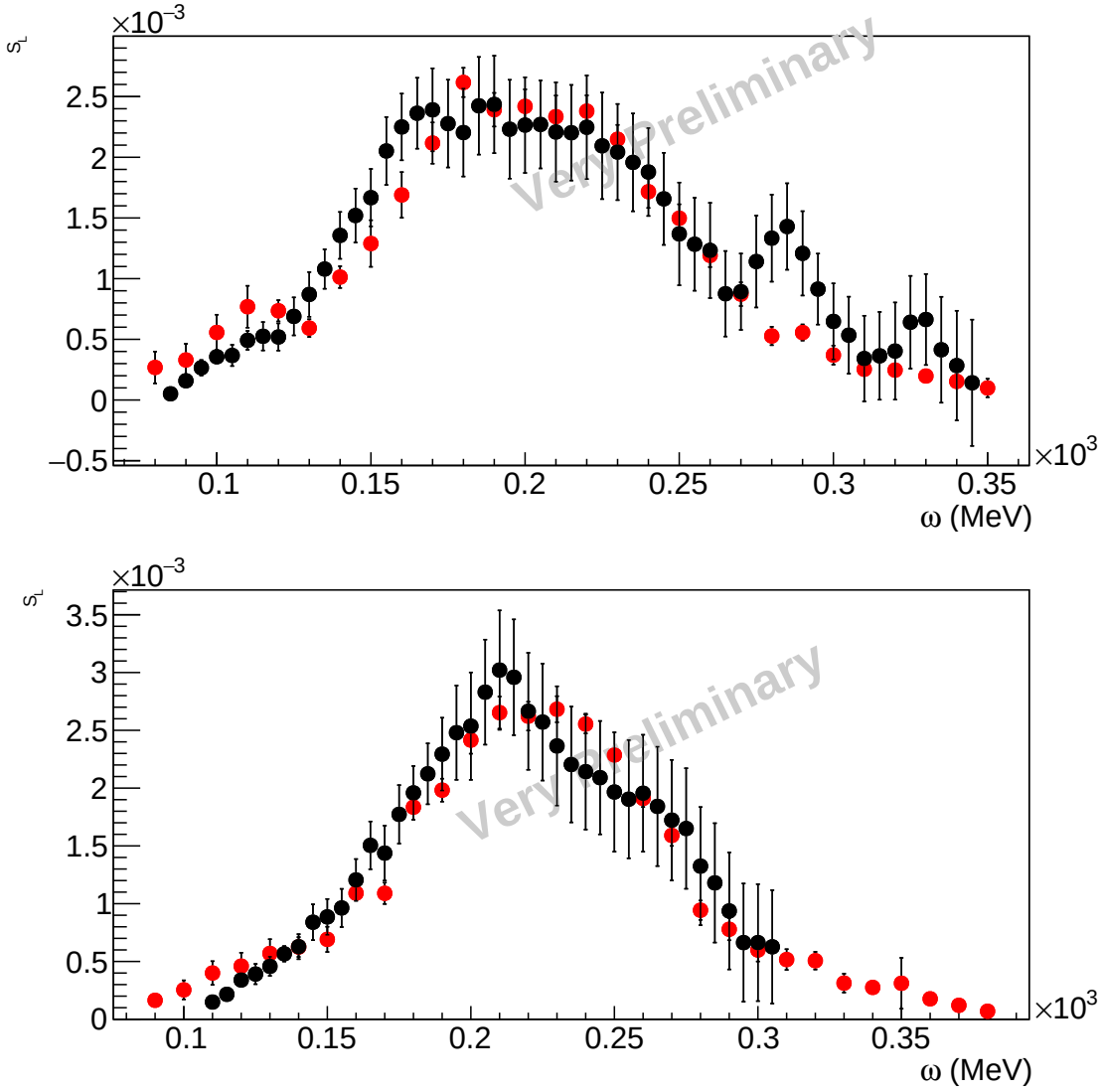

Figure 5-21: Preliminary results of this experiment (red) and Saclay data (black) [54] on R_L of ^{4}He at $|\vec{q}| = 600$ and 640 MeV.

5.2.3 Comparison with Fermi Gas Model

Here we compare our results on R_L and R_T with a relativistic Fermi gas model [47] [55]. In this model R_L and R_T are calculated using:

$$R_L(|\vec{q}|,\omega) = \frac{\pi V}{|\vec{q}|}\int_{E_0}^{\infty} dE n(E)(1-n(E+\bar{\omega}))\big[(E+\frac{\omega}{2})^2\frac{T_2(Q^2)}{M^2} - \frac{\vec{q}^2}{Q^2}T_1(Q^2)\big], \quad (5.1)$$

$$R_T(|\vec{q}|,\omega) = \frac{\pi V}{|\vec{q}|}\int_{E_0}^{\infty} dE n(E)(1-n(E+\bar{\omega})) \times \left\{2T_1(Q^2) + \left[E^2 - M^2 - (\frac{\vec{q}^2-\bar{\omega}^2-2E\bar{\omega}}{2|\vec{q}|})^2\right]\frac{T_2(Q^2)}{M^2}\right\}, \quad (5.2)$$

where $\bar{\omega} = \omega - \epsilon_s$, with ϵ_s the average separation energy. E_0 is the lower bound of the integral:

$$E_0 = \max\left(M, \frac{|\vec{q}|}{2}\sqrt{1+\frac{4M^2}{\vec{q}^2-\bar{\omega}^2}} - \frac{\bar{\omega}}{2}\right). \quad (5.3)$$

T_1 and T_2 are related to the electric and magnetic form factors G_E and G_M:

$$T_1(Q^2) = Q^2G_M^2/2, T_2(Q^2) = 2M^2\left(\frac{G_E^2+\tau G_M^2}{1+\tau}\right), \quad (5.4)$$

where $\tau = Q^2/4M^2$ and $G^2_{E(M)} = G^2_{E(M)p} + \frac{N}{Z}G^2_{E(M)n}$ with p and n stand for proton and neutron, respectively. Different types of form factors can be used, the most simple one is the dipole form factor:

$$G_{Ep}(Q^2) = [1+Q^2/(0.71(\mathrm{GeV}/c)^2)]^{-2}, \quad (5.5)$$

$$G_{En}(Q^2) = 0, \quad (5.6)$$

$$G_{Mp(n)}(Q^2) = \mu_{p(n)}G_{Ep}(Q^2), \quad (5.7)$$

where $\mu_p = 2.793$ and $\mu_n =$ -1.913 are the proton and the neutron magnetic moments, respectively. V is the normalization volume for the momentum distribution $n(p)$:

$$V \int d^3p\, n(p) = Z. \tag{5.8}$$

The most simple form of momentum distribution is a step function:

$$n(p) = \Theta(k_F - p) = \begin{cases} = 1 & \text{if } p \leq k_F \\ = 0 & \text{if } p > k_F \end{cases} \tag{5.9}$$

where k_F is the Fermi momentum. The parameters used for ^{4}He are: $k_F = 200$ MeV/c and $\epsilon_s = 20$ MeV.

The comparison is shown in Figs. 5-22 and 5-23. Because the simple Fermi gas model contains only the quasi-elastic scattering process, we expect the transverse response function R_T differ significantly from the model prediction. The real R_T from data contains contributions from MEC, Δ resonance and other processes. On the other hand, the longitudinal response function R_L is mainly from the quasi-elastic scattering and is relative clean from background of the other mechanism. Therefore we expect predictions on R_L from the simple Fermi gas model to agree with data. The long and the short range correlations, center-of-mass correction are not included in the model.

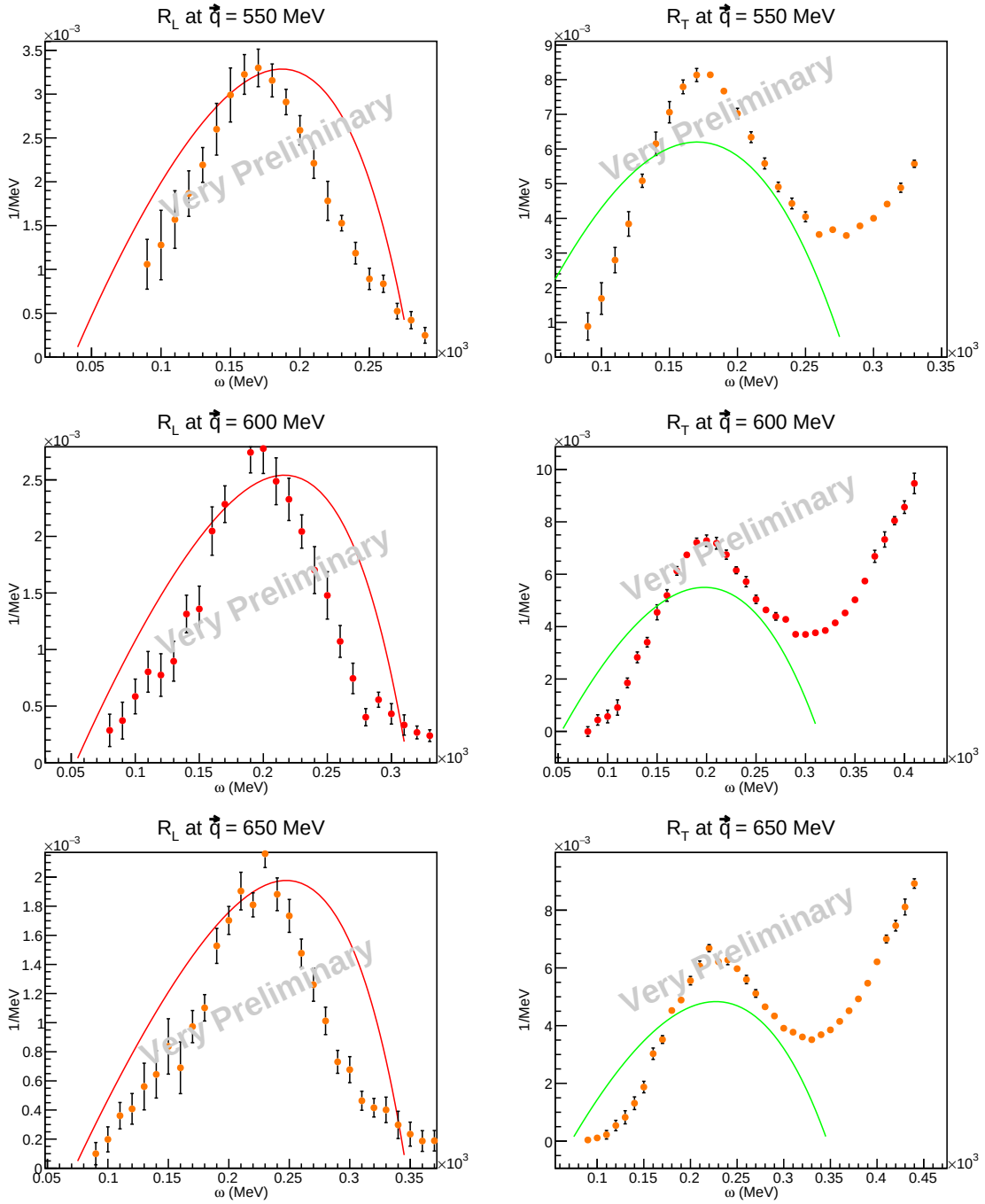

Figure 5-22: Comparison of longitudinal (left) and transverse (right) response function at $|\vec{q}| = 550$ (top), 600 (middle), 650 (bottom) MeV compared with a simple Fermi gas model. Left: R_L data (orange points) and simple Fermi gas model prediction (red curve); right: R_T data (orange points) and simple Fermi gas model prediction (green curve).

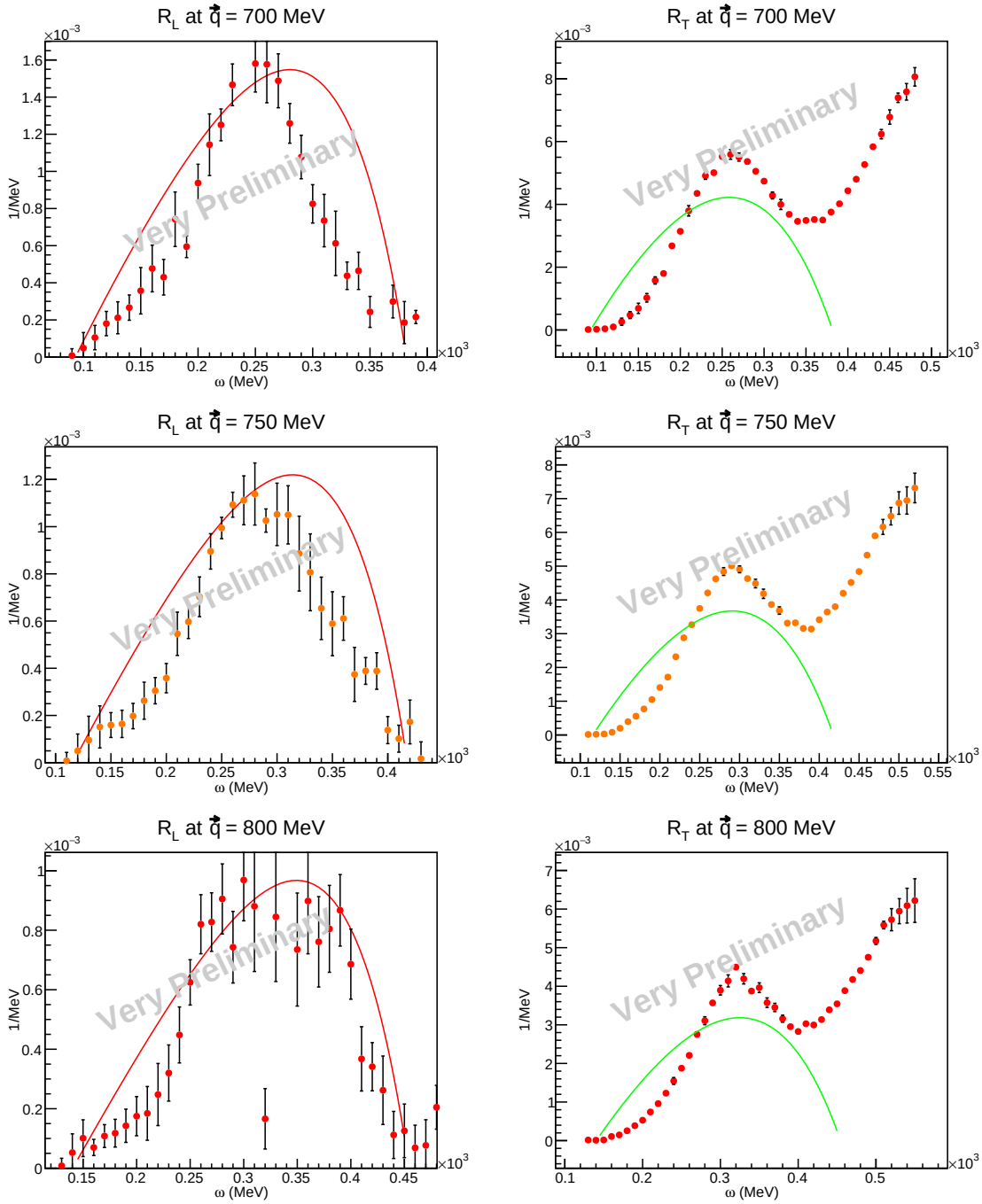

Figure 5-23: Comparison of longitudinal (left) and transverse (right) response function at $\vec{q} = 700$ (top), 750 (middle), 800 (bottom) MeV compared with a simple Fermi gas model. Left: R_L data (orange points) and simple Fermi gas model prediction (red curve); right: R_T data (orange points) and simple Fermi gas model prediction (green curve).

5.3 Coulomb Sum

Preliminary results on the Coulomb Sum as a function of $|\vec{q}|$ is shown in Fig. 5-24. Existing data from Saclay, Bates and SLAC are also shown in the same figure. As one can see, the value of S_L for ^{4}He stays below 1.0 for the range measured in our experiment (which is different from the prediction of GFMC model in Fig. 1-17), and agree well with previous world data within uncertainties.

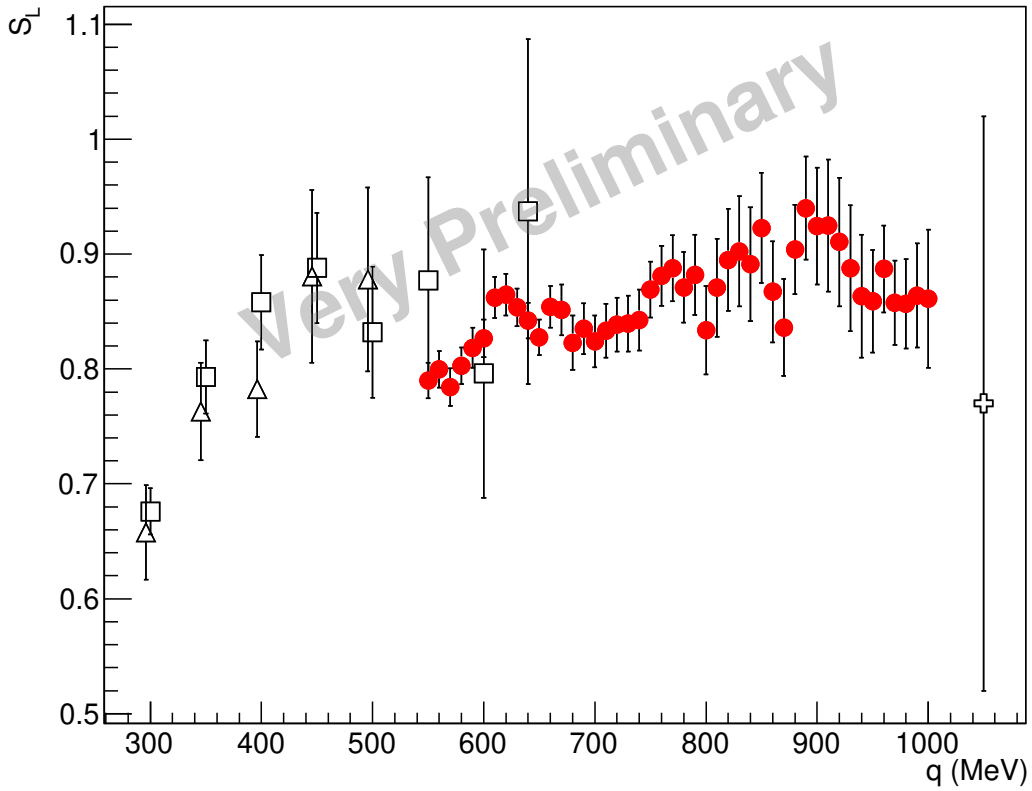

Figure 5-24: Preliminary results of ^{4}He Coulomb sum of this experiment (red filled circle), compared with previous data from Saclay (open box) [11], Bates (open triangles) [54] and SLAC (open crossing) [56].

Appendix A

Rosenbluth Formula

The derivation of Rosenbluth formula which describes the electron nucleus scattering is presented here briefly.

In the Plane Wave Born Approximation (PWBA), an inclusive unpolarized electron scattering process occurs through the exchange of a single virtual photon. Using Feynman rules, the cross section can be written as:

$$d\sigma = 2Z^2\alpha^2 \frac{d\vec{k}_f}{2E_f} \frac{1}{Q^4} W_{\mu\nu}\eta_{\mu\nu} \frac{1}{[(k_i \cdot P_i)^2 - m_e^2 M^2]^{1/2}}, \tag{A.1}$$

The leptonic tensors is:

$$\eta_{\mu\nu} = -\frac{1}{2}\sum_{s_i}\sum_{s_f} E_i E_f \overline{\mu}(k_i)\gamma_\nu \mu(k_f)\overline{\mu}(k_f)\gamma_\mu \mu(k_i), \tag{A.2}$$

where $\mu(k_i)$ and $\mu(k_f)$ are the initial and final electron plane wave functions, respectively.

The hadronic tensor is

$$W_{\mu\nu} = \frac{(2\pi)^3\Omega}{Z^2}\sum_{S_i}\sum_{S_f} E_t \gamma^{(4)}(P_i - P_f - q)\langle i|J_\nu(0)|f\rangle\langle f|J_\mu(0)|i\rangle, \tag{A.3}$$

where $J_{mu}(0)$ is the electromagnetic current operator of the nucleus at the space-time point $x_\mu = 0$. $|i\rangle$, $|f\rangle$ are the initial and final nuclear states, Ω is the normalization

volume, E_t is the initial target energy. The average over the initial leptonic spin states s_i gives a factor 1/2 and the average over the initial target spin states S_i is indicated by $\sum$. The final spin states of the lepton and nucleus, s_f and S_f are to be summed over.

The leptonic tensor can be simplified as:

$$\eta_{\mu\nu} = -\frac{1}{2} Tr\gamma_\mu(m_e - i\gamma \cdot k_i)\gamma_\nu(m_e - i\gamma \cdot k_f) \tag{A.4}$$

where m_e is the electron mass. If neglecting the electron mass, Eq. A.4 can be written as:

$$\eta_{\mu\nu} = -\frac{1}{2}[(k_1)_\mu(k_2)_\nu + (k_2)_\mu(k_1)_\nu - (k_1 \cdot k_2)g_{\mu\nu}] \tag{A.5}$$

The hardronic tensor $W_{\mu\nu}$ is a second order tensor built out of the two independent 4-vectors P and q With the target mass known, there are only two independent Lorentz scalers, Q^2 and $q \cdot P$. The most general tensor we can make out of P and q that satisfies the parity symmetry is

$$\begin{aligned} W_{\mu\nu} = & W_1(Q^2, q \cdot P)g_{\mu\nu} + W_2(Q^2, q \cdot P)\frac{P_\mu P_\nu}{M^2} \\ & + A\frac{q_\mu q_\nu}{M^2} + B\frac{1}{M^2}(P_\mu q_\nu + P_\nu q_\mu) + C\frac{1}{M^2}(P_\mu q_\nu - P_\nu q_\mu). \end{aligned} \tag{A.6}$$

Using current conservation:

$$q_\mu W_{\mu\nu} = W_{\mu\nu} q_\nu = 0, \tag{A.7}$$

the hardronic tensor can be simplified with only two independent terms:

$$\begin{aligned} W_{\mu\nu} = & W_1(Q^2, q \cdot P)\left(g_{\mu\nu} - \frac{q_\mu q_\nu}{Q^2}\right) \\ & + W_2(Q^2, q \cdot P)\frac{1}{M^2}\left(P_\mu - \frac{P \cdot q}{Q^2}q_\mu\right)\left(P_\nu - \frac{P \cdot q}{Q^2}q_\nu\right) . \end{aligned} \tag{A.8}$$

In the laboratory frame where $P \cdot q = \omega M$, one obtains the cross section:

$$\frac{d^2\sigma}{d\Omega d\omega} = \frac{Z^2 \sigma_M}{M} \left[W_2(Q^2, \omega) + 2W_1(Q^2, \omega) \tan^2 \frac{\theta}{2} \right], \tag{A.9}$$

where W_1 and W_2 are the structure functions of the target nucleus and are related to the longitudinal and transverse response functions:

$$R_T(Q^2, \omega) = \frac{2Z^2}{M} W_1(Q^2, \omega), \tag{A.10}$$

$$R_L(Q^2, \omega) = \frac{Z^2}{M} \left[\left(\frac{|\vec{q}|^4}{Q^4} \right) W_2(Q^2, \omega) - \left(\frac{|\vec{q}|^2}{Q^2} \right) W_1(Q^2, \omega) \right]. \tag{A.11}$$

Then we can obtain the Rosenbluth formula, Eq. 1.10.

Appendix B

Radiative Corrections

The cross section in the Rosenbluth formula is derived to the lowest order in the fine-structure constant α that includes only the amplitude due to exchange of a single virtual photon between the incident electron and the nucleon. This is known as Born approximation. The cross section measured in electron scattering has large contributions from higher order processes and the straggling effect. So the raw cross sections extracted from experiments need to be corrected in order to extract Born cross sections. This correction is called "radiative correction".

Feynman diagrams of the second order and third order processes are shown in Fig. B-1. Diagram (a) is the vacuum polarization which modifies the photon propagator and partly renormalizes the electron charge. Diagram (b) is the vertex correction which cancels the wave function renormalization in (c) and (d). Diagrams (c) and (d) are the self-energy diagrams which contribute to the renormalization of the electron mass and wave function. Diagrams (e) and (f) describe the bremsstrahlung process before and after scattering. The hadronic radiations are negligible due to the large hadronic masses.

The radiation processes that happen during the main scattering are called “internal” processes. Bremsstrahlung and ionization happen when electrons pass through target material before and after the main scattering, and are referred to as “external” processes. The internal processes are proportional to the target thickness T, while the external processes are proportional to T^2.

In this section, a summary of theory and procedures of radiative correction is given, including subtraction of the elastic tail, radiative corrections for quasi-elastic data and radiative corrections for elastic data.

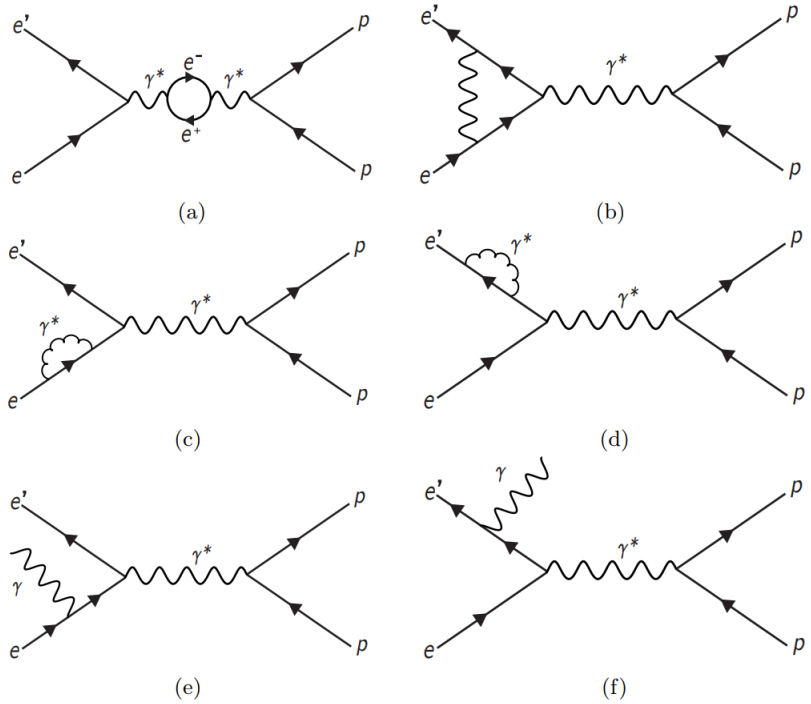

Figure B-1: Next to leading order Feynman diagrams for internal radiative corrections: (a) vacuum polarization, (b) vertex correction, (c)/(d) electron self-energy, and (e)/(f) Bremsstrahlung before and after scattering.

B.1 Subtraction of the Elastic Radiative Tail

Following the formalism of Mo and Tsai [49] and Stein [57], the cross section for the elastic radiative tail includes several parts:

$$\sigma_{eltail} = (\sigma_{int} + \sigma_{ext}) \cdot F_{soft} \tag{B.1}$$

where σ_{int}, σ_{ext} and F_{soft} represent the internal bremsstrahlung, external bremsstrahlung and soft photon corrections, respectively. Cross sections for single photon emission from both internal and external processes are corrected by including the multiple soft

photon emission:

$$F_{soft} = \left(\frac{\omega_s}{E_s}\right)^{b(t_b+t_r)} \left(\frac{\omega_p}{E_p+\omega_p}\right)^{b(t_a+t_r)}, \tag{B.2}$$

where t_b, t_a are the radiation thicknesses before and after scattering. The "equivalent radiator" thickness t_r is used to describe the effect of internal Bremsstrahlung, which can be approximated by two external radiators with one placed before and one after the scattering process, each with thickness:

$$t_r = \left(\frac{\alpha}{b\pi}\right)\left[\ln\left(\frac{Q^2}{m_e^2}\right) - 1\right]. \tag{B.3}$$

B.1.1 Internal Elastic Tail

The internal Bremsstrahlung cross section for elastic scattering can be calculated exactly to the lowest order order of α if we assume one-photon exchange:

$$\sigma_{int} = \int B_{\mu\nu} T_{\mu\nu} d\Omega_k, \tag{B.4}$$

where $B_{\mu\nu}$ is the internal Bremsstrahlung tensor and $T_{\mu\nu}$ is the lepton tensor which includes the form factors W_1 and W_2.

The exact cross section for the elastic radiative tail is expressed as:

$$\begin{aligned}
\sigma_{exact} \;=\; & \left(\frac{d^2\sigma}{d\Omega dE_p}\right) = \frac{\alpha^3}{2\pi}\left(\frac{E_p}{E_s}\right)\int_{-1}^{1} \frac{2M_T\omega d\cos\theta_k}{q^4(u_0 - |\vec{u}|\cos\theta_k)} \\
& \times\Bigg(\tilde{W}_2(q^2)\Bigg\{\frac{-am^3}{x^3}\left[2E_s(E_p+\omega)+\frac{q^2}{2}\right] - \frac{a'm^2}{y^3}\left[2E_p(E_s+\omega)+\frac{q^2}{2}\right] \\
& -2+2\nu(x^{-1}-y^{-1})\{m^2(s\cdot p-\omega^2)+(s\cdot p)[2E_sE_p-(s\cdot p)+\omega(E_s-E_p)]\} \\
& +x^{-1}\left[2(E_sE_p+E_s\omega+E_p^2)+\frac{q^2}{2}-(s\cdot p)-m^2\right] \\
& -y^{-1}\left[2(E_pE_s+E_p\omega+E_s^2)+\frac{q^2}{2}-(s\cdot p)-m^2\right]\Bigg\} \\
& +\tilde{W}_1(q^2)\Bigg[\left(\frac{a}{x^3}+\frac{a'}{y^3}m^2(2m^2+q^2)+4+4\nu(x^{-1}-y^{-1})(s\cdot p)(s\cdot p-2m^2)\right) \\
& +(x^{-1}-y^{-1}(2s\cdot p+2m^2-q^2))\Bigg]\Bigg).
\end{aligned} \tag{B.5}$$

The kinematic parameters (ω, ν, s, p...) are defined in [57]. The two terms $\tilde{W}_1$ and $\tilde{W}_2$ contain elastic form factors and are defined as:

$$\tilde{W}_1(q^2) = \tilde{F}(q^2)W_1(q^2), \tag{B.6}$$

$$\tilde{W}_2(q^2) = \tilde{F}(q^2)W_2(q^2). \tag{B.7}$$

The function $\tilde{F}(q^2)$ represents corrections that are independent of photon energy ω:

$$\tilde{F}(q^2) = (1 + 0.5772 \cdot bT) + \frac{2}{\pi}\left[-\frac{14}{9} + \frac{13}{12}\ln\frac{Q^2}{m^2}\right] + \frac{\alpha}{\pi}\left[\frac{1}{6}\pi^2 - \Phi(\cos^2\frac{\theta}{2})\right] \ , \tag{B.8}$$

where the first term is a normalization factor from the expression for the external Bremsstrahlung, the second term is the sum of vacuum polarization and vertex corrections, and the last term is from Schwinger [58]. $\Phi(x)$ is the Spence function:

$$\Phi(x) = \int_0^x \frac{-\ln|1-y|}{y}dy, \tag{B.9}$$

$$b = \frac{4}{3}\{1 + \frac{1}{9}[(Z+1)/(Z+\eta)][\ln(183Z^{-1/3})]^{-1}\}, \tag{B.10}$$

$$\eta = \ln(1440Z^{-2/3})/\ln(183Z^{-1/3}), \tag{B.11}$$

B.1.2 External Elastic Tail

The probability of an electron with energy E_0 emitting a photon with energy E in material thickness t can be expressed as:

$$I(E_0, E, t) = \frac{1}{\Gamma(1+bt)}\left(\frac{E_0 - E}{E_0}\right)^{bt}\left[\left(\frac{bt}{E_0 - E}\right)\phi\left(\frac{E_0 - E}{E_0}\right) + \frac{\xi}{(E_0 - E)^2}\right], \tag{B.12}$$

where $\Gamma(x)$ is the gamma function, and $\phi(v) \approx 1 - v + \frac{3}{4}v^2$ is the shape of the Bremsstrahlung spectrum. The internal Bremsstrahlung cross section σ_r is weighted by this probability function and integrated over all possible incoming and outgoing

electron energies to obtain the external elastic tail:

$$\sigma_{ext}(E_s, E_p) = \int_0^T \frac{dt}{T} \int_{E_s^{min}}^{E_s} \int_{E_p}^{E^{max}} dE'_p I(E_s, E'_s, t)\sigma_r(E'_s, E'_p)I(E_p, E'_p, T-t), \quad \text{(B.13)}$$

where the limits of the integration are:

$$E_p^{max} = \frac{E'_s}{1 + \frac{E_s}{M}(1 - \cos\theta)}, \quad \text{(B.14)}$$

$$E_s^{min} = \frac{E_p}{1 + \frac{E_p}{M}(1 - \cos\theta)}. \quad \text{(B.15)}$$

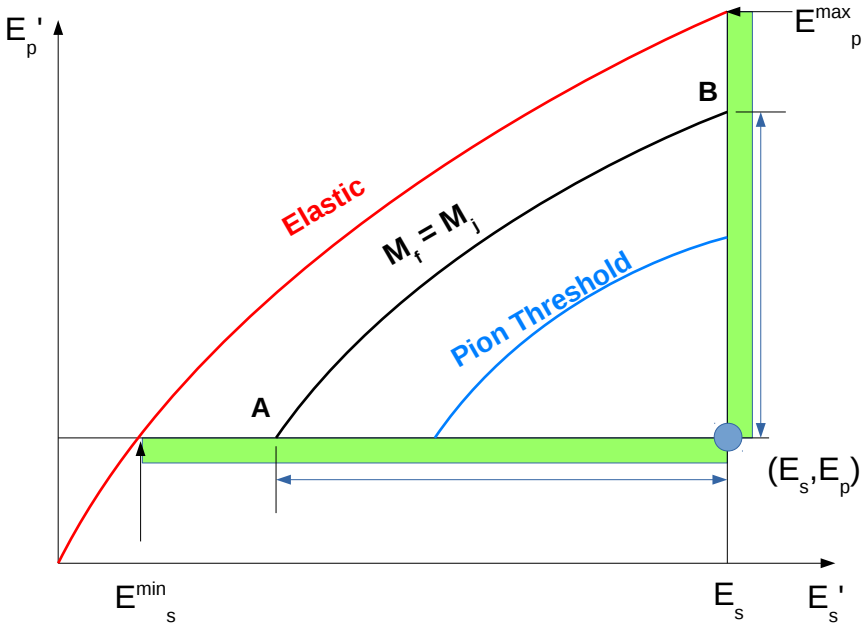

Figure B-2: two-dimensional integral area for external Bremsstrahlung.

The integration region for Eq. B.13 is shown in Fig. B-2. The integration is heavily peaked near the green horizontal and vertical regions, therefore this two-dimensional

integral can be approximated by two one-dimensional integrals:

$$\sigma_{ext}(E_s, E_p) \approx \int_0^T \frac{dt}{T}\Bigg[\tilde{\sigma}(E_s) I(E_p+\omega_p, E_p, T-t) \int_{E_s-\omega_s}^{E_s} dE_s' I(E_s, E_s', t) + \tilde{\sigma}(E_s-\omega_s)\frac{M+(E_s+\omega_s)(1-\cos\theta)}{M-E_p(1-\cos\theta)} I(E_s, E_s-\omega_s, t) \times \int_{E_p}^{E_p+\omega_p} dE_p' I(E_p', E_p, T-t)\Bigg]. \tag{B.16}$$

If we complete the integral including external Bremsstrahlung as well as ionization loss before and after scattering, the external elastic tail can be written as:

$$\sigma_{ext}(E_s, E_p) = \frac{M_T + 2(E_s-\omega_s)\sin^2\frac{\theta}{2}}{M_T - 2E_p\sin^2\frac{\theta}{2}} \times \tilde{\sigma}_{el}(E_s-\omega_s)\left[\frac{bt_b}{\omega_s}\phi(\nu_s) + \frac{\xi}{2\omega_s^2}\right] + \tilde{\sigma}_{el}(E_s)\left[\frac{bt_a}{\omega_p}\phi(\nu_p) + \frac{\xi}{2\omega_p^2}\right] \tag{B.17}$$

where

$$\omega_s = E_s - \frac{E_p}{1-2\frac{E_p}{M_T}\sin^2\frac{\theta}{2}}, \tag{B.18}$$

$$\omega_p = \frac{E_s}{1+2\frac{E_s}{M_T}\sin^2\frac{\theta}{2}} - E_p, \tag{B.19}$$

$$\xi = \frac{\pi m}{2\alpha}\frac{t_a+t_b}{(Z+\eta)\ln(183/Z^{1/3})}, \tag{B.20}$$

$$\nu_s = \omega_s/E_s, \tag{B.21}$$

$$\nu_p = \omega_p/(E_p+\omega_p), \tag{B.22}$$

$$\tilde{\sigma}_{el} = \tilde{F}(q^2)\sigma_{el}(E), \tag{B.23}$$

σ_{el} is the elastic cross section defined from the elastic form factors. The approximation for the shape of the Bremsstrahlung spectrum $\phi(\nu)$ holds for $E > 100$ MeV and $\nu < 0.8$ (in unit of 1).

B.2 Radiative Corrections for Quasi-elastic Data

While the radiative correction for elastic tail is for a discrete state, the radiative corrections for quasi-elastic data are reached by integrating over all states. In order to simplify the calculation, the integral Bremsstrahlung spectrum is approximated by the external Bremsstrahlung spectrum, and the method of equivalent radiators is used. Radiative corrections for quasi-elastic data were calculated using formula of Stein *et al.* [57]:

$$\begin{aligned}\left(\frac{d^2\sigma}{d\Sigma d\omega}\right)_{exp} &= \left(\frac{R\Delta E}{E_s}\right)^{bt'_b}\left(\frac{\Delta E}{E_p}\right)^{bt'_a}\left[1-\frac{\xi/\Delta E}{1-b(b(t'_a+t'_b))}\right]\tilde{\sigma}(E_s,E_p)\\ &+\int_{E_s^{min}}^{E_s-R\Delta E}\tilde{\sigma}(E'_s,E_p)\left(\frac{E_s-E'_s}{RE_p}\right)^{bt'_a}\left(\frac{E_s-E'_s}{E_s}\right)^{bt'_b}\\ &\times\left[\frac{bt'_b}{E_s-E'_s}\phi\left(\frac{E_s-E'_s}{E_s}\right)+\frac{\xi}{2(E_s-E'_s)^2}\right]dE'_s\\ &+\int_{E_p+\Delta E}^{E_p^{max}}\tilde{\sigma}(E_s,E'_p)\left(\frac{E'_p-E_p}{E'_p}\right)^{bt'_a}\left(\frac{R(E'_p-E_p)}{E_s}\right)^{bt'_b}\\ &\times\left[\frac{bt'_a}{E'_p-E_p}\phi\left(\frac{E'_p-E_p}{E'_p}\right)+\frac{\xi}{2(E'_p-E_p)^2}\right]dE'_p\ ,\end{aligned} \tag{B.24}$$

where the first term is the integral of low energy photon, the second term is the integral due to energy loss before scattering, and the last term is the integral due to energy loss after scattering. In Eq. B.24, $t'_a = t_a + t_r$ and $t'_b = t_b + t_r$ are radiation thicknesses include the equivalent radiator. The integration limits are given by:

$$E_s^{min} = \frac{M_T E_p}{M_T - 2E_p\sin^2(\theta/2)}, \tag{B.25}$$

$$E_p^{max} = \frac{M_T E_s}{M_T + 2E_s\sin^2(\theta/2)}, \tag{B.26}$$

and

$$R = \frac{M_T + 2E_i\sin^2(\theta/2)}{M_T - 2E_f\sin^2(\theta/2)}. \tag{B.27}$$

B.3 Radiative Corrections for Elastic Data

The radiative correction to the elastic peak has been well studied. The relation between the cross section measured in experiments and the Born cross section is:

$$\left(\frac{d\sigma}{d\Omega}\right)_{exp} = (1+\delta)\left(\frac{d\sigma}{d\Omega}\right)_{Born}, \tag{B.28}$$

where δ is the radiative correction factor. Higher order corrections can be taken into account by replacing $1+\delta$ with e^{δ}.

The expression of δ is given as a sum of the external and internal terms:

$$\delta = \delta_{int} + \delta_{ext}. \tag{B.29}$$

The internal term include contribution from internal Bremsstrahlung, vacuum polarization and nucleus recoil and photon emission:

$$\begin{aligned}
\delta_{int} \;=\; & \frac{-\alpha}{\pi}\left(\frac{28}{9} - \frac{13}{6}\ln\left(\frac{Q^2}{m_e^2}\right) + \left(\ln\left(\frac{Q^2}{m_e^2}\right) - 1 + 2Z\ln\left(\frac{E_s}{E_p}\right)\right)\right. \\
& \times\left[2\ln\left(\frac{E_s}{\Delta E}\right) - 3\ln\left(\frac{E_s}{E_p}\right)\right] \\
& -\Phi\left(\frac{E_p - E_s}{E_p}\right) - Z^2\ln\left(\frac{E_T}{M_T}\right) + Z^2\ln\left(\frac{M_T E_p}{E_s \Delta E}\right)\left(\frac{1}{\beta_t}\ln\left(\frac{1+\beta_t}{1-\beta_t}\right) - 2\right) \\
& +\frac{Z^2}{\beta_t}\left\{\frac{1}{2}\ln\left(\frac{1+\beta_t}{1-\beta_t}\right)\ln\left(\frac{E_T+M_T}{2M_T}\right) - \Phi\left[-\left(\frac{E_T - M_T}{E_T+M_T}\right)\left(\frac{1+\beta_t}{1+\beta_t}\right)^{\frac{1}{2}}\right]\right\} \\
& -Z\Big[\Phi\left(-\frac{E_T - E_p}{E_p}\right) - \Phi\left(\frac{M_T(E_T - E_p)}{2E_s E_T - M_T E_p}\right) + \Phi\left(\frac{2E_s(E_T - E_p)}{2E_s E_T - M_T E_p}\right) \\
& +\ln\left|\frac{2E_s E_T - M_T E_p}{E_p(M_T - 2E_s)}\right|\ln\left(\frac{M_T}{2E_s}\right)\Big] \\
& -\Big[\Phi\left(-\frac{M_T - E_p}{E_p}\right) - \Phi\left(\frac{M_T - E_p}{E_p}\right) + \Phi\left(\frac{2(M_T - E_p)}{M_T}\right) \\
& +\ln\left|\frac{M_T}{2E_p - M_T}\right|\ln\left(\frac{M_T}{2E_p}\right)\Big] \\
& \left.+\frac{Z^2}{\beta_t}\left\{\Phi\left[\left(\frac{E_T - M_T}{E_T+M_T}\right)^{\frac{1}{2}}\left(\frac{1-\beta_t}{1+\beta_t}\right)^{\frac{1}{2}}\right] - \Phi\left[\left(\frac{E_T - M_T}{E_T+M_T}\right)^{\frac{1}{2}}\right] + \Phi\left[-\left(\frac{E_T - M_T}{E_T+M_T}\right)^{\frac{1}{2}}\right]\right\}\right),
\end{aligned} \tag{B.30}$$

where E_T is the final energy of the target nucleus, $\beta_t = v_t/c$ is the final velocity of target nucleus. ΔE is the E_p cutoff of the elastic tail.

The external terms include straggling by the electron before and after the scattering, and is given by:

$$\delta_{ext} = -\left[(b_w t_{iw} + b t_i)\ln\left(\frac{E_p^2}{E_s \Delta E}\right) + (b_w t_{fw} + b t_f)\ln\left(\frac{E_p}{\Delta E}\right)\right], \tag{B.31}$$

where t_i and t_f are the target thicknesses before and after scattering in radiation lengths. t_{iw} and t_{fw} are the thicknesses of the entrance and exit windows. b and b_w are given in Eq. B.10, calculated using Z the charge numbers of the target and the window, respectively.

Appendix C

Longitudinal and Transverse Response Function Results

The longitudinal and transverse response functions for ^{4}He extracted from this analysis are listed below. The 1^{st} to 6^{th} columns are, respectively, magnitude of three-momentum-transfer $|\vec{q}|$ in MeV, energy loss of electron ω in MeV, longitudinal response function R_L and its uncertainty δR_L, transverse response function R_T and its uncertainty δR_T. The unit of all response functions and their uncertainties are in 1/MeV.

Table C.1: Longitudinal and transverse response function R_L and R_T for ^{4}He from this analysis.

q	ω	R_L	δR_L	R_T	δR_T
600	80	2.8543e-04	1.4294e-04	-5.0933e-06	1.8350e-04
600	90	3.7168e-04	1.6262e-04	4.3654e-04	1.9791e-04
600	100	5.8499e-04	1.5352e-04	5.6812e-04	2.4204e-04
600	110	8.0270e-04	1.7999e-04	9.1163e-04	2.9171e-04
600	120	7.7443e-04	1.8825e-04	1.8518e-03	1.8480e-04
600	130	8.9635e-04	1.7611e-04	2.8263e-03	2.0603e-04
600	140	1.3140e-03	1.6618e-04	3.4039e-03	1.8168e-04
600	150	1.3585e-03	2.0189e-04	4.5463e-03	2.8706e-04

Table C.1 – continued from previous page

q	ω	R_L	δR_L	R_T	δR_T
600	160	2.0472e-03	2.1389e-04	5.1888e-03	2.2187e-04
600	170	2.2847e-03	1.6214e-04	6.1269e-03	1.6389e-04
600	180	2.9266e-03	1.2211e-04	6.7386e-03	1.2262e-04
600	190	2.7424e-03	1.8120e-04	7.2094e-03	1.6840e-04
600	200	2.7764e-03	2.2031e-04	7.2812e-03	2.1583e-04
600	210	2.4874e-03	2.0688e-04	7.1820e-03	2.2317e-04
600	220	2.3275e-03	1.8689e-04	6.7471e-03	1.7444e-04
600	230	2.0432e-03	1.4740e-04	6.1510e-03	1.3129e-04
600	240	1.7022e-03	2.0736e-04	5.7165e-03	1.9525e-04
600	250	1.4784e-03	2.0925e-04	5.0405e-03	1.5990e-04
600	260	1.0716e-03	1.4062e-04	4.6380e-03	1.2579e-04
600	270	7.4452e-04	1.3467e-04	4.3897e-03	1.4340e-04
600	280	4.0182e-04	7.5738e-05	4.2767e-03	1.0564e-04
600	290	5.5618e-04	6.6471e-05	3.7063e-03	9.1532e-05
600	300	4.3147e-04	9.0104e-05	3.7014e-03	1.0875e-04
600	310	3.3287e-04	8.9670e-05	3.7646e-03	8.0070e-05
600	320	2.6702e-04	5.6598e-05	3.8528e-03	4.7285e-05
600	330	2.3859e-04	5.1771e-05	4.1439e-03	3.2430e-05
600	340	1.9309e-04	7.1121e-05	4.5224e-03	1.6658e-05
600	350	8.6450e-05	6.0033e-05	5.0230e-03	6.7345e-05
700	110	1.0497e-04	6.5471e-05	3.8546e-05	5.9645e-05
700	120	1.8037e-04	6.5336e-05	9.7562e-05	7.5207e-05
700	130	2.1154e-04	8.6119e-05	2.6255e-04	1.1434e-04
700	140	2.6635e-04	6.7946e-05	4.7497e-04	1.1104e-04
700	150	3.5726e-04	1.2497e-04	6.8900e-04	1.6357e-04
700	160	4.7695e-04	1.2570e-04	1.0248e-03	1.3692e-04
700	170	4.3007e-04	9.5887e-05	1.5771e-03	1.1557e-04
700	180	7.4226e-04	1.4684e-04	1.7989e-03	1.0592e-04

Table C.1 – continued from previous page

q	ω	R_L	δR_L	R_T	δR_T
700	190	5.9453e-04	5.8698e-05	2.6790e-03	8.5948e-05
700	200	9.3741e-04	1.0104e-04	3.1418e-03	8.4991e-05
700	210	1.1435e-03	1.6594e-04	3.7942e-03	1.6585e-04
700	220	1.2505e-03	8.5646e-05	4.3499e-03	6.8792e-05
700	230	1.4664e-03	1.1229e-04	4.9118e-03	1.1564e-04
700	240	1.7523e-03	1.2702e-04	5.0080e-03	6.9416e-05
700	250	1.5807e-03	1.5338e-04	5.5219e-03	1.0571e-04
700	260	1.5764e-03	2.0685e-04	5.5894e-03	1.5502e-04
700	270	1.4878e-03	1.4511e-04	5.5059e-03	1.3040e-04
700	280	1.2586e-03	1.0684e-04	5.3630e-03	2.3201e-05
700	290	1.0773e-03	1.1719e-04	5.0538e-03	7.5844e-05
700	300	8.2505e-04	1.0338e-04	4.7384e-03	2.1508e-05
700	310	7.3507e-04	1.4117e-04	4.2837e-03	1.1015e-04
700	320	6.1230e-04	1.7345e-04	3.9962e-03	1.6077e-04
700	330	4.3778e-04	7.3898e-05	3.6824e-03	4.6625e-05
700	340	4.6445e-04	1.0040e-04	3.4592e-03	9.8322e-05
700	350	2.4321e-04	8.3413e-05	3.4878e-03	5.7593e-05
700	370	2.9899e-04	8.8143e-05	3.5009e-03	7.0059e-05
700	380	1.8591e-04	1.1323e-04	3.7546e-03	4.2434e-05
700	390	2.1575e-04	3.5339e-05	4.0182e-03	3.3599e-05
700	410	1.1265e-04	7.8502e-05	4.8016e-03	3.3976e-05
700	440	8.0508e-05	2.4802e-04	6.2348e-03	1.4909e-04
700	450	6.2064e-05	3.4044e-04	6.7797e-03	2.2799e-04
700	470	3.1232e-04	4.0371e-04	7.5828e-03	2.6402e-04
700	480	1.6139e-04	2.9918e-04	8.0602e-03	2.9359e-04
800	140	5.2469e-05	6.3081e-05	1.0342e-05	3.9651e-05
800	150	1.0095e-04	6.1816e-05	1.6527e-05	5.0043e-05
800	160	6.9779e-05	2.7131e-05	1.0762e-04	2.3419e-05

Table C.1 – continued from previous page

q	ω	R_L	δR_L	R_T	δR_T
800	170	1.0813e-04	3.8368e-05	1.4745e-04	4.8304e-05
800	180	1.1774e-04	4.6622e-05	2.5586e-04	6.4750e-05
800	190	1.4268e-04	5.5854e-05	3.8690e-04	5.3191e-05
800	200	1.7494e-04	6.5771e-05	5.2829e-04	5.3668e-05
800	210	1.8428e-04	9.0308e-05	7.4223e-04	5.9421e-05
800	220	2.4772e-04	1.0440e-04	9.5905e-04	8.6449e-05
800	230	3.1996e-04	9.4332e-05	1.2290e-03	7.9132e-05
800	240	4.4801e-04	9.4049e-05	1.5462e-03	8.8981e-05
800	250	6.2466e-04	7.6165e-05	1.8767e-03	5.7792e-05
800	260	8.2011e-04	9.9291e-05	2.2093e-03	8.2245e-05
800	270	8.2734e-04	9.8366e-05	2.7528e-03	8.4899e-05
800	280	9.0520e-04	1.1770e-04	3.1071e-03	1.0303e-04
800	290	7.4290e-04	1.2033e-04	3.5690e-03	6.7599e-05
800	300	9.6879e-04	1.3722e-04	3.8959e-03	1.2271e-04
800	310	8.8033e-04	2.1906e-04	4.1386e-03	1.5584e-04
800	320	1.6605e-04	1.0145e-04	4.4959e-03	4.2993e-05
800	330	8.4481e-04	2.1723e-04	4.1933e-03	1.3390e-04
800	340	1.0633e-03	1.5817e-04	3.8753e-03	8.5219e-05
800	350	7.3503e-04	1.8996e-04	3.9633e-03	1.2504e-04
800	360	8.9823e-04	1.7745e-04	3.5748e-03	1.2329e-04
800	370	7.6103e-04	1.5185e-04	3.4506e-03	1.0755e-04
800	380	8.0460e-04	1.4600e-04	3.1581e-03	9.1204e-05
800	390	8.6690e-04	1.2010e-04	2.9530e-03	8.2096e-05
800	400	6.8590e-04	1.1782e-04	2.8274e-03	8.0168e-05
800	410	3.6754e-04	1.0808e-04	3.0293e-03	8.7189e-05
800	420	3.4120e-04	8.0968e-05	2.9969e-03	7.8901e-05
800	430	2.6206e-04	1.1505e-04	3.1373e-03	8.6993e-05
800	440	1.1187e-04	7.9192e-05	3.3896e-03	5.2880e-05

Table C.1 – continued from previous page

q	ω	R_L	δR_L	R_T	δR_T
800	450	1.2567e-04	9.0091e-05	3.5440e-03	6.5920e-05
800	460	6.8505e-05	7.6119e-05	3.8856e-03	3.1525e-05
800	470	7.6737e-05	8.6148e-05	4.1764e-03	4.9007e-05
800	480	2.0489e-04	7.3688e-05	4.4084e-03	5.7815e-05
800	490	2.1798e-04	8.5965e-05	4.7514e-03	7.2599e-05
800	500	2.0971e-04	1.4372e-04	5.1740e-03	9.0138e-05
800	510	8.1747e-05	1.3151e-04	5.5852e-03	9.7790e-05
800	520	4.1556e-04	3.6348e-04	5.7248e-03	2.8648e-04
800	530	5.0730e-04	3.7290e-04	5.9449e-03	3.2413e-04
800	540	7.3472e-04	5.4406e-04	6.0890e-03	4.5041e-04
800	550	9.8142e-04	7.4741e-04	6.2198e-03	5.6506e-04
900	200	6.0024e-05	4.3481e-05	3.3367e-05	3.4419e-05
900	220	6.4692e-05	2.9197e-05	1.1062e-04	3.0073e-05
900	230	5.8982e-05	2.7410e-05	1.6954e-04	1.6878e-05
900	240	7.4389e-05	5.2727e-05	2.3172e-04	3.8182e-05
900	250	7.7250e-05	5.6591e-05	3.3134e-04	5.2671e-05
900	260	1.0440e-04	6.6223e-05	4.2838e-04	2.4101e-05
900	270	1.3079e-04	7.0179e-05	5.6457e-04	4.5072e-05
900	280	1.6675e-04	7.4559e-05	7.1872e-04	4.8205e-05
900	290	2.3286e-04	1.0304e-04	8.6095e-04	6.3102e-05
900	300	3.6060e-04	6.4985e-05	1.0028e-03	4.9180e-05
900	310	4.3106e-04	1.0940e-04	1.2161e-03	7.1772e-05
900	320	6.1385e-04	9.5658e-05	1.3857e-03	6.7878e-05
900	330	5.8847e-04	1.2897e-04	1.7646e-03	9.9765e-05
900	340	6.9987e-04	1.7999e-04	2.0113e-03	1.4189e-04
900	350	6.6886e-04	1.8167e-04	2.3796e-03	1.4469e-04
900	360	5.3115e-04	1.0006e-04	2.8010e-03	7.7502e-05
900	370	6.9206e-04	2.1801e-04	2.8636e-03	1.5256e-04

Table C.1 – continued from previous page

q	ω	R_L	δR_L	R_T	δR_T
900	380	5.8618e-04	2.5036e-04	3.0796e-03	1.4874e-04
900	390	3.3911e-04	1.6147e-04	3.2886e-03	7.2117e-05
900	400	7.0527e-04	1.4024e-04	3.0315e-03	9.3753e-05
900	410	1.9291e-04	1.7665e-04	3.1915e-03	7.7126e-05
900	420	4.0931e-04	1.7136e-04	3.0825e-03	1.0752e-04
900	430	6.3052e-04	1.0154e-04	2.7407e-03	6.3694e-05
900	440	4.2964e-04	5.2566e-05	2.7522e-03	4.4806e-05
900	450	4.1964e-04	9.7827e-05	2.5917e-03	5.3113e-05
900	460	4.0476e-04	1.3228e-04	2.4980e-03	7.2362e-05
900	470	6.2791e-04	1.3521e-04	2.2879e-03	7.9602e-05
900	480	5.0708e-04	1.3568e-04	2.3833e-03	9.2775e-05
900	490	4.3182e-04	1.0430e-04	2.4006e-03	5.1124e-05
900	500	5.7135e-04	1.0916e-04	2.5262e-03	7.4131e-05
900	510	5.8170e-04	1.0149e-04	2.5543e-03	4.6212e-05
900	520	3.5382e-04	1.1583e-04	3.0157e-03	6.9331e-05
900	530	4.0631e-04	1.3966e-04	3.0824e-03	6.7937e-05
900	540	8.9554e-04	1.0108e-04	3.0744e-03	5.3261e-05
900	550	4.9622e-04	1.4678e-04	3.5059e-03	8.9666e-05
900	560	5.1543e-04	1.8444e-04	3.7214e-03	1.0537e-04
900	570	7.3812e-04	1.8736e-04	3.8599e-03	9.2028e-05
900	580	8.6335e-04	2.4755e-04	4.0580e-03	1.3475e-04
900	590	1.0061e-03	3.2007e-04	4.2912e-03	1.7389e-04
900	600	8.8758e-04	2.3200e-04	4.5119e-03	1.9842e-04
900	610	1.0181e-03	4.6944e-04	4.7133e-03	2.5141e-04
900	620	8.2445e-04	4.4932e-04	5.1195e-03	2.5039e-04
900	630	6.8175e-04	2.7231e-04	5.3950e-03	1.9337e-04
1000	310	5.8333e-05	5.6945e-05	2.1486e-04	2.0042e-05
1000	320	6.9113e-05	6.5485e-05	2.7035e-04	3.2808e-05

Table C.1 – continued from previous page

q	ω	R_L	δR_L	R_T	δR_T
1000	330	8.8743e-05	6.5814e-05	3.4532e-04	2.9804e-05
1000	340	1.1209e-04	8.1222e-05	4.3115e-04	3.1533e-05
1000	350	1.2259e-04	8.3911e-05	5.4328e-04	3.4732e-05
1000	360	1.5579e-04	1.2203e-04	6.7140e-04	7.3874e-05
1000	370	2.0184e-04	1.2663e-04	8.1111e-04	8.5837e-05
1000	380	2.5819e-04	1.8599e-04	9.6088e-04	1.1563e-04
1000	390	3.2448e-04	2.1752e-04	1.1146e-03	1.3440e-04
1000	400	4.0338e-04	2.3237e-04	1.2702e-03	1.3553e-04
1000	410	4.2614e-04	2.9214e-04	1.4487e-03	1.6666e-04
1000	420	4.4033e-04	3.0494e-04	1.6370e-03	1.7943e-04
1000	430	5.2240e-04	1.5796e-04	1.8143e-03	1.4364e-04
1000	440	3.5085e-04	3.7606e-04	2.0241e-03	2.1434e-04
1000	450	2.5035e-04	4.6419e-04	2.1807e-03	2.3892e-04
1000	460	2.2677e-04	5.0075e-04	2.2699e-03	2.4725e-04
1000	470	2.5298e-04	5.3024e-04	2.2968e-03	2.9021e-04
1000	480	2.1058e-04	5.3895e-04	2.3260e-03	2.7766e-04
1000	490	2.8700e-04	4.9172e-04	2.2557e-03	2.3875e-04
1000	500	2.6439e-04	5.0468e-04	2.2045e-03	2.7199e-04
1000	510	1.9096e-04	4.9110e-04	2.1874e-03	2.2479e-04
1000	520	1.6750e-04	4.5480e-04	2.1266e-03	1.9814e-04
1000	560	8.9054e-05	3.2612e-04	2.1100e-03	2.0522e-04
1000	570	1.7445e-04	2.8484e-04	2.1544e-03	1.7584e-04
1000	580	3.0325e-04	2.2058e-04	2.2782e-03	1.2999e-04
1000	590	2.7038e-04	2.0716e-04	2.4568e-03	1.4305e-04
1000	610	2.2475e-04	2.6221e-04	2.8519e-03	1.4550e-04
1000	620	1.0748e-04	1.8952e-04	3.1471e-03	1.0762e-04
1000	630	2.7963e-04	2.1302e-04	3.1171e-03	1.8233e-04
1000	640	4.2486e-04	2.3117e-04	3.2584e-03	1.9730e-04

Table C.1 – continued from previous page

q	ω	R_L	δR_L	R_T	δR_T
1000	650	4.5870e-04	2.3228e-04	3.5155e-03	2.1930e-04
1000	660	6.4708e-04	2.8889e-04	3.5841e-03	2.7854e-04
1000	670	9.3588e-04	4.1514e-04	3.5431e-03	3.6692e-04
1000	680	1.0430e-03	4.8140e-04	3.5939e-03	4.3209e-04
1000	690	9.3463e-04	6.2631e-04	3.8185e-03	4.6205e-04
1000	700	8.0316e-04	9.0018e-04	4.0548e-03	7.2294e-04

Appendix D

Coulomb Sum Results

Results on the Coulomb sum S_L for ^{4}He from this analysis, from $|\vec{q}| = 550$ MeV to 1100 MeV, are listed below. The 1^{st} to 3^{rd} columns are, respectively, $|\vec{q}|$ in MeV, Coulomb Sum S_L, and its uncertainty δS_L.

$\|\vec{q}\|$	S_L	δS_L
550	0.714	0.019
560	0.787	0.025
570	0.721	0.018
580	0.752	0.019
590	0.733	0.019
600	0.748	0.019
610	0.737	0.020
620	0.733	0.019
630	0.722	0.019
640	0.710	0.019
650	0.705	0.016
660	0.734	0.019
670	0.739	0.022
680	0.737	0.024
690	0.732	0.024
700	0.707	0.025

$\|\vec{q}\|$	S_L	δS_L
710	0.714	0.028
720	0.710	0.027
730	0.697	0.027
740	0.679	0.028
750	0.728	0.033
760	0.737	0.030
770	0.761	0.033
780	0.792	0.036
790	0.846	0.042
800	0.841	0.042
810	0.874	0.044
820	0.924	0.045
830	0.964	0.049
840	0.962	0.052
850	1.006	0.049
860	1.054	0.048

$\|\vec{q}\|$	S_L	δS_L
870	1.099	0.049
880	1.172	0.048
890	1.269	0.054
900	1.184	0.058
910	1.121	0.069
920	1.090	0.077
930	1.064	0.086
940	1.037	0.095
950	1.001	0.092
960	1.032	0.098
970	0.978	0.121
980	0.941	0.144
990	0.917	0.160
1000	0.953	0.174

Bibliography

[1] H. Atac. *Precision Measurement of Quasi-Elastic Transverse and Longitudinal Response Functions in the Range 0.55 GeV/c* $\leq |\vec{q}| \leq$ *1.0 GeV/c*. PhD thesis, Temple University, 2017.

[2] D.Drechsel. Intern. School on Electron and Photonuclear Reactions, Eric,1976. *Lecture Notes in Physics Physics*, 62:92, 1977.

[3] T. C. Ferrée and D. S. Koltun. Relativistic coulomb sum rules for (e,e'). *Phys. Rev. C*, 49:1961–1975, Apr 1994.

[4] R Rosenfelder. Quasielastic electron scattering from nuclei. *Annals of Physics*, 128(1):188 – 240, 1980.

[5] A. Dellafiore and M. Traini. Effects of c.m. motion in nuclear electron scattering. *Nuclear Physics A*, 344(3):509 – 525, 1980.

[6] G. Orlandini and M. Traini. Sum rules for electron-nucleus scattering. *Reports on Progress in Physics*, 54:257, 1991.

[7] J.W. Lightbody. Electron scattering sum rule for 12c-experiment and theory. *Physics Letters B*, 33(2):129 – 132, 1970.

[8] A. Dellafiore and D.M. Brink. Effects of neutron-proton interactions on elastic electron scattering. *Nuclear Physics A*, 286(3):474 – 482, 1977.

[9] S. Stringari. Long range dipole correlations and electron scattering sum rules. *Phys. Rev. C*, 29:1482–1485, Apr 1984.

[10] J. Morgenstern and Z.E. Meziani. Is the Coulomb sum rule violated in nuclei? *Phys. Lett.*, B515:259, 2001.

[11] S. A. Dytman, A. M. Bernstein, K. I. Blomqvist, T. J. Pavel, B. P. Quinn, R. Altemus, J. S. McCarthy, G. H. Mechtel, T. S. Ueng, and R. R. Whitney. Inclusive electron scattering from ^{2}H, ^{3}He, and ^{4}He. *Phys. Rev. C*, 38:800–812, Aug 1988.

[12] P. Barreau *et al.* Deep-inelastic electron scattering from carbon. *Nuclear Physics A*, 402(3):515 – 540, 1983.

[13] Z. E. Meziani *et al.* Coulomb sum rule for ^{40}Ca, ^{48}Ca, and ^{56}Fe for $|\vec{q}| \leq 550$ mev/c. *Phys. Rev. Lett.*, 52:2130–2133, Jun 1984.

[14] C. C. Blatchley *et al.* Quasi-elastic electron scattering from ^{238}U. *Phys. Rev. C*, 34:1243–1247, Oct 1986.

[15] J. P. Chen *et al.* Longitudinal and transverse response functions in ^{56}Fe(e,e') at momentum transfer near 1 gev/c. *Phys. Rev. Lett.*, 66:1283–1286, Mar 1991.

[16] J. Jourdan. Longitudinal response functions: the coulomb sum revisited. *Physics Letters B*, 353(2):189 – 195, 1995.

[17] A. Fabrocini and S. Fantoni. Microscopic calculation of the longitudinal response of nuclear matter. *Nuclear Physics A*, 503(2):375 – 403, 1989.

[18] Madeleine Soyeur, Gerald E. Brown, and Mannque Rho. In-medium behaviour of vector mesons and the longitudinal and transverse response functions in (e, e'p) reactions. *Nuclear Physics A*, 556(3):355 – 372, 1993.

[19] R. Schiavilla, D.S. Lewart, V.R. Pandharipande, Steven C. Pieper, R.B. Wiringa, and S. Fantoni. Structure functions and correlations in nuclei. *Nuclear Physics A*, 473(2):267 – 289, 1987.

[20] M. Traini, G. Orlandini, and W. Leidemann. Longitudinal response functions of heavier nuclei. *Phys. Rev. C*, 48:172–177, Jul 1993.

[21] D. *et al.* Lonardoni. Auxiliary field diffusion monte carlo calculations of light and medium-mass nuclei with local chiral interactions. *Phys. Rev. C*, 97:044318, Apr 2018.

[22] Marco Traini. Dwba (e,e) cross section and coulomb sum rule. *Physics Letters B*, 213(1):1 – 6, 1988.

[23] M. Traini, S. Turck-Chièze, and A. Zghiche. Deep inelastic electron scattering in the distorted-wave born approximation: An analytic approach. *Phys. Rev. C*, 38:2799–2812, Dec 1988.

[24] Yanhe Jin, D. S. Onley, and L. E. Wright. Single particle analysis of (e,e') and the value of separated structure functions. *Phys. Rev. C*, 45:1333–1338, Mar 1992.

[25] P.*et al.* Guèye. Coulomb distortion measurements by comparing electron and positron quasielastic scattering off ^{12}C and ^{208}Pb. *Phys. Rev. C*, 60:044308, Sep 1999.

[26] J. V. Noble. Modification of the nucleon's properties in nuclear matter. *Phys. Rev. Lett.*, 46:412–415, Feb 1981.

[27] L. S. Celenza, A. Harindranath, and C. M. Shakin. Sum rules for the longitudinal response in inclusive electron scattering. *Phys. Rev. C*, 33:1012–1019, Mar 1986.

[28] P.J. Mulders. Effective hadronic degrees of freedom in electron-nucleus scattering. *Nuclear Physics A*, 459(3):525 – 556, 1986.

[29] R. Altemus, A. Cafolla, D. Day, J. S. McCarthy, R. R. Whitney, and J. E. Wise. Longitudinal and transverse inelastic electron scattering from ^{56}Fe. *Phys. Rev. Lett.*, 44:965–968, Apr 1980.

[30] H. Yao. *Precision Measurement of Longitudinal and Transverse Response Functions of Quasi- Elastic Electron Scattering in the Momentum Transfer Range 0.55 GeV/c* $\leq |\vec{q}| \leq$ *1.0 GeV/c.* PhD thesis, Temple University, 2012.

[31] X. Yan. *Precision Measurement Longitudinal and Transverse Response Functions of Quasi-Elastic Electron Scattering in the Momentum Transfer Range in the Range 0.55 GeV/c $\leq |\vec{q}| \leq$ 1.0 GeV/c*. PhD thesis, University of Science and Technology of China, 2011.

[32] Y. Oh. *Study of Quasi-Elastic Scattering on Nuclei: Experimental Verification of the Coulomb Sum Rule*. PhD thesis, Seoul National University, 2013.

[33] X. Zheng. *Precision Measurement of Neutron Spin Asymmetry A_1^n at Large x_{Bj} Using CEBAF at 5.7 GeV*. PhD thesis, Massachusetts Institute of Technology, 2002.

[34] J. Alcorn *et al.* Basic Instrumentation for Hall A at Jefferson Lab. *Nucl. Instr. Meth. Phys. Res. A*, 522:294, 2004.

[35] Analyzing bpms. https://hallaweb.jlab.org/podd/doc/bpm.html.

[36] N. K. Liyanage. *Optics Calibration of the Hall A High Resolution Spectrometers Using the New Optimizer*. Technical Note, Jefferson Lab, 2002.

[37] Y. Qiang. *Search for Pentaquark Partners Θ++, Σ0 and N^0 in H(e,e'K(π))X Reactions at Jefferson Lab Hall A*. PhD thesis, MASSACHUSETTS INSTITUTE OF TECHNOLOGY, 2007.

[38] C. Gu. *The Spin Structure of the Proton at Low Q^2 : A Measurement of the Structure Function g_p^2*. PhD thesis, University of Virginia, 2017.

[39] Root user guide. https://root.cern.ch/guides/users-guide/.

[40] Extended target corrections. https://hallaweb.jlab.org/data_reduc/AnaWork2009/Extended-Target-Corrections-Jin.pdf.

[41] Samc package. https://userweb.jlab.org/~yez/Work/SAMC/.

[42] N. K. Liyanage. *Spectrometer constant determination for the Hall-A High Resolution Spectrometer pair*. Technical Note, Jefferson Lab, 2001.

[43] J. Alcorn *et al.* Basic instrumentation for hall a at jefferson lab. *Nuclear Instruments and Methods in Physics Research Section A: Accelerators, Spectrometers, Detectors and Associated Equipment*, 522(3):294 – 346, 2004.

[44] Zhihong Ye, John Arrington, Richard J. Hill, and Gabriel Lee. Proton and neutron electromagnetic form factors and uncertainties. *Physics Letters B*, 777:8 – 15, 2018.

[45] Useful Codes for Fitting and Analysis. https://hallcweb.jlab.org/resdata/codes/.

[46] J. W. Lightbody and J. S. O'Connell. Modeling single arm electron scattering and nucleon production from nuclei by gev electrons. *Computers in Physics*, 2(3):57–64, 1988.

[47] J.P. Chen. *The Longitudinal and Transverse Response Functions in* ^{56}*Fe(e,e') at* Q^2 *Near 1 (GeV/c)*^{2}. PhD thesis, University of Virginia, 1990.

[48] J.Ravenhal. ravenshift.f.

[49] L. W. MO and Y. S. TSAI. Radiative corrections to elastic and inelastic ep and up scattering. *Rev. Mod. Phys.*, 41:205–235, Jan 1969.

[50] I. Sick and J.S. McCarthy. Elastic electron scattering from 12c and 16o. *Nuclear Physics A*, 150(3):631 – 654, 1970.

[51] W. Reuter, G. Fricke, K. Merle, and H. Miska. Nuclear charge distribution and rms radius of ^{12}C from absolute elastic electron scattering measurements. *Phys. Rev. C*, 26:806–818, Sep 1982.

[52] I. Angeli. A consistent set of nuclear rms charge radii: properties of the radius surface r(n,z). *Atomic Data and Nuclear Data Tables*, 87(2):185 – 206, 2004.

[53] C. Ciofi degli Atti, E. Pace, and G. Salmè. y-scaling analysis of quasielastic electron scattering and nucleon momentum distributions in few-body systems, complex nuclei, and nuclear matter. *Phys. Rev. C*, 43:1155–1176, Mar 1991.

[54] A. Zghiche *et al.* Longitudinal and transverse responses in quasi-elastic electron scattering from 208pb and 4he. *Nuclear Physics A*, 572(3):513 – 559, 1994.

[55] J. Van Orden. *Deep-inelastic Electron Scattering from Nuclei.* PhD thesis, Stanford University, 1978.

[56] J. P. Chen *et al.* Z. E. Meziani. High momentum transfer $r_{t,}$l inclusive response functions for ^{3,4}He. *Phys. Rev. Lett.*, 69, Jul 1992.

[57] S. Stein, W. B. Atwood, E. D. Bloom, R. L. A. Cottrell, H. DeStaebler, C. L. Jordan, H. G. Piel, C. Y. Prescott, R. Siemann, and R. E. Taylor. Electron scattering at 4° with energies of 4.5-20 gev. *Phys. Rev. D*, 12:1884–1919, Oct 1975.

[58] Julian Schwinger. Quantum electrodynamics. ii. vacuum polarization and self-energy. *Phys. Rev.*, 75:651–679, Feb 1949.